

Gerard O'Reilly
Gian Michele Calvi *Editors*

Engineering Research Infrastructures for European Synergies

Proceedings of ERIES-IW2025

OPEN ACCESS



Springer

Series Editors

Marco di Prisco, *Politecnico di Milano, Milano, Italy*

Sheng-Hong Chen, *School of Water Resources and Hydropower Engineering, Wuhan University, Wuhan, China*

Ioannis Vayas, *Institute of Steel Structures, National Technical University of Athens, Athens, Greece*

Sanjay Kumar Shukla, *School of Engineering, Edith Cowan University, Joondalup, Australia*

Anuj Sharma, *Iowa State University, Ames, USA*

Nagesh Kumar, *Department of Civil Engineering, Indian Institute of Science Bangalore, Bengaluru, India*

Chien Ming Wang, *School of Civil Engineering, The University of Queensland, Brisbane, Australia*

Zhen-Dong Cui, *China University of Mining and Technology, Xuzhou, China*

Xinzheng Lu, *Department of Civil Engineering, Tsinghua University, Beijing, China*

Lecture Notes in Civil Engineering (LNCE) publishes the latest developments in Civil Engineering—quickly, informally and in top quality. Though original research reported in proceedings and post-proceedings represents the core of LNCE, edited volumes of exceptionally high quality and interest may also be considered for publication. Volumes published in LNCE embrace all aspects and subfields of, as well as new challenges in, Civil Engineering. Topics in the series include:

- Construction and Structural Mechanics
- Building Materials
- Concrete, Steel and Timber Structures
- Geotechnical Engineering
- Earthquake Engineering
- Coastal Engineering
- Ocean and Offshore Engineering; Ships and Floating Structures
- Hydraulics, Hydrology and Water Resources Engineering
- Environmental Engineering and Sustainability
- Structural Health and Monitoring
- Surveying and Geographical Information Systems
- Indoor Environments
- Transportation and Traffic
- Risk Analysis
- Safety and Security

To submit a proposal or request further information, please contact the appropriate Springer Editor:

- Pierpaolo Riva at pierpaolo.riva@springer.com (Europe and Americas);
- Swati Meherishi at swati.meherishi@springer.com (Asia—except China, Australia, and New Zealand);
- Wayne Hu at wayne.hu@springer.com (China).

All books in the series now indexed by Scopus and EI Compendex database!

Gerard O'Reilly · Gian Michele Calvi
Editors

Engineering Research Infrastructures for European Synergies

Proceedings of ERIES-IW2025

Editors

Gerard O'Reilly
ROSE Centre
Scuola Universitaria Superiore IUSS
Pavia, Italy

Gian Michele Calvi
ROSE Centre
Scuola Universitaria Superiore IUSS
Pavia, Italy



ISSN 2366-2557

ISSN 2366-2565 (electronic)

Lecture Notes in Civil Engineering

ISBN 978-3-031-98892-9

ISBN 978-3-031-98893-6 (eBook)

<https://doi.org/10.1007/978-3-031-98893-6>

This work was supported by European Commission.

© The Editor(s) (if applicable) and The Author(s) 2025. This book is an open access publication.

Open Access This book is licensed under the terms of the Creative Commons Attribution 4.0 International License (<http://creativecommons.org/licenses/by/4.0/>), which permits use, sharing, adaptation, distribution and reproduction in any medium or format, as long as you give appropriate credit to the original author(s) and the source, provide a link to the Creative Commons license and indicate if changes were made.

The images or other third party material in this book are included in the book's Creative Commons license, unless indicated otherwise in a credit line to the material. If material is not included in the book's Creative Commons license and your intended use is not permitted by statutory regulation or exceeds the permitted use, you will need to obtain permission directly from the copyright holder.

The use of general descriptive names, registered names, trademarks, service marks, etc. in this publication does not imply, even in the absence of a specific statement, that such names are exempt from the relevant protective laws and regulations and therefore free for general use.

The publisher, the authors and the editors are safe to assume that the advice and information in this book are believed to be true and accurate at the date of publication. Neither the publisher nor the authors or the editors give a warranty, expressed or implied, with respect to the material contained herein or for any errors or omissions that may have been made. The publisher remains neutral with regard to jurisdictional claims in published maps and institutional affiliations.

This Springer imprint is published by the registered company Springer Nature Switzerland AG
The registered company address is: Gewerbestrasse 11, 6330 Cham, Switzerland

If disposing of this product, please recycle the paper.

Preface

Natural hazards continue to cause immense harm worldwide through their direct and indirect impacts on the built environment, the economy, and the overall functionality of society. In particular, direct damage, financial losses, and operation interruptions caused by earthquakes and strong wind, combined with the impact of soil-structure interaction and hazards of geotechnical origin (i.e., liquefaction), are critical issues that still need to be addressed fully via innovative research and development. When considered collectively, the multi-hazard nature of their impacts, interaction, and cascading effects also forms a critical area requiring advanced research.

Past seismic events (e.g., L’Aquila 2009, Central Italy 2016–2017, Samos Island Aegean Sea 2020, Albania 2019, Croatia 2020), just to mention the most recent ones, have had an immense impact on society and continually highlight the need for future research and innovation. For example, the 2020 Aegean Sea earthquake left approximately 15,000 people homeless and had an estimated damage in excess of €400M, not to mention the numerous casualties. Local soil conditions of the Durrës coastal area played a significant role in the seismic performance of buildings during the November 2019 Earthquake in Albania, which took 52 human lives, saw more than 3,000 people injured, 14,000 remain homeless, and 14,000 buildings damaged. Geotechnical instabilities, soil liquefaction, and the appearance of sinkholes during the 2020 Petrinja, Croatia earthquake amplified the total damage and made the reconstruction efforts much more complicated and costly. Similarly, climate-related hazards also have the potential for notable impact on structures and infrastructures. During the past decades, strong storms have induced severe human losses and extensive damage to properties. For example, the great storm of 15th October 1987 caused €5M in damage and killed 34 people in France and the UK. The Lothar and Martin storms in December 1999 caused €13.5M of damage in Europe and killed 125 people. These impacts of storms are continually growing in terms of economic losses along with their occurrence frequency as a result of climate change. The database of the European Severe Storm Laboratory (ESSL) documents almost 60,000 cases of structural damage and collapse due to extreme winds recorded in Europe in the last 3 years, with enormous economic damage, situations of discomfort, and risk for people. Many of these are associated with tornadoes and thunderstorms, the intensity of which could increase in the coming years due to global warming, leading to increasingly destructive events. According to Munich Re (GeoRisk Research Group), economic losses due to natural hazards are approximately equally distributed between earthquakes (35%), floods (30%), and windstorms (28%). In terms of fatalities, earthquakes (47%) and windstorms (45%) are predominant compared to floods (7%).

The ongoing impacts of these disasters underline the need for further research and technological innovations. Addressing this need, the ERIES project (European Research Infrastructures for European Synergies, www.ries.eu) responds to the European Commission’s Horizon Europe call INFRA-2021-SERV-01-07. ERIES aims to provide transnational access (TA) to advanced research infrastructures in structural,

seismic, wind, and geotechnical engineering, enabling ground-breaking research. This project offers access to leading experimental facilities, facilitating research that addresses hazard-related losses, risk management, and the development of innovative solutions for a greener, more sustainable society.

The 2025 International Workshop in Engineering Research Infrastructures for European Synergies (ERIES-IW2025) aims to bring transnational access (TA) users involved in the ERIES project, providing a unique platform to exchange experiences, share results, and explore future directions in seismic, wind, and geotechnical engineering research. This event aims to strengthen collaboration and knowledge-sharing within the ERIES community, fostering impactful research, guiding future policy, and influencing building standards that will drive resilience and sustainability in European engineering for years to come.

Gerard J. O'Reilly
Gian Michele Calvi

Acknowledgements

This work is supported by the Engineering Research Infrastructures for European Synergies (ERIES) project (www.ries.eu), which has received funding from the European Union's Horizon Europe Framework Programme under Grant Agreement No. 101058684.

Contents

CLIMATHUNDER: A Combined Impinging Jet and Gravity Current Technique to Investigate Thermal Effects on Downburst Winds	1
<i>Federico Canepa, Anthony Guibert, Andi Xhelaj, Josip Žužul, Djordje Romanic, Alessio Ricci, Horia Hangan, Jean-Paul Bouchet, Philippe Delpech, Olivier Flamand, and Massimiliano Burlando</i>	
Evaluation of Force Coefficients on a Lattice Structure by Experimental Wind Tunnel Tests	14
<i>Bruno Clavelo, Kristof Maes, Patricia Martín, Vivian Elena, Federica Tubino, Giuseppe Piccardo, Maria Pia Repetto, and Geert Lombaert</i>	
Ligurian Downslope Winds Assessed Using LiDAR Scanner for the Safety Management of Port Areas	21
<i>Ivana Ivančić, Alessio Ricci, Massimiliano Burlando, Djordje Romanic, Branko Grisogono, and Hrvoje Kozmar</i>	
Wind Tunnel Measurements and CFD Correlation of Gas Dispersion Around Offshore Supply Vessel	29
<i>Felipe Sanchez Castro, João Muralha, Guilherme Vaz, Eric Roosenboom, Tristan Andrewartha, Anjali Radhakrishnan, and Stefanie Gillmeier</i>	
Code Calibration in Wind Engineering: Shortcomings and Needs	44
<i>Francesco Ricciardelli, Vincenzo Picozzi, and Alberto Maria Avossa</i>	
Downburst-Induced Loads on a Six-Row Array of Ground-Mounted Solar Trackers	54
<i>Antonio J. Álvarez, Félix Nieto, Petar Škvorc, Hrvoje Kozmar, Jeroen van Beeck, Tibebu Birhane, Kimberley Adamek, and Girma Bitsuamlak</i>	
Effects of Small-Scale Turbulence on the Aerodynamic and Aeroelastic Responses of a 3:2 Rectangular Prism	64
<i>Antonio J. Álvarez, Kenny C. S. Kwok, Luca Patruno, Giuseppe Piccardo, Félix Nieto, and Maria Pia Repetto</i>	

Thunderstorm-Induced Loading on Tall Buildings	74
<i>Aldereguía Sánchez Camila, Torre Stefano, Ruffini Edoardo, Bagnara Anna, Tubino Federica, Giuseppe Piccardo, and Maria Pia Repetto</i>	
ValUr: A High-Fidelity Dataset for Validation of Urban Pollution Dispersion Models – Project Overview and Geometry Preparation	83
<i>Mariya Pantusheva, Radostin Mitkov, Petar O. Hristov, Evgeny Shirinyan, Vasilis Naserentin, A. K. R. Jayakumari, Stefanie Gillmeier, and Anders Logg</i>	
The VORSEA Wind Tunnel Experiments	95
<i>Olivier Flamand, Andi Xhelaj, Andrea Orlando, Alessio Torrielli, and Alessandro Giusti</i>	
Wet-Snow Accretion on Overhead Conductors: Experimental Study in a Climatic Wind Tunnel	105
<i>Francesca Lupi, Erick Ulloa Jimenez, Norbert Hoelscher, Susanne Diburg, Jean-Paul Bouchet, Bruno Gauduchean, Philippe Delpech, and Olivier Flamand</i>	
Wind Tunnel Tests on a High Rotational Urban Savonius Turbine	118
<i>Krzysztof Doerffer, Piotr Doerffer, Joanna Grzelak, Józef Kotus, Abdelgalil Eltayesh, Luisa Pagnini, Giuseppe Piccardo, and Maria Pia Repetto</i>	
Real Scale Experimental Assessment of Pile Group Dynamic Impedance	125
<i>Raffaele Di Laora, Raffaele Cesaro, Emmanouil Rovithis, Luca de Sanctis, George Anoyatis, Stjin Francois, Eleni Filoglou, Chiara Amendola, Georgia Kroupi, Anastasios Anastasiadis, and Dimitris Pitilakis</i>	
Seismic Residual Displacements of RC U-Shaped Core Walls: Preliminary Findings	132
<i>João Pacheco de Almeida and Ryan Hoult</i>	
Shake Table Testing of Masonry-Infilled RC Frames with Flexible Joints for Seismic-Resilient Structural Performance	144
<i>Enrico Tubaldi, Filip Manojlovski, Aleksandra Bogdanovic, Zoran Rakicevic, Julijana Bojadjieva, Vlatko Sesov, Marko Marinković, Matija Bošković, Christoph Butenweg, Matija Gams, Nemanja Krtinić, Fabio Freddi, Daniele Losanno, Prateek Dhir, Hamid Ahmadi, and Alessandro Lotti</i>	

Response Analysis of Column-Base Connections in Existing Steel Frames	159
<i>Luigi Di Sarno, Mario D'Aniello, Fabio Freddi, Stathis Bousias, Jing-ren Wu, and Reza Khani</i>	
Geographically Distributed Hybrid Testing of a Multi-Storey Timber Structure on Compliant Soil: Pilot Design	170
<i>İhsan E. Bal, Eleni Smyrou, Stylianos Kallioras, Kamer Özdemir, Tansu Gökçe, Adam Crewe, George Mylonakis, Roberto Tomasi, Angelo Aloisio, Solomon Tesfamariam, Stathis Bousias, Oh-Sung Kwon, and Anastasios Sextos</i>	
Dynamic In-Situ Testing of a 15-Year-Old Friction-Pendulum Base Isolation System	182
<i>A. Rapone, P. M. Calvi, G. Gabbianelli, T. C. Becker, H. Sucuoğlu, B. Chalarca, Igor Lanese, Elisa Rizzo-Parisi, F. Dacarro, and Gerard J. O'Reilly</i>	
Experimental Investigation of Pallet Sliding in Steel Racking Systems via Shake Table Testing	194
<i>Dimitrios Tsarpalis, Dimitrios Vamvatsikos, Christos Lachanas, Akrivi Chatzidaki, Michalis Vassiliou, Kemal Can Struja, Dimitrios Konstantinidis, Christoph Adam, Nicholas Kyriakides, Athanasia Kazantzzi, Konstantinos Bakalis, Giuseppe Abbiati, Filippo Delladonna, Giuseppe Fabbri, Luca Sutera, Igor Lanese, and Gerard J. O'Reilly</i>	
Project RecycleSlab - Structural Behaviour of Recycled Aggregate Reinforced Concrete Flat Slabs with Drop Panels Under Seismic and Cyclic Actions	206
<i>António Ramos, Carla Marchão, Dario Coronelli, Duarte Faria, Fausta Fiorillo, Gianpaolo Rosati, Jaroslav Halvoník, João Pacheco de Almeida, Jorge de Brito, Luca Martinelli, Marco Lamperti, Miguel Fernandez Ruiz, Monica Lavagna, Robert Vollum, and Rui Marreiros</i>	
ERIES-RESTORING: REtrofitting of STOne MasonRy Using INnovative Grid-Based Composites	217
<i>Madalena Ponte, Larisa Garcia-Ramonda, Igor Lanese, Gerard J. O'Reilly, Elisa Rizzo-Parisi, Francesco Graziotti, Luca Pelà, Andrea Penna, Guido Magenes, Rita Bento, and Gabriele Guerrini</i>	

The Resume Project: Numerical Analyses and Laboratory Test	230
<i>Antonio Formisano, Emilia Meglio, Vlatko Sesov, Aleksandra Bogdanovic, Julijana Bojadjieva, Zoran Rakicevic, Antonio Shoklarovski, Filip Manojlovski, Angela Poposka, Toni Kitanovski, Dejan Ivanovski, Marco Domaneschi, Raffaele Cucuzza, Valentina Villa, and Giuseppe Carlo Marano</i>	
Design and Analysis of Large-Scale Tests of a Self-centring Seismic-Resilient Steel MRF	243
<i>Elena Elettore, Ali Roumeh, Fabio Freddi, Massimo Latour, Antonella B. Francavilla, Sabatino Di Benedetto, Fernando Gutiérrez-Urzúa, Ludovica Pieroni, Barbara Simpson, Andrea R. Barbosa, Shahab Ramhormozian, Damian N. Grant, Giovanni Rizzano, Filipe L. Ribeiro, and Antonio A. Correia</i>	
Seismic Retrofitting of RC Buildings Using Cross-Laminated Timber Panels: Insights from the ERIES-STRONG Project	255
<i>Ivan Giongo, Francesco Graziotti, Nikolaos Stathas, Stathis Bousias, Francesco Smiroldo, Andrea Bartolotti, Nicolò Damiani, Albino Angeli, and Dmytro Dizhur</i>	
Out-of-Plane Shake-Table Tests on Unreinforced Masonry Gables Considering Different Roof Configurations	268
<i>Nicolò Damiani, Marta Bertassi, Satyadhrik Sharma, Marco Smerilli, Michele Mirra, Igor Lanese, Elisa Rizzo-Parisi, Gerard J. O'Reilly, Francesco Messali, and Francesco Graziotti</i>	
3D Shaking Table Tests of a Full Scale 2-Storey Building with Fiber-Reinforced Elastomeric Isolators	280
<i>Daniele Losanno, S. Prakash, P. Medaglia, F. Parisi, Dimitrios Konstantinidis, Enrico Tubaldi, Hamid Ahmadi, A. Strauss, D. De Domenico, Dimitrios Vamvatsikos, Christos Lachanas, Michalis Vassiliou, Filipe L. Ribeiro, and Antonio A. Correia</i>	
Author Index	280



CLIMATHUNDERR: A Combined Impinging Jet and Gravity Current Technique to Investigate Thermal Effects on Downburst Winds

Federico Canepa¹(✉), Anthony Guibert², Andi Xhelaj¹, Josip Žužul¹, Djordje Romanic³, Alessio Ricci⁴, Horia Hangan⁵, Jean-Paul Bouchet², Philippe Delpech², Olivier Flamand², and Massimiliano Burlando¹

¹ Department of Civil, Chemical and Environmental Engineering (DICCA), University of Genoa, 16145 Genoa, Italy

federico.canepa@unige.it

² Centre Scientifique Et Technique du Bâtiment (CSTB), 44300 Nantes, France

³ Department of Atmospheric and Oceanic Sciences, McGill University, Montreal, QC H3A 0E2, Canada

⁴ Department of Science, Technology and Society, University School for Advanced Studies IUSS Pavia, 27100 Pavia, Italy

⁵ Faculty of Engineering and Applied Science, Ontario Tech University, Oshawa, ON L1G 0C5, Canada

Abstract. A comprehensive experimental campaign was conducted as part of the ERIES-CLIMATHUNDERR project (CLIMAtic Investigation of THUNDER-storm Winds) at the Jules Verne Climatic Wind Tunnel, CSTB, Nantes, France. The study aimed to investigate the thermal effects driving downdraft winds from thunderstorm clouds and their influence on downburst outflow dynamics near the ground.

Downbursts are typically simulated using two methods: (i) the gravity current (GC), which models jet formation through density instability between two fluids, and (ii) the impinging jet (IJ), which generates the downdraft mechanically using wind tunnel fans. While the IJ method is preferred in wind engineering for its scalability, it lacks the thermodynamic contributions intrinsic to GC-based simulations.

For the first time, the CLIMATHUNDERR project combines these two techniques at large scale, leveraging varied temperature differentials between the jet and its surroundings to analyze the dynamic and geometric evolution of downburst outflows and associated vortex structures, particularly the leading primary vortex (PV). The experiments also include testing these reproduced flows over a scaled topographic model of the Polcevera Valley in Genoa, Italy, to assess real-world applications. Evolving flow and temperature fields are captured using state-of-the-art measurement techniques, including Large-Scale Particle Image Velocimetry (LS-PIV) and high-response thermocouples.

Keywords: Thunderstorm downbursts · Gravity current · Impinging jet · Thermal effects · LS-PIV

1 Introduction

The pioneering studies of Ted Fujita [1] and Mark R. Hjelmfelt [2] on thunderstorm downbursts were primarily motivated by their role in aviation disasters, where unexpected, sudden, high-speed vertical winds (i.e., the downdraft wind component) near airports led to fatal crashes. Initially, these extreme winds were often misidentified as turbulence or poor pilot control until meteorologists started investigating their true nature. While advancements in onboard radar systems and other early-warning instruments have significantly reduced downburst-related aviation accidents, research in wind engineering over the past decades has increasingly focused on the characterization of the horizontal outflow component of thunderstorm winds near the ground. This research is particularly relevant for understanding wind loading and its effects on structures [3–5].

A downdraft originates when cold air within a thunderstorm cloud—formed by the condensation of warm updrafts from the surface—buoyantly descends toward the ground. The greater the temperature difference between the downdraft air and its surroundings, the stronger the resulting gravity current and, consequently, the higher the wind speeds during the outflow stage. Upon impact with the ground, the downdraft creates a radially expanding outburst of wind, driven by the high-pressure zone at the impingement point. Maximum horizontal wind speeds in the outflow typically occur between 30 and 150 m above ground level (AGL) [6], posing a severe threat to both natural and built environments.

Despite more than 50 years of research, many aspects of thunderstorm downbursts remain poorly understood. This is largely due to their localized and transient nature: downbursts typically span only a few kilometers horizontally, last for tens of minutes, and exhibit their most intense phase within just a few tens of seconds. Ultrasonic anemometers and other high-temporal resolution instruments capture wind data at a single fixed point, often missing the full structure of the phenomenon unless the event occurs precisely within the instrument’s vicinity. Additionally, the complex flow interactions governing downbursts are difficult to discern from full-scale measurements alone, further complicating efforts to develop accurate analytical models capable of describing the spatiotemporal evolution of both mean and turbulent flow fields. Standards and codes are mainly based on large-scale and stationary winds, i.e., extra-tropical cyclones, while not accounting for non-stationary and localized winds, such as downbursts.

Recently, a collaborative research team from Italy and Canada experimentally characterized the full dynamics of downburst winds, analyzing their spatiotemporal evolution and the contributions of different flow components to the overall storm system [7, 8]. These experiments were conducted under the European Research Council (ERC) project THUNDERR (Principal Investigator: Prof. Giovanni Solari) at the WindEEE Dome laboratory at Western University, Canada—one of the world’s largest wind simulators, capable of replicating non-stationary extreme wind events [9].

This study introduces the ERIES project CLIMATHUNDERR (CLIMAtic Investigation of THUNDERstorm Winds), which builds upon the findings of its predecessor, THUNDERR, while aiming to make groundbreaking contributions to the study of downburst winds. Traditionally, downbursts have been analyzed using two primary experimental approaches: impinging jet (IJ) simulations [7, 10–12], which generate a mechanically induced downdraft using wind tunnel fans, and gravity current (GC) simulations [13, 14],

which reproduce density-driven outflows. CLIMATHUNDERR innovatively combines these two techniques at the Jules Verne Climatic Wind Tunnel (JVCWT) – Thermal Unit SC2 at the Centre Scientifique et Technique du Bâtiment (CSTB) in Nantes, France. This project investigates thermal effects on downburst dynamics and morphology, with a particular focus on the leading vortex ring (primary vortex, PV) responsible for the highest near-ground wind intensities. Additionally, CLIMATHUNDERR includes experiments on a 1:2000 scale orographic model of the Polcevera Valley in Genoa, Italy. The Mediterranean region is particularly prone to convective storm phenomena [15], including downburst winds, and is highly vulnerable to the effects of climate change [16]. The Polcevera Valley, which extends from Genoa’s port—a common entry point for downbursts forming over the Mediterranean Sea—to inland areas, serves as an ideal case study for analyzing the flow channeling effects of thermal downburst winds and their associated vortex structures.

A further innovation of this study lies in its measurement techniques: Large-Scale Particle Image Velocimetry (LS-PIV) was employed to capture variation of the flow field over a large field of view (FOV), while thermocouples were used to monitor temperature profiles before and during downburst onset.

2 Experimental Setup

2.1 Facility and Generation of Buoyant Impinging-Jet Downbursts

The experimental campaign was conducted within the thermal circuit of the JVCWT (Fig. 1a), a facility capable of replicating a wide range of climatic conditions, including rain, ice, snow, and solar radiation [17, 18].

The test section measures 10 m in width (W), 7 m in height (H), and 25 m in length (L). The axial fan, with a diameter of 6.2 m, can generate wind speeds ranging from 1 to 40 m/s, powered by a maximum output of 1100 kW. Downstream of the fan, heat exchangers are installed to regulate ambient air temperature between -32°C and $+55^{\circ}\text{C}$ within the testing chamber.

Unlike the WindEEE Dome laboratory, which was specifically designed to reproduce vertical-axis winds—such as downbursts and tornadoes—through an opening (bell mouth) at the ceiling level for air injection or suction, respectively, the CSTB climatic wind tunnel primarily generates horizontal, straight-line winds. It is a versatile wind tunnel designed to address issues related to the construction and transportation sector. As a result, the main technical challenge at the base of the entire project was the need to manufacture a mechanism capable of producing a downdraft-like flow.

Leveraging the expertise of CSTB’s technical team, an impinging-jet plenum (IJP) measuring $2 \times 2 \times 2 \text{ m}^3$ was fabricated and installed at a height $H = 3 \text{ m}$ above the laboratory floor (Fig. 1b). The IJP was constructed from plywood lined with insulation material to minimize thermal losses, in the view of stabilizing the thermal difference between the IJP air and the surrounding environment. A circular nozzle, with diameter $D = 1 \text{ m}$, was opened at the center of the IJP’s bottom surface, ensuring a height-to-diameter ratio $H/D > 1$, which facilitates full vertical expansion of the downburst outflow and vortices [19]. To minimize turbulence and homogenize the downward flow at the nozzle outlet, the nozzle was equipped with a honeycomb structure. An electromagnetic

mechanism was developed to control the nozzle opening, enabling the reproduction of the transient nature of downburst winds. Additionally, this mechanism allowed for precise synchronization of measurements, facilitating comparisons of flow evolution across different thermal configurations.

The IJP was mounted on a rigid wooden frame with horizontal dimensions $5 (L) \times 2 (W) \text{ m}^2$ (see Fig. 1b). A piston measuring $2 \times 2 \times 0.6 \text{ m}^3$ was positioned at the top of the IJP and suspended from the testing chamber ceiling using a winch. At the designated time—1000 ms after the nozzle opening—the piston was lowered over a 2 m vertical distance until it reached the IJP bottom surface. Two vertical piston velocities, $w_p = 0.15 \text{ m/s}$ and 0.25 m/s , were tested, generating corresponding jet velocities at the nozzle outlet of $w_{IJ} = 0.8$ and 1.3 m/s , respectively, based on mass flow conservation. This piston motion contributed to the mechanically driven impinging-jet component of the generated downburst winds.

In addition to the IJ component, a buoyancy-driven jet (GC) naturally developed due to the temperature difference ΔT between the cooled IJP air and the warmer chamber air. To achieve this temperature contrast, a 7.3 kW air conditioning unit was installed adjacent to one of the IJP's sidewalls and connected via three insulated tubes in a closed-loop thermal circuit. This system enabled cooling of the internal IJP air to a minimum temperature below 10°C , while the ambient temperature in the testing chamber, without active heating from the heat exchangers, was maintained at approximately 25°C . During the experiments, ΔT ranged from 0°C to 25°C . Theoretical calculations, based on the Navier-Stokes equations and assumptions such as treating air as an ideal gas under hydrostatic approximation, estimated the maximum buoyancy-driven jet velocity before impingement to be $w_B = 2.18 \text{ m/s}$. While an ideal downburst would be best represented by the buoyancy-driven GC jet alone, the mechanically induced IJ component was necessary to control the initial test conditions.

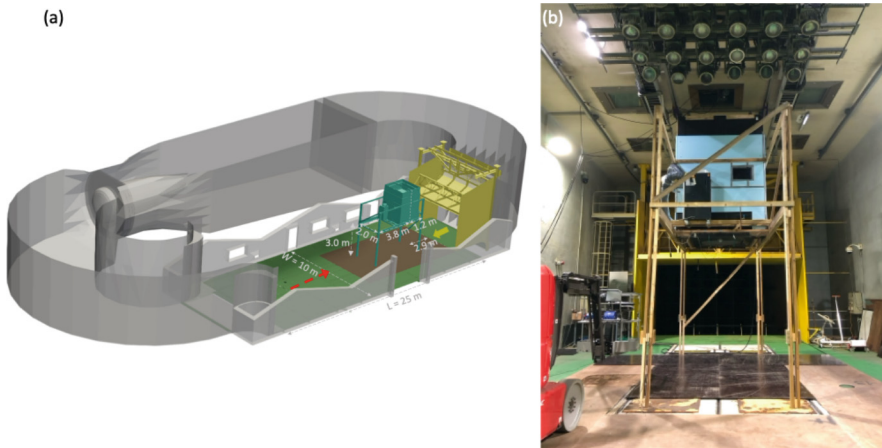


Fig. 1. (a) Schematics of the JVCWT thermal unit; (b) Photograph of the experimental setup without orography model.

Maintaining stable temperatures inside the IJP and testing chamber presented several challenges due to factors such as large geometric dimensions, thermal diffusion, incomplete insulation, and the efficiency of the air conditioning system. To mitigate vertical temperature stratification, both the chamber fan and air conditioning unit were operated for approximately five minutes before each experiment to distribute warm and cool air within the chamber and the IJP, respectively. These systems were turned off one minute before each test to minimize external disturbances.

2.2 Orography Model

The generated downburst flows were tested on a 1:2000 scale model of the Polcevera Valley, located in the Municipality of Genoa, Italy (Fig. 3). The model represented a 7 km (L) \times 4 km (W) portion of terrain (scaled to 3.5 m \times 2 m) extending from the Genoa-Volti commercial port in the northern Mediterranean to the inland hilly region that marks the city's northern boundary. The terrain elevation ranged from sea level to approximately 600 m above sea level (ASL).

The model was 3D-milled from lightweight expanded polystyrene (EPS) and installed in the chamber with its transverse section centered at the geometric location of the jet touchdown. The longitudinal position was varied between two configurations: the southern edge of the model, representing the port dam, was positioned ± 0.3 m from the jet touchdown center, corresponding to real-world downbursts landing 600 m onshore or offshore of the port area.

2.3 Measurement Techniques

Large-Scale Particle Image Velocimetry (LS-PIV). Traditional point-velocity measurement techniques, such as multi-hole pressure probes, were deemed unsuitable due to the low wind speeds of the experimental flow. Instead, LS-PIV was employed to capture vortex-dominated downbursts, which exhibit low wind speeds and strong recirculations, over a large field of view (FOV) with high spatial resolution.

The fluid was seeded with Helium-Filled Soap Bubbles (HFSB), averaging 300 μm in diameter, introduced through a rectangular opening at the bottom of one of the IJP's lateral walls. A dual-pulsed Nd:YAG laser, with a wavelength of 532 nm, was used to illuminate the particles. Two LaVision cameras were employed for flow field imaging: the first, with a resolution of 4 MP at 7 Hz, and, after failure during experiment #15, a second camera with a resolution of 6 MP at 14 Hz. The respective FOVs were $2.5 \times 2.5 \text{ m}^2$ and $3.2 \times 2.5 \text{ m}^2$ with the coordinate origin (r_0, z_0) set at the jet vertical centerline and floor level. In non-dimensional terms, the FOV extended horizontally from $r/D = 0$ to 2.5 or 3.2 and vertically from $z/D = 0$ to 2.5 (0.5 m below the nozzle outlet), covering all critical regions of the downburst wind [20]. Figure 2 provides a schematic of the LS-PIV setup.

For experiments involving the orography model, the FOV was adjusted to consistently capture the same region of the model in both test configurations. The FOV center was shifted + 0.5 m downstream of the IJ center to record the evolution of the downburst outflow and any resulting flow channeling effects within the range of approximately $r/D = 0.3$ to 3.5 and $r/D = 0.9$ to 4.2 for the two model positions.

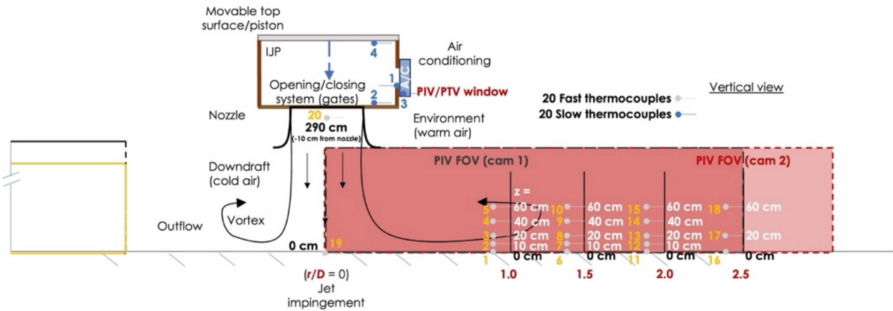


Fig. 2. Schematics (vertical view) of the LS-PIV and thermocouples setup.

Temperature Measurements. To record transient temperature profiles during downburst passage, 20 fast-response thermocouples (reaction time ≈ 0.5 s) were deployed (Fig. 2). 18 thermocouples were placed in the outflow region at various radial positions, while the remaining two were positioned along the jet vertical centerline at $z/D = 0$ and 2.90. Additionally, four slower-response thermocouples were placed inside the IJP and at its connection to the air conditioning unit.

During experiments with the orography model, the 18 fast-response thermocouples were relocated to the model surface, covering both valley and ridge locations (Fig. 3). Key areas, including the Erzelli Hill—soon to house the new engineering campus of the University of Genoa—and the San Giorgio Bridge, which replaced the Morandi Bridge following its tragic collapse in August 2018, were monitored for flow channeling. Furthermore, thermocouples were strategically located to assess the potential development of heat/cool islands.

2.4 Test Plan

A total of 57 experimental runs were conducted in the thermal unit of the JVCWT. The first 39 runs focused on analyzing the reproduced downburst flows without the orography model, while the remaining 18 runs included the model. The test cases varied based on several key parameters, including the temperature difference (ΔT) between the IJP and the testing chamber, the mechanical impinging-jet velocity (w_{IJ}), and the model's installation position. During the initial phase of the experimental campaign, three temperature differences were tested: $\Delta T = 0$ °C, 10 °C, and 20 °C for $w_{IJ} = 1.3$ m/s, and $\Delta T = 0$ °C, 10 °C, and 25 °C for $w_{IJ} = 0.8$ m/s. When the model was installed, time constraints limited the study to only two temperature differences, $\Delta T = 0$ °C and 20 °C. Additionally, the number of experimental repetitions per configuration was reduced from the planned eight to just two runs with the model in place. Unlike conventional fluid mechanics studies, where a high number of repetitions is required to achieve statistical significance, each experiment in this campaign was considered unique due to inherent variations in parameter values between repetitions of the same configuration.

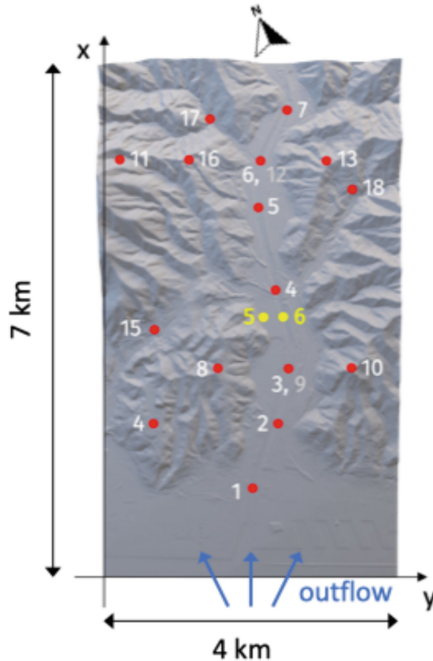


Fig. 3. 3D stereolithography (STL) orography showing thermocouple positions. White numbers indicate thermocouples installed on the model surface; grey numbers represent thermocouples positioned at elevated heights (0.095 m and 0.100 m above the model surface for thermocouples #9 and #12m, respectively). Yellow numbers denote thermocouples relocated from experiment #50. Full-scale dimensions of the orography domain are also indicated in the figure, as well as the geographic north direction and incoming direction of the experimental downburst outflow.

3 Results

3.1 Thermal Effects on Downburst Outflows and Interaction with the Orography Model

Figure 4 highlights the crucial role of buoyancy in shaping the dynamics and geometry of downburst outflows, as well as their interaction with the orography model. The two experiments, conducted with thermal differences of $\Delta T = 0\text{ }^{\circ}\text{C}$ and $20\text{ }^{\circ}\text{C}$ between the IJP and its surroundings, are shown at the moment when the PV is approximately at the radial location $r/D = 1.5$. However, the two scenarios occur at different times, specifically $t = 10\text{ s}$ for $\Delta T = 0\text{ }^{\circ}\text{C}$ and $t = 6\text{ s}$ for $\Delta T = 20\text{ }^{\circ}\text{C}$. This indicates that a temperature difference of $20\text{ }^{\circ}\text{C}$ significantly accelerates the jet and its evolving outflow at the ground, causing the PV to reach $r/D = 1.5$ approximately 4 s earlier than in the base case ($\Delta T = 0\text{ }^{\circ}\text{C}$).

Buoyancy is observed to narrow the width of the descending jet, which is dominated by trailing vortices (TVs) following the leading PV. The PV flow field appears more turbulent and dispersed, with strong shear even in the rear part of the vortex. As a result, the PV center is less well-defined compared to the pure IJ case. Additionally, the PV

is more compressed toward the ground. This, combined with the inherent increase in flow velocity due to buoyancy, results in maximum horizontal velocities at the interface between the lower end of the PV and the ground [20], approximately doubling those observed for the base IJ case.

In the pure IJ scenario, the well-organized PV structure generates a clearly defined secondary counter-rotating vortex (secondary vortex, SV) in front of the PV. This occurs due to boundary layer separation and reattachment caused by air being pushed outward as the PV expands [20]. Conversely, in the buoyant configuration, the more dispersed PV leads to a more turbulent SV. This effect is further amplified by the interaction with the orography model, which influences the development of both the PV and SV. The weaker flow structure in the $\Delta T = 20^\circ\text{C}$ case is more pronounced for the topography of the Polcevera Valley, causing the PV-SV structure to break apart near the ridges surrounding the San Giorgio Bridge.

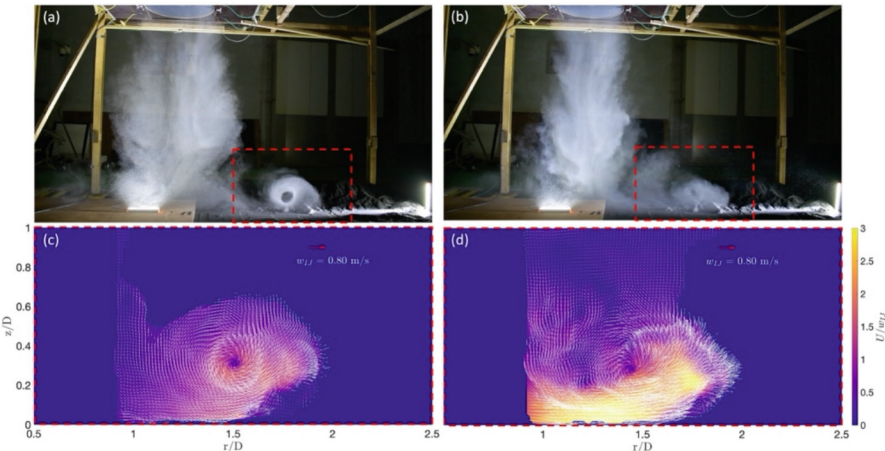


Fig. 4. Experiments with the model in place, $w_{IJ} = 0.8 \text{ m/s}$, $\Delta T = 0^\circ\text{C}$ (a,c) and 20° (b,d), captured at the time $t = 10 \text{ s}$ and 6 s , respectively, of PV passing over $r/D = 1.5$ (approximate location of the San Giorgio bridge in Genoa): flow visualizations (a,b) and zoom-in (red dashed rectangle) on the velocity field from PIV measurements (c,d).

3.2 Tracking of the Primary Vortex Center

Figure 5 illustrates the temporal evolution of the PV center in the vertical (r, z) plane obtained from PIV measurements. The PV center at each time instant was identified as the location of maximum vorticity, defined as:

$$\omega = \delta w / \delta r - \delta u / \delta z \quad (1)$$

Where u and w are the velocity component in the radial (r) and vertical (z) directions, respectively.

The legend in Fig. 5 indicates the actual thermal differentials ΔT between the IJP and the surrounding air at the time of nozzle opening. Both the IJ (w_{IJ}) and buoyancy (ΔT) contributions significantly influence the evolution of the PV. The role of thermal instability becomes more pronounced at lower jet velocities: as ΔT increases, buoyancy enhances the vertical convection of the PV toward the ground. Conversely, for lower ΔT , the descending jet and PV expand more laterally, entraining ambient air. Notably, in the case ($w_{IJ} = 0.8 \text{ m/s}$, $\Delta T = 17.0^\circ\text{C}$), the PV transitions from a vertical to a horizontal trajectory at a relatively high elevation of approximately $z/D = 0.7$. In contrast, for other cases, the PV deflects horizontally at lower heights, typically below $z/D = 0.5$, and increasingly closer to $r/D = 1$ as ΔT decreases or w_{IJ} increases. Interestingly, the configurations ($w_{IJ} = 0.8 \text{ m/s}$, $\Delta T = 10.6^\circ\text{C}$) and ($w_{IJ} = 1.3 \text{ m/s}$, $\Delta T = 13.0^\circ\text{C}$) exhibit a minimum PV height below $z/D = 0.3$ following the IJ touchdown. Beyond $r/D = 1.5 - 2$, the PV height stabilizes around $z/D = 0.3 - 0.4$, aligning with other experimental cases.

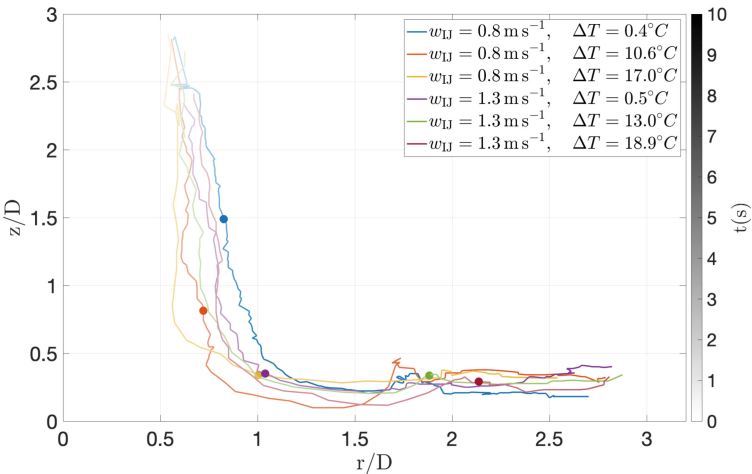


Fig. 5. Tracking of the PV center for different experimental cases with varying w_{IJ} and actual ΔT (see legend), without model installed. The color gradient represents the temporal evolution (see colorbar), while the circle marker indicates the time instant $t = 6 \text{ s}$ for each case. (Color figure online)

3.3 Wind Speed and Temperature Vertical Profiles

For the same cases presented in Fig. 5, Fig. 6 shows the vertical profiles of wind speed captured at the moment of its absolute maximum within the flow field. In general, the profiles exhibit a peak wind speed near the ground, below $z/D = 0.2$. As the thermal difference (ΔT) increases, the PV becomes more compressed to the surface. Consequently, the vertical plateau of nearly constant velocities surrounding the absolute maximum is more confined to the ground, characterizing the flow field beneath the PV determined by the combination of the PV's advection velocity at the surface and its vorticity [20].

Above this region, velocity decreases sharply as it follows the counterflow direction in the upper part of the PV. A second velocity inversion point is observed at a higher altitude, where velocity approaches zero due to the nearly stagnant flow above the PV. This second inversion point may serve as an indicator of the PV height, which decreases with increasing ΔT .

When normalized by the jet velocity (w_{IJ}), the velocity profiles follow a consistent trend for corresponding values of ΔT . A significant deviation is observed in the case ($w_{IJ} = 1.3$ m/s, $\Delta T = 13.0$ °C) where the maximum velocity occurs at a higher position of approximately $z/D = 0.3$ and at larger radial distances ($r/D = 1.89$). For other cases, the maximum velocity is observed at progressively lower radial and height positions as ΔT increases. The highest thermal differences result in maximum velocities reaching approximately three times the jet velocity (w_{IJ}). The overall maximum wind speed among all cases is observed for ($w_{IJ} = 0.8$ m/s, $\Delta T = 10.6$ °C), occurring at the first velocity inversion point ($z/D \approx 0.06$).

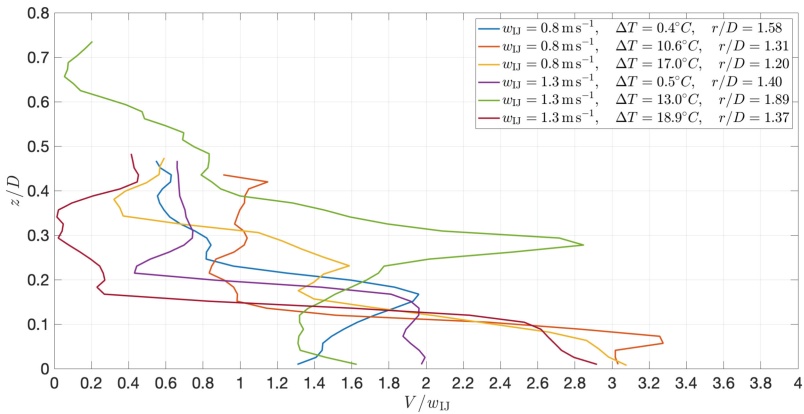


Fig. 6. Vertical profiles of wind speed at the moment of its absolute maximum within the flow field. The radial location of this occurrence, along with the experimental configuration parameters, is provided in the figure legend.

Figure 7 presents the corresponding normalized vertical temperature profiles, recorded at the moment of maximum velocity (see Fig. 6) using thermocouples positioned as schematized in Fig. 2. As expected, configurations with $\Delta T \approx 0$ °C show no significant temperature change with the passage of the downburst outflow. As ΔT increases, the passage of the cold front driven by the PV results in a sharp temperature drop. In general, the lowest temperatures are observed near the ground and increase with height, though not in a strictly monotonic fashion. This pattern reflects the temperature transition from the cold flow confined beneath the PV to the warmer inner and upper regions of the vortex. Notably, the lowest jet velocity ($w_{IJ} = 0.8$ m/s) results in lower outflow temperatures compared to $w_{IJ} = 1.3$ m/s. This supports the idea that higher jet velocities enhance mixing with the warmer chamber air, leading to increased outflow temperatures.

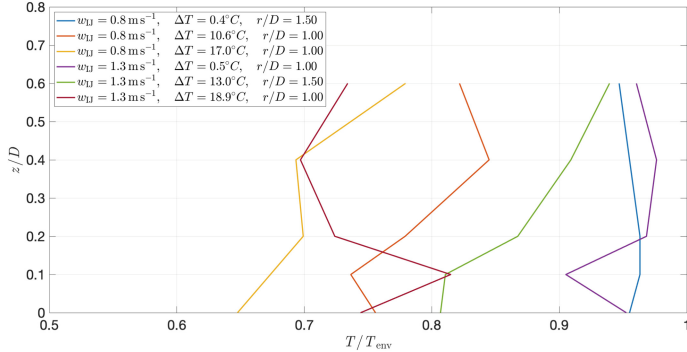


Fig. 7. Vertical temperature profiles normalized by the chamber ambient air temperature prior to the jet release. Profiles were recorded at the time of maximum wind speed at the nearest radial location behind the maximum velocity position, corresponding to the instantaneous location of the PV (see r/D in Fig. 6 legend), thus immersed in the outflow.

4 Conclusions and Prospects

The ERIES-CLIMATHUNDER project introduces an innovative approach to modeling downburst winds by incorporating thermal effects, which are the primary drivers of these winds in nature. For the first time, experimental impinging jet and gravity current approaches are combined to investigate how different thermal instabilities (ΔT) between the downdraft jet and the surrounding ambient air influence the dynamics and geometry of the evolving outflow and vortex structures.

The results demonstrate that higher ΔT values lead to more compressed outflows and vortices near the surface, with two key effects: (i) an increase in maximum velocity magnitude and (ii) a decrease in the height at which this maximum occurs. These conclusions have important structural loading implications. Additionally, increasing the jet velocity and thermal difference disrupts the regular structure of the outflow and the symmetry of the primary vortex. This, in turn, enhances mixing with the surrounding environment, raising the temperature of the evolving outflow and altering the PV-SV interaction. This overall dynamic is found to be strongly influenced by the orographic features of the terrain model.

Future studies will focus on quantifying and modeling the contributions of both mechanical and thermal components to the resulting downburst flow. Additionally, further research will explore their interaction with the scaled model of the Polcevera Valley in Genoa, Italy, whose complex orography can significantly impact the evolution of thermal downburst flows.

Acknowledgements. This work is part of the transnational access project “ERIES-CLIMATHUNDER”, supported by the Engineering Research Infrastructures for European Synergies (ERIES) project (www.erries.eu), which has received funding from the European Union’s Horizon Europe Framework Programme under Grant Agreement No. 101058684. This is ERIES publication number C69.

FC acknowledges the RETURN Extended Partnership and received funding from the European Union NextGeneration EU (National Recovery and Resilience Plan – NRRP, Mission 4, Component 2, Investment 1.3 – D.D. 1243 2/8/2022, PE0000005).

References

1. Fujita TT (1978) Manual of downburst identification for Project NIMROD
2. Hjelmfelt, M.R.: Structure and life cycle of microburst outflows observed in Colorado. *J. Appl. Meteorol.* **27**(7), 900–927 (1988)
3. Lombardo, F.T., Smith, D.A., Schroeder, J.L., Mehta, K.C.: Thunderstorm characteristics of importance to wind engineering. *J. Wind Eng. Ind. Aerodyn.* **125**, 121–132 (2014). <https://doi.org/10.1016/j.jweia.2013.12.004>
4. Solari G, Burlando M, De Gaetano P, Repetto MP (2015) Characteristics of thunderstorms relevant to the wind loading of structures. *Wind Struct* 20(6):763–791. <https://doi.org/10.12989/WAS.2015.20.6.763>
5. Zhang, S., Solari, G., De Gaetano, P., Burlando, M., Repetto, M.P.: A refined analysis of thunderstorm outflow characteristics relevant to the wind loading of structures. *Probab. Eng. Mech.* **54**, 9–24 (2018). <https://doi.org/10.1016/j.probengmech.2017.06.003>
6. Canepa, F., Burlando, M., Solari, G.: Vertical profile characteristics of thunderstorm outflows. *J. Wind Eng. Ind. Aerodyn.* **206**, 104332 (2020). <https://doi.org/10.1016/j.jweia.2020.104332>
7. Canepa, F., Burlando, M., Romanic, D., Solari, G., Hangan, H.: Downburst-like experimental impinging jet measurements at the WindEEE Dome. *Sci Data* **9**, 243 (2022). <https://doi.org/10.1038/s41597-022-01342-1>
8. Canepa, F., Romanic, D., Hangan, H., Burlando, M.: Experimental translating downbursts immersed in the atmospheric boundary layer. *J. Wind Eng. Ind. Aerodyn.* **243**, 105570 (2023). <https://doi.org/10.1016/j.jweia.2023.105570>
9. Hangan, H., et al.: Novel techniques in wind engineering. *J. Wind Eng. Ind. Aerodyn.* **171**, 12–33 (2017). <https://doi.org/10.1016/j.jweia.2017.09.010>
10. McConville, A.C., Sterling, M., Baker, C.J.: The physical simulation of thunderstorm downbursts using an impinging jet. *Wind Struct.* **12**(2), 133–149 (2009)
11. Mason, M.S., Letchford, C.W., James, D.L.: Pulsed wall jet simulation of a stationary thunderstorm downburst, Part A: Physical structure and flow field characterization. *J. Wind Eng. Ind. Aerodyn.* **93**(7), 557–580 (2005). <https://doi.org/10.1016/j.jweia.2005.05.006>
12. Romanic, D., LoTufo, J., Hangan, H.: Transient behavior in impinging jets in crossflow with application to downburst flows. *J. Wind Eng. Ind. Aerodyn.* **184**, 209–227 (2019). <https://doi.org/10.1016/j.jweia.2018.11.020>
13. Lundgren, T.S., Yao, J., Mansour, N.N.: Microburst modelling and scaling. *J. Fluid Mech.* **239**, 461 (1992). <https://doi.org/10.1017/S002211209200449X>
14. Yao, J., Lundgren, T.S.: Experimental investigation of microbursts. *Exp. Fluids* **21**(1), 17–25 (1996). <https://doi.org/10.1007/BF00204631>
15. Burlando, M., Zhang, S., Solari, G.: Monitoring, cataloguing, and weather scenarios of thunderstorm outflows in the northern Mediterranean. *Nat. Hazards Earth Syst. Sci.* **18**(8), 2309–2330 (2018). <https://doi.org/10.5194/nhess-18-2309-2018>
16. Lolis, C.J.: On the variability of convective available potential energy in the Mediterranean region for the 83-year period 1940–2022; signals of climate emergency. *Theor. Appl. Climatol.* **155**, 9273–9288 (2024). <https://doi.org/10.1007/s00704-024-05183-3>
17. Gandemer, J., Palier, P., Boisson-Kouznetzoff, S.: Snow simulation within the closed space of the Jules Verne Climatic Wind Tunnel. In: Proceedings of 3rd International Symposium, Sendai, Balkema

18. Matejicka, L., Delpech, P., Georgakis, C.T., Flamand, O.: An experimental investigation of ice and snow shedding from bridge cables with and without surface modifications. *Cold Reg. Sci. Technol.* **220**, 104148 (2024). <https://doi.org/10.1016/j.coldregions.2024.104148>
19. Junayed, C., Jubayer, C., Parvu, D., Romanic, D., Hangan, H.: Flow field dynamics of large-scale experimentally produced downburst flows. *J. Wind Eng. Ind. Aerodyn.* **188**, 61–79 (2019). <https://doi.org/10.1016/j.jweia.2019.02.008>
20. Canepa, F., Burlando, M., Romanic, D., Solari, G., Hangan, H.: Experimental investigation of the near-surface flow dynamics in downburst-like impinging jets. *Environ. Fluid Mech.* **22**, 921–954 (2022). <https://doi.org/10.1007/s10652-022-09870-5>

Open Access This chapter is licensed under the terms of the Creative Commons Attribution 4.0 International License (<http://creativecommons.org/licenses/by/4.0/>), which permits use, sharing, adaptation, distribution and reproduction in any medium or format, as long as you give appropriate credit to the original author(s) and the source, provide a link to the Creative Commons license and indicate if changes were made.

The images or other third party material in this chapter are included in the chapter's Creative Commons license, unless indicated otherwise in a credit line to the material. If material is not included in the chapter's Creative Commons license and your intended use is not permitted by statutory regulation or exceeds the permitted use, you will need to obtain permission directly from the copyright holder.





Evaluation of Force Coefficients on a Lattice Structure by Experimental Wind Tunnel Tests

Bruno Clavelo^{1,3()}, Kristof Maes², Patricia Martín³, Vivian Elena³, Federica Tubino⁴, Giuseppe Piccardo⁴, Maria Pia Repetto⁴, and Geert Lombaert²

¹ KU Leuven, Department of Civil Engineering, Leuven, Belgium
brunojorge.claveloelena@kuleuven.be

² KU Leuven, Department of Civil Engineering, Leuven, Belgium
³ Department of Civil Engineering, CUJAE, Havana, Cuba

⁴ Department of Civil, Chemical and Environmental Engineering, UNIGE, Genova, Italy

Abstract. Antenna masts are particularly vulnerable to dynamic wind forces, and the inclusion of ancillaries has been shown to substantially influence the loads acting on the mast. This study outlines an experimental investigation aimed at evaluating the drag, lift, and moment coefficients of a functional antenna mast. Wind tunnel experiments were carried out on a scaled 3D mast model under both smooth and turbulent airflow conditions, with five distinct ancillary configurations modeled after commonly observed patterns. Aerodynamic coefficients were derived for angles of attack spanning 0° to 360° . Measurements of drag, lift, and moment forces were taken using two six-axis force sensors attached to the model's ends, while downstream three-dimensional velocity data were captured using a Cobra probe mounted on a rigid vertical mast. The results provide a detailed analysis of the force coefficients, emphasizing the impact of both linear and discrete ancillaries on the aerodynamic behavior of the mast.

Keywords: Aerodynamic Coefficients · Wind Tunnel Test · Antenna Mast

1 Introduction

The reliable estimation of the wind forces acting on structures is crucial to improve the current understanding of their structural response mechanisms and reduce the risk of failure. This is particularly relevant in the case of slender, flexible structures such as antenna masts, which are highly sensitive to dynamic wind loads, resulting in numerous collapses due to strong wind phenomena [1]. Recent research at KU Leuven focuses on applying model-based system inversion techniques as an alternative to estimate wind loads on tall guyed masts. These techniques integrate measured response data with dynamic structural models to estimate the forces acting on the structure. A valuable set of full-scale response data and wind flow measurements has been acquired on an operating 80-m-tall mast (see Fig. 1) located in Santa Cruz del Norte, Cuba, but accurate estimation of the aerodynamic coefficients is vital to establish a reliable reference model for the wind loads.



Fig. 1. Picture of the 80-m-tall antenna mast located in Santa Cruz del Norte, Cuba

Current design codes and guidelines [2–4] offer simplified methods to estimate such coefficients based on the solidity ratio,. However, experimental studies [5, 6] have shown that the presence of ancillary components, such as linear and discrete elements, can significantly influence aerodynamic coefficients, depending on their placement and the wind incidence angle. Furthermore, significant discrepancies between wind loads derived from experimental tests and those predicted by design standards have been observed for skewed wind conditions [6–8]. Overall, wind tunnel tests [8–10] remain one of the most reliable methods for accurately determining aerodynamic coefficients for lattice structures.

This study presents a recent experimental campaign conducted as part of the ERIES Horizon Project at the Giovanni Solari Wind Tunnel Facility at the University of Genoa [11]. The main aim of the experimental test is to characterize the aerodynamic coefficients of the aforementioned mast. The drag forces, lift forces and moments are determined through static wind tunnel tests performed in both smooth and turbulent wind flow conditions. Five test models are considered, each corresponding to a specific configuration of linear and discrete ancillaries. For each configuration, angles of attack from 0° to 360° are tested, with a maximal angular step of 10° . Additionally, the three-component downstream wind velocities are acquired, allowing to investigate wake characteristics.

The complete dataset is made available online in the open-access repository Zenodo [12]. The dataset is highly valuable for developing and validating methods to quantify wind forces from measured wind velocities, as well as investigating wind-induced effects on lattice structures equipped with both linear and discrete ancillaries. It expands the limited experimental data available for static and aerodynamic tests on triangular spatial arrays. A notable feature of this dataset is the inclusion of double angle members angled at 60° , commonly used in antenna masts but not yet studied as part of a complete lattice structure. These results also serve as benchmarks for validating analytical and computational methods for estimating wind forces and force coefficients across varying wind incidence angles.

2 Test Description

Figure 2 shows the test setup and mounting system for the test models. Drag force, lift force, and moments are measured using two Kistler 9257B six-dimensional force balances mounted at each end of the model (see Fig. 2b). To analyse downstream wind flow characteristics, a Cobra probe is positioned to capture three-component velocity data, allowing a detailed investigation of wake turbulence. Inlet wind velocities are monitored with a Pitot tube, and stepper motors are used to rotate the model, capturing a full range of wind attack angles from 0° to 360° , in maximal steps of 10° . Additional measurements are performed at specific angles of attack to enable a more accurate estimation of the first derivative of the force coefficients in the ranges where they show stronger variations.

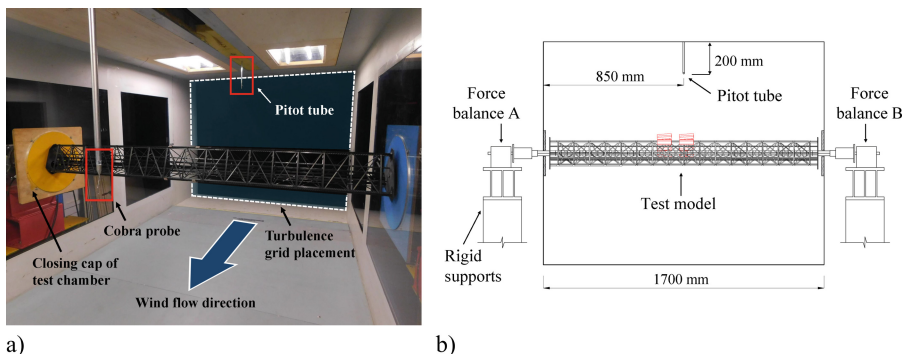


Fig. 2. Test setup showcasing the elements inside the test section for (a) smooth flow and (b) turbulent flow.

The tests are performed using a carbon-fiber scaled sectional model of the 80-m-tall antenna mast, with a triangular lattice cross-section. A 1:10 scale is chosen to ensure both model stiffness and manageable blockage ratios within the wind tunnel's test section, resulting in a sectional model of length $h = 1680$ mm and width $b = 160$ mm. The model is fitted with both linear ancillaries (ladders, power supply and feeder cables) and discrete ancillaries (UHF, VHF III, and VHF Dipole antenna systems), representing the most common configurations observed in the mast. The linear ancillaries are recreated using 3D-printed carbon fiber, whereas the discrete ancillaries, attached at the mid-section of the model, are replicated using a combination of carbon fiber, high-density foam and aluminium components.

A total of 5 different test model configurations (see Fig. 3) are tested. These configurations reflect the predominant patterns of linear and discrete ancillaries present on the real structure: 1. (**Bare**) bare model of the structure representing the geometry of the modular section composed by the columns, crossed diagonals, braces and internal braces (Fig. 3a); 2. (**Linear**) bare model equipped with linear ancillaries, i.e. internal ladder, feeder cables and data cables for discrete antennas (Fig. 3b); 3. (**Linear + UHF**) bare model equipped with linear ancillaries and four polarized UHF panels (Fig. 3c); 4. (**Linear + VHF III**) bare model equipped with linear ancillaries and three band III

VHF antennas (87.5–108 MHz), mounted on a circular frame (Fig. 3d); 5. (**Linear + VHF Dipole**) bare model equipped with linear ancillaries and four VHF closed dipole antennas (174–230 MHz), mounted on a square frame (Fig. 3e).

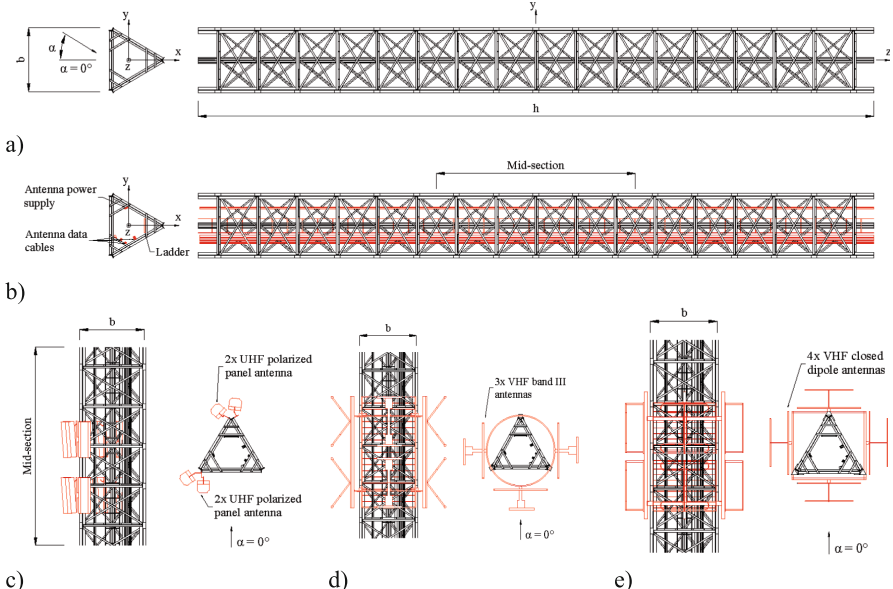


Fig. 3. Sectional model of (a) the bare specimen without ancillaries, and the specimen equipped with (b) linear ancillaries (ladder and cables), (c) UHF polarized panel antennas, (d) VHF band III antennas, and (e) VHF closed-dipole antennas, highlighted in red.

Experiments were conducted under both smooth flow (turbulence intensity < 0.2%) and turbulent flow conditions (turbulence intensity ~7–8%) generated by using a passive grid device. Data are recorded at each angle of attack α for 60 s at a 400 Hz sampling rate. Additionally, environmental conditions in the laboratory are monitored by measuring the room temperature, atmospheric pressure and relative humidity throughout the experiment. Table 1 summarizes the main characteristics of each test setup.

3 Aerodynamic Coefficients

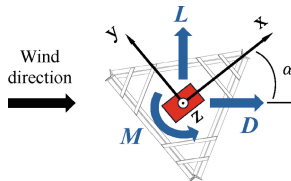
To compute the aerodynamic coefficients, the forces and moments measured from each force balance are combined to obtain the total forces and moments (F_x , F_y , M_z). Then, the mean values of the total forces, obtained by averaging over the total measurement time, are decomposed to obtain the drag force (\bar{D}), lift force (\bar{L}) and moment (\bar{M}) acting on the model (see Fig. 4).

The drag, lift and moment coefficients are respectively computed as indicated in Eq. (1):

$$C_D = \frac{2\bar{D}}{\rho \bar{U}^2 A_s}; \quad C_L = \frac{2\bar{L}}{\rho \bar{U}^2 A_s}; \quad C_M = \frac{2\bar{M}}{\rho \bar{U}^2 A_s b} \quad (1)$$

Table 1. Setup characteristics

No	Test model	Flow type	\bar{U} [m/s]	Angles of attack [°]	
				Basic	Additional
1	Bare	Smooth	15.2	0:10:360	5,15,25,35, 85, 95, 115
2	Linear	Smooth	15.2	0:10:360	5,15,115,195,205,315,325
3	Linear	Turbulent	11.1	0:30:360	[-]
4	Linear + UHF	Smooth	15.2	0:10:360	5,15,115,155,195,205,325
5	Linear + VHF III	Smooth	15.2	0:10:360	5,15,115,185,195,198,202
6	Linear + VHF Dipole	Smooth	15.3	0:10:360	5,15,115,195,205

**Fig. 4.** Force decomposition scheme and definition of coordinate systems (z-axis pointing outwards).

where ρ is the air density; \bar{D} , \bar{L} and \bar{M} are the mean values of the drag force, lift force and moment, respectively; \bar{U} is the reference mean wind velocity; and b is the reference dimension of the model, taken as the model width, equal to 0.16 m. The coefficients are normalized with respect to the solid area A_s for an angle of attack $\alpha = 0^\circ$, taken as the total projected area of the structural elements and ancillaries located in the windward face.

Figure 5 presents the aerodynamic coefficients obtained using Eq. (1). The drag coefficients are notably higher than the lift and moment coefficients, which remain close to zero across most configurations and angles of attack, aligning with the quasi-symmetric layout of the lattice. The drag coefficients for the bare model are generally the lowest. In contrast, configurations equipped with UHF and VHF antennas and linear ancillaries exhibit values up to 16% higher than those of the bare model, particularly at angles of attack around 90° and 270° .

The study also finds substantial variation in the drag resistance across different configurations, with drag resistance consistently increasing with the addition of ancillaries, as shown in Table 2. This study found that adding linear ancillaries increases drag resistance by up to 30%, while incorporating both linear and discrete ancillaries can raise drag resistance by up to 45%.

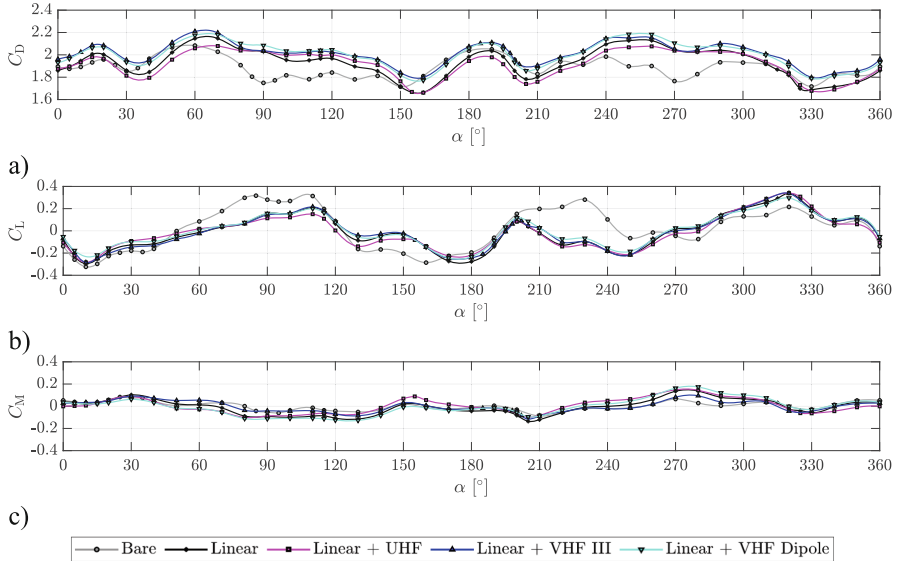


Fig. 5. Aerodynamic coefficients: (a) drag C_D , , (b) lift C_L , , and (c) moment C_M , as a function of the angle of attack α (markers), with a third-order cubic spline interpolation (solid line) superimposed.

Table 2. Drag resistance ($C_D \cdot A_S$) in m^2 for different test configurations.

α	Bare	Linear	Linear + UHF	Linear + VHF III	Linear + VHF Dipole
0°	0.16	0.19 (20.1)*	0.21 (30.9)	0.22 (34.9)	0.21 (33.1)
60°	0.18	0.22 (26.1)	0.23 (30.9)	0.25 (38.3)	0.24 (36.4)
120°	0.16	0.21 (30.8)	0.23 (43.8)	0.22 (43.4)	0.23 (45.1)

*: number in parentheses indicates the percentage difference with respect to the bare structure

4 Conclusions

This study presents a comprehensive dataset aimed at the identification of aerodynamic coefficients for an antenna mast for different ancillary configurations and various flow conditions. The drag, lift and moment coefficients are obtained for angles of attack ranging from 0° to 360° , allowing the full characterization of the aerodynamic forces of the guyed mast under study. The results highlight the influence of linear and discrete ancillaries, which increase the drag resistance of the mast in up to 30% and 45%, respectively. Lastly, the dataset generated serves as a valuable resource for future research and structural engineering applications. Potential for reuse is observed in several applications, including comparison with experimental data obtained from other wind tunnel tests, validation of analytical and numerical CFD models with similar characteristics and estimation of wind loads due to ancillaries.

Acknowledgements. This work is part of the transnational access project “ERIES-EOLICS”, supported by the Engineering Research Infrastructures for European Synergies (ERIES) project (www.ries.eu), which has received funding from the European Union’s Horizon Europe Framework Programme under Grant Agreement No. 101058684. This is ERIES publication number C51.

References

1. Elena, V., Fernández, I., Martín, P.: Structural failure on telecommunication guyed mast under extreme winds. In: Proceedings of the 14th International Conference on Wind Engineering. ICWE, Porto Alegre, Brasil (2010)
2. ESDU ESDU 81028, lattice structures; Part 2: Mean fluid forces on tower-like space frames. Engineering Science Data Unit, London, UK (1993)
3. EN, BS, others Eurocode 3: Design of Steel Structures—Part 3–1: Towers, Masts and Chimneys—Towers and Masts. BSI London, London, UK (2006)
4. ASCE (2010) Manual no. 74, Guidelines for electrical transmission line structural loading. 3rd edn. American Society of Civil Engineers, Virginia, USA
5. Carril, C., Jr., Isyumov, N., Brasil, R.: Experimental study of the wind forces on rectangular latticed communication towers with antennas. *J. Wind Eng. Ind. Aerodyn.* **91**(8), 1007–1022 (2003)
6. Tapia-Hernández, E., Cervantes-Castillo, J.A.: Influence of the drag coefficient on communication towers. *Int. J. Civil Eng.* **16**(5), 499–511 (2018)
7. Georgiou, P.N., Vickery, B. J.: Wind loads on building frames. In: Proceedings of the 5th International Conference, pp. 421–433. Elsevier, Colorado, USA (1980)
8. Yang, F., Niu, H.: Wind tunnel tests on wind loads acting on steel tubular transmission towers under skewed wind. *Wind Struct.* **35**(2), 93–108 (2022)
9. Calotescu, I., Torre, S., Freda, A., Solari, G.: Wind tunnel testing of telecommunication lattice towers equipped with ancillaries. *Eng. Struct.* **241**, 112526 (2021)
10. Martín, P., Elena, V., Fernández, I., Loredo-Souza, A.: Drag coefficients of lattice towers with VHF antennas on wind tunnel. *Revista Técnica De La Facultad De Ingeniería Universidad Del Zulia* **42**(3), 118–125 (2019)
11. Windyn Homepage, <https://www.gs-windyn.it/wind-tunnel/>. Accessed 20 July 2024
12. Clavelo B, et al.: Wind tunnel test data for the evaluation of aerodynamic coefficients on a triangular lattice with ancillaries. Zenodo: dataset (2024)

Open Access This chapter is licensed under the terms of the Creative Commons Attribution 4.0 International License (<http://creativecommons.org/licenses/by/4.0/>), which permits use, sharing, adaptation, distribution and reproduction in any medium or format, as long as you give appropriate credit to the original author(s) and the source, provide a link to the Creative Commons license and indicate if changes were made.

The images or other third party material in this chapter are included in the chapter’s Creative Commons license, unless indicated otherwise in a credit line to the material. If material is not included in the chapter’s Creative Commons license and your intended use is not permitted by statutory regulation or exceeds the permitted use, you will need to obtain permission directly from the copyright holder.





Ligurian Downslope Winds Assessed Using LiDAR Scanner for the Safety Management of Port Areas

Ivana Ivančić¹(✉), Alessio Ricci¹, Massimiliano Burlando², Djordje Romanic³, Branko Grisogono⁴, and Hrvoje Kozmar⁵

¹ University School for Advanced Studies IUSS, Pavia, Italy
ivana.ivanovic@iusspavia.it

² Department of Civil, Chemical and Environmental Engineering, University of Genoa, Genoa, Italy

³ Department of Atmospheric and Oceanic Sciences, McGill University, Montreal, QC, Canada

⁴ Department of Geophysics, Faculty of Science, University of Zagreb, Zagreb, Croatia

⁵ Faculty of Mechanical Engineering and Naval Architecture, University of Zagreb, Zagreb, Croatia

Abstract. Severe weather conditions may affect the structural integrity of buildings and infrastructures in port areas. Recommendations provided in international codes are currently based on the quasi-steady atmospheric boundary layer (ABL) winds which are not entirely representative of all the winds that may occur in the lower atmosphere. For example, ABL winds are often characterized by a lower mean wind velocity near the ground compared to other types of winds such as downbursts, tornadoes, and downslope winds (DWs). DWs develop when cold air flows over a mountain ridge with a steep lee slope, where the orographic wave breaking commonly occurs, and the cold air further slides down the mountain. DWs are well-known to occur all over the world. Thus, investigating the nature of DWs is mandatory to improve the current standards and safety management procedures of port infrastructure and operations. In this study, a measurement campaign was carried out using the LiDAR installed in the Port of Genoa to analyze DWs descending from the Apennines to the Ligurian coastline through the Turchino Valley. LiDAR scans were conducted from December 2024 to early March 2025, when DWs occur more frequently. RHI and PPI scans were carried out during six strong DW events using azimuthal angles from 295° to 330°, scanning elevations from 0° to 15°, range gates from 0.3 to 14.3 km, and 100 m resolution. The representative results of the studied DW events are presented here.

Keywords: ERIES-LIDAR · Downslope winds · Scanning Lidar · Scanning strategies

1 Introduction

The broad field of wind engineering encompasses the social and economic impacts of wind effects, wind characteristics, local wind environments, wind loads on structures, and the structural response and resilience to wind actions. All these topics are particularly

relevant in port areas, which are commonly exposed to extreme meteorological phenomena, especially extreme winds [1] that can cause accidents and pose risks to human life [2, 3]. To properly address these problems, it is sometimes of particular interest to learn more about the exact characteristics of some strong unique winds that can affect a port at the local scale. This is the case of some ports in the northern Mediterranean which are locally affected by strong downslope windstorms (DWs) that develop especially during the winter season.

DWs typically occur when the air flows over high mountains, where orographic wave breaking is present, and the cold air slides down the steep lee slopes and accelerates because of the negative buoyancy, eventually producing internal gravity waves that develop in a stable stratified environment [4–6]. Strong downslope windstorms can occur all around the world with similar characteristics, e.g., in Mendoza, Argentina [7], Hokkaido, Japan [8, 9], over the Pennine hills, Yorkshire, England [10], Boulder, Colorado, USA [11]. In the Mediterranean, Bora wind, which blows in the north-eastern Italy and Croatia, causing often disruptions in the ports of Trieste and Monfalcone, is likely the most famous and well-known DW, e.g., [12–17].

Similar DWs occur in other Mediterranean regions, like in north-western Italy, where strong DWs can occasionally blow at the end of the main valleys [18]. This is a special kind of downslope winds, called gap winds, that often occur along the main valleys of Liguria, Italy, especially when the air from the North of the Maritime Alps and Apennines reaches the top of the mountains and blows down the slope towards the sea because it is cooler and denser than the maritime air above the warmer Mediterranean water.

According to [19], these gap flows are strong gusty winds present in the lee of mountain gaps or passes, with their highest speed at the valley outlet. Their presence over the Ligurian Sea is sometimes reinforced by larger scale low-pressure systems, as during secondary cyclogenesis events in the Gulf of Genoa [20], so that stronger gusty slope winds can develop under certain meteorological conditions.

In the western part of the Genoa city, the exit of the Turchino Valley is a hotspot of strong DWs, which often develop in winter, blowing from the inland to the sea even for several consecutive days. When this type of event is expected to occur, based on weather forecast predictions, most of the port services in this area are halted, with detrimental consequences regarding maritime operations.

The Giovanni Solari Wind Engineering and Structural Dynamics (GS-WinDyn) Research Group of the University of Genoa operates a scanning Doppler wind lidar infrastructure installed at the tip of a dam about 2.5 km southeast of the Turchino Valley. This is an ideal position to measure DWs, both to study the phenomenon from the physical point of view and compare the observations with other major DWs that occur around the globe.

The major goal is to enhance the codification of DWs in engineering standards and codes. The scope of the Project ERIES-LIDAR was to accordingly perform field measurements of DWs using the Doppler lidar of the University of Genoa in the winter season 2024–2025. In the following, the measurement campaign that took place from December 2024 to early March 2025 is described and some preliminary results are shown.

2 Doppler Lidar Campaign

The Doppler Lidar operated by the University of Genoa is a WindCube 400S (version 2018), which is the most powerful scanning Lidar developed and produced by Vaisala/Leosphere. The Lidar is installed at the tip of a quay in the western part of the Port of Genoa, 5 m above the sea level (ASL), Fig. 1. In this position, the Lidar is sheltered from the sea waves by the 8 m high port dam. The Lidar has the field of view ranging from the azimuthal angle 70° to 30° , considering a clockwise rotation, while it is partially sheltered in the 30° - 70° range due to the presence of the red light that indicates the port entrance, Fig. 1d.

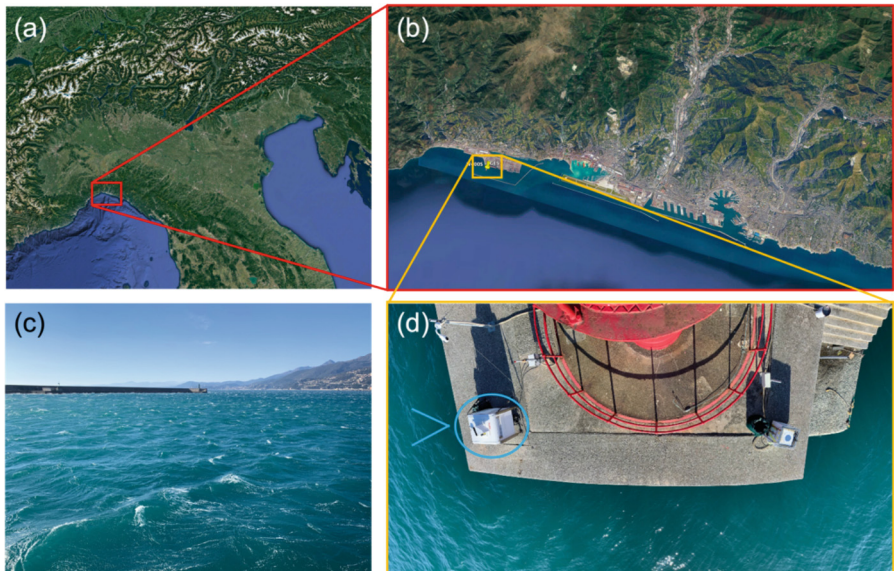


Fig. 1. Scanning Lidar in the Port of Genoa: (a) City of Genoa in the north-western Italy; (b) location of the Lidar in the western part of the city; (c) photograph was taken westward from the scanning Lidar position during an event of DWS; (d) the scanning Lidar at the tip of the quay (blue circle). Since the Turchino Valley is to the northwest of the Lidar, the instrument can measure DWS blowing within the 270° - 360° range. For safety reasons, the Lidar site is located in a restricted area managed by the Port Authority. To allow for the system to be fully operational 24/7, it is directly connected to the power supply network. The communication with the instrument and data transfer are via a 4G mobile connection based on a router accessible through a private VPN. (Color figure online)

2.1 Experimental Details

Some relevant technical specifications of the scanning lidar are provided in Table 1. In the third column the values selected for the measurement campaign are reported.

Table 1. Performance specifications and measurement parameters of the WindCube 400S.

Parameter	Values/Specification	
Maximum range	14 km	14 km
Wind velocity range	Doppler velocity from -30 to +30 m s ⁻¹	-
Precision of velocity measurements	0.5 m s ⁻¹	-
Time record length	0.5–10 s (1 s is standard)	1 s
Physical range resolution	75, 100, 150, 200 m	100 m
Scanning patterns	PPI (Plan Position Indicator); RHI (Range Height Indicator); DBS (Doppler Beam Swing); fixed LOS (Line-Of-Sight)	Mixed PPI and RHI
Output data	Radial wind velocity and Doppler spectrum broadening; Carrier-to-Noise Ratio (CNR); three-dimensional wind components (DBS scenario)	-
Scanning angles	Azimuth: 0 to 360° (with 0.01° increment); Elevation: 0° to 90° (with 0.01° increment); Endless rotation	Azimuth: 295° to 330°; Elevation: 2.5° to 12.5°

2.2 Observed DW Events

The measurement campaign lasted from the beginning of December 2024 to the beginning of March 2025. During this period 6 DW events were observed. Table 2 provides an overview of these events, classified by the synoptic meteorological conditions during DW events. The events T1-T4 are all associated to the Omega-like blocks.

In T1-T2, the cold advection of the air over northern Italy originates from high latitudes due to the presence of a stationary high-pressure system that slowly moved from Scandinavia to Siberia (from T1 to T2) coupled to a low-pressure system over central Italy. In T3 a trough was relevant for the cold air advection from the northern Atlantic Ocean to the Mediterranean, when the air was more humid than for T1 and T2. T4 was similar to T3 but the high pressure was stronger and displaced over northern Europe. During T5 the strong northerly DWs were mainly due to the presence of a very low and wide pressure system over the Atlantic Ocean that entrained the air from the Mediterranean through the gap between the Alps and Pyrenees, following a wind pattern opposite to the Mistral in southern France. Finally, T6 was a weaker event with lower differences in temperature between the Padana Plain and the Mediterranean.

In the third column of Table 2, the scanning approach regarding the studied events is described. In T1 and T2, only RHI scans were utilized, ranging from the azimuthal angle 295° to 330° with step 5° (i.e., 295°, 300°, ..., 330°). In all the other events, except

T5, a mixed scanning strategy based on both RHI and PPI scans was used. If the wind is persistent and quasi steady-state conditions can be assumed over about 10 min (i.e., the typical averaging times in boundary layer meteorology), combining RHI and PPI data is expected to provide a relatively dense grid for mapping DWs, thus offering a comprehensive spatial view of the wind field and its evolution over time. Finally, also because T5 was quite a short event, a rapid scan strategy was adopted using a single RHI pointing at the azimuthal angle 320° with the specific aim of studying the evolution of the bi-dimensional turbulent eddies.

Table 2. Performance specifications and measurement parameters of the WindCube 400S.

ID	Period (ddmmyy)	Synoptic condition	Scanning approach
T1	031224–061224	Low pressure over central Italy. Cold air advection from Scandinavia	8 RHI*
T2	061224–131224	Low pressure over central Italy. Cold air advection from Siberia	8 RHI*
T3	131224–141224	High pressure over the Balkans, trough extending over the Mediterranean from northern Atlantic	8 RHI* + 5 PPI**
T4	060225–100225	Omega block with high pressure over Scandinavia	8 RHI* + 5 PPI**
T5	190225–200225	Low pressure over the Atlantic, high pressure over central Europe	1 RHI***
T6	010325–050325	Azores anticyclone extending over central Europe	8 RHI* + 5 PPI**

* RHI: Azimuth 295° - 330° (step 5°); Elevation 0° - 15° (step 0.5°)

** PPI: Azimuth 295° - 330° (step 0.5°); Elevation 2.5° - 12.5° (step 2.5°)

*** RHI: Azimuth 320° ; Elevation 0° - 15° (step 0.5°)

3 Preliminary Results

The parameters assessed during the project include the integral flow and turbulence parameters, e.g., the mean wind speed, turbulence intensity, turbulence length scales, etc., while in the frequency domain, the power spectral density of the wind velocity fluctuations is accounted for.

As an example, in Fig. 2 the Doppler velocity measured along the RHI scans taken at the azimuthal angle 310° in the period from 0926 UTC to 0956 UTC are shown for the event T3. Firstly, it can be noted that, despite the maximum scanning range of 14 km, the availability of measurements is limited to 2.5 km ASL, while above this threshold no backscattered signal was observed. This can be due to either the reduced concentration of aerosol in the upper atmosphere or the presence of clouds. It is also interesting to note that, during this event, an upper air flow from sea to land (yellow contours) occurs above 2 km ASL, whereas the stronger DW (from land to sea) is present in the lower ABL, i.e., the ASL, exhibiting the gravitational nature of the DW flow. 1000 m is the height

of the top of the mountains at the position where DWs develop, i.e., the gap between the Padana Plain and the lee slope that leads to the exit of the Turchino Valley at the sea level.

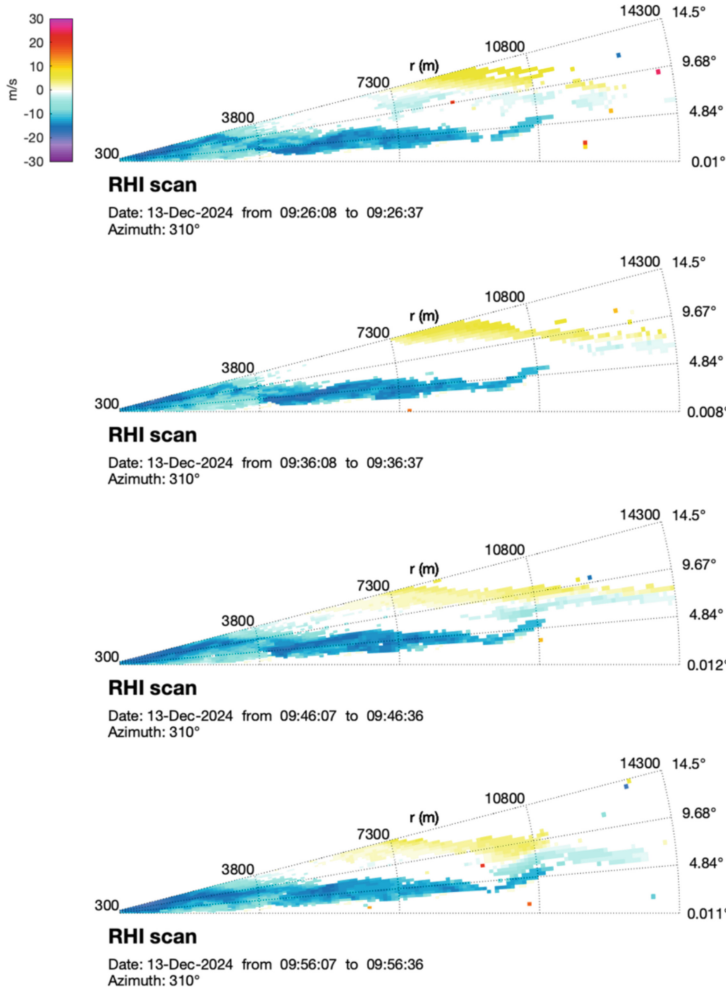


Fig. 2. RHI scans showing the Doppler velocity measured by the Lidar in the Port of Genoa on December 13, 2024, from 0926 to 0956 UTC. Negative values correspond to the flow direction towards the instrument.

The DW is stronger close to the ground from the mountain gap to about 4 km (radial distance from the Lidar), while it becomes weaker close to the ground and stronger aloft, and finally strong again nearby the instrument. What is particularly interesting is that this seems to be a recurrent pattern, because the RHI scans in Fig. 2 are recorded every 10 min and they all show the same behaviour. However, it is not clear at the moment why the strong wind detaches from the ground at 4 km and reattaches nearby the Lidar.

Something similar to a hydraulic jump could be argued, but further investigations on turbulence as well as on the three-dimensional structure of the flow are required to clarify this phenomenon.

4 Conclusions

The database of downslope winds measured during six events that occurred in winter 2024–2025 in Genoa (north-western Italy) is presented in the framework of the ERIES-LIDAR project. Measurements were performed using a Doppler scanning Lidar installed in the Port of Genoa close to the exit of the Turchino Valley, where DWs commonly blow, often causing harsh environmental conditions regarding port activities.

Only the portion of one event (T3) is analysed here in a preliminary way to show the relevance of this type of measurements. Further work is required regarding various aspects of DWs that are of interest for the wind engineering and atmospheric science communities. It is expected that the forthcoming findings will yield substantial improvements and validation of subsequent studies on DWs and their effects on structures, and encourage a detailed codification of these winds.

Acknowledgements. This work is part of the transnational access project “ERIES-LIDAR”, supported by the Engineering Research Infrastructures for European Synergies (ERIES) project (www.ries.eu), which has received funding from the European Union’s Horizon Europe Framework Programme under Grant Agreement No. 101058684. This is ERIES publication number C57. This work was supported by the Croatian Science Foundation under the project number HRZZ-IP-2022-10-9434.

References

1. Castillo, A.P.P., Heranza, J.C.M.: A review of wind impact on container port operations: current technologies, strategies and future perspectives. *Proc. Comput. Sci.* **251**, 783–788 (2024)
2. Kozmar, H., Butler, K., Kareem, A.: Transient cross-wind aerodynamic loads on a generic vehicle due to bora gusts. *J. Wind Eng. Ind. Aerodyn.* **111**, 73–84 (2012)
3. Zhang, Y., Lam, J.S.L.: Estimating the economic losses of port disruption due to extreme wind events. *Ocean Coast. Manag.* **116**, 300–310 (2015)
4. Peltier, W.R., Clark, T.L.: The evolution and stability of finite-amplitude mountain waves. part ii: surface wave drag and severe downslope windstorms. *J. Atmos. Sci.* **36**(8):1498–1529 (1979)
5. Smith, R.B.: On severe downslope winds. *Journal of Atmos. Sci.* **42**(23), 2597–2603 (1985)
6. Kozmar, H., Grisogono, B.: Characteristics of Downslope Wind Storms in the View of the Typical Atmospheric Boundary Layer. In: Hangan, H., Kareem, A. (eds.) *The Oxford Handbook on Non-Synoptic Wind Storms*, pp. 84–114. Oxford Academic (2021)
7. Georgii, W.: Studie über den Zondawind der Kordillere von Mendoza. *Meteor. Rund.* **7**, 125–129 (1954)
8. Arakawa, S.: Climatological and dynamical studies on the local strong winds, mainly in Hokkaido. *Japan. Geophys. Mag.* **34**, 359–425 (1969)

9. Takimoto, I.: Case study of the downslope wind of Japan “Rokko-oroshi.” *Atmosph. Sci. Lett.* **23**(9), e1097 (2022)
10. Aanensen, C.J.M.: Gales in Yorkshire in February 1962. *Geophys. Mem.* **14**, 1–44 (1965)
11. Klemp, J.B., Lilly, D.K.: The dynamics of wave-induced downslope winds. *J. Atmos. Sci.* **32**, 320–339 (1975)
12. Babić, N., Večenaj, Ž., Kozmar, H., Horvath, K., De Wekker, S.F.J., Grisogono, B.: On turbulent fluxes during strong winter bora wind events. *Boundary-Layer Meteorol.* **158**, 331–350 (2016)
13. Lepri, P., Večenaj, Ž., Kozmar, H., Grisogono, B.: Near-ground turbulence of the Bora wind in summertime. *J. Wind Eng. Ind. Aerodyn.* **147**, 345–357 (2015)
14. Romanic, D.: Local winds of Balkan Peninsula. *Int. J. Climatol.* **39**(1), 1–17 (2018)
15. Golem, P., Toman, I., Večenaj, Ž., Kozmar, H., Grisogono, B.: Unique windward measurements and a mesoscale simulation of an extremely long-lasting severe bora event. *Boundary-Layer Meteorol.* **183**, 495–504 (2022)
16. Golem, P., Večenaj, Ž., Kozmar, H., Grisogono, B.: The effect of orography on bora wind turbulence. *Boundary-Layer Meteorol.* **187**, 193–212 (2023)
17. Golem, P., Večenaj, Ž., Kozmar, H., Grisogono, B.: Misalignment between the propagation direction of the bora wind and its pulsations. *Q. J. Roy. Met. Soc.* **150**, 1194–1205 (2024)
18. Burlando, M., Tizzi, M., Solari, G.: Characteristics of downslope winds in the Liguria Region. *Wind Struct.* **24**(6), 613–635 (2020)
19. Zängl, G.: Stratified flow over a mountain with a gap: Linear theory and numerical simulation. *Q. J. R. Meteorol. Soc.* **128**, 927–949 (2002)
20. Trigo, I.F., Bigg, G.R., Davies, T.D.: Climatology of cyclogenesis mechanisms in the mediterranean. *Mon. Wea. Rev.* **130**(3), 549–569 (2002)

Open Access This chapter is licensed under the terms of the Creative Commons Attribution 4.0 International License (<http://creativecommons.org/licenses/by/4.0/>), which permits use, sharing, adaptation, distribution and reproduction in any medium or format, as long as you give appropriate credit to the original author(s) and the source, provide a link to the Creative Commons license and indicate if changes were made.

The images or other third party material in this chapter are included in the chapter’s Creative Commons license, unless indicated otherwise in a credit line to the material. If material is not included in the chapter’s Creative Commons license and your intended use is not permitted by statutory regulation or exceeds the permitted use, you will need to obtain permission directly from the copyright holder.





Wind Tunnel Measurements and CFD Correlation of Gas Dispersion Around Offshore Supply Vessel

Felipe Sanchez Castro¹(✉) , João Muralha² , Guilherme Vaz² , Eric Roosenboom³ , Tristan Andrewartha¹ , Anjali Radhakrishnan⁴ , and Stefanie Gillmeier⁴

¹ Knud E. Hansen, Elsinore, Denmark

FEC@knudehansen.com

² blueOasis, Ericeira, Portugal

³ Damen Naval, Vlissingen, the Netherlands

⁴ Eindhoven University of Technology, Eindhoven, the Netherlands

Abstract. ERIES-POLISHED studies the influence of sea-like atmospheric boundary layers (ABL) wind conditions on the pollutant dispersion on deck of a service operation vessel. Moreover, the influence of ship-ship interaction on pollutant dispersion on deck of service operation vessels is assessed and compared to the reference case. Also, an investigation is performed on the influence on pollutant dispersion on deck of the service operation vessel close to typical harbour structures to identify differences to the previous cases. The investigations of the above-mentioned configurations were tested in the closed-circuit Atmospheric Boundary Layer Wind Tunnel (ABLWT) at Eindhoven University of Technology. The results of the wind tunnel measurements are used to validate CFD models of ReFRESCO, OpenFOAM and Star-CCM + flow solvers both at model and full-scale conditions, by research groups in Portugal, the Netherlands and Denmark. This paper presents the early results of objective 1 of the ERIES-POLISHED project, where the ongoing activities for the validation studies of Industry 4.0 methods is being performed.

Keywords: Exhaust Smoke Dispersion · Atmospheric boundary layer · Wind tunnel · CFD · Star-CCM + · OpenFOAM · ReFRESCO

1 Introduction

Operating ships in a harbour environment increases the likelihood of interference between neighbouring ships. Moreover, exhaust gas dispersion into the surroundings can potentially cause hindrance for residents [1] and during operation in harbour, emissions may be higher than during regular operations in open sea [2]-[3]. There is a shift towards zero emissions and decarbonization, as air pollution is considered one the largest health risks [4]. While these developments are ongoing, air pollution remains an issue. The majority of existing vessels are dependent on fossil fuels. As various harbours are

enforcing stricter emission regulations, it becomes important to predict and quantify exhaust gas emissions for existing vessels.

Vessels encounter various wind conditions while operating at open seas or manoeuvring in a harbour. In all such conditions, either the crew is working on open deck spaces or gases are recirculated into ventilation intakes, potentially exposing crew and passengers to noxious exhaust gases. Moreover, during harbour operations, there is potential dispersion of exhaust gases into the urban environment which leads to more local pollution.

The project of ERIES-POLISHED is dedicated to provide detailed wind tunnel dispersion experiments as validation data for various CFD software tools. As vessels are operating in a harbour, the local atmospheric boundary layer will be disturbed by the presence of neighbouring structures, such as passing vessels or harbour buildings. Precisely the influence of dispersion for neighbouring ships and dispersion into the atmosphere under disturbance is evaluated within this project.

The project aims to investigate the following three objectives:

Objective 1:Investigation of the dispersion from a single ship under various wind directions. This serves as a baseline study and is a typical investigation for these types of studies where the neighbouring structures are neglected.

Objective 2:Determination of the influence and interference on exhaust gas dispersion with neighbouring ships within a ship's length distance. This is relevant for ships operating close to one other in harbours, offshore in wind turbine parks or in shipping lanes.

Objective 3:Influence of exhaust gas dispersion with neighbouring harbour-like structures. Buildings and harbour-like structures have a larger wake, and this objective is very relevant for ships in a harbour.

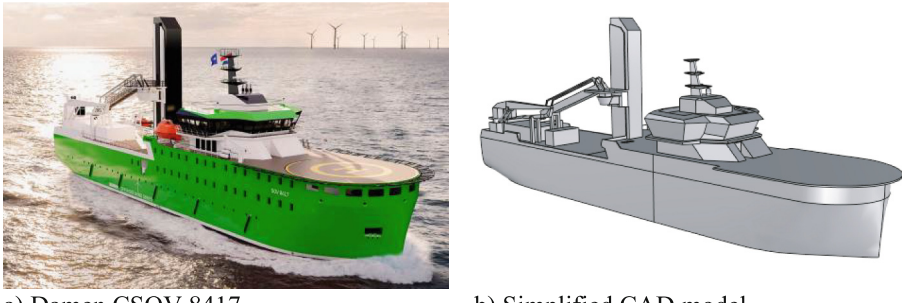
A measurement campaign was carried out at the end of 2024 in the Atmospheric Boundary Layer Wind Tunnel at Eindhoven University of Technology to gather concentration levels around different ship configurations for each of the three objectives. These configurations are now remodelled for CFD validation and simulation.

This paper presents the ongoing activities of the numerical modelling.

2 Details of Vessel

The vessel used in this project is a generic Construction and/or Service Operation Vessel (CSOV) [5]. A picture of a Csov is shown in Fig. 1a. The investigated Csov has a length of 84 m and beam of 17 m. Although it is related to other Csov vessels in the portfolio, the model studied contains a few simplifications and modifications. The simplifications basically consist of removing various deck and equipment components that are relatively small. These smaller elements only influence the flow field locally and given that one of the primary aims of the investigation is to provide data for CFD validation, the additional complication is unnecessary. Moreover, such finer details are difficult to 3D-print for the wind tunnel model and will result in an unnecessarily high cell count in CFD modelling.

The geometry has been simplified for experimental and numerical modelling as can be seen in Fig. 1b.



a) Damen CSOV 8417

b) Simplified CAD model

Fig. 1. Images of the vessel.

The most notable modification is that for the sole purpose of this project, it has been decided to install the exhaust outlets on top of the wheelhouse. In practice the exhaust outlets will be installed on top of the elevator, which is the highest available location on the vessel. This location is, of course, beneficial for reducing issues with exposure to exhaust gas on lower decks, but it would reveal very limited data for the validation study. Therefore, the exhaust outlet has been placed at lower height to purposely increase the exhaust gas concentration at working deck level.

2.1 Operational Profile of CSOV

These multi-role vessels service offshore wind farms by transferring crew and cargo to various offshore wind turbines multiple times per day. At each wind turbine a dynamic positioning system is used to safely and slowly manoeuvre towards the turbine. When the vessel is near the wind turbine, the motion-compensated access system (attached to the vertical elevator) will connect to the wind turbine to safely transfer crew and cargo to or from the wind turbine. When the transfer is completed, the vessel slowly manoeuvres away from the wind turbine and proceeds to its next mission. This process is carried out several times per day. While doing the operations within a wind farm, the CSOV operates most likely in the wake of wind turbines. Hence the incoming atmospheric boundary layer may be disturbed. During manoeuvring and transfer phases some of the crew work at open-deck spaces and therefore can be exposed to gas emissions from the vessel.

3 Experimental Set-Up

This paragraph briefly summarizes the experiments. More details can be found in dedicated publications about the experiments [6]- [7]. A wind tunnel model at a scale of 1:100 was tested in the closed-circuit Atmospheric Boundary Layer Wind Tunnel (ABLWT) at Eindhoven University of Technology. A schematic of the ABLWT is presented in Fig. 2a. A picture of the model in the wind tunnel is shown in Fig. 2b.

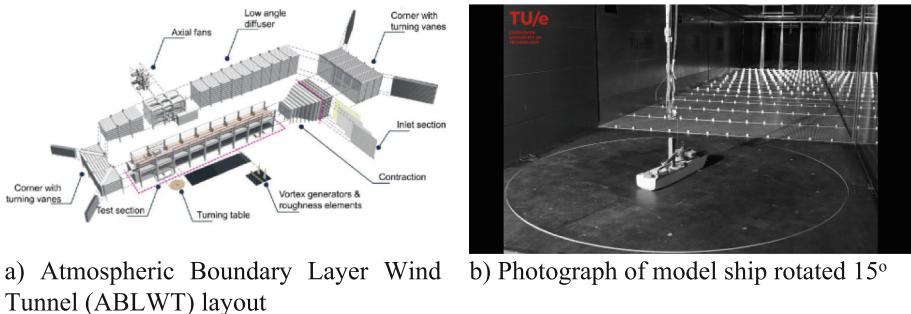


Fig. 2. Wind tunnel set-up.

A neutral maritime-like atmospheric boundary layer wind profile was generated with vortex generators and surface roughness elements. The wind profile follows a power law defined (with full-scale properties) with a reference velocity of 10 m/s at a reference height of 20.2 m, which corresponds to the height of the centre of the exhaust outlet above sea-level. The exponent of the power-law is 0.12.

Exhaust emissions are modelled with a mixture of synthetic air, ethylene and helium. The exhaust gas is emitted at a reduced-scale velocity of 0.88 m/s (for Froude number similitude). This corresponds to a 25% engine loading condition at full-scale (approx. 8.8 m/s).

The concentration of the emitted gas is measured at a height of 1.5 m (full-scale) at multiple locations on deck of the vessel using a fast flame ionisation detector from Cambustion Ltd. At each location, a 300-s-long time series of pollutant concentrations is recorded at a frequency of 85 Hz. (Note that the sample locations (Fig. 10) is shown later in the paper for easier comparison to CFD results.)

4 CFD Model Description

4.1 CFD-Tools

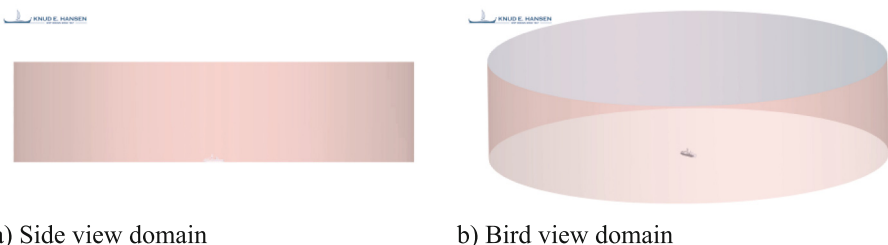
Star-CCM is a commercial CFD solver employed for RANS simulations that are part of this study. Version 24.10.0001 has been used for this study [8]. Star-CCM + uses the finite volume method on cell centre unstructured meshes. Second order upwind and central differences schemes are used to discretize the convection and diffusion terms. The SIMPLE algorithm solves the pressure-velocity coupling. The turbulence model used in this study is the $k-\omega$ SST.

ReFRESCO is a community based open-usage viscous-flow CFD code [9]. It solves multiphase, unsteady incompressible viscous flows using the Navier-Stokes equations, complemented with turbulence models and volume-fraction transport equations for the pollutant species. The equations are discretized using a finite-volume approach with cell-centered collocated variables, in strong-conservation form. Pressure-correction equation based on the SIMPLE algorithm is used to ensure mass conservation. For turbulence modelling, a RANS approach was used in this study, but URANS and SRS (scale-resolving simulations) approaches like DDES, PANS and LES are also available.

OpenFOAM is a free, open source CFD software primarily developed by OpenCFD Ltd, which is a subsidiary of the ESI Group [10]. OpenFOAM incorporates various numerical modelling techniques including DES and LES modelling. In this study, OpenFOAM v2306 is used with the industrial standard steady-state Reynolds Averaged Navier-Stokes (RANS) solver. A dedicated solver for buoyancy effects (`buoyantSimpleFoam`) is used with a time-independent SIMPLE pressure-velocity coupling algorithm. The solver is a steady state solver for compressible laminar or turbulent flow including buoyancy effects. Turbulence is modelled using the k- ω -SST RANS turbulence model and the near wall boundary layers are modelled with a wall-function. The k- ω -SST is an accurate model for external flow simulations, and this model is appropriate for bluff body flows, such as superstructure flow analysis). Air is modelled with an ideal gas (i.e. incompressible perfect gas) description and (dynamic) viscosity, μ , is determined using a Sutherland viscosity model. Exhaust gas dispersion is modelled with a passive scalar transport equation.

4.2 Domains and Numerical Mesh

Star-CCM. The domain has been modelled as a cylinder with a radius of 10x Lpp (ship lengths) and a height of 6x Lpp m to avoid interference of the domain boundaries with the calculations by reducing the risk of having blockage effects. A global view of the mesh is presented in Fig. 3.



a) Side view domain

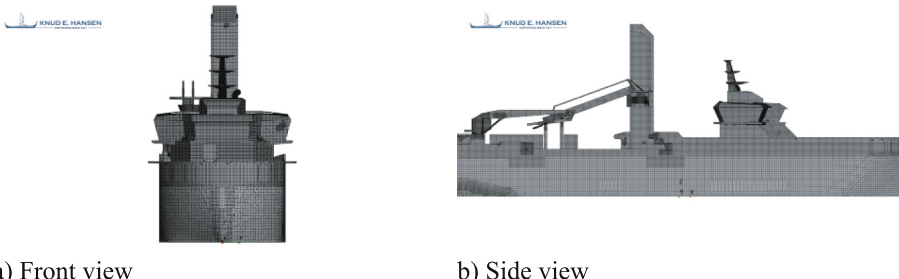
b) Bird view domain

Fig. 3. Star-CCM Mesh views.

Discretization of the volume elements has been achieved by using trimmed hexahedral cells with several local refinements and the prism layer that extends from the surface of the hull. The refinements were located close to the vessel and especially in those areas where a finer mesh was required such as the superstructure, and the wake refinement zone to capture the plume of exhaust gases. The $y +$ values for the simulations stay in the range $30 \leq y + \leq 600$ independently of environmental conditions i.e., density, reference speed among others. The cell count for this mesh is 16.4 million cells.

Views of the surface mesh of the vessel are shown in Fig. 4. To resolve the Atmospheric Boundary Layer (ABL), a set of refinements in the bulk domain are depicted in Fig. 5.

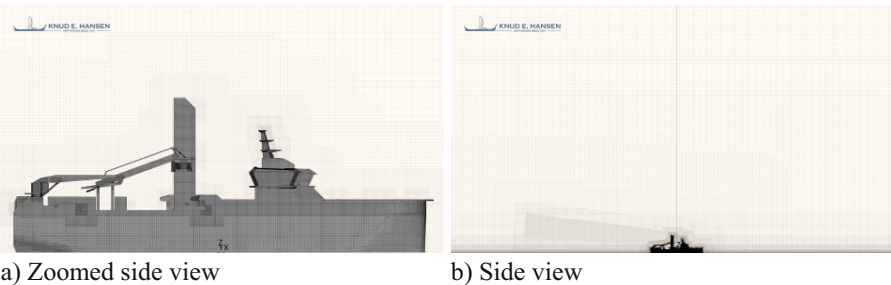
ReFRESCO. For the ReFRESCO simulations, a full hexahedral mesh was generated using Fidelity-Hexpress. The used cylindrical domain is illustrated in Fig. 6a. It is centred around the vessel and has a radius of 10 LOA and a height of 410 m. The mesh,



a) Front view

b) Side view

Fig. 4. Star-CCM surface mesh.

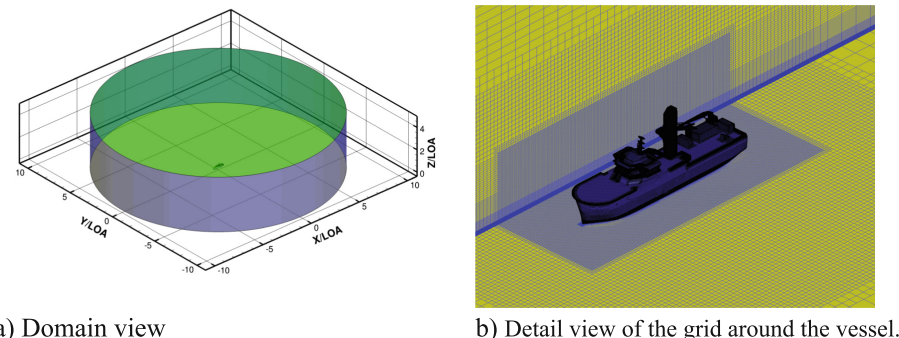


a) Zoomed side view

b) Side view

Fig. 5. Star-CCM Volume mesh.

illustrated in Fig. 6b, has a base cell size of 32 m. The mesh contains two refinement boxes that reduce the cell size from the initial base size to cells of approximately 0.5 m near the vessel and additional surface refinements to fully capture the vessel geometry as illustrated in Fig. 6b. Post-anisotropic refinement was also used to capture the atmospheric boundary layer profile. Viscous layers were also included in the vessel surfaces with a first cell height of 9.1 mm, which resulted in an average y^+ value of 100. The mesh contains a total of 16.6 million cells and 0.86 million surfaces.



a) Domain view

b) Detail view of the grid around the vessel.

Fig. 6. Computational domain used in ReFRESCO simulations.

OpenFOAM (ANSA) Mesh. The mesh for OpenFOAM has been generated with ANSA from Beta CAE Systems. The mesh (for full scale simulations) is cylindrical with a diameter of 3000 m and a height of 250 m. The total cell count of the mesh is 53 million, and it is divided into 10 million prism cells in the boundary layer and 43 million tetrahedra cells in the volume. A mesh overview is shown in Fig. 7, and details of the surface mesh are presented in Fig. 8.

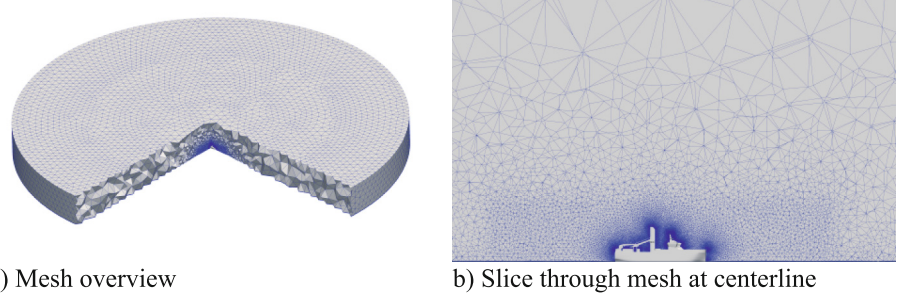


Fig. 7. Views of the ANSA volume mesh.

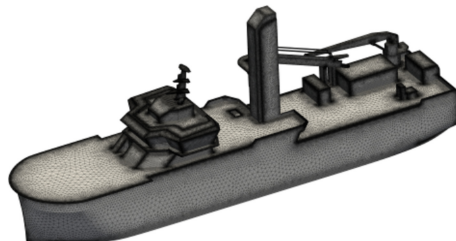


Fig. 8. ANSA surface mesh.

4.3 Environmental Conditions in CFD Simulations

Exhaust gas simulations are performed for the full-scale environmental conditions listed in Table 1.

In Star-CCM + the exhaust gas is modelled as a multi-component mixture where a miscible mixture of He, C₂H₄, O₂ and N₂ in the same phase. For the CFD simulations the Synthetic air is assumed to be composed of 80% nitrogen and 20% oxygen. The gas then is assumed to be composed of 0.61% He, 0.2% C₂H₄, 0.038% O₂, and 0.152% N₂.

In ReFRESCO and OpenFOAM the gas is simulated with a passive scalar, where a variable is assigned to a fluid phase that does not affect the physical properties of the simulation but can be used to track one or various quantities and for this project it is used to colour and track a gas stream of ethylene to be compared to the ABLWT measurements.

Table 1. Environmental conditions.

Variable	Unit	Value
Reference velocity	m/s	10
Reference height	m	20.2
Density	kg/m ³	1.22
Ambient temperature	°C	15
Air viscosity	Pa·s	1.802 × 10E-5
Inflow angle	°	15
Exhaust gas temperature	°C	350
Exhaust gas velocity	m/s	8.8

5 Results

The results for objective 1 of this project investigates gas dispersion for an isolated ship for different wind directions. Prior to performing an extended validation of gas dispersion with several CFD solvers, one case with an inflow angle of 15 degrees is used to develop the baseline model setup, calibrate the model, establish a common workflow for interrogating the models and develop a solid foundation to perform the CFD validation. This section presents the results of gas dispersion obtained for an inflow angle of 15 degrees.

5.1 Wind Profile

The wind profile simulated in the various CFD solvers are sampled in the free upstream of the vessel. The CFD results compared to the Log and Power law wind profiles are shown in Fig. 9. The deviation below 5 m height between the wind profiles from the CFD codes, the measurement and theory are noticeable. However, ReFRESCO and Star-CCM + tend to slightly underpredict the power law and experimental data. OpenFOAM has a tendency of overpredicting the speed near the boundary layer. The overall correlation above 10 m height is acceptable and the velocity at the exhaust height is correct.

The difference in the simulated wind profiles is caused due to the difference in how the different meshing tools used in this project allow various settings for generating the necessary refinements to capture properly the boundary layer near the bottom wall of the domain, around the vessel and how each solver deals with the mesh properties.

5.2 Gas Dispersion

The results of the gas dispersion analysis with the different solvers are analysed by probing the parts per million (ppm) of helium in the case of Star-CCM + as this is the gas that amounts to 61% of the gas mixture. For ReFRESCO and OpenFOAM, the gas composition has been simulated as a passive scalar and the sampling method therefore tracks the Passive Scalar. The wind tunnel measurements reported the concentration of

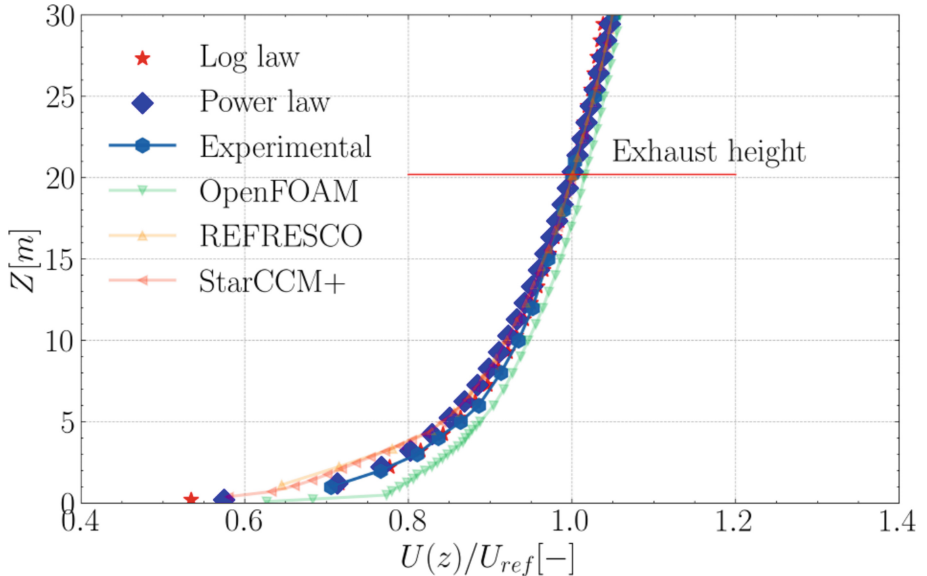


Fig. 9. Comparison between the numerical and experimental wind profiles.

ethylene. Therefore, the results of ReFRESCO and OpenFOAM track the concentration of ethylene.

The different gas components are probed at 34 locations, as shown in Fig. 10, and compared to the wind tunnel measurements on the same locations. The comparison between numerical and experimental values is presented in Fig. 11.

The data shows the capability of the numerical methods to identify the presence of the exhaust gas for most of the probe locations, but all codes tend to underestimate the relative concentration of the tracer gas. The results of probes P211, P212, P311, P312, P21 and P23 predict higher gas concentration values as these probes are located inside the exhaust plume. At these probe locations Star-CMM + and ReFRESCO present clear overshoots.

The gas concentration measured at the probes shown in Fig. 10 are presented in Fig. 11. Here the measurement at each probe is normalized by the total concentration of gas emitted.

5.3 Helium Gas Dispersion

The simulations performed with Star-CCM + are based on a RANS approach. The solver simulates a multi-component gas where helium (He) is the gas with the larger percentage of the gas mixture. Any of the gas components of the gas mix can be analysed but, in this section, only the results for helium concentrations are presented.

Figure 12 presents the results for the iso-surface contours for 0.01%, 0.25% and 0.8% content of helium. These iso-surfaces display the results only for the helium component of the gas emitted at the exhaust gas and not the whole gas mixture.

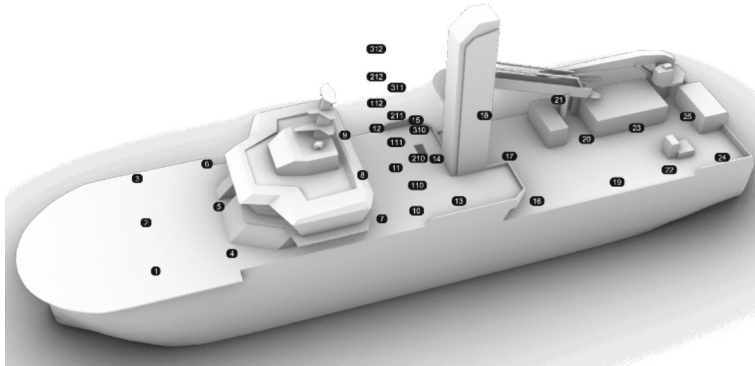


Fig. 10. Sample point locations.

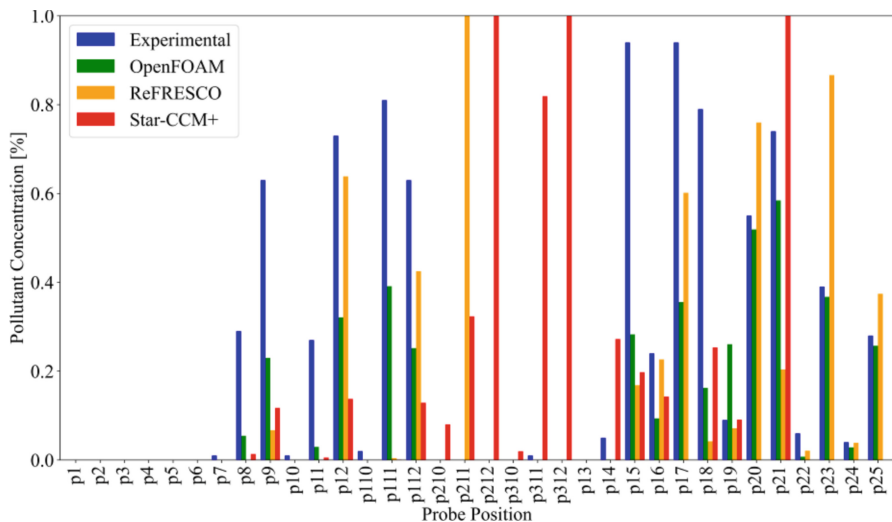


Fig. 11. Concentration levels at probe locations for 15° inflow angle.

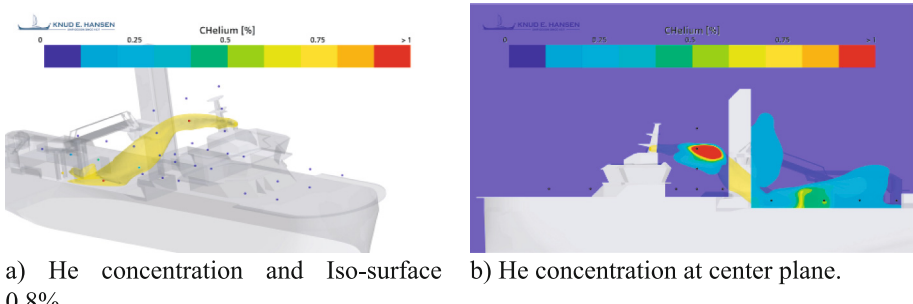


a) 0.01% He Iso-surface b) 0.25% He Iso-surface H c) 0.80% He Iso-surface

Fig. 12. Iso-surface of the percentage of helium obtained using Star-CCM +.

Figure 13 shows the concentration of helium measured at the centre plane and an iso-surface of 0.8% of helium. The probes that measure higher values are the ones located within or in the wake of the iso-surface shown in Fig. 13a.

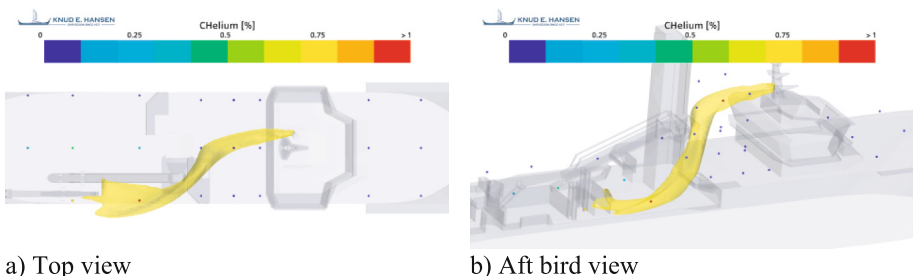
Probe 211 is the probe located right after the exhaust outlet and it has the higher concentration of helium for this condition, as shown in Fig. 13b and Fig. 14. It can be inferred that conducting a CFD campaign before starting a wind tunnel campaign can assist in assessing probe locations effectively therefore improving the measurement success of a wind tunnel campaign.



a) He concentration and Iso-surface 0.8%.
b) He concentration at center plane.

Fig. 13. Relative concentration of Heat probes locations and centre plane using Star-CCM +.

Furthermore, it is needed to device a procedure to better display the averaged gas dissipation throughout the simulation to better understand the diffusion process because the results presented here are the instantaneous results obtained at the end of the simulation and not an averaged value that can account for dispersion and diffusion.



a) Top view
b) Aft bird view

Fig. 14. Probes location and 0.8% iso-surface content helium using Star-CCM +.

5.4 Ethylene Gas Dispersion

The simulations performed with ReFRESCO and OpenFOAM track a passive scalar to simulate the gas dispersion and the results are presented for the dispersion of ethylene.

ReFRESCO. The simulations conducted using ReFRESCO are based on a RANS modelling approach, so the results are already time-averaged and can be directly compared to the experimental results.

The simulation results are presented in Fig. 15 and Fig. 16. Figure 15 present illustrations of three iso-surface levels of the percentage of ethylene, and Fig. 16 a slice showing the contour of the same quantity in the vessel centre line.

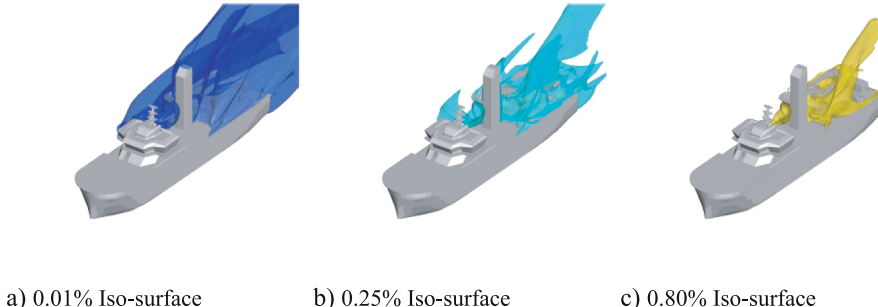


Fig. 15. Iso-surfaces of the percentage of ethylene using ReFRESCO.

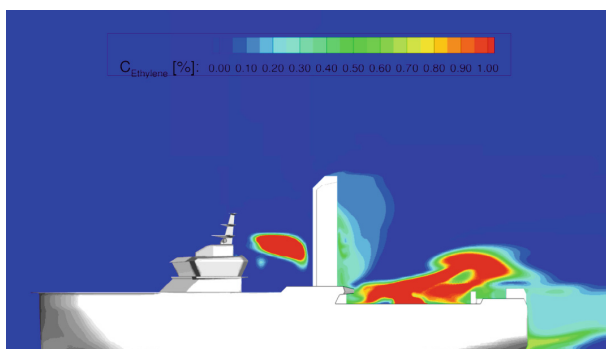


Fig. 16. Contour of the percentage of ethylene in vessel centre line using ReFRESCO.

The figures show that for this incidence angle and reference velocity, the flow transports the exhaust gas into the lower deck area, with this zone presenting high concentrations of ethylene as areas near the emission source.

OpenFOAM. Figure 17 shows the 3D contours of exhaust gas for OpenFOAM. The results are obtained from a passive scalar transport, where the emission has been specified at 1 (i.e. 100%). The contours represent various percentages of this emitted scalar. With the dispersion of a passive scalar it is assumed that the tracer is behaving as ideal gas and is following the flow. The distribution of exhaust gas concentration at exhaust outlet level is presented in Fig. 18. It shows the highest concentration just after the exhaust outlet, and it can be clearly seen how the exhaust gas is dispersed around, and into the wake of the vertical elevator.

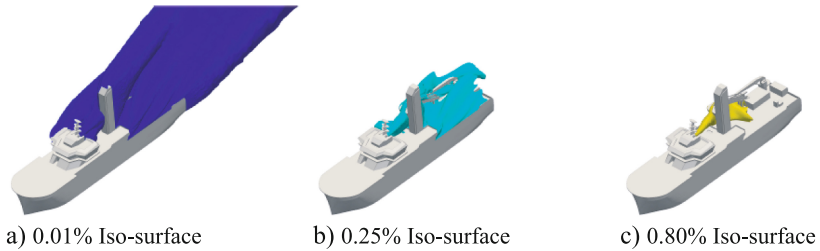


Fig. 17. Iso-surface of the percentage passive scalar using OpenFOAM.

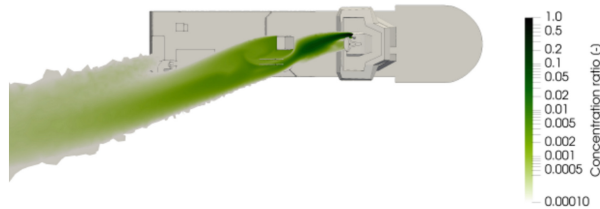


Fig. 18. Horizontal slice at height of exhaust outlet, with a logarithmic concentration distribution using OpenFOAM.

6 Conclusions and Future Work

The present work presents preliminary work conducted for the ERIES-POLISHED project, where recently dispersion measurements on an offshore vessel have been conducted in the Atmospheric Boundary Layer Wind Tunnel at the Technical University in Eindhoven. Initial work is starting for validation with different CFD codes: Star-CCM +, ReFRESCO and OpenFOAM. All codes used a RANS model. The current work shows the first results of simulations with three different solvers and different meshes for one of the configurations at a yaw angle of 15°. The preliminary results indicate some differences of matching the power-law wind profiles, Star-CCM + and ReFRESCO slightly underestimate the wind profile, while in the OpenFOAM set-up the profile is overestimated. A comparison of the exhaust gas concentrations shows that all codes can predict the presence of exhaust gas in most of the probe locations. However, when compared with the experimental results, they underpredict the exhaust gas relative concentrations. Also, the iso-surface analysis shows that the qualitative results shown by Star-CCM + are lower than the results from ReFRESCO and OpenFOAM. The qualitative results for the gas concentration represented by the iso-surface at different content levels between the flow solvers show differences that can be attributed to the multi-component gas and passive scalar physics models used by the flow solvers. However, more study on this subject has to be done.

Future work will focus on improvements in the numerical set-up used, for example, utilizing a URANS approach or even a hybrid turbulence closure, both un-steady approaches that can better capture the flow around the vessel. Grid refinement studies in both full and model scales should also be conducted to assess the impact of the scaling

effects. Improving the setup by using different physics models to capture more accurately the gas concentrations will be performed. The analysis and post-processing of the relative gas concentrations should also improve in quantifying exposure limits and quantify and account more accurately for gas diffusion and dispersion in a given time period where the gas emitting source is operated.

Acknowledgements. This work is part of the transnational access project “ERIES-POLISHED”, supported by the Engineering Research Infrastructures for European Synergies (ERIES) project (www.ries.eu), which has received funding from the European Union’s Horizon Europe Framework Programme under Grant Agreement No. 101058684. This is ERIES publication number C54.

References

1. Zubiaga, A., Madsen, S., Khawaja, H., Boiger, G.: Atmospheric contamination of coastal cities by the exhaust emissions of docked marine vessels: the case of Tromsø. *Environments* **8**(9), 88 (2021). <https://doi.org/10.3390/environments8090088>
2. Bogdanowicz, A., Kniaziewicz, T.: Marine diesel engine exhaust emissions measured in ship's dynamic operating conditions. *Sensors* **20**(22), 6589 (2020)
3. German-Galkin, S., Tarnapowicz, D.: Energy optimization of the ‘shore to ship’ system - a universal power system for ships at berth in a port. *Sensors* **20**(24), 3815 (2020)
4. World Health Organization (WHO), Ambient (outdoor) air pollution . [https://www.who.int/news-room/fact-sheets/detail/ambient-\(outdoor\)-air-quality-and-health](https://www.who.int/news-room/fact-sheets/detail/ambient-(outdoor)-air-quality-and-health). Accessed 19 Mar 2025
5. Sankaramoorthy K, Cerro Diaz de Teran M A.: New paradigm in CSOV ship design – a performance study. In: 16th Symposium on High-Performance Marine Vehicles HIPER'24, Drübeck, Germany (2024)
6. Gillmeier, S., Roosenboom, E.W.M., Sánchez Castro, L.F., Muralha, J., Beleza Vaz, G., Andrewartha, T.: Pollutant dispersion of ship emissions under realistic operating conditions. In: PHYSMOD 2024 – International Workshop on Physical Modelling of Flow and Dispersion Phenomena, Lyon, France (2024)
7. Gillmeier, S., Krishnan Radhakrishnan Jayakumari, A., Roosenboom, E.W.M., Muralha J., Beleza Vaz, G., Sánchez Castro, L.: (2025-to be presented) experimental assessment of the pollutant dispersion of ship emissions. In: EACWE 2025, 9th European-African Conference on Wind Engineering, Trondheim, Norway
8. Siemens Simcenter STAR-CCM+ user guide (Version 2410), website. <https://www.plm.automation.siemens.com/>. Accessed 21 Mar 2025
9. Vaz, G., Jaouen, F., Hoekstra, M.: Free-Surface viscous flow computations: validation of URANS code FreSCo. In: 28th International Conference on Ocean, Offshore and Arctic Engineering. Volume 5: Polar and Arctic Sciences and Technology; CFD and VIV, pp. 425–437. ASMEDC, Honolulu, Hawaii (2009)
10. OpenFOAM Homepage, <https://www.openfoam.com/>. Accessed 06 Mar 2025

Open Access This chapter is licensed under the terms of the Creative Commons Attribution 4.0 International License (<http://creativecommons.org/licenses/by/4.0/>), which permits use, sharing, adaptation, distribution and reproduction in any medium or format, as long as you give appropriate credit to the original author(s) and the source, provide a link to the Creative Commons license and indicate if changes were made.

The images or other third party material in this chapter are included in the chapter's Creative Commons license, unless indicated otherwise in a credit line to the material. If material is not included in the chapter's Creative Commons license and your intended use is not permitted by statutory regulation or exceeds the permitted use, you will need to obtain permission directly from the copyright holder.





Code Calibration in Wind Engineering: Shortcomings and Needs

Francesco Ricciardelli^(✉) , Vincenzo Picozzi , and Alberto Maria Avossa

Università Della Campania “L. Vanvitelli”, Aversa, CE, Italy
friccia@unicampania.it

Abstract. The writing of the Second Generation Eurocode on wind actions on structures, prEN1991–1–4 has revealed a number of shortcomings. Well established as well as more recent action and response models are available, which have been incorporated into the new Code. Nevertheless, the issue remains of calibration, which affects not only the assessment of the characteristic value of the action given by EN1991–1–4, but also the code factors given by EN 1990. Among the parameters needed in a wind loading code, some are site-dependent, some are not. For site-dependent parameters, the task of code-writers is limited to the drafting of simple and clear rules for their derivation, so that no difference arises when the code is used in one country or another. As to site-independent parameters, the effort can be much bigger and should benefit from the exploitation of up-to-date research results, as well as from coordination among different communities of code-writers around the world. This paper tries to summarise what are the most urgent needs for calibration of wind loading codes, and how experimental research in Wind Engineering can help filling gaps.

Keywords: Wind Loading Codes · Wind Loading Models · Full Scale Experiments · Wind Tunnel Testing · Computational Analyses · Code Calibration

1 Introduction

Issued in December 2012, Mandate M/515 of the European Commission to CEN started the long process of the transition towards the Second Generation of the EN Eurocodes. Within Phase 2 of the reaction of CEN to Mandate M/515, between August 2017 and April 2020, a Project Team prepared a draft of the new *EN 1991–1–4 Eurocode 1 - Actions on structures - Part 1–4: General actions - Wind actions* [1, 2]. The draft was then handled by a Task Group within CEN TC250/SC1, and was submitted to public enquiry in March 2024, and will undergo Formal Vote in October 2025 [3], to supersede the current version [4].

During these nine years, a tremendous amount of work was carried out by a number on European wind engineering experts working on the project, and 2000 + comments were placed by 34 National Standardization Bodies, which gave rise to a similar number modifications to the intermediate drafts.

Such a long and complex process has revealed several shortcomings in the chain through which wind actions and effects are assessed. Besides that, the additional issue remains of calibration, which affects not only the assessment of the characteristic value of the action given by EN 1991–1–4, but also the code factors provided by EN 1990 [5, 6].

Most of the parameters contained in the Code, either in the form of European values or in that of Nationally Determined Parameters (NDPs), were spontaneously produced by a number of research institutions in the ‘60s, ‘70s and ‘80s of the last century, a time in which the principles of structural reliability [7] had not yet made their disruptive entrance into structural design and design codes. As such, their values suffer from a number of deficiencies among which: (a) heterogeneity and inconsistency, as they were produced by different subjects and using different approaches; (b) being dated, as new and more efficient measurement and processing techniques have meanwhile become available; (c) incompleteness, as they describe a limited number of situations that need to be largely expanded; (d) not complying with the structural reliability models set by Eurocode 0 [8].

Among the parameters needed in a wind loading code, some are site-dependent, some are not. For site-dependent parameters, the task of the writers of International codes, such as the Eurocodes, is limited to the drafting of simple and clear rules for their derivation, so that no difference arises when the code is used in one country or another. For site-independent parameters, the effort can be much bigger and should benefit from the exploitation of up-to-date research results, as well as from coordination among different communities of code-writers around the World.

Within the framework of the ERIES initiative, this paper tries to summarise what are the most urgent needs for calibration of wind loading codes, and how experimental activity carried out in large scale facilities for Wind Engineering research can help filling gaps. It refers to parameters appearing in the first three link of the Alan G. Davenport Wind Loading Chain, in turn corresponding to the first three terms of the load equation, i.e. the reference wind velocity, the exposure coefficient and the aerodynamic coefficients. As to the experimental techniques, these can be grouped into the three broad areas of full scale testing, wind tunnel testing and numerical simulations.

2 Design Wind Speeds

Design wind speeds are given in EN 1991–1–4 in the form of fundamental values of the basic wind velocity. These are NDPs, and are therefore provided by the National Annex. Current values have been prepared over the last decades at the national level, using data from each particular country, and not including those coming from neighbouring countries. This has given rise to unjustified and unacceptable inconsistencies across borders where no physical discontinuities exist that could justify differences; it is, e.g., the case of the border between Germany and Denmark, featuring differences between 3 and 6 ms^{-1} . In other cases, such as the borders between Italy and neighbouring France, Switzerland, Austria and Slovenia, differences are justified by the presence of mountains; however, also in that case sometimes the values provided may be found questionable due to the strong effects expected to come from local circulation.

In addition to that, both datasets, preprocessing techniques and statistical analysis methods are often outdated; they are also not the same for all countries and this contributes to the above-mentioned discontinuities. Finally, current design wind speeds incorporate only long duration phenomena, among which are large scale synoptic storms as well as strong local winds, such as bora striking the province of Trieste in Italy and the north of Croatia, or mistral in the south of France. This was acceptable at the time of the writing of the ENVs, when use of the Eurocodes was expected to be limited to European countries and when the European extreme wind climate was dominated by such winds. It is definitely inappropriate thirty years later, when the European wind climate has been and will be further modified by the climate change, and when the Eurocodes are used and will potentially be used by countries all over the world.

To overcome the issues above, two main actions would be in order; first is that of incorporating other types of wind into the code, second is that of establishing up-to-date, homogeneous criteria for assessing design wind speed and of applying them to produce a European synoptic extreme wind map. To the aim of the second action, large scale research facilities can provide useful support, as it will be detailed in the next paragraphs.

Current mean and extreme wind maps are built based on measured wind speeds. These come from a network of anemometers, most of which are located in airports. Details about the standardization of wind speeds are provided by WMO [9]. Among the weak points associated with the use of experimental data there are that these are:

measured at a small number of locations, when compared to the area of interest; for example, the density of measurements used to build the current extreme wind map of Italy [10] is of $4,800 \text{ m}^{-2}$; it is of $6,900 \text{ m}^{-2}$ for France and of $1,900 \text{ m}^{-2}$ for Germany [11];

- a. the measurement windows are not the same for all (European) countries, and the length of the records can also differ substantially from one station to another, and on average from one country to another; it is 22 years for Italy, 42 years for France and of 40 years for Germany [11];
- b. the characteristics of the anemometers, of the acquisition chain as well as the preprocessing techniques differ from one country to another, the first two sometimes differing also from one station to another within the same country; in addition, changes can occur in time within the same station, due to replacement of the hardware.

As an alternative to the use of anemometric data, in the last couple of decades the possibility has been explored of using data from climatic reanalysis by a number of researchers. Perhaps the first attempt is that carried out in Denmark by Frank [12], and more recent ones have been carried out in China [13] and in Indonesia [14]. Use of reanalysis data would in one fell swoop resolve all the issues above, and in addition to that would allow future projections when climate change scenarios are investigated through forecasts rather than hindcasts. But there's no free lunch, and number of issues seem at the moment to jeopardise such possibility.

Main issue is here identified in the inability of climatic reanalysis data to accurately reproduce the wind speed fluctuations at the meso scales, i.e., for periods ranging between 24 h and $\frac{1}{2}$ hour. These do not substantially affect the statistics of the mean wind speed, but tend to bring an underestimate of those of the extreme values, therefore giving rise to lower and unsafe design wind speeds.

Even though recipes for correction of reanalysis data to compensate the energy deficit in the meso scale range have been proposed [15], it seems that still some amount work shall be carried out to prove that corrected records bring reliable estimates of return wind speeds, when these are calculated using the most up-to-date techniques of statistical analysis, e.g. [16].

Another rather important aspect is that of the correspondence between instantaneous values produced by reanalysis and averaged values required for the definition of design wind speeds. Most of the recent reanalysis datasets provide hourly readings of the instantaneous wind speed, calculated with a time step from 20 s for the Very High Resolution REA over Italy (VHR-REA_IT) dataset [17] to 12 min for the ECMWF ERA5 and ERA5L datasets [18]. These correspond in principle to 20 s and 12 min averages sampled every hour, respectively. Correction for downsampling can be carried out using literature procedures, e.g., that proposed in [19, 20], but the issue remains of the relationship between 20 s and 12 min averages (or that coming from any other integration time step) with the 10 min averages needed to define design wind speed.

Finally, reanalysis data are available on coarser or finer grids; e.g., the ERA5 dataset is available on a 31 km grid (corresponding to a density of 961 km^{-2}), the ERA5L dataset is available on a 9 km grid (corresponding to a density of 81 km^{-2}), and the VHR-REA_IT dataset is available on a 2.2 km grid (corresponding to a density of 4.8 km^{-2}). An even finer grid is that of the AEOLIAN dataset [21] of 1.33 km (corresponding to a density of 1.8 km^{-2}), obtained by nesting the original ERA5 dataset through WRF [22]. Finer grids allow accounting for local effects associated with orography and roughness changes, therefore the question arises of how reliable a map would be for structural design purposes when having a resolution of few km, therefore being expected to reproduce local effects down to the upper range of the micro scales.

3 Flow Structure and Terrain Effects

A second aspect needing calibration within wind loading codes is the so-called wind model, i.e. the model describing the vertical variation of the mean and fluctuating components of the wind velocity. Three wind models are commonly used within codes, the power law [23], the logarithmic law [24] and the Deaves and Harris model [25]. In [26] the different choices are described as in 2009. Current version of EN 1991–1-4 [4] is based on use of the logarithmic law; this has been retained in the second generation EN 1991–1-4 [3], with the linearised Deaves and Harris model added only for use for slender structures up to 300 m of height.

The validity of the three models in the inertial sublayer over flat, open terrain with uniform roughness is well ascertained, with the power law and the logarithmic laws performing well up to 200 m and the linearised Deaves & Harris model being applicable up to 300 m. This, however, is a situation seldom encountered in structural design. Most of constructions are located either in city centres, or close to orographic features, or in the proximity of abrupt roughness changes (e.g., close to the coast), or a combination of these, which jeopardise the use of these models.

As to roughness changes, these can be accounted for through the so-called transition profiles, whose modelling is tackled in [27] and in [28, 29]. The approach was also

borrowed by the current EN 1991–1-4 [4], bringing the questionable result that, e.g., to design a 10 m tall structure in category III exposure, one should make sure that such category applies over a fetch of 1 to 20 km upstream the site of interest. In fact, this approach has been abandoned in the second generation EN 1991–1-4 [3] for much simpler, though rough rules.

Nevertheless, the problem exists, and ERIES-WhICH ROUGH project aims at assessing whether it is possible to establish a simple equivalence in terms of structural loads between transition and equilibrium profiles, so to simplify the loading model. Tests will be carried out at the Technical University of Eindhoven in April 2025, therefore no result is yet available at the time of writing of this paper.

On the other hand, most of construction works are located within or in the proximity of city centres, where an urban boundary layer develops, whose features are rather different from those of the atmospheric boundary layer. In particular, almost all constructions are located either within the roughness sublayer, extending up to a maximum of about 5 times the average height of constructions, or even within the canopy layer, whose height approximately equals the average height of constructions. The wind flow within the roughness sublayer is not well caught by any of the three models listed above, and it is common practice to assume the mean wind speed and intensity of turbulence are constant in the roughness sublayer [30]. This is on average true, but local conditions may largely vary, and this creates an issue when it comes to assessing the reliability of wind loading models.

Finally, there are construction works located in the vicinity of orographic features, or even worse in complex orography. The first case is handled by EN 1991–1-4 [3, 4] following the approach proposed in [31] and implemented in [32]. It is based on the numerical solution of the quite simple condition of the flow hitting two-dimensional discontinuities at a right angle. Reality may deviate largely from such situation, and no provision is available to cover the cases when this happens.

To conclude with, besides the aspects listed above all pertaining boundary layer flows associated with synoptic winds, the further problem arises of modelling flows deriving from non-synoptic winds, whose relevance to the wind loading of structures has become evident in the last couple of decades. The ERIES framework has already provided a contribution in this direction by funding ERIES-TNG and ERIES-ProMoTWA. The first project is aimed at “*Understanding near-ground tornado flows – pressure, shear and turbulence, and their importance in structural design*”; the latter project, for which wind tunnel tests will be carried out at the WindEEE Research Institute most probably in the summer 2025, is aimed at the “*Probabilistic Modelling of Thunderstorm Wind Actions*”.

4 Aerodynamics

The third area where calibration of wind loading codes would benefit from testing is that of aerodynamics. In the second generation EN 1991–1-4 [3], aerodynamic coefficients are given in three annexes (Annex B, C and D), featuring a total of about 110 pages. It is a large amount of data, most of which have been borrowed from the current version of the code [4] and some other have been added coming from research carried out in

the last two decades. In spite of such large amount of data, the issue remains of their consistency with the probabilistic format of Eurocode 0 [6], which had already been pointed out in 2001, at the time of the writing of the current EN 1991–1–4 [33]. The aerodynamic coefficients provided within the code are heterogeneous in terms of their statistical meaning, and for some of them the origin is not even documented. An attempt is currently being made by Task Group 2 (Wind Actions) under TC 250/SC 1 to provide a detailed background document to EN 1991–1–4, but it is anticipated that this will not be able to cover all the material contained in the code.

A similar problem concerning the consistency of aerodynamic coefficients has been faced and is currently being faced by committees in charge of writing other wind loading codes worldwide, an example being ASCE 7 [34, 35]. On the other hand, large and more recent databases exist for pressure coefficients of buildings, which can be exploited to this aim. Examples are the TPU [36] and the UWO/NIST [37] aerodynamic databases, covering low- and high-rise square plan buildings with either flat or sloped roofs. In spite of the rectangular geometry being the most common, a much broader variety of geometries exists (most of which are combinations of rectangles) for which little or no information is available.

An even stronger need for aerodynamic data emerges for structures other than buildings, among which are bridges. Available data are poorly documented, and assumed to cover altogether bridges having totally different geometries by enveloping available experimental data. Besides that, only a poor coverage exists of the interference effects that arise when two bridge decks are placed close to each other, which is indeed a common situation.

Apart from the broader or narrower range of geometries covered by a code, the further issue arises of the statistical definition of the aerodynamic coefficients it provides. A common requisite is that the values of the coefficients provided by the code should be such that combined with the reference wind speed associated with a given reliability level, they should provide actions having the same level of reliability. In the case of EN 1991–1–4 this is phrased by saying that the aerodynamic coefficients should be such that combined with the 50-year return, 10-min averaged value of the wind speed, they should provide the 50-year return wind action, regardless of exposure category and height from the ground [38]. Such requisite is not necessarily met by the coefficients given in EN 1991–1–4 [39]. On the other hand, peak action effects depend on the loaded area, and a clear definition of the action-to-effect path is not always available, leaving it ambiguous the meaning of the coefficients, therefore of the load patterns.

Finally, as already stated in Sect. 3 about the wind flow, the issue arises of the aerodynamic coefficients associated with flows other than those developed within a neutral atmospheric boundary layer. These aspects are currently being addressed by ERIES-TNG [31] and ERIES-ProMoTWA for tornadic winds and for thunderstorm outflows, respectively, and possible step forward is expected and desired.

5 Discussion

Sections 2, 3 and 4 above have outlined a number of shortcomings in the calibration of wind loading codes in general and of EN 1991–1-4 in particular. To mitigate the effects of these, collaborative research in large scale infrastructures can prove largely beneficial. Some areas where in our opinion this can be the case are listed below.

The use of large-scale computing resources would allow assessing under what circumstances reanalysis datasets combined with downscaling to the meso scale could supplement and eventually replace historical anemometric records when assessing extreme wind climate and building wind hazard maps. It is the authors' opinion that research in this field should aim at first investigating the capacity of numerical techniques to reproduce extreme wind events, and at explaining and quantifying the discrepancy with measurements [40]. In doing this, the use of LiDAR wind profilers allows comparison of high elevations above the ground, where met mast measurements are difficult and expensive to obtain [41, 42]. In addition to that, for the purpose of assessing design wind speeds a statistical description of storm maxima is sufficient, and equivalence between measured and calculated values should be established by matching the data both in the frequency and probability domains.

On the other hand, full scale and wind tunnel experiments should be designed and performed such to improve the modelling of the mean and fluctuating wind flow within the roughness sublayer of densely built areas. Results from such research activities would help increasing knowledge of wind actions in urban areas, and increase the reliability of loading models. Similarly, increased knowledge of flows in more or less complex orography would allow parametrization, therefore providing a more solid ground over which to build simplified models for use in the engineering practice and for codification.

Finally, it is envisaged that in a future aerodynamic data for structural design of civil engineering works could be gathered in the form of large shared databases, from which wind loading codes could borrow the required information. To achieve such an ambitious goal, first standardisation of the data format should be achieved and then smaller or larger scale wind tunnel experimental campaigns should be designed such to start populating databases. To this end, CFD analyses can supplement wind tunnel testing.

6 Conclusions

This paper has briefly listed some of the shortcomings associated with the calibration of wind loading codes in general, and of EN 1991–1-4 in particular. Many of this derive from the use of old and inconsistent data, which were produced spontaneously and independent of each other, in a time where the principles of structural reliability had not yet been fully acknowledged by structural design codes. Some of these can be resolved by gathering new and consistent data from coordinated experimental campaigns, and these would benefit from the transnational use of large-scale facilities. It is advisable that large projects allowing access to such facilities could help building such an opportunity.

Acknowledgements. This work was presented at the 2025 International Workshop in Engineering Research Infrastructures for European Synergies (ERIES-ProMoTWA), supported by the Engineering Research Infrastructures for European Synergies (ERIES) project (www.ries.eu), which

has received funding from the European Union's Horizon Europe Framework Programme under Grant Agreement No. 101058684.

References

1. European Committee for Standardization (CEN): Eurocode 1 – Actions on structures – Part 1–4: General actions – Wind actions, prEN 1991-1-4. Belgium, Brussels (2021)
2. Ricciardelli, F.: PrEN 1991-1-4:2021: the draft second generation eurocode on wind actions on structures - a personal view. *Wind Struct.* **37**(2), 79–94 (2023)
3. European Committee for Standardization (CEN) Eurocode 1 – Actions on structures – Part 1–4: General actions – Wind actions, FprEN 1991–1–4, Brussels, Belgium. CEN/TC 250/SC 1 N 2425 (2024)
4. European Committee for Standardization (CEN) Eurocode 1 – Actions on structures – Part 1–4: General actions – Wind actions, EN 1991–1–4 Brussels, Belgium (2005)
5. Picozzi, V., Landi, F., Avossa, A.M., Croce, P., Formichi, P., Ricciardelli, F.: The climatic action uncertainty chain. *Eng. Struct.* **301**, 117357 (2024)
6. Picozzi, V., Ricciardelli, F., Sørensen, J.D.: Calibration of wind action combination factors from experimental data. In: P. Schito and A. Zasso (eds.): Lecture notes in civil engineering. Proceedings of the XVII Conference of the Italian Association for Wind Engineering, INVENTO 2022, 461:90–101 (2024)
7. Madsen, H.O., Krenk, S., Lind, N.C.: Methods of Structural Safety. Prentice-Hall, Englewood Cliffs, NJ (1986)
8. European Committee for Standardization (CEN): Eurocode 0 – Basis of Structural and Geotechnical Design, EN 1990. Belgium, Brussels (2023)
9. World Meteorological Organization (WMO) Guide to Instruments and Methods of Observation Volume I – Measurement of Meteorological Variables, vol. 752, no.-8, Geneva, Switzerland (2019)
10. Ballio, G., Lagomarsino, S., Piccardo, G., Solari, G.: Probabilistic analysis of Italian extreme winds: reference velocity and return criterion. *Wind Struct.* **2**, 51–68 (1999)
11. Raffaele, L., Bruno, L., Colucci, E.: Reanalysis-based mesoscale wind maps for the design of structures and infrastructures with an application to Italy. *J. Wind Eng. Ind. Aerodyn.* **253**, 105844 (2024)
12. Frank, H.P.: Extreme Winds over Denmark from the NCEP/NCAR Reanalysis. Risø National Laboratory, Risoe-R No. 1238, Roskilde, Denmark (2001)
13. Mo, H.M., Hong, H.P., Fana, F.: Estimating the extreme wind speed for regions in China using surface wind observations and reanalysis data. *J. Wind Eng. Ind. Aerodyn.* **143**, 19–33 (2015)
14. Abdillah, M.R., et al.: Extreme wind variability and wind map development in Western Java. Indonesia. *Int. J. Disaster Risk Sci.* **13**, 465–480 (2022)
15. Larsén, X., Ott, S., Badger, J., Hahmann, A.N., Mann, J.: Recipes for correcting the impact of effective mesoscale resolution on the estimation of extreme winds. *J. of Applied Meteorol. Climatol.* **51**, 521–533 (2012)
16. Harris, R.I.: XIMIS, a penultimate extreme value method suitable for all types of wind climate. *J. Wind Eng. Ind. Aerodyn.* **97**, 271–286 (2009)
17. Raffa, M., et al.: VHR-REA_IT dataset: very high resolution dynamical downscaling of ERA5 reanalysis over Italy by COSMO-CLM. *Data* **6** (2021)
18. Hersbach, H., et al.: The ERA5 global reanalysis. *Q. J. R. Meteorol. Soc.* **146**, 1999–2049 (2020)

19. Picozzi, V., Akbaba, A., Avossa, A.M., Ricciardelli, F.: Correction of historical records to improve the reliability of design wind speeds. *Eng. Struct.*, 114473 (2022)
20. Akbaba, A., Picozzi, V., Avossa, A.M., Ricciardelli, F.: Effects of downsampling on the prediction of the Italian extreme winds. In: P. Schito and A. Zasso (eds.): Lecture notes in civil engineering. Proceedings of the XVII Conference of the Italian Association for Wind Engineering, IN-VENTO 2022, vol. 461, pp.41–51, Milano, Italy (2024)
21. Sperati, S., et al.: The new Italian Wind Atlas – Atlante EOLico ItaliANO (AEOLIAN). In: IOP Conference Series: Earth and Environmental Science, 1073, 20th World Wind Energy Conference & Exhibition (WWEC 2022) (2022)
22. Skamarock, W., Klemp, J., Dudhia, J.: A description of the Advanced Research WRF Version 3. Tech. Note NCAR 475 (2008)
23. Hellman, G.: Über die Bewegung der Luft in den untersten Schichten der Atmosphäre. *Meteorol. Z.*, **34**(273). In German (1916)
24. Tennekes, H.: The logarithmic wind profile. *J. Atmos. Sci.* **30**, 234–238 (1973)
25. Deaves, D.M., Harris, R.I.: A mathematical Model of the Structure of Strong Winds. CIRIA Report 76, Construction Industry Research and Information Association, London, UK (1978)
26. Choi ECC: Proposal for unified terrain categories exposures and velocity profiles. In: Proceedings of the Seventh Asia-Pacific Conference on Wind Engineering, Taipei, Taiwan (2009)
27. Deaves, D.M.: Computations of wind flow over changes in surface roughness. *J. Wind Eng. Ind. Aerodyn.* **7**, 65–94 (1981)
28. ESDU :Wind Speed Profiles Over Terrain with Roughness Changes. Data Item 84011, EDSU International, London, UK (1984)
29. ESDU.: Longitudinal Turbulence Intensities over Terrain with Roughness Changes. Data Item 84030, EDSU International, London, UK (1984)
30. Grimmond, C., Oke, T.: Aerodynamic properties of urban areas derived from analysis of surface form. *J. Appl. Met.* **38**, 1262–1292 (1999)
31. Deaves, D.M.: Computations of wind flow over two-dimensional hills and embankments. *J. Wind Eng. and Ind. Aerodyn.* **6**, 89–112 (1980)
32. ESDU: Mean Wind Speeds Over Hills and Other Topography. Data Item 91043, EDSU International, London, UK (1991)
33. Geurts, C.P.W., et al.: Transparency of pressure and force coefficients. In: Proc. 3rd European & African Conference on Wind Engineering, Eindhoven, The Netherlands (2001)
34. Wang, J., Kopp, G.A.: Comparisons of aerodynamic data with the main wind force-resisting system provisions of ASCE 7–16. I: Low-rise buildings. *J. Struct. Eng. ASCE* **147**(3):04020347 (2021)
35. Wang J., Kopp, G A.: Comparisons of aerodynamic data with the main wind force–resisting system provisions of ASCE 7–16. II: mid-and high-rise buildings. *J. Struct. Eng. ASCE*, **147**(3), 04020348 (2021)
36. Quan, Y., Tamura, Y., Matsui, M., Cao, S.Y., Yoshida, A.: TPU aerodynamic database for low-rise buildings. In: Proceedings of the 12th International Conference on Wind Engineering (ICWE12), vol. 2: 1615–1622, Cairns, Australia (2007)
37. Ho, T.E., Surry, D., Morrish, D., Kopp, G.A.: The UWO contribution to the NIST aerodynamic database for wind loads on low buildings: part 1. archiving format and basic aerodynamic data. *J. Wind Eng. Ind. Aerodyn.* **93**(1):1–30 (2005)
38. Picozzi, V., Malasomma, A., Avossa, A.M., Ricciardelli, F.: The relationship between wind pressure and pressure coefficients for the definition of wind loads on buildings. *Buildings*, **12**(2) (2022)
39. Malasomma, A., Picozzi, V., Avossa, A.M., Ricciardelli, F :Global pressure coefficients for building roofs revisited. In: P. Schito and A. Zasso (eds.): Lecture notes in civil engineering.

Proceedings of the XVII Conference of the Italian Association for Wind Engineering, INVENTO 2022, 461: Milano, Italy (2024)

40. Sepe, V., Montelpare, S., Ricciardelli, F., Avossa, A.M.: Comparison between LIDAR measurements and reanalysis wind velocities: a case study. In: Proceedings of the 9th European and African Conference on Wind Engineering, EACWE, Trondheim, Norway (2025)
41. Sepe, V., Avossa, A.M., Rizzo, F., Ricciardelli, F.: Calibration of mean wind profiles using wind Lidar measurements. *Appl. Sci.* **13**, 5077 (2023)
42. Ricciardelli, F., Pirozzi, S., Mandara, A., Avossa, A.M.: Accuracy of mean wind climate predicted from historical data through wind LIDAR measurements. *Eng. Struct.* **201**, 109771 (2019)

Open Access This chapter is licensed under the terms of the Creative Commons Attribution 4.0 International License (<http://creativecommons.org/licenses/by/4.0/>), which permits use, sharing, adaptation, distribution and reproduction in any medium or format, as long as you give appropriate credit to the original author(s) and the source, provide a link to the Creative Commons license and indicate if changes were made.

The images or other third party material in this chapter are included in the chapter's Creative Commons license, unless indicated otherwise in a credit line to the material. If material is not included in the chapter's Creative Commons license and your intended use is not permitted by statutory regulation or exceeds the permitted use, you will need to obtain permission directly from the copyright holder.





Downburst-Induced Loads on a Six-Row Array of Ground-Mounted Solar Trackers

Antonio J. Álvarez¹ , Félix Nieto¹ , Petar Škvorc² , Hrvoje Kozmar² , Jeroen van Beeck³ , Tibebu Birhane⁴ , Kimberley Adamek⁴ , and Girma Bitsuamlak⁴

¹ University of A Coruña, A Coruña, Spain
felix.nieto@udc.es

² Faculty of Mechanical Engineering and Naval Architecture, University of Zagreb, Zagreb, Croatia

³ Von Karman Institute for Fluid Dynamics, Sint-Genesius-Rode, Belgium

⁴ Western University, London, Canada

Abstract. This work presents the preliminary analysis of the tests conducted at the WindEEE Dome in the framework of the ERIES-SOLAR project for downburst flow. The wind tunnel characteristics, the instrumentation and reduced scale model of a six-row array of solar trackers is briefly described. The flow, similar to a vertical downburst with impinging jet velocity $U_{ij} = 8.6$ m, is characterized based on the velocity records at various heights and distances from the downburst axis, obtaining the ensembles of several repetitions, PDFs, spectra and Morlet wavelets, identifying the ramp-up, plateau and decay stages. The downburst action on the array of solar trackers is assessed based on the time-dependent pressure coefficients recorded simultaneously by 576 pressure taps. In this work, the results are presented for one case of a vertical downburst, with the center of the six-row array model located at a distance $0.7D$ from the downburst vertical axis. Strong increments in the net pressure coefficients are identified, associated with the effect of the deflected flow and the primary vortex reaching the vicinity of the panels. The detailed analysis of the large amount of data generated will be instrumental to identify the peak actions on solar trackers due to downburst occurrences, enabling the recommendation of load cases to be included in the best practice guidelines and structural codes for storm-prone regions.

Keywords: downburst · solar tracker · non-synoptic wind · pressure tests · ERIES · WindEEE Dome

1 Introduction

Non-synoptic high wind episodes are associated with convective storms, with time and spatial scales several orders of magnitude smaller than synoptic-scale meteorological disturbances (Bluestein, 2021). Non-synoptic peak wind velocities close to the ground may be well above 25 m/s (Zhang et al., 2019), therefore with potential for causing severe structural damage in civil engineering structures. Only in recent years the wind

engineering community has started to address in a systematic fashion the characterization of non-synoptic wind episodes and their effects on structures, advancing the seminal and pioneering work by Fujita and co-workers. This ERIES-SOLAR project, developed in the framework of the ERIES (Engineering Research Infrastructures for European Synergies) initiative, has the overarching goal of improving the understanding of non-synoptic wind effects on solar energy infrastructures, especially solar trackers.

Among the different types of non-synoptic wind systems described in the literature, this work addresses downbursts, that are “*intense, localized downdrafts produced in convective storms*” ranging “*from almost 1 km to about 10 km in diameter*” (Bluestein, 2021). A downdraft is a descending cold air jet that goes through the atmospheric boundary layer impinging the ground and deflecting in a large and intense annular primary vortex creating a strong radial flow in the near-ground level (Canepa, Bin and Brusco, 2025). Downburst may cause significant damage in energy infrastructures, such as transmission towers (Elawady et al., 2017; Alawode et al., 2023; Zhong et al., 2025), which are of strategic importance.

Similarly, solar farms, whose land usage may range between 0.16 km² (40 acres) for 5 MW power generation (Coldwell Solar, 2023), up to, for instance, 53 km² (13000 acres) for the 2.05 GW of the Pavagada Solar Park in India (Gill, 2024), may be severely affected by downburst occurrences with typical diameter between 1 km and 10 km (Fujita, 1981). It seems logical to consider that a significative fraction of structural failures in solar panels caused by the wind action may be related with downburst episodes; however, structural design codes do not include this loading scenario, enabling potentially sensitive structures in areas prone of convective storms. Solar farms are typically installed in rural areas, sparsely populated, therefore posing minor risks; however, the economic impact associated with the partial or total destruction of the solar energy infrastructure may be substantial for the developer.

The current state of the art is relatively mature for downburst reduced-scale experimental modeling (Li et al., 2024) and analytical and semi-empirical models (Romanic and Hangan, 2021). Similarly, synoptic wind actions on fixed solar panels and solar trackers have been studied by the means of experimental wind tunnel campaigns such as Aly and Bitsuamlak (2013), Warsido et al. (2014), or Browne, et al. (2020), to mention a few examples. However, to the best of the authors’ knowledge, no studies addressing the effect of downburst-created loads on arrays of solar trackers have been reported so far. There is, therefore, a lack of knowledge about the load assessment associated with downburst episodes, and uncertainty regarding the safety of structural design based on stipulations provided in structural codes based on synoptic events.

This work reports the preliminary results of the experimental campaign carried out at the WindEEE Dome considering the impingement of downbursts with different characteristics in the vicinity of a six-row array model of solar trackers. The model is instrumented with 576 pressure taps, enabling the measurement of peak pressures on the panels, assessing the interference effects among rows of solar trackers and the effect of the angle of incidence between the annular primary vortex and the rows of solar trackers. The information gathered will be instrumental in identifying load cases representative of downburst-related loads to be included in the best practice guidelines and structural codes for solar energy infrastructure in thunderstorm-prone areas.

2 Formulation

2.1 Time-Dependent Pressure Coefficients and Velocity Components

Results presented in this paper are based on the following analysis applied to the measured velocity and surface pressure data.

The velocity components $u_i(t)$ are decomposed into a slowly varying mean value $u^*_i(t)$ and a residual fluctuating component $u'_i(t)$:

$$u_i * (t, \tau) = \frac{1}{\tau} \int_t^{t+\tau} u_i(t) dt; u'(t, \tau) = u_i(t) - u_i * (t, \tau). \quad (1)$$

where the subscript values $i = 1, 2, 3$ denote the radial, the tangential and vertical components of the velocity, t is the time and τ is the time step adopted for computing the moving average.

The flow-induced actions on the solar trackers are assessed based on the time-dependent net pressure coefficients, $C_p(t)$, recorded at the pressure taps distributed over the six-row array model and normalized by the reference dynamic pressure:

$$C_{pn}(y, t) = (P_{Up}(y, t) - P_{Lo}(y, t)) / (0.5 \rho U_{ref}^2), \quad (2)$$

where $P_{Up}(y, t)$ is the time-dependent upper pressure at the pressure tap location y , P_{Lo} is the lower surface pressure at tap location y , ρ is the air density and U_{ref} is the reference wind speed calculated as the ensemble average of the maximum velocity magnitude at the sampling frequency for each test repetition at 0.075 m above the test chamber ground at the location of the center of the six-row array of solar trackers, with the model absent.

Similarly, the pressure coefficient can be decomposed into a slowly varying mean pressure coefficient $C_p^*(t)$ and the residual non-stationary fluctuation $C'_p(t)$, where t represents the time:

$$C_p(t) = (C_p^*(t) + C'_p(t)). \quad (3)$$

2.2 Morlet Wavelet Transform

The Morlet wavelet transform enables the time-frequency analysis of a time-dependent signal, improving the information provided by the Fourier transform by describing the frequency content evolution over time. According to, A wavelet is defined as a family of functions constructed from translations and dilations of a single function ϕ named “mother wavelet” (Yadav 2018). It is defined as:

$$\phi_{a,b}(t) = \frac{1}{\sqrt{a}} \phi\left(\frac{t-b}{a}\right), a, b \in R, a \neq 0. \quad (4)$$

The parameters a and b are the scaling and translation parameters, respectively. The I wavelet transform of a general time-dependent function $h(t)$ is:

$$W_\phi(a, b) = \frac{1}{\sqrt{a}} \int_{-\infty}^{+\infty} h(t) \phi^*\left(\frac{t-b}{a}\right) dt. \quad (5)$$

Here, the Morlet wavelet is defined as:

$$\phi(t) = e^{i\omega_0 t - \frac{t^2}{2}}. \quad (6)$$

3 Test Campaign Description

The WindEEE Dome at Western University is a world-class facility that is capable of creating scaled downburst flows releasing an air jet by opening the pressurizing plenum, housing six large fans, located at the upper level of the hexagonal test chamber. The experimental campaign considered various downburst intensities, with the constant downdraft diameter of $D = 3.2$ m that ensures negligible confinement effects by the walls and ceiling of the test chamber 25 m in diameter (Canepa, Bin and Brusco, 2025). Most of the test cases considered a vertical downburst, but for some of them, the vertical downburst was combined with an atmospheric boundary layer flow.

Flow profiling is based on the high-frequency (1.25 kHz) three-component velocity measurements using a rake of Cobra probes, placed at different positions. In Fig. 1a), an image of the Cobra probes rake is provided.

A rigid 1:20 length scale model of a six-row array of solar trackers was manufactured, instrumenting each row with 12×4 pressure taps equally distributed at the bottom and upper surfaces (see Fig. 1b). Consequently, the model comprises 576 pressure taps ($8 \times 12 \times 6$), requiring 18 scanners of 32 pressure ports each. Each row is 1.05 m long, with a chord width of 0.10 m, featuring a distance to the ground of 0.05 m (all dimensions at the model scale).

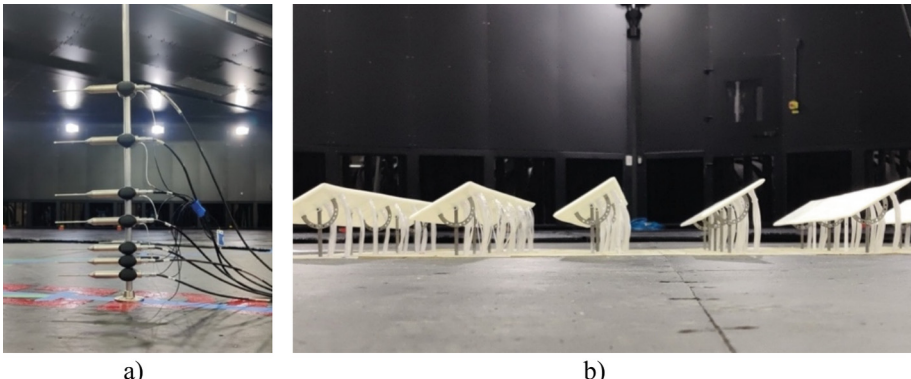


Fig. 1. Instrumentation and test model a) Cobra probes rake and b) six-row solar tracker array.

In this work, the reduced-scale vertical downburst flow characterization for an impinging jet velocity of $U_{ij} = 8.6$ m/s ($Re = 1.8e + 06$, taking downdraft opening diameter D as reference dimension) is reported, while the pressure measurements on the six-row array solar tackers model correspond to the cases where the center of the model is located at the distance of $0.7D$ from the vertical axis of the downburst flow, with azimuth angle of 180° , and tilt angles of $+30^\circ$ and -30° . In Fig. 2, schematic views (not to scale) of the layout of the model in the test chamber are provided.

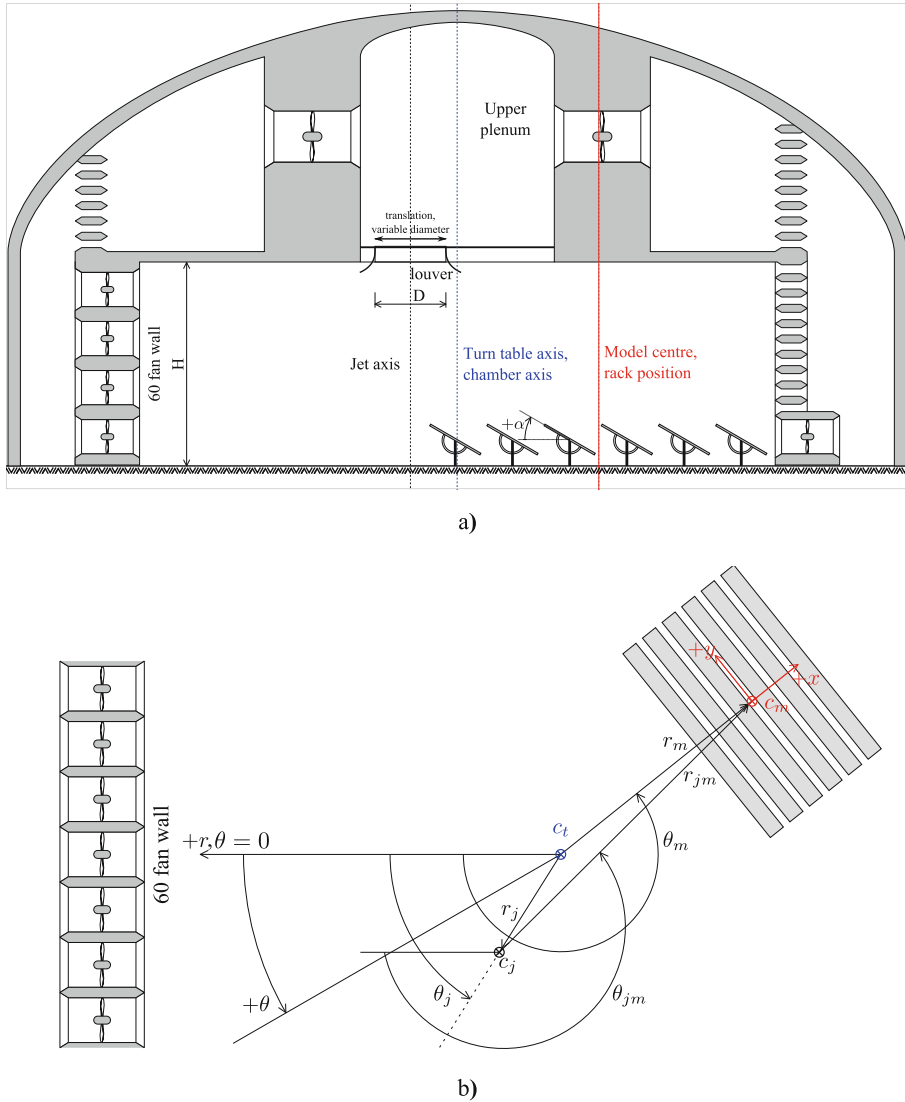


Fig. 2. Schematic view of the wind tunnel tests: a) vertical layout, b) plane layout.

4 Downburst Flow Characterization

The downburst flow corresponding to an impinging jet velocity $U_{ij} = 8.63$ m/s is described based on ensembles of 8 records for each position of the Cobra probes rake along the radial direction. The range of heights from the ground of the test chamber where the velocity measurements were performed is (0.05, 0.4) m, and the range of radial distances, measured from the axis of the vertical downburst, is (0.75, 4.20) m. For the flow characterization, the following dataset was considered for the velocity timeseries

recorded by each Cobra probe: the mean ensemble of the wind speed magnitude considering the three components of the velocity vector for the 8 experimental repetitions, along with the moving mean with averaging interval of 0.4 s, the PDF of the velocity magnitude, the Morlet wavelet and the frequency spectra. In Figs. 3 and 4, these data are reported for the flow velocities at the 0.15 m height and distances from the vertical downburst axis of 2.25 m and 3.20 m.

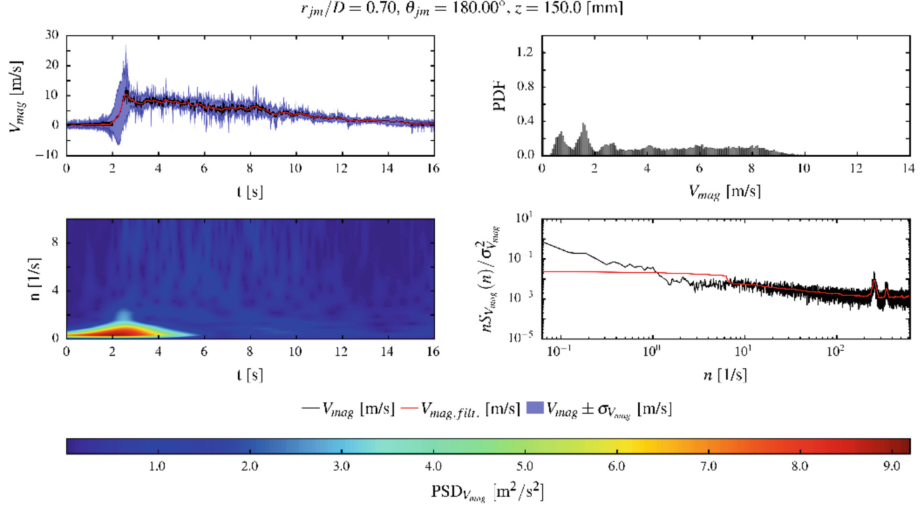


Fig. 3. Flow velocity magnitude characterization for a vertical downburst at $r_{jm}/D = 0.70$ and $z = 0.15$ m.

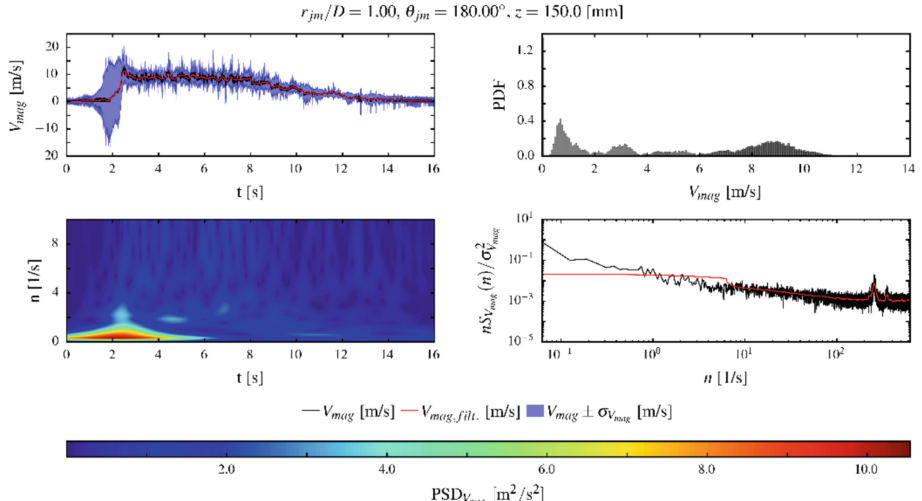


Fig. 4. Flow velocity magnitude characterization for a vertical downburst at $r_{jm}/D = 1.0$ and $z = 0.15$ m.

The timeseries of the ensemble of 8 records exhibit the typical pattern of downburst flows, i.e., an initial ramp-up associated to the primary vortex passing, a plateau representing the primary vortex moving away and the trailing vortices that exhibit a signature of low-amplitude oscillations, and finally the velocity decay as the downburst dissipates. The time-frequency analysis shows higher energy content at the velocity ramp-up and initial stages of plateau, associated with the primary vortex. It is to note that the high energy at very low frequencies does not have some physical meaning, as it is rather associated with the length of the signal (Canepa, Bin and Brusco, 2025).

5 Pressure Loading on Solar Trackers

For the vertical downburst of impinging jet velocity $U_{ij} = 8.63$ m/s, with the center of the model located at a distance $0.7D$ from the downburst vertical axis, the timeseries of the net pressure coefficient at four pairs of pressure probes on panels #1 and #4 along the same ring, identified as probes A, B, C, ...and H in Fig. 5, are reported in Fig. 6 for the 30° and -30° tilt angle cases (probes A, C, E and G are located on the top surface and probes B, D, F and H are on the bottom surface).

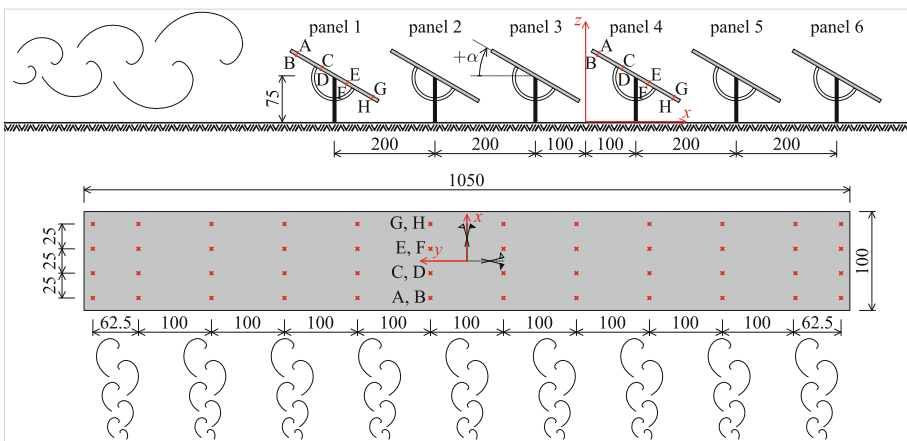


Fig. 5. Panels and probes naming convention (upper image), and layout of pressure probes on the panel (lower image).

Panel #1 is very close to the ground area directly hit by the impinging jet; therefore, it is expected that the primary vortex may be not properly developed when the flow deflects and expands in the radial direction. Consistently with this observation, in Fig. 6, a strong peak in net pressure coefficient is identified for all the pressure probes pairs, which is associated with the impingement of downdraft, followed by a decay in the net pressure without an apparent plateau in the wind-induced load, although oscillation in the pressure coefficient can be depicted, which may be associated with the formation of trailing vortices. For the -30° tilt angle, the upper side of the panel withstands higher pressures over time, yielding positive net pressure coefficients during the whole duration of the

downburst episode. For tilt angle $+30^\circ$, the timeseries of the net pressure coefficients show a similar trend, with a strong peak associated with the initial impingement of the downdraft, followed by an oscillatory decay. In this case, net pressure coefficients are negative as the lower side of panel #1 is facing the incoming flow. Interestingly, the peak net pressure magnitude is similar for the two tilt angles considered in this study.

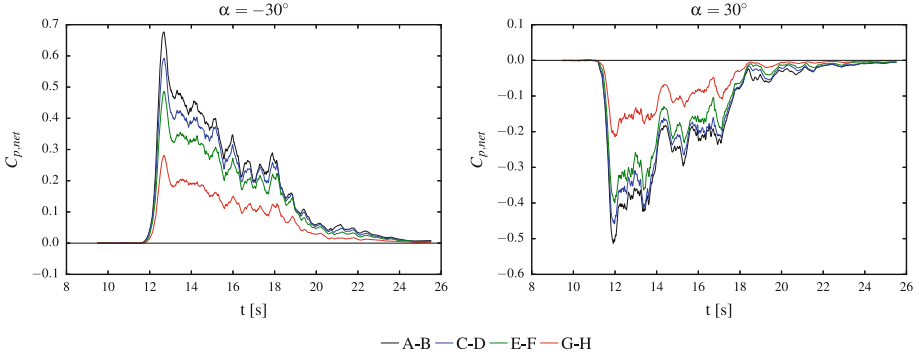


Fig. 6. Net pressure coefficient timeseries for four pairs of pressure probes located along the same ring in panel #1 for tilt angles -30° and 30° (averaging time window: 0.4 s).

The patterns of the net pressure coefficients on panel #4, depicted in Fig. 7, present some differences with respect to panel #1. For panel #4 a strong increase in the net pressure coefficient is identified for the initial stages of the downburst loading episode. However, a plateau is identified afterwards, with the peak values of the net pressure coefficient being reached along this second stage in the loading process. It is noted that high-frequency and low-frequency oscillations coexist, being still an open question whether these oscillations are due to trailing vortices associated with the downburst flow, the signature of the wakes detached from upwind panels or a combination of both effects. Similar to panel #1, the negative tilt angle produces positive net pressures, while the positive tilt angle gives rise to negative net pressure timeseries. For the negative tilt angle, panel #4 presents lower peak net pressure coefficient values, which might be due to the sheltering effect of upwind panels; conversely, for the positive tilt angle the peak values are similar for both panel #1 and #4.

6 Concluding Remarks

An experimental campaign was carried out in the WindEEE Dome to assess downburst-induced actions on solar trackers. Multiple tests considering various downburst impinging jet velocities for vertical downbursts and downbursts combined with atmospheric boundary layer flow were conducted. A vast amount of experimental data was gathered, and so far, only limited preliminary analyses were carried out.

In this work, the characterization of the flow for a vertical downburst with reference velocity of the impinging jet $U_{ij} = 8.6$ m/s was reported based on the ensemble average of 8 tests, along with the PDF of the velocity and frequency and time-frequency analysis.

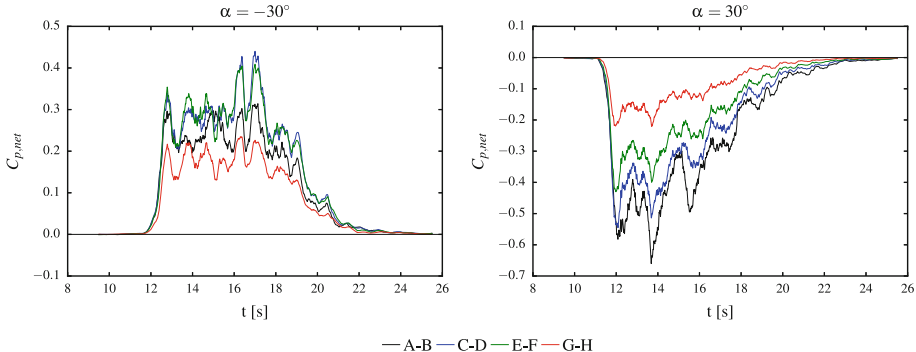


Fig. 7. Net pressure coefficient timeseries for four pairs of pressure probes located along the same ring in panel #4 for tilt angles -30° and 30° (averaging time window 0.4 s).

The downburst-induced action on a six-row array of solar trackers was assessed based on the net pressure coefficient timeseries for 576 pressure taps distributed on both the top and bottom surfaces of the solar panels. Preliminary analyses indicate strong surge in net pressure due to the drifting of the primary downburst vortex along with potential interference between panels.

The analysis of the peak values of the net pressure coefficients for the most critical cases will enable the recommendation of design loads to be included in the best practice guidelines and structural codes for solar trackers in downburst-prone areas.

Acknowledgements. This work is part of the transnational access project “ERIES-SOLAR”, supported by the Engineering Research Infrastructures for European Synergies (ERIES) project (www.ries.eu), which has received funding from the European Union’s Horizon Europe Framework Programme under Grant Agreement No. 101058684. This is ERIES publication number C56.

Antonio J. Álvarez has received funding from the 2024 postdoctoral research stays internal grants program of the University of A Coruña. This work was supported by the Croatian Science Foundation under the project number HRZZ-IP-2022-10-9434.

References

- Alawode, K.J., Azzi, Z., Elawady, A., Chowdhury, A.G.: Dynamic properties of an aeroelastic transmission tower subjected to synoptic and downburst-like outflows. *J. Wind Eng. Ind. Aerodyn.* **242**, 105557 (2023)
- Aly, A.M., Bitsuamlak, G.T.: Aerodynamics of ground-mounted solar panels: Test model scale effects. *J. Wind Eng. Ind. Aerodyn.* **123**, 250–260 (2013)
- Bluestein, H.: The types of non-synoptic wind systems. In: Hangan, H., Kareem, A. (eds.) *The Oxford Handbook of Non-synoptic Wind Storms*, pp. 9–42. Oxford University Press, New York (2021)
- Browne, M.T.L., Taylor, Z.J., Li, S., Gamble, S.: A wind load design method for ground-mounted multi-row solar arrays based on a compilation of wind tunnel experiments. *J. Wind Eng. Ind. Aerodyn.* **205**, 104294 (2020)

- Canepa, F., Bin, H.Y., Brusco, S.: Time-frequency vortex characterization in large-scale experimental downbursts. *Phys. Fluids* **37**(3), 036610 (2025)
- Coldwell Solar Homepage, <https://coldwellsolar.com/commercial-solar-blog/how-big-is-a-small-solar-farm/>. Accessed 09 Mar 2025
- Elawady, A., Aboshosha, H., El Damatty, A., Bitsuamlak, G., Hangan, H., Elatar, A.: Aero-elastic testing of multi-spanned transmission line subjected to downbursts. *J. Wind Eng. Ind. Aerodyn.* **169**, 194–216 (2017)
- Fujita, T.T.: Tornadoes and downbursts in the context of generalized planetary scales. *J. Atmosph. Sci.* **38**, 1511–1534 (1981)
- Gill, T.: The world's biggest solar farms. the ecoexperts website, <https://www.theecoexperts.co.uk/solar-panels/biggest-solar-farms> Accessed 09 Mar 2025 (2004)
- Li, S., Catarelli, R.A., Phillips, B., Bridge, J.A., Gurley, K.R.: Physical simulation of downburst winds for civil structures: a review. *J. Wind Eng. Ind. Aerodyn.* **254**, 105900 (2024)
- Romanic, D., Hangan, H.: Analytical and semi-empirical models of tornados and downbursts. In: Hangan, H., Kareem, A. (eds.) *The Oxford Handbook of Non-synoptic Wind Storms*, pp. 203–238. Oxford University Press, New York (2021)
- Warsido, W.P., Bitsuamlak, G.T., Barata, J., Chowdhury, A.G.: Influence of spacing parameters on the wind loading of solar array. *J. Fluids Struct.* **48**, 295–315 (2014)
- Yadav, P.: A brief description of wavelet and wavelet transforms and their applications. *Int. J. Appl. Math. Stat.* **3**(1), 266–271 (2018)
- Zhang, S., Solari, G., Burlando, M., Yang, Q.: Directional decomposition and properties of thunderstorm flows. *J. Wind Eng. Ind. Aerodyn.* **189**, 71–90 (2019)
- Zhong, Y., Savory, E., Liu, Y., Yan, Z., Li, Y., Wei, Q.: Experimental simulation of downburst-like outflows and the associated dynamic properties of a self-supported transmission tower. *J. Wind Eng. Ind. Aerodyn.* **259**, 106032 (2025)

Open Access This chapter is licensed under the terms of the Creative Commons Attribution 4.0 International License (<http://creativecommons.org/licenses/by/4.0/>), which permits use, sharing, adaptation, distribution and reproduction in any medium or format, as long as you give appropriate credit to the original author(s) and the source, provide a link to the Creative Commons license and indicate if changes were made.

The images or other third party material in this chapter are included in the chapter's Creative Commons license, unless indicated otherwise in a credit line to the material. If material is not included in the chapter's Creative Commons license and your intended use is not permitted by statutory regulation or exceeds the permitted use, you will need to obtain permission directly from the copyright holder.





Effects of Small-Scale Turbulence on the Aerodynamic and Aeroelastic Responses of a 3:2 Rectangular Prism

Antonio J. Álvarez¹ , Kenny C. S. Kwok² , Luca Patruno³ , Giuseppe Piccardo⁴ , Félix Nieto¹ , and Maria Pia Repetto⁴

¹ CITEEC – University of A Coruña, 15071 A Coruña, Spain
felix.nieto@udc.es

² School of Civil Engineering, The University of Sydney, Sydney, NSW 2006, Australia
³ DICAM, University of Bologna, 40121 Bologna, Italy

⁴ DICCA, Polytechnic School, University of Genoa, 16145 Genoa, Italy

Abstract. The scope of the ERIES-SSTURBO project is reviewed in this work, emphasizing the importance of gaining a deeper understanding of the effects that turbulence in general, and turbulent length scale in particular, have in the flow-induced response of bluff bodies. The planned experimental campaign at the Giovanni Solari Wind Tunnel of the University of Genoa is described, testing a 3:2 rectangular prism in smooth flow, as a reference flow-induced response assessment. The effects of large-scale turbulence will be studied based on grid-induced turbulence, while those of small-scale turbulence will be analyzed using rod-induced turbulence, as proposed by Gartshore in 1973. Details are provided about the experimental facility and the instrumentation. Aiming at highlighting the complementarity between the wind tunnel data and high-fidelity 3D LES simulations in the study of turbulent flow effects on the response of bluff bodies, computational results obtained in the frame of an independent project are briefly introduced. It is expected that the results of this experimental campaign will shed light on our understanding of the role played by the turbulent length scale in the interaction between the flow and flexible structures prone to suffer flow-induced excitation. Furthermore, this experimental dataset will be instrumental for the detailed validation of CFD simulations addressing this highly complex problem, allowing to assess the accuracy of computational results.

Keywords: smooth flow · small-scale turbulence · large-scale turbulence · 3:2 rectangular prism · rod turbulence · grid turbulence

1 Introduction

Flow-induced excitation of civil engineering structures poses an obvious risk, as this may cause discomfort, have a negative impact on fatigue performance and even provoke the collapse of the structure. The atmospheric boundary layer is intrinsically turbulent, however there are still gaps in our understanding of turbulent flow effects on flexible structures, prone to flow-induced vibration.

Adopting the ratio 3:2 rectangular prism as a canonical application case of a geometry showing vortex-induced vibration (VIV) and galloping excitation risk at low Scruton numbers, the existing literature is relatively short. In Nguyen et al. (2022) a fixed 3:2 rectangular prism is comprehensively studied in smooth flow, while in Mannini et al. (2018) the same geometry is studied in smooth and grid-generated turbulent flow for the fixed prism and free to oscillate in the heave degree of freedom. The last reference describes a general trend for higher turbulence intensity flows to produce lower amplitudes in oscillations, remarking the role played by the scale of turbulence in the aeroelastic response of the 3:2 rectangular prism. There are still multiple gaps in our understanding about the interaction between turbulence and aeroelastic response and this project aims at gaining additional insights by focusing on the effects of small-scale rod-induced turbulent flow using the approach proposed originally in Gartshore (1973). Given the complexity of the problem under consideration, high-fidelity 3D LES models may be instrumental in deciphering the interactions between turbulence and structural oscillations, hence the planned experimental campaign has the additional value of providing validation data for numerical simulations addressing this type of problem.

In the remaining of the paper, the experimental campaign that will be developed in the forthcoming months is described, focusing on the main tasks: flow characterization, aerodynamic response of the fixed 3:2 rectangular prism and its aeroelastic response considering smooth flow, grid-induced turbulent flow and rod-induced turbulent flow. Afterwards, CFD-based results conducted in the frame of an independent research project are introduced to show the potential for a synergetic experimental-computation approach to this problem, emphasizing the need for the validation of the numerical results with wind tunnel data.

It is expected that the gained understanding about turbulence effects on the aeroelastic response of bluff bodies may be used to design some aerodynamic device for mitigating flow-induced oscillation of flexible structures.

2 Formulation

2.1 Turbulent Flow Characterization

The characterization of the turbulent flow in the wind tunnel will be based on the turbulence intensity evaluated from the timeseries of the velocity components recorded by X-wire probes.

The instantaneous flow velocity for any component $u_i(\mathbf{x}, t)$ is:

$$u_i(x, t) = U_1(x)\delta 1i + u'_i(x, t), \quad (1)$$

being \mathbf{x} the position vector, t time, U_1 the time-averaged velocity of the longitudinal component, δ the Kronecker delta and u'_i the fluctuating velocity.

The turbulence intensity is computed as:

$$Ii(x) = \sigma(u'_i(x))/U_1(x), \quad (2)$$

where $\sigma(u'_i(\mathbf{x}))$ is the standard deviation of the turbulent velocity fluctuations.

The turbulent length scale is computed as:

$$L_{u_i x_i} = \int_0^\infty R_{u_i}(x_i) dx_i, \quad (3)$$

where R_{ui} is the correlation coefficient of the u_i velocity component between points situated along the x_i axis.

2.2 Aerodynamic Coefficients and Pressure Coefficients

The aerodynamic coefficients of the bluff body are computed as:

$$\begin{aligned} C_D &= F_D / (0.5 \rho U^2 H), \\ C_L &= F_L / (0.5 \rho U^2 H), \\ C_M &= M / (0.5 \rho U^2 H^2). \end{aligned} \quad (4)$$

In the above equations, F_D and F_L are the drag and lift forces, while M is the pitch moment at the centroid of the bluff body, ρ is the air density, U is the reference freestream velocity and H is the prism's height. A sketch depicting the sign convention for aerodynamic forces is provided in Fig. 1.

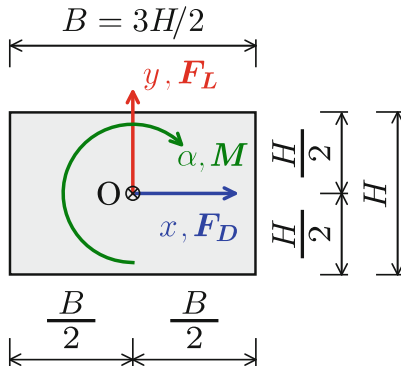


Fig. 1. Sign convention for aerodynamic forces acting on the 3:2 rectangular prism (wind flow from left to right).

Pressure coefficients are evaluated from the pressure taps records as:

$$C_p(t) = (p(t) - p_0) / (0.5 \rho U^2), \quad (5)$$

where $p(t)$ is the time-dependent pressure recording at each pressure tap and p_0 is the reference static pressure. For convenience, mean pressure coefficients and standard deviation of pressures are used to characterize time-averaged and fluctuating pressure distributions acting on the bluff body.

3 Experimental Campaign

The overarching goal of this ERIES-SSTURBBO project is to shed additional light on the impact that small-scale and large-scale turbulent flow may have on the aerodynamic and aeroelastic response of bluff bodies. There are still important gaps in knowledge in this area (Mannini, 2020) that this project aims to address. In wind tunnel testing, the method that is usually adopted for generating freestream turbulent flow consists of placing a grid upstream of the test section producing relatively large-scale turbulence. Alternatively, in Gartshore (1973) an approach based on the placement of a small-diameter rod upstream of bluff body under study was proposed. Gartshore showed that the small-scale turbulent wake generated by the rod impinging on the stagnation line of the sectional model was as reliable as grid-induced turbulent flow to study turbulent flow effects (see sketch in Fig. 2). Gartshore's method has not been widespread adopted (Kwok and Melbourne, 1980, Lander et al., 2016), thus it is revisited in the project targeting specifically small-scale turbulent flow, making comparisons with equivalent grid-induced turbulent flow, adopting the experimental outputs for validation of CFD models and exploring the possibility of using rods as mitigation devices for flow-induced oscillation of bluff bodies.

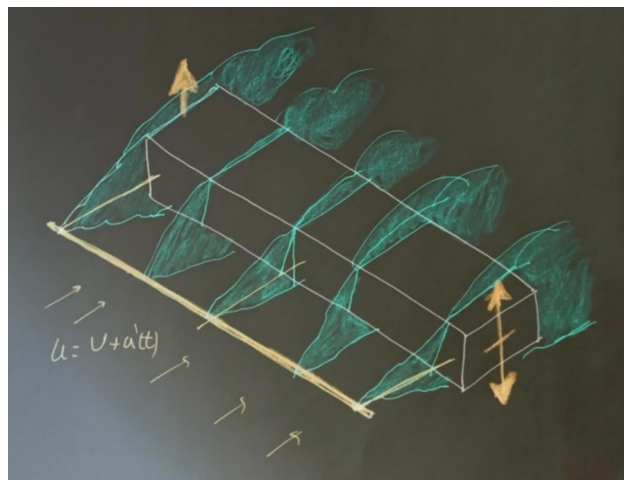


Fig. 2. Sketch for the rod-induced turbulent impinging of a downstream bluff body.

3.1 Scope

The scope of the experimental campaign covers the aerodynamic and aeroelastic response of a nominally two-dimensional ratio 3:2 rectangular prism. This is in fact a canonical case prone to suffer galloping and, depending on the Scruton number, VIV-galloping interference.

In broad terms, the main tasks in the project are the following:

- a) Flow characterization in the empty test chamber: for smooth flow, grid-induced turbulence for two different grid arrangements, and rod-induced turbulence.
- b) Aerodynamic response of the fixed 3:2 rectangular prism considering 19 different angles of attack in the range (-2.5°, 90°) for smooth flow, rod-induced turbulence at two different upstream distances from the prism (two different levels of turbulent intensity) and two different grid arrangements for grid-induced turbulent flow.
- c) Aeroelastic response in the heave degree of freedom of the 3:2 rectangular prism under the following flow conditions: smooth flow, rod-induced turbulence at two different upstream distances from the prism (two different levels of turbulent intensity) and two different grid arrangements for grid-induced turbulent flow.
- d) Proof-of-concept tests under smooth and grid-induced turbulent flow of the 3:2 rectangular prism with two rods attached to explore their effect for the mitigation of flow-induced oscillations.

3.2 Wind Tunnel and Instrumentation

The wind tunnel testing campaign will take place at the Giovanni Solari boundary layer Wind Tunnel of the University of Genoa (Italy). The working section of the facility is 8.8 (length) m by 1.70 (width) m by 1.35 (height) m, obtaining a turbulence level below 0.25% and uniformity of $\pm 1\%$ in the upstream test section. The wind flow is generated by one 1.8 m diameter fan, reaching a maximum flow velocity in the working section of approximately 32 m/s. An image of the wind tunnel test chamber is provided in Fig. 3.



Fig. 3. Test chamber at the “Giovanni Solari” Wind Tunnel at the University of Genoa.

The sectional model is manufactured in carbon fiber, and it has dimensions of 60 (depth) mm by 90 (width) mm, spanning the test section and contains 136 pressure taps arranged in 9 rings. The pressure scanners and the balance will be sampled at 800 Hz in the static and dynamic tests. For the dynamic tests, displacements will be measured by laser sensors at 2 kHz sampling.

For the flow characterization, a recently refurbished traverse will be used, making the sampling process more efficient. Flow velocities will be measured using 4 X-wire probes, sampling at 8 kHz per channel.

The up-stream rod has a diameter $d = 5$ mm ($1/12H$) and will be placed a distance from the rectangular prism between $50d$ and $150d$.

4 Complementarity with High-Fidelity CFD Simulations

The experimental campaign aims at delving into the effects of small-scale turbulence in the aerodynamic and aeroelastic responses of bluff bodies, but it will also support the validation of CFD simulations exploring the efficiency and accuracy of the computational implementation of the Small-Scale Rod-Induced Turbulence method, SSRITM. Specific areas of interest are commented upon next.

4.1 Characterization of the Flow in the Wake of the Rod

The turbulence intensity and length scale of the flow impinging on the studied bluff body depends on the distance between the upstream rod and the windward side body. It is therefore of utmost importance to assess the accuracy of the CFD simulations for reproducing the decaying turbulence intensity in the wake of the rod, along with the length scale and also the energy spectra for the wind velocity components. Previous research by the authors has addressed this aspect by analyzing the decay in the turbulence intensity of the along wind component depending on the distance downwind the rod (Álvarez et al., 2023; Álvarez et al. 2024). However, additional experimental information comprising spectra and length scales is required for a comprehensive assessment of the numerical approach potential. In Fig. 4, an image of the turbulent wake obtained from a 3D LES simulation is depicted, showing the complexity of the wake flow.

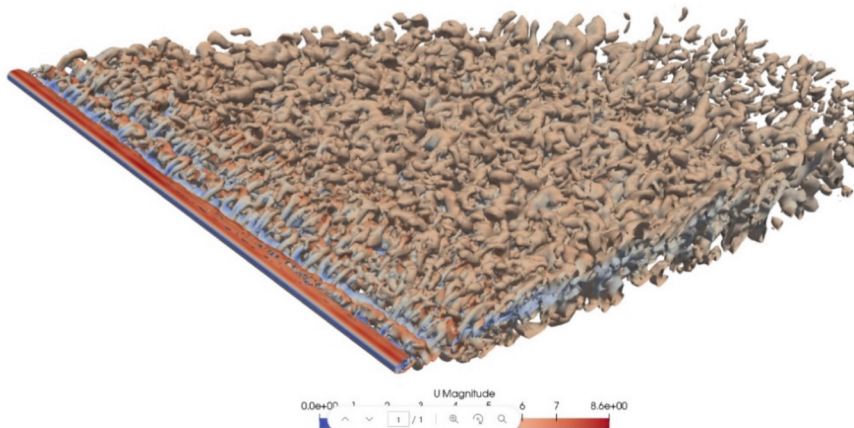


Fig. 4. Q-criterium snapshot of the vortical structures in the wake of the isolated rod.

In Fig. 5 an example of the energy spectrum of the along wind component of the velocity in a point on the wake centerline at distance of $50d$ downwind from the rod is reported, providing in the figure caption one value of the turbulent length scale matrix.

For the accurate assessment of these CFD-based results, high-quality experimental data are required to assess the impact of the mesh resolution and the turbulence modeling approach.

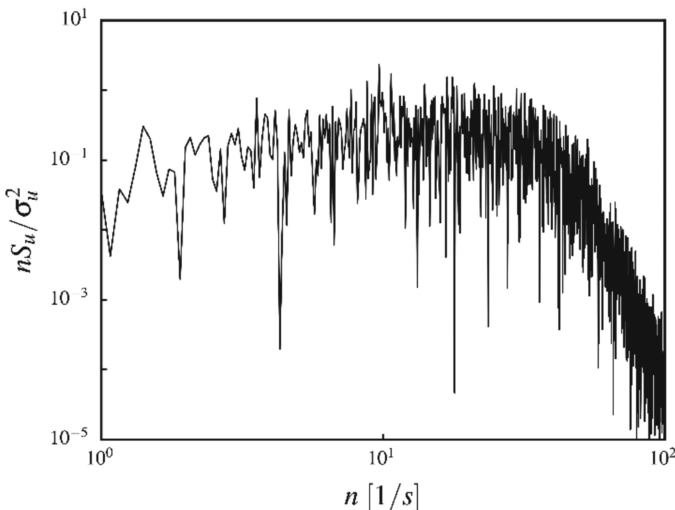


Fig. 5. Power spectrum of the along wind component of the fluctuating velocity at one point on the wake center line at $50d$ from the rod. The turbulent length scale of the along wind component in the along wind direction is $1.9d$.

4.2 Aerodynamic Force Coefficients of the 3:2 Rectangular Prism for Different Angles of Attack and Turbulence Intensities

The experimental data obtained for the fixed 3:2 rectangular prism will complement the studies carried out so far. Experimental data of the aerodynamic coefficients of a 3:2 rectangular prism at different angles of attack under turbulent incoming flow are limited. To the authors' knowledge only in Mannini et al. (2018) this geometry has been studied experimentally adopting grid-induced turbulent flow. Previous CFD-based research conducted by the authors for the SSRITM showed qualitative agreement with experimental data in Mannini et al. (2018); however experimental tests implementing the SSRITM are very much required to shed light on the impact of the turbulence generating method in the wind tunnel and assist in the interpretation of the numerical results. In table 1, the SSRITM CFD results of the aerodynamic coefficients obtained for 0° , 4° and 12° angles of attack for different levels of turbulence intensities in the along-wind component are compared with equivalent experimental grid-induced turbulence results in Mannini et al. (2016, 2018) as reported in Álvarez et al. (2024).

Table 1. Aerodynamic coefficients CFD vs Experimental (Re \approx 145000).

3D LES					EXPERIMENTAL (Mannini et al. 2016, 2018)				
<i>I</i>	AoA	C_D	C_L	<i>St</i>	<i>I</i>	AoA	C_D	C_L	<i>St</i>
0.0%	0.0°	1.74	0.00	0.10	1.0%	0.0°	1.76	0.01	0.11
0.0%	4.0°	1.55	-0.36	0.11	1.0%	4.0°	1.66	-0.35	0.11
0.0%	12.0°	1.48	-0.71	0.14	1.0%	12.0°	1.68	-0.47	0.13
7.5%	0.0°	1.39	0.04	0.09	6.1%	0.0°	1.52	0.01	
7.5%	4.0°	1.33	-0.57	0.11	6.1%	4.0°	1.43	-0.63	
7.5%	12.0°	1.46	-0.53	0.13	6.1%	12.0°	1.70	-0.21	
12.5%	0.0°	1.12	0.01	0.10	11.5%	0.0°	1.35	-0.01	
12.5%	4.0°	1.20	-0.73	0.08	11.5%	4.0°	1.26	-0.51	
12.5%	12.0°	1.60	-0.31	0.13	11.5%	12.0°	1.52	-0.07	

4.3 Aeroelastic Response of the 3:2 Rectangular Prism

One of the key contributions of this project will be the study of the impact that rod-induced small-scale turbulence may have on the amplitude of oscillation of the 3:2 rectangular prism and how this response compares with the one obtained for grid-induced turbulence. These results will also be adopted for validation of the computational simulations currently in execution. A detail of the oscillation timeseries obtained for the 3:2 rectangular prism under smooth flow and rod-induced 9% turbulence intensity obtained by means of 3D LES simulations is reported in Fig. 6 for a reduced velocity of 15. It can be noticed the smaller amplitude of oscillation obtained under incoming turbulent flow, in agreement with experimental tests conducted adopting grid-induced turbulent flow (Mannini et al., 2018).

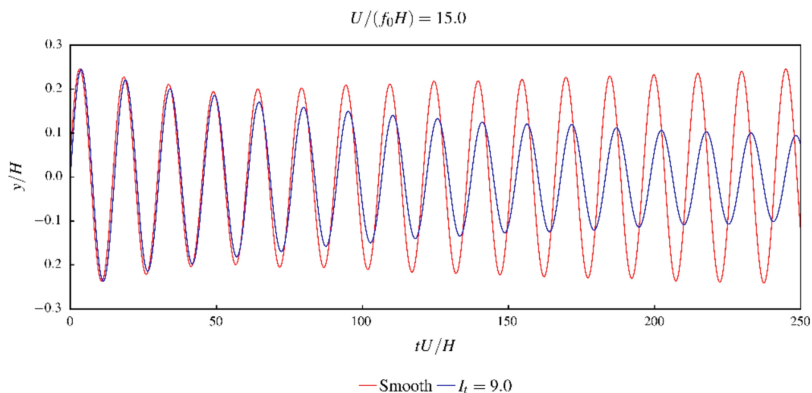


Fig. 6. Timeseries of the heave oscillation of the 3:2 rectangular prism at reduced velocity 15 for smooth flow and 9% turbulence intensity rod-induced turbulent flow (3D LES simulations).

5 Concluding Remarks

The scope of the ERIES-SSTURBO, which is the analysis of turbulent flow of different intensities and length scales in the aerodynamic and aeroelastic behavior of a 3:2 rectangular prism was explained. The planned experimental campaign to be conducted these next months at the “Giovanni Solari” Wind Tunnel of the University of Genoa was described, providing some details about the facility, instrumentation and methodology. Finally, some CFD results obtained in the frame of an independent research project were introduced to show the potential for complementarity between the experimental and computational approaches. It is expected that this experimental study will shed light on the effects of turbulence on the flow induced response of bluff bodies, while providing also a sound database for the validation high-fidelity 3D LES simulations.

At the Workshop presentation, preliminary results of the tests conducted in the previous weeks will be presented.

Acknowledgements. This work is part of the transnational access project “ERIES-SSTURBBO”, supported by the Engineering Research Infrastructures for European Synergies (ERIES) project (www.ries.eu), which has received funding from the European Union’s Horizon Europe Framework Programme under Grant Agreement No. 101058684. This is ERIES publication number C71.

F. Nieto and A.J. Álvarez are supported by grant TED2021-132243B-I00 funded by MICIU/AEI/<https://doi.org/10.13039/501100011033> and by “European Union NextGenerationEU/PRTR. Funding has also been obtained from the Galician Regional Government through action ED431C 2021/33.

The HPC resources at the Galician Supercomputing Centre (CESGA) have been used for the numerical simulations reported herein.

References

- Álvarez, A.J., Nieto, F., Kwok, K.C.S., Hernández, S.: A simplified approach for bluff-body aerodynamics under small scale free stream turbulent flow. *J. Wind Eng. Ind. Aerodyn.* **241**, 105500 (2023)
- Álvarez, A.J., Nieto, F., Kwok, K.C.S., Patruno, L., Laws, P.: 3D LES simulation of the rod-induced small-scale turbulent flow around a 3:2 rectangular prism. In: Proceedings of the 9th International Colloquium on Bluff Body Aerodynamics and Applications. Birmingham, UK (2024)
- Gartshore, I.S.: The effects of the free stream turbulence on the drag of rectangular two-dimensional prisms. Technical Report BLWT-4-T3, University of Western Ontario (1973)
- Kwok, K.C.S., Melbourne, W.H.: Freestream turbulence effects o galloping. *J .Eng. Mech. Div.* **106**, 273–288 (1980)
- Lander, D.C., Letchford, C.W., Amitay, M., Kopp, G.A.: Influence of the bluff body shear layers on the wake of a square prism in turbulent flow. *Phys. Rev. Fluids* **1**, 044406 (2016)
- Mannini, C., Marra, A.M., Massai, T., Bartoli, G.: Interference of vortex-induced vibration and transverse galloping for a rectangular cylinder. *J. Fluids Struct.* **66**, 403–423 (2016)
- Mannini, C., Massai, T., Marra, A.M.: Unsteady galloping of a rectangular cylinder in turbulent flow. *J. Wind Eng. Ind. Aerodyn.* **173**, 210–226 (2018)

Mannini, C.: Incorporation of turbulence in a nonlinear wake-oscillator model for the prediction of unsteady galloping response. *J. Wind Eng. Ind. Aerodyn.* **200**, 104141 (2020)

Nguyen, C.H., Nguyen, D.T., Owen, J.S., Hargreaves, D.M.: Wind tunnel measurements of the aerodynamic characteristics of a 3:2 rectangular cylinder including non-Gaussian and non-stationary features. *J. Wind Eng. Ind. Aerodyn.* **220**, 104826 (2022)

Open Access This chapter is licensed under the terms of the Creative Commons Attribution 4.0 International License (<http://creativecommons.org/licenses/by/4.0/>), which permits use, sharing, adaptation, distribution and reproduction in any medium or format, as long as you give appropriate credit to the original author(s) and the source, provide a link to the Creative Commons license and indicate if changes were made.

The images or other third party material in this chapter are included in the chapter's Creative Commons license, unless indicated otherwise in a credit line to the material. If material is not included in the chapter's Creative Commons license and your intended use is not permitted by statutory regulation or exceeds the permitted use, you will need to obtain permission directly from the copyright holder.





Thunderstorm-Induced Loading on Tall Buildings

Aldereguía Sánchez Camila^{1,2}, Torre Stefano³, Ruffini Edoardo³, Bagnara Anna³,
Tubino Federica^{1(✉)}, Giuseppe Piccardo¹, and Maria Pia Repetto¹

¹ University of Genoa, Genoa, Italy
federica.tubino@unige.it

² Technological University of Havana Jose A. Echevarría, Havana, Cuba

³ NOVA Fluid Mechanics Ltd., London, UK

Abstract. Tall buildings are very sensitive to wind-induced excitation. Currently, in the design of structures, the wind-induced loading is commonly estimated based on the models available for synoptic events. However, in many parts of the world, thunderstorms tend to dominate the local wind climate. Thunderstorm downbursts differ from synoptic events due to their nose-shaped mean wind speed profile and non-stationary behavior over short intervals (10 min to 1 h). Wind tunnel testing is an effective method for analyzing wind effects on structures. However, simulating thunderstorms in traditional facilities requires specialized equipment. Disregarding the non-stationary characteristics of thunderstorm outflows, ERIES-TLTB Project focuses on the wind-induced effects on tall buildings caused by thunderstorms and synoptic events, focusing on the impact of the variation of the mean wind speed profile. Experimental tests are conducted using high-frequency force balance and pressure integration techniques on different tall building models. A comparison of the pressure coefficient distribution is provided for the two types of events.

Keywords: Tall Buildings · Thunderstorms · Wind Tunnel Tests

1 Introduction and Research Motivation

In the design of structures, wind-induced loading is currently derived using the cyclone model for synoptic events; however, in many parts of the world, thunderstorms tend to dominate the local wind climate. Several investigations [1, 2] have confirmed the different characteristics of thunderstorms with respect to synoptic events such as the mean wind speed profile and non-stationary nature; therefore, a different analysis is required in order to assess the loading induced by such events. In the case of tall buildings, the consideration of a logarithmic mean wind speed profile as established in the standards, could provide an overestimation of wind actions compared to that arising from downburst profiles, characterized by a maximum velocity close to the ground. The effect of thunderstorm downbursts on real structures is rarely studied through full-scale measurements and it is typically investigated using laboratory experiments and numerical

simulation. Wind tunnel testing is a reliable method for assessing wind-induced loads and structural dynamic response. Experimental downburst modeling can either replicate entire events or focus solely on their outflows [3, 4]. The latter is a more practical and cost-effective approach, commonly used in atmospheric Boundary Layer Wind Tunnel (BLWT). Aldereguía Sánchez et al. [5] proposed the use of a passive device to simulate thunderstorm mean wind speed profiles. However, this device is not able to reproduce the non-stationary characteristics of the incoming flow, limiting its application to studying the mean wind speed profile effect on the loading induced on structures.

This study, conducted within the ERIES project Thunderstorm Loading on Tall Buildings (ERIES-TLTB), aims to conduct experimental tests in a classic BLWT in order to compare the actions and effects induced by synoptic and thunderstorm events on tall buildings. The study involves testing two tall building models: the benchmark case of the CAARC building, and a real project, called Project X. Tests on the CAARC building model are carried out using High-Frequency Force Balance (HFFB) and High-Frequency Pressure Integration (HFPI), while only HFPI tests are carried out on the Project X model. This paper describes the wind tunnel campaign that has been carried out and provides some preliminary results obtained in term of pressure distributions. In the following steps of the research, the measured quantities from each test will be analyzed to estimate the mean and peak base wind loads, allowing for an assessment of the global effects of downbursts and their comparison with those induced by synoptic winds. From the HFPI measurements, pressure and load distribution on individual floors will be analyzed to understand how wind pressures vary along the height of the building, providing insights into localized effects. Additionally, wind-induced accelerations at several locations will be assessed and checked against comfort criteria to determine whether the building's response under thunderstorm conditions meets acceptable standards for occupant comfort.

2 Wind Tunnel Campaign

The experiments are conducted at the Giovanni Solari Wind Tunnel at the University of Genoa.

The initial stage of the study involves tests to derive wind loads based on HFFB and HFPI techniques on the CAARC benchmark building. A model scale of 1:400 is adopted, and all tests are performed in isolation to accurately capture the key differences between synoptic events and thunderstorm downbursts (Fig. 1a). Project X is a 165 m tall building, tested within the context of its surroundings using the HFPI technique on a 1:300 model scale (Fig. 1b).

The mean wind speed profiles of thunderstorms replicated in this work are derived from a previous study [5], based on the Wood and Kwok model [6].

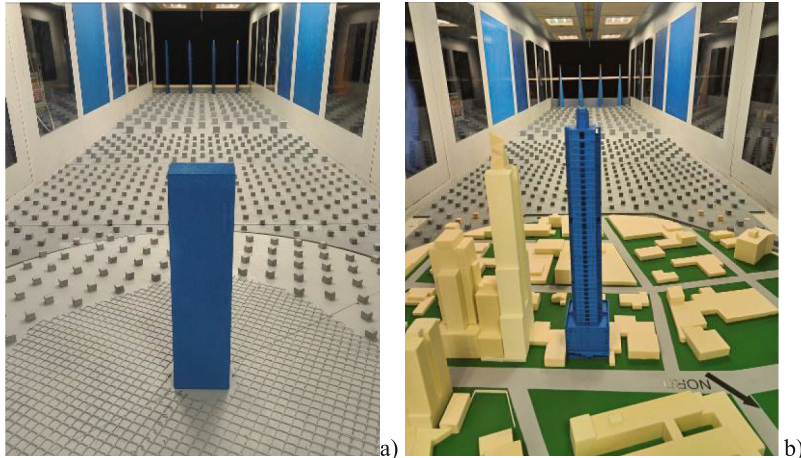


Fig. 1. Wind tunnel models: a) CAARC building, b) Project X building.

The tests on the CAARC building model were conducted at two levels of turbulence intensity, corresponding to average values of approximately 10% and 15% along the height of the building. For the low turbulence intensity, two full-scale nose height $z_m = 60$ m and $z_m = 100$ m above the ground are simulated, while for the higher turbulence intensity, tests have been conducted only with $z_m = 100$ m. For comparison with classical synoptic events, the mean wind speed and turbulence intensity profiles with a roughness length of $z_0 = 0.003$ m (corresponding to the low turbulence intensity) and $z_0 = 0.05$ m (corresponding to the higher turbulence intensity) are also simulated based on the expressions established in EN1991-1-4 [7]. Figure 2 shows the mean wind speed and turbulence intensity profiles considered, normalized with respect to the mean wind speed at 10 m height.

Project X is located in a mixed climate area, where thunderstorms are very frequent events. Thus, the analysis of the wind-induced loads and effects on this real project case study is carried out based on design wind speeds derived from a statistical analysis of the wind data in the area, distinguishing between thunderstorm and synoptic events, and considering the corresponding mean wind speed profile.

In particular, three analyses will be carried out: Synoptic (S) considers the synoptic profile and the design velocity for synoptic events evaluated from the statistical analysis; Thunderstorm (TS) considers the thunderstorm profile and the design velocity for thunderstorm events evaluated from the statistical analysis; Mixed (M) considers the synoptic profile and the design velocity derived from a mixed distribution combining synoptic and thunderstorm events based on the statistical analysis.

Tests have been carried out considering a synoptic target profile corresponding to a wind direction of 120° . For comparison, the mean wind speed profile of the worst-case thunderstorm, derived from the CAARC analysis, was used. This profile is characterized by an average turbulence intensity level along the height of the building of approximately 15%, and, at the model scale 1:300 adopted for Project X, by a nose height $z_m = 75$. Figure 3 shows the mean wind speed and turbulence intensity profiles considered.

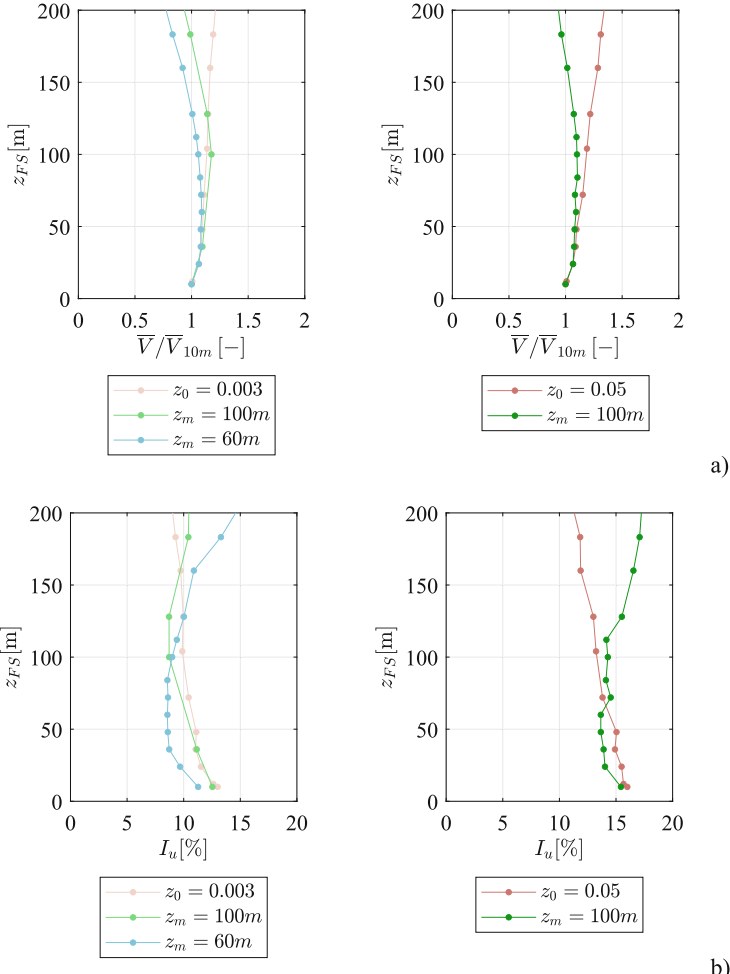


Fig. 2. CAARC building model tests target profiles: a) Mean wind speed normalized by the mean wind speed at 10 m height, b) Turbulence intensity.

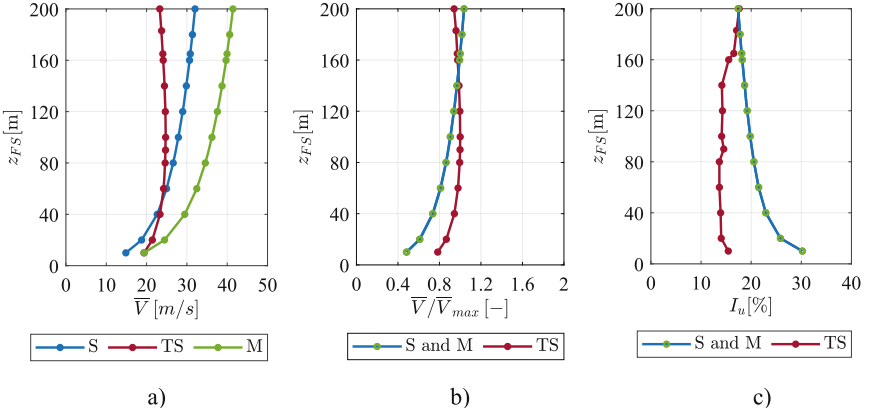


Fig. 3. Project X target profiles: a) Mean wind speed b) Mean wind speed normalized with respect to its maximum, c) Turbulence intensity. S = Synoptic, TS = Thunderstorm, M = Mixed.

3 Mean Pressure Coefficients

3.1 CAARC Building

During the HFFB tests on the CAARC building model, the time histories of the base loads in terms of shear forces, bending moments, and torque for 18 wind directions (10° increments) are acquired, while for HFPI tests, the time histories of the pressures acting on the external surface are measured. At a first step, the base wind loads obtained from HFFB and HFPI measurements have been compared and a good agreement for all wind directions has been found. Then, analyses of pressure distributions have been carried out.

As an example, Fig. 4 illustrates the mean pressure coefficient distribution for wind coming from 0° on the windward façade (Façade 1, Fig. 4a), normalized with respect to the maximum mean kinetic pressure, for the low turbulence (Fig. 4b) and high turbulence (Fig. 4c) profiles. The results show that the distribution of the mean pressure coefficients on the windward face (Façade 1) generally mirrors the shape of the approaching mean wind profile. This observation aligns with findings in the literature [8], where only one turbulence intensity level and a single height of the nose were considered. The maximum pressure coefficient for the synoptic profiles can be found around 130–150 m above the ground level. For the thunderstorm profiles, the height corresponding to the maximum mean pressure coefficients depends on the height of the nose, as could be expected. The differences between the two thunderstorm profiles with $z_m = 100$ m can be attributed to variations in the turbulence intensity: higher turbulence intensities in the approaching winds affect the mean pressure coefficient gradient.

Starting from measured pressures, base wind loads, floor-by-floor loads, and accelerations at various locations can be derived enabling a comparison of the local and global loads and effects induced by thunderstorms and synoptic events.

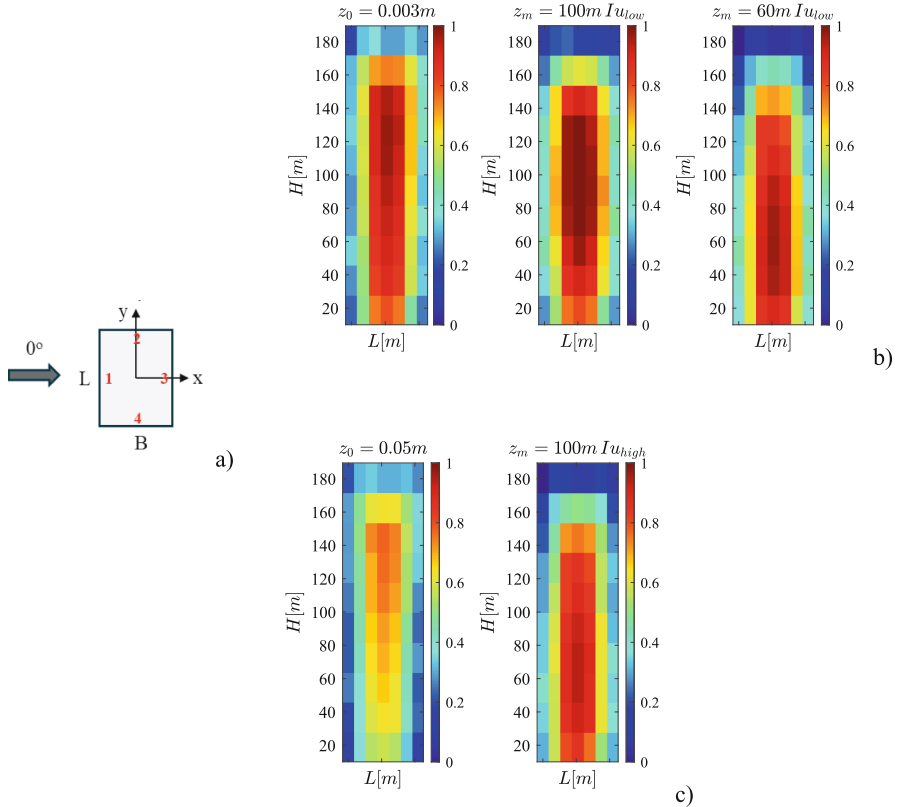


Fig. 4. CAARC Building, comparison of mean pressure coefficients on the windward façade (Façade 1, a)) for synoptic and thunderstorm events: b) low turbulence intensity profiles, c) high turbulence intensity profiles.

3.2 Project X

Figure 5 illustrates a representative case of the mean pressure coefficient distribution, normalized with respect to the maximum mean kinetic pressure, for wind approaching from the direction $\alpha = 50^\circ$ (almost orthogonal to Façade 1), considering Synoptic and Mixed (S and M) and Thunderstorm (TS) profiles. It is important to highlight that, due to the adopted normalization, the mean pressure coefficients depend solely on the shape of the wind profile, which remains identical for Synoptic and Mixed analyses (see Fig. 3b). As previously observed in Fig. 4 for the CAARC building case study, the distribution of the mean pressure coefficients on the windward face (Façade 1) generally follows the shape of the approaching mean wind profile. While the distributions corresponding to the two profiles exhibits a similar overall trend, notable differences may arise in some specific areas (e.g., in the lower region of Façade 3).

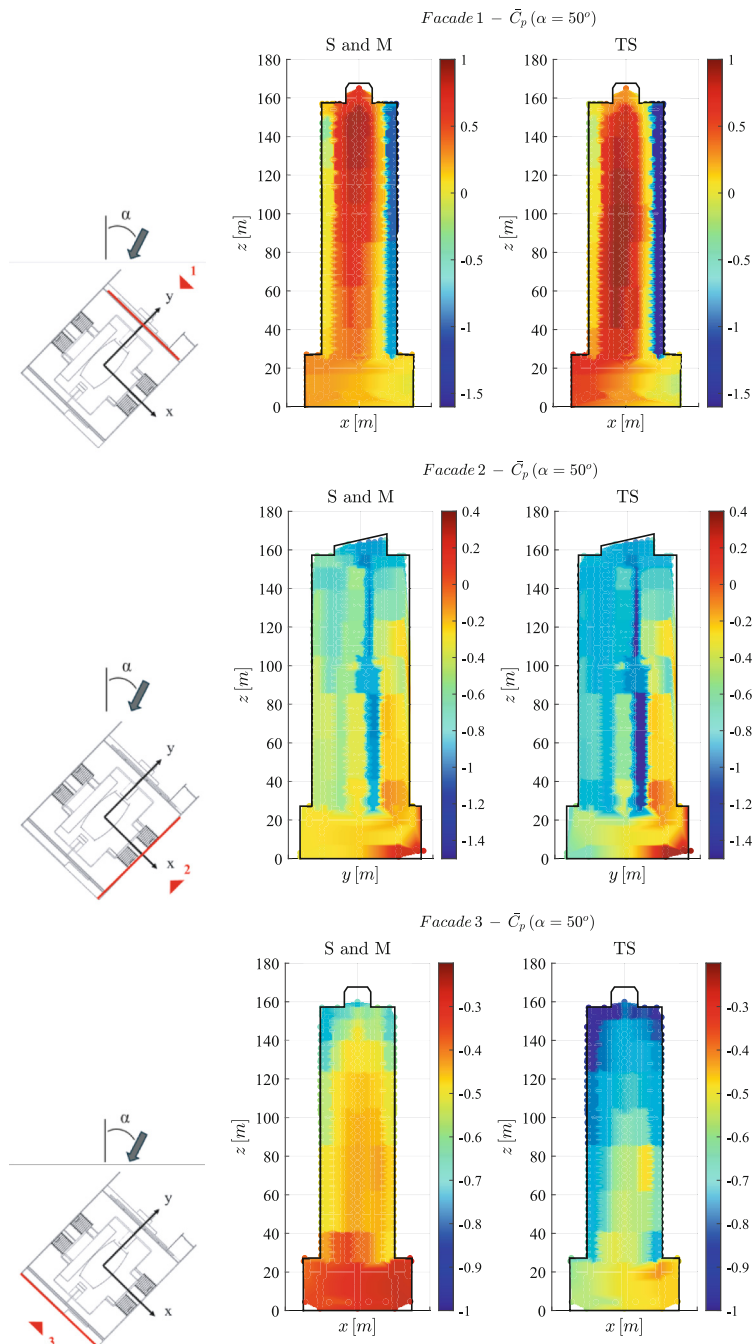


Fig. 5. Project X, mean pressure coefficients for Synoptic and Mixed (S and M) and Thunderstorm (TS) profiles.

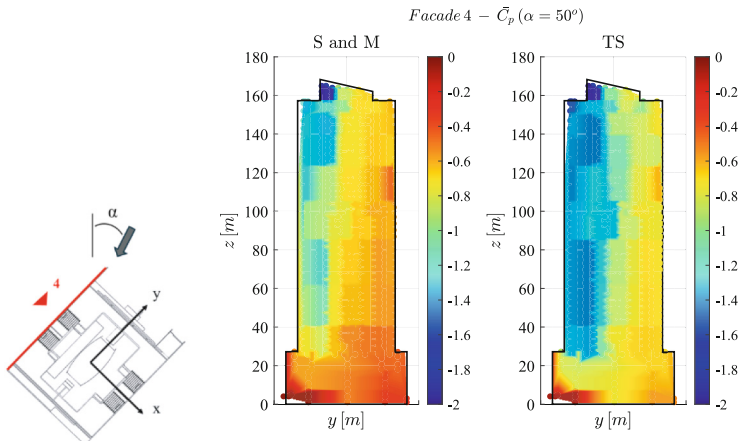


Fig. 5. (continued)

4 Conclusions

The ERIES-TLTB Project aims at comparing the wind-induced loading and response of tall buildings subjected to thunderstorms and synoptic events, focusing exclusively on the effect of the mean wind speed profile shape while neglecting its transient nature. Analyses are carried out on a benchmark case study (CAARC building) and on a real project. The study of the CAARC building benchmark enables a detailed analysis of the global and local effects, also allowing comparisons with a recent study from the literature, where a different technology has been adopted to simulate thunderstorm profile [8]. Furthermore, the effect of the variation the nose height and turbulence intensity are studied in this research. The analysis of Project X, a building located in a thunderstorm-prone area, provides insights into the global and local effects of both thunderstorms and synoptic events in the context of a real structure, considering the specific characteristics of the local climate.

Acknowledgements. This work is part of the transnational access project “ERIES-TLTB”, supported by the Engineering Research Infrastructures for European Synergies (ERIES) project (www.ries.eu), which has received funding from the European Union’s Horizon Europe Framework Programme under Grant Agreement No. 101058684. This is ERIES publication number C50.

References

1. Canepa, F., Burlando, M., Solari, G.: Vertical profile characteristics of thunderstorm outflows. *J. Wind Eng. Ind. Aerodyn.* **206**, 104332 (2020)
2. Solari, G.: Thunderstorm downbursts and wind loading of structures: progress and prospect. *Front. Built Environ.* **6**, 63 (2020)
3. Aboutabikh, M., Ghazal, T., Chen, J., Elgamal, S., Aboshosha, H.: Designing a blade-system to generate downburst outflows at boundary layer wind tunnel. *J. Wind Eng. Ind. Aerodyn.* **186**, 169–191 (2019)

4. Canepa, F., Burlando, M., Romanic, D., Solari, G., Hangan, H.: Experimental investigation of the near-surface flow dynamics in downburst-like impinging jets. *Environ. Fluid Mech.* **22**, 921–954 (2022)
5. Aldereguía Sánchez, C., Tubino, F., Bagnara, A., Piccardo, G.: Experimental simulation of thunderstorm profiles in an atmospheric boundary layer wind tunnel. *Appl. Sci.* **13**, 8064 (2023)
6. Wood, S., Kwok, K.: An empirically derived estimate for the mean velocity profile of a thunderstorm downburst. In: Proceedings of the 7th Australian Wind Engineering Society Workshop, Auckland (1998)
7. European Committee for Standardization: Eurocode 1: actions on structures - Part 1–4: General actions - Wind actions (EN 1991-1-4). CEN (2004)
8. Li, Y., Mason, M.S., Bin, H.-Y., Lo, Y.L.: Aerodynamic characteristics of a high-rise building in a steady thunderstorm outflow-like flow field. *J. Wind Eng. Ind. Aerodyn.* **240**, 105501 (2023)

Open Access This chapter is licensed under the terms of the Creative Commons Attribution 4.0 International License (<http://creativecommons.org/licenses/by/4.0/>), which permits use, sharing, adaptation, distribution and reproduction in any medium or format, as long as you give appropriate credit to the original author(s) and the source, provide a link to the Creative Commons license and indicate if changes were made.

The images or other third party material in this chapter are included in the chapter's Creative Commons license, unless indicated otherwise in a credit line to the material. If material is not included in the chapter's Creative Commons license and your intended use is not permitted by statutory regulation or exceeds the permitted use, you will need to obtain permission directly from the copyright holder.





ValUr: A High-Fidelity Dataset for Validation of Urban Pollution Dispersion Models – Project Overview and Geometry Preparation

Mariya Pantusheva¹(✉) , Radostin Mitkov¹ , Petar O. Hristov¹ , Evgeny Shirinyan¹ , Vasilis Naserentin² , A. K. R. Jayakumari³ , Stefanie Gillmeier³ , and Anders Logg²

¹ GATE Institute, Sofia University “St. Kliment Ohridski”, Sofia 1164, Bulgaria
mariya.pantusheva@gate-ai.eu

² Department of Mathematical Sciences, Chalmers University of Technology,
412 969 Gothenburg, Sweden

³ Building Physics and Services, Department of the Built Environment, Eindhoven University
of Technology, P.O. Box 513, 5600 MB Eindhoven, The Netherlands

Abstract. Computational fluid dynamics (CFD) models, used independently or integrated into city digital twins, can predict air pollution dispersion and support informed decision-making in urban planning. While modelling complexity and capabilities have increased, systematic validation and uncertainty quantification remain crucial, yet are among the least understood and applied aspects of the analysis process.

To address this issue, the ValUr project, supported by the ERIES programme, aims to establish a best-practice protocol for urban CFD validation and to generate a high-quality, open-access pollution dispersion dataset.

This work introduces the project scope, motivation, and goals, detailing early project activities, including the identification of the study area - part of the city centre of Sofia, Bulgaria, where air quality is a pressing concern, and the creation of a scaled geometry suitable for physical model-making, wind tunnel testing, and CFD simulations. The geometry goes beyond the basic level of detail (LoD) 1, typically used in validation databases and reaches LoD 2.2, capturing the complex building morphologies and realistic urban conditions of the area.

By sharing protocols and data openly, ValUr seeks to promote the importance of model reliability and to encourage validation consistency within the computational wind engineering community.

Keywords: Model validation · Urban pollution dispersion modelling · Wind tunnel testing · Geometry preparation

1 Introduction

1.1 Project Motivation

Urban areas today face serious challenges related to air pollution, a problem that directly affects public health and quality of life. In many cities, including Sofia, measured levels of particulate matter and gaseous pollutants frequently exceed the thresholds recommended by health organizations.

Despite advances in computational fluid dynamics (CFD) models, reliably predicting how pollutants spread through complex urban environments remains challenging. The issue of reliability is made even more significant in the paradigm of digital twin creation, which sees multiple models and data streams being connected in a system to provide real time insights into the operation of a physical asset. Contrary to the popular technocratic opinion, digital twins and massive volumes of data do not automatically provide a reliable representation of the investigated system. The core tenet of model reliability, instead, is bringing trust in the model not by its complexity or resolution, but by careful uncertainty quantification and validation, tailored to the intended application of the model.

The ValUr project aims to establish this perspective through the design and execution of an experimental wind tunnel campaign, judicial uncertainty quantification and validation, and objective predictive capability estimation for urban pollution dispersion CFD models.

1.2 Overview of ValUr Work

To achieve the goals described in Sect. 1, the project is split into four general stages – model making, wind tunnel testing, data analysis and validation.

Model making includes the selection of a suitable region in Sofia, the creation of the geometry and the manufacturing of the test article to be used during the experimental campaign. The rest of the paper is dedicated to this process.

The experimental campaign will be carried out in the atmospheric boundary layer wind tunnel of Eindhoven University of Technology (TU/e). To ensure good quality data is collected during the experimental campaign, the tests will focus on one flow direction and the detailed concentration measurements of a passive scalar gas, released from two point sources in turn. Measurements will be done at locations flagged as important to the area and by preparatory CFD simulations.

The raw data of pollutant concentrations, approach flow conditions, and release rates, among others, will be analysed and cast into a format suitable for validation work. Particular focus is placed on quantifying uncertainty from different sources to ensure the effect of potential errors and various unknowns is accounted for.

Reynolds-averaged Navier-Stokes (RANS) solvers will be used for some of the preliminary screening tests, but for the core of the validation work, the modelling paradigm will be large-eddy simulation (LES). The computational and validation aspects of the work will be covered in a future work.

1.3 State of the Art of Geometry Preparation for Wind Tunnel Testing

Scale modelling for urban wind tunnel testing for pollution dispersion has progressed considerably since the early work of Castro and Robins [1] and Stathopoulos and Baskaran [2], who used handcrafted wooden blocks to represent simplified environments with limited geometric fidelity. The advent of CAD-based approaches [3] and parametric modelling [4] allowed more systematic geometry variations, while 3D printing methods outlined in [5] pushed physical models toward unprecedented amount of detail, including entire and GIS-based workflows in the process [6, 7].

However, this has given rise to another area of research, namely, the identification of the level of geometric detail to be included in the model. To this end, Hertwig et al. [8] proposed methods for selecting essential features when refining models. Carpentieri and Robins [9] built on their work by assessing how different abstraction levels affect flow predictions. A notable example of such an abstraction level is the inclusion of roof profiles, which Yassin [10] demonstrated can significantly alter dispersion behaviour. Despite the significant amount of work done over the years, some challenges, such as representing urban structures at multiple scales [11] and adapting geometric detail to target areas [12], remain open issues.

Manufacturing techniques have also seen significant advancement, integrating precision stereolithography [13], multi-material 3D printing [14], among others. These developments allow the focus of physical modelling to shift to high utilisation and sustainability using modular designs [3] and standardized connections [15].

1.4 Objectives and Outcomes

This paper focuses on creating a scaled model for the ValUr project wind tunnel tests, which preserves critical features that affect the flow, while addressing practical fabrication constraints. It is meant to document the process of geometry creation for wind tunnel testing and CFD modelling, so that it can be used and improved on by the computational and experimental wind engineering communities. The practical implementation of the workflow is illustrated on the ERIES ValUr project geometry. The remainder of the paper is structured as follows and is shown in Fig. 1. Section 2 describes the requirements and selection process for the test area and some scaling considerations. The main body of the work on preparing the geometry for validation tests is presented in Sect. 3. Section 4 summarises the main conclusions of the work and outlines the next steps in ValUr.

2 Study Area and Model Setup

Given that the overall goal of ValUr is to promote the importance of validation in computational wind engineering, the region of the city to use and the most appropriate scale of the wind tunnel model had to be carefully determined.

2.1 Region Selection

The main driver behind the choice of region was the level of air pollution it experiences and a somewhat inhibited ventilation. In an urban context, elevated levels of air pollution

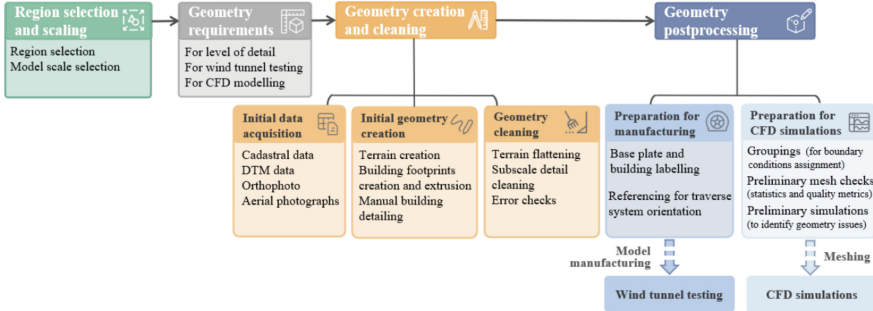


Fig. 1. Graphical representation of the geometry preparation workflow.

is associated with proximity to a pollution source in the direction opposing the prevailing winds for the region. The principal pollution source in Sofia is road traffic, which means that built-up areas with roads, running perpendicular to the wind, are candidates for elevated pollution levels. To identify suitable test model locations, major roads in the city were listed, with those roads that frequently experience congested traffic chosen for the next stage of the selection process. Sofia has five official meteorological and air quality stations in the city, which do measure wind velocity, but these measurements are not reliable because they are strongly affected by the presence of buildings and local terrain. Instead of using this data to determine the prevailing wind direction over the city, annual data from the airport for several years was obtained and aggregated [16]. The resultant directional wind rose is shown in Fig. 2, which clearly indicates west-northwesterly, east-southeasterly and easterly winds dominating the landscape. Thus, a region with a busy road running north-northeast to south-southwest is a good filter for locations to conduct the validation experiments.

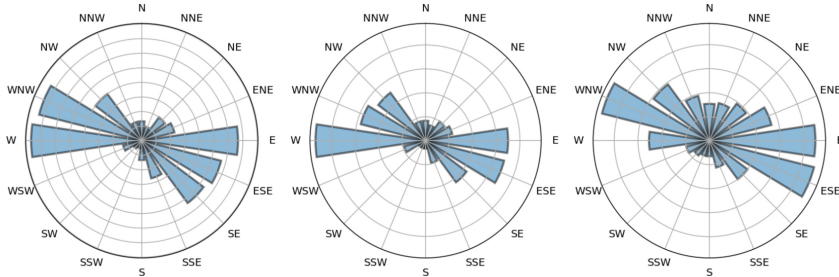


Fig. 2. Directional wind roses for Sofia airport for 2007, 2010, and 2018 (left to right).

Several sites around the city fit this requirement. A subset of these is shown in Fig. 3. The next major selection criteria were that the area around the road be heterogeneous in terms of building heights and layouts close to where the measurements are to be taken (referred to hereafter as the *inner region*) to promote flow.

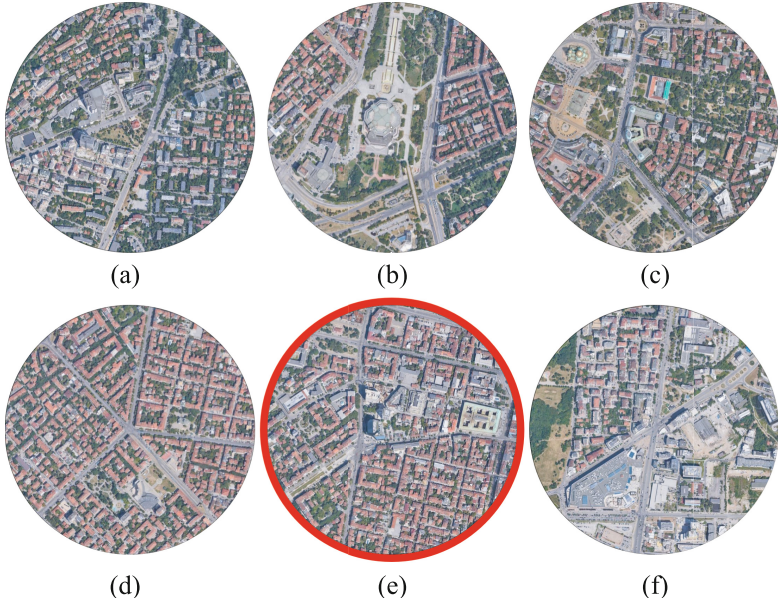


Fig. 3. Shortlisted locations in Sofia (selected region marked in red), images source: Google Maps

mixing, but at the same time exhibit a degree of homogeneity in the *outer region* to ensure the flow reaches a steady state more quickly. It can be seen that the regions depicted on Fig. 3(b)-(e) all fit this criterion relatively well. Another criterion that was enforced concerning the test area is that regions with large green spaces and dense vegetation were avoided, to minimise the extent of uncertain and unidentifiable phenomena in the test campaign and, ultimately, maximise the quality of validation [17, 18]. This rules out the regions in Fig. 3(b) and (c). Finally, regions with large roads aligned with the wind direction, or other means of quick ventilation were also discarded to focus on challenging setups commonly avoided in validation. Thus, the region around Sofia Courthouse, shown in Fig. 3(e) was chosen, as it exhibits all desirable features outlined above. It is worth noting that even though none of the areas shown in Fig. 3 would have made a better candidate by small relocations of the circular perimeter, there are, naturally, many other regions in Sofia that could have been considered. Some additional factors that weighed in on the decision were the presence of many pedestrian streets and points of interest, cultural buildings, and the overall interesting architectural landscape, featuring what will be Sofia's fourth-largest building upon its completion.

2.2 Model Scale

Urban wind tunnel model scales used in literature vary from 1:225 to 1:350 or smaller¹. There are several constraints in choosing the model scale for the ValUr experimental campaign. Perhaps the most important of these is the *blockage ratio*, computed as the

¹ Models used in the CEDVAL database.

ratio of the sum of the projected frontal areas of the model and of any test equipment to the overall area of the test section of the wind tunnel. The overall blockage ratio should be below 5% for closed section wind tunnels, such as the one at TU/e, unless appropriate correction for edge effects are applied [19, 20]. Since the goal of this project is to produce a high-quality dataset, all effort is made to keep such empirical corrections to a minimum. For the 6 m^2 test section of the tunnel, this translates to a maximum overall frontal area of 0.3 m^2 . Another important constraint for the scale is the minimum manufacturable detail size, which in this case was determined at 1 mm. Considering these two constraints and considering points of interest in the region, the scale was chosen to be 1:350. For the 2.6 m diameter turntable at the wind tunnel, this resulted in a 910 m region, with a scaled, projected, windward area of 0.254 m^2 (approx. 4.2%), enough to accommodate the test equipment within the allowable 5% blockage ratio.

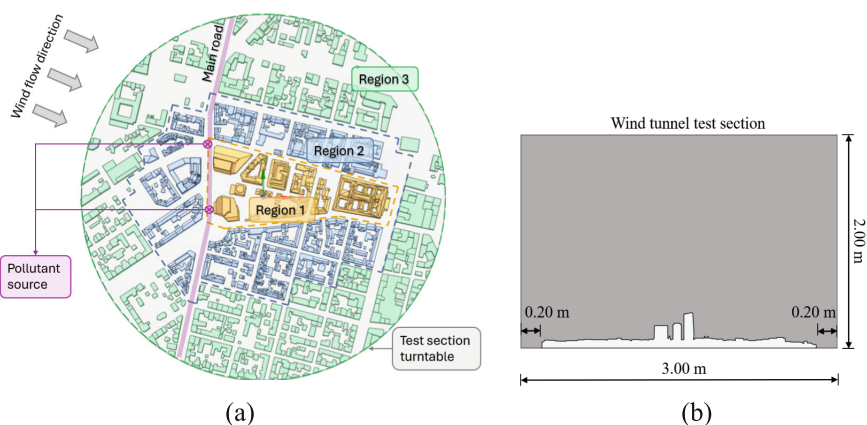


Fig. 4. Scaled model. (a) Zoning; (b) Cross-section.

3 Geometry Preparation

In the next step, creation of the urban geometry representation, it was important that it can be effectively utilized for both experimental and computational modelling. Having such a geometry can facilitate the compatibility and consistency between the two analysis types, reduce uncertainties, and improve the quality of the validation dataset on urban pollution dispersion that will be produced under the ValUr project.

This section describes the procedure how the selected target region, identified in Sect. 2, was transformed into a 3D-printed wind-tunnel model that captures relevant urban features with an adequate level of detail. For this purpose, a framework of requirements was formulated based on the best practices outlined in wind-engineering standards and existing guideline documents, further denoted as best-practice guidelines (BPGs) [17–27]. These requirements were followed in all stages of geometry preparation - from data acquisition, geometry creation and processing steps, through the final stage of physical model making.

3.1 Requirements and Best Practices (RBP)

RBPs related to the **level of detail** (LoD) of urban representation must balance capturing sufficient geometric features to reproduce realistic flow patterns and maintaining correct similarity scales, against the practical requirements of manufacturing, physical testing, and the computational efficiency needed for subsequent CFD simulations. In this work, that balance was achieved by applying the highest fidelity to a selected target region and progressively simplifying the outer areas, as recommended also by the BPGs [17, 18, 22]. In addition, the wind-tunnel model manufacturing technique imposed a minimum feature size of 1 mm in reduced scale (0.35 m at full scale). To respect these constraints, the domain described in Sect. 3 was subdivided into three zones of decreasing geometric complexity, depicted in Fig. 4(a). **Region 1** (inner zone) encompasses the city area with the highest community significance (urban landmarks, pedestrian zones, and main roads, including the pollutant source). The measurement points that require highest quality and densest grid are located here. The buildings in this area are modelled to LoD 2.2, according to the classification presented in [28], considering architectural features larger than or equal to 1 m at full scale (approximately 2.8 mm in model scale). Smaller features, if present, are simplified. **Region 2** (middle zone) extends outward by at least one city block from, retains the same LoD as Region 1, but has a comparatively sparser measurement grid. Finally, **Region 3** (outer zone) covers the remainder of the turntable without having any measurement points in this area. Here the captured LoD is reduced to 1.3 as per [28], preserving only protrusions or gaps exceeding 2 m at full scale (about 5.7 mm in model scale).

RBPs related to **wind tunnel testing** mandate an adequate offset between the test-section obstructions (walls, ceiling, or equipment) and the scaled model to prevent boundary-layer mismatch and artificial flow acceleration. The same principle applies for CFD simulations, where the obstructions are the computational domain boundaries. In this work, these considerations were applied as discussed in Sect. 2. A common practice in wind tunnel testing is using a flat surface for the ground representation in the scaled model. This assumption is acceptable given the terrain does not exhibit major elevation changes across the modelled area, and can facilitate the manufacturing process and reduce measurement uncertainties. A practical standpoint requirement is ensuring adequate referencing and labelling for a precise alignment between the base plate, the buildings, and the instrumentation.

Although the focus of the collaboration activities under ValUr is on a wind tunnel testing campaign, the ultimate goal is generating a high-quality dataset that can be used for validation of urban pollution dispersion models. For this reason, any requirements related to **CFD simulations** must also be considered at the early stages of geometry preparation. Along with the topics discussed so far, additional CFD-specific considerations include:

- Geometry cleaning and simplification: Along with simplifying the geometry to the selected level of detail, features with very sharp angles (e.g., below 30°) should also be simplified or smoothed during geometry preparation, as they can produce highly skewed or distorted elements in the computational mesh and decrease numerical accuracy and solver stability.
- Mesh resolution and Courant–Friedrichs–Lewy (CFL) considerations: the BPGs for CFD simulations [17, 18, 21–23] recommend a certain resolution of urban features

in the computational mesh. For instance, AIJ suggests using approximately 10 cells per cube root of the building volume and applying finer grids near building corners to effectively capture flow separation zones [22]; VDI 3783 Part 9:2017 guidelines recommend having at least 3 grid points per spatial direction, and at least 5 grid points in areas with relevant flow phenomena [17], etc.

On the other hand, in transient simulations such as LES or Unsteady Reynolds-Averaged Navier–Stokes (URANS), the CFL condition links the mesh resolution, the flow velocity, and the time-step size [29]. Hence, preliminary calculations on the CFL criterion can be a good practice to define a threshold for capturing small geometric features and maintain a practical balance between accuracy, stability, and computational resource demand.

- **Analysis Considerations:** once the geometry is error-free and ready for simulation, it is essential to assess its suitability for the specific modelled phenomena and analysis type. Initial grid tests statistics, mesh quality metrics, and preliminary CFD simulations, that weren't detected in previous steps, can help avoid major changes at later design stages.

The general requirements established in this section, including the level of geometric detail and considerations specific to wind tunnel testing and CFD modelling, should ensure that the geometry preparation phase provides consistency and a sound foundation for all subsequent project activities.

3.2 Initial Data Acquisition

Key datasets for geometry creation were acquired from open sources of spatial data. The building footprints were obtained from the cadastral map of Sofia as 2D contours with attributes in .shp format. The terrain dataset was downloaded from a portal of a municipal enterprise Sofiaplan as the Digital Terrain Model (DTM) in .geotiff format. The resolution of the raster files was 1 m/px. In the absence of a drone survey, rooftop heights of buildings with flat roofs in Regions 1 and 2 and the buildings in Region 3, were derived from publicly available aerial photographs and pedestrian-level images using photogrammetric methods of geometry reconstruction. An aerial orthophoto of the study area with a resolution of 10 cm/px was also utilized.

3.3 Initial Geometry Creation

Terrain raster datasets were imported as meshes in Rhino® Grasshopper® using a plugin Heron dedicated for the integration with geospatial data. Then the terrain meshes were regularized with Quadremesh and converted to a patch surface. The resulting NURBS surface was clipped with the boundaries of the study area; thus, the solid body of the terrain was generated.

Building footprints of Region 1 from the cadastral map were draped onto the terrain and extruded. The rest of the modelling process was manual. The heights of the roofs and building details were taken from the orthophoto and site surveys. The building footprints of Region 2 were optimized beforehand using FME Form®. This step included the removal of small polygons, aggregation of groups of touching buildings, generalization

of contours, the removal of spike vertices, and manual refinements. Then the optimized 2D footprints were extruded to a rooftop level with Heron.

Once the footprints were extruded, roofs and additional details on in Regions 1 and 2 were created manually in Rhino 7. Roof and facade features were added according to the requirements related to the level of geometric detail - details larger than 1 m in full scale were added. Figure 5 shows the initial extrusion of the building footprints and the outcome of the manual construction of the roofs on a set of buildings in Region 2. Sets of buildings, touching each other as in Fig. 5, were then combined into a single object to facilitate geometry management.

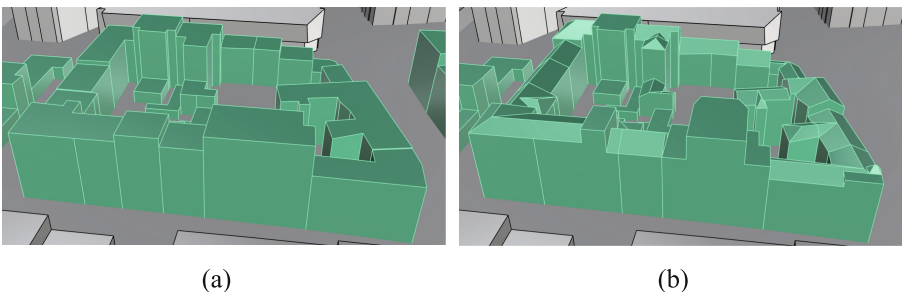


Fig. 5. Example set of buildings in Region 2 (a) before and (b) after roof creation

3.4 Geometry Cleaning

Once the initial geometry creation was completed, the .step file was exported to Ansys® SpaceClaim®, Release 2024 R2 for further cleaning and processing.

To fulfil the requirement of a flat ground surface in the scaled geometry model, the urban terrain had to be flattened, while preserving the true building elevations above ground. For this purpose, first, the footprints of all buildings extracted from Rhino were used to cut each structure at the midpoint between its highest and lowest intersection points with the terrain. This resulted in objects with horizontal bases which were then aligned on a horizontal plane at $z = 0$ m (see Fig. 6).

Next, architectural features below 1 m for Regions 1 and 2, and 2 m for Region 3, where still present, were removed. These included facade protrusions which resulted from the extrusion of footprints obtained from the cadastral map, as well as roof details in Regions 1 and 2. Additionally, small gaps less than 1 m between buildings were removed by connecting the corresponding buildings. Such modifications were made in Regions 2 and 3 where they are not expected to greatly influence the measurements in the area of interest. Finally, the geometry was checked for non-manifold vertices, extra edges, duplicate, small or non-planar faces, among other defects which may have resulted from inaccuracies in the input data, its processing, or the integration between the different tools used for geometry preparation. These checks were performed to ensure smooth and easy manufacturing and meshing processes.

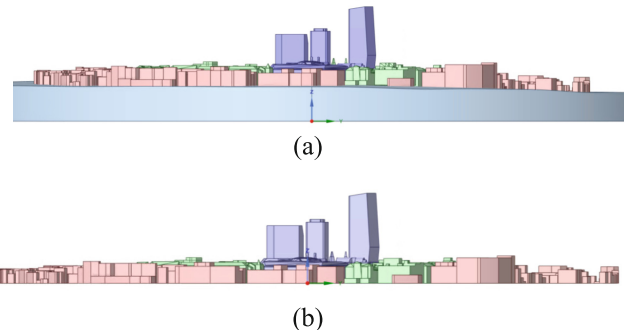


Fig. 6. Complete geometry with (a) real-world terrain and (b) idealized horizontal base.

3.5 Geometry Post-processing

The geometry preparation process concluded with post-processing related to the intended use of the model. Preliminary discretisation tests assessing the grid statistics and quality metrics were performed, as well as initial RANS simulations. Based on their results, minor geometry changes (fixing misaligned nodes at two roofs) were applied. Geometry post-processing activities, related to physical model-making, included base plate and building labelling. The final geometry was exported into a .step file as requested by the manufacturer.

3.6 Model Making

The base plate, with a diameter of 2.6 m, was made of plexiglass (PMMA). The outlines of the buildings were scored onto the base plate, along with their corresponding labels, to ensure accurate positioning and alignment. The 3D models of the buildings were printed using a Bambu Lab X1 Carbon 3D printer, featuring a high-speed CoreXY motion system and a 7 µm LIDAR-assisted first-layer inspection for precision and detail. PLA filament was used as the primary printing material, allowing for details to be printed with a resolution of up to 1 mm. The building models were then glued onto the base plate and positioned in the test section.

4 Conclusions and Next Steps

This paper presented geometry preparation for ValUr, a project which aims to establish a high-quality validation and predictive capability estimation protocols for computational wind engineering. The main purpose of reporting the geometry preparation procedure in detail is to promote consistency and reliability in future urban CFD validation efforts by enabling other researchers to replicate, adapt, and enhance the current workflow. The reasoning behind the test region selection, scaling, geometric modelling and preparation were all discussed in detail, providing the foundation for the experimental and modelling work to follow in ValUr.

Subsequent effort will concentrate on details of the experimental campaign setup and testing, the analyses of measurement data, and the validation process itself.

Acknowledgements. This work is part of the transnational access project “ERIES-ValUr”, supported by the Engineering Research Infrastructures for European Synergies (ERIES) project (www.ries.eu), which has received funding from the European Union’s Horizon Europe Framework Programme under Grant Agreement No. 101058684. This is ERIES publication number C61. The research was also supported by the GATE project funded by the Horizon 2020 WIDESPREAD-2018-2020 TEAMING Phase 2 programme under grant agreement no. 857155, the programme "Research, Innovation and Digitalization for Smart Transformation" 2021–2027 (PRIDST) under grant agreement no. BG16RFPR002-1.014-0010-C01, and the Sweden’s Innovation Agency Vinnova under Grant No. 2024-03904. The research team would like to express their sincere gratitude to Geert-Jan Maas and the rest of TU/e wind tunnel technical team, TU/e Innovation Space, and all the students who helped with the 3D printing of the scaled model of Sofia.

References

1. Castro, I., Robins, A.: The flow around a surface-mounted cube in uniform and turbulent streams. *J. Fluid Mech.* **79**, 307–335 (1977)
2. Stathopoulos, T., Baskaran, A.: Computer simulation of wind environmental conditions around buildings. *Eng. Struct.* **18**, 876–885 (1996)
3. Kubota, T., Miura, M., Tominaga, Y., Mochida, A.: Wind tunnel tests on the relationship between building density and pedestrian-level wind velocity: Development of guidelines for realizing acceptable wind environment in residential neighborhoods. *Build. Environ.* **43**, 1699–1708 (2008)
4. Bruno, L., Salvetti, M.V., Ricciardelli, F.: Benchmark on the aerodynamics of a rectangular 5:1 cylinder: an overview after the first four years of activity. *J. Wind Eng. Ind. Aerodyn.* **126**, 87–106 (2014)
5. Tominaga, Y., Stathopoulos, T.: CFD simulation of near-field pollutant dispersion in the urban environment: a review of current modeling techniques. *Atmos. Environ.* **79**, 716–730 (2013)
6. Amorim, J.H., et al.: Pedestrian exposure to air pollution in cities: modeling the effect of roadside trees. *Adv. Meteorol.* **2013**, 1–7 (2013)
7. Buccolieri, R., Sandberg, M., Di Sabatino, S.: City breathability and its link to pollutant concentration distribution within urban-like geometries. *Atmos. Environ.* **107**, 1–38 (2015)
8. Hertwig, D., Efthimiou, G.C., Bartzis, J.G., Leitl, B.: CFD-RANS model validation of turbulent flow in a semi-idealized urban canopy. *J. Wind Eng. Ind. Aerodyn.* **111**, 61–72 (2012)
9. Carpentieri, M., Robins, A.G.: Influence of urban morphology on air flow over building arrays. *J. Wind Eng. Ind. Aerodyn.* **145**, 61–74 (2015)
10. Yassin, M.F.: Impact of height and shape of building roof on air quality in urban street canyons. *Atmos. Environ.* **45**, 5220–5229 (2011)
11. Blocken, B.: Computational Fluid Dynamics for Urban Physics: Importance, scales, possibilities, limitations and ten tips and tricks towards accurate and reliable simulations. *Build. Environ.* **91**, 219–245 (2015)
12. Tominaga, Y., Stathopoulos, T.: Ten questions concerning modeling of near-field pollutant dispersion in the built environment. *Build. Environ.* **105**, 390–402 (2016)
13. Toparlar, Y., Blocken, B., Maiheu, B., van Heijst, G.: A review on the CFD analysis of urban microclimate. *Renew. Sustain. Energy Rev.* **80**, 1613–1640 (2017)
14. Aliabadi, A.A., et al.: Effects of roof-edge roughness on air temperature and pollutant concentration in urban canyons. *Bound.-Layer Meteorol.* **164**, 249–279 (2018)

15. Yazid, A.W.M., Sidik, N.A.C., Salim, S.M., Saqr, K.M.: A review on the flow structure and pollutant dispersion in urban street canyons for urban planning strategies. *Simulation* **90**(8), 892–916 (2014)
16. Sofia Municipality Report: A comprehensive programme for the improvement of the quality of atmospheric air in Sofia Municipality for the period 2021–2026 (2020). (in Bulgarian)
17. VDI 3783: Part 9, Environmental meteorology - Prognostic microscale wind field models - Evaluation for flow around buildings and obstacles, Berlin, Germany, 2017
18. Franke, J., Hellsten, A., Schlünzen, H., Carissimo, B.: Best practice guideline for the CFD simulation of flows in the urban environment: COST action 732 quality assurance and improvement of microscale meteorological models (2007)
19. ASCE 49-21: Wind tunnel testing for buildings and other structures (2021)
20. VDI 3783 Part 12: Physical modelling of flow and dispersion processes in the atmospheric boundary layer – application of wind tunnels, Berlin, Germany (2000)
21. Franke, J., et al.: Recommendations on the use of CFD in wind engineering. In: Proceedings of the International Conference on Urban Wind Engineering and Building Aerodynamics (2004)
22. Tominaga, Y., et al.: AJJ guidelines for practical applications of CFD to pedestrian wind environment around buildings. *J. Wind Eng. and Ind. Aerodyn.* **96**, 1749–1761 (2008)
23. Casey, M., Wintergerste, T.: ERCOFTAC Special Interest Group on “Quality and Trust in Industrial CFD”: Best Practice Guidelines, ERCOFTAC (2000)
24. Bartzis, J.G., Vlachogiannis, D., Sfetsos, T.: Thematic area 5: Best practice advice for environmental flows. *QNET-CFD Netw. Newslett.* **2**, 34–39 (2004)
25. Eurocode 1: Actions on structures - Part 1–4: General actions - Wind actions
26. Blocken, B., Stathopoulos, T., Carmeliet, J.: CFD simulation of the atmospheric boundary layer: wall function problems. *Atm. Environ.* **41**, 238–252 (2007)
27. Pantusheva, M., Mitkov, R., Hristov, P.O., Petrova-Antanova, D.: Air pollution dispersion modelling in urban environment using CFD - a systematic review. *Atmosphere* (2022)
28. Biljecki, F., Ledoux, H., Stoter, J.: An improved LOD specification for 3D building models. *Comput. Environ. Urban Syst.* **59**, 25–37 (2016)
29. Courant, R., Friedrichs, K., Lewy, H.: Über die partiellen Differenzengleichungen der mathematischen Physik. *Math. Ann.* **100**, 32–74 (1928)

Open Access This chapter is licensed under the terms of the Creative Commons Attribution 4.0 International License (<http://creativecommons.org/licenses/by/4.0/>), which permits use, sharing, adaptation, distribution and reproduction in any medium or format, as long as you give appropriate credit to the original author(s) and the source, provide a link to the Creative Commons license and indicate if changes were made.

The images or other third party material in this chapter are included in the chapter's Creative Commons license, unless indicated otherwise in a credit line to the material. If material is not included in the chapter's Creative Commons license and your intended use is not permitted by statutory regulation or exceeds the permitted use, you will need to obtain permission directly from the copyright holder.





The VORSEA Wind Tunnel Experiments

Olivier Flamand¹(✉), Andi Xhelaj², Andrea Orlando², Alessio Torrielli³,
and Alessandro Giusti³

¹ CSTB, Nantes, France

olivier.flamand@cstb.fr

² Department of Civil, Chemical and Environmental Engineering,
University of Genoa, Genoa, Italy

³ Siemens Gamesa Renewable Energy A/S, Brande, Denmark

Abstract. When preparing the installation of offshore wind turbines, the towers (cylindrical masts of large height supporting the hub and rotating blades) are first stored on harbor quayside and then moved on a special vessel for on-site installation. The possible vortex-induced vibration excitation of towers by wind is a main concern for the handler, leading to additional dampers need which are a source of expenditure and risks. The interest of the wind energy industry towards the response of finite-length circular cylinders encouraged recent research works on gust buffeting (e.g., Mannini et al., 2023) and vortex shedding (e.g., Kurniawati et al., 2024) aimed to clarify subject matters where design standards lack information; however, many aspects are still missing as a clear understanding of how the aerodynamic loads evolve from subcritical to supercritical Reynolds number regimes and the influence on wind-induced vibrations of the movement of the base of the tower associated with the motion of the vessel during navigation. These wind tunnel experiments aim to investigate vortex shedding on finite-length circular cylinders. The geometry is compatible with real cases of the wind energy industry and Reynolds numbers from subcritical to supercritical regimes are investigated with focus on aerodynamic loads and the effect of the tilting movement of the base.

Keywords: finite-length circular cylinders · aerodynamic coefficients · high Reynolds number regime · vortex induced vibration · rolling base

1 Experimental Setup

The study focuses on vortex shedding on towers (without rotor-nacelle assembly) of offshore wind turbines during sea transit, and it aims to investigate the development of vortex shedding and aerodynamic loads from subcritical to supercritical Reynolds number regime and the influence of the base movement due to the motion of the vessel during navigation. The study is addressed by wind tunnel tests carried out at the Centre Scientifique et Technique du Bâtiment (CSTB), Jules Verne facility. The test setup consists of three main parts (see Figs. 1 and 2), namely (a) the tilting table reproducing a vessel-like motion; (b) the base collar, which concentrates the bending stiffness

at the base of the cylinder (pivot model); (c) the finite-length cylinder equipped with accelerometers and/or pressure taps; in some tests it is combined with a dummy cylinder to investigate the case of two cylinders in tandem. The model consists of a parallel sided aluminum cylinder of about 3.20 m in height and 0.36 m in diameter, and it has a geometry equivalent to a split tower, i.e., corresponding to the case when the wind turbine tower is vertically transported divided in two parts, namely bottom half and top half. By contrast, the modeling of a full tower would have required either a taller wind tunnel or a smaller diameter, with the consequent reduction of the maximum Reynolds number achievable in the experiments. The cylinder is connected through the base collar to the titling table, placed on the floor of the wind tunnel. The titling table is meant to apply to the cylinder the motion given by the rolling of the installation vessel, to study the influence of such a source of interaction with vortex shedding. The rolling is fixed at $\pm 3^\circ$, whereas the frequency is changed across the tests from a minimum of 0.70 Hz to a maximum of 1.50 Hz (see Table 1), besides the case of fixed tilting table, i.e., no roll motion. A wind tunnel blockage ratio of about 8.7% is estimated, considering a 6 m x 5 m working section. Along with the 200 pressure taps distributed on 8 rings, the measuring cylinder is equipped with a 3D accelerometer mounted at the top of the cylinder. In addition, another accelerometer is also connected to the tilting table.

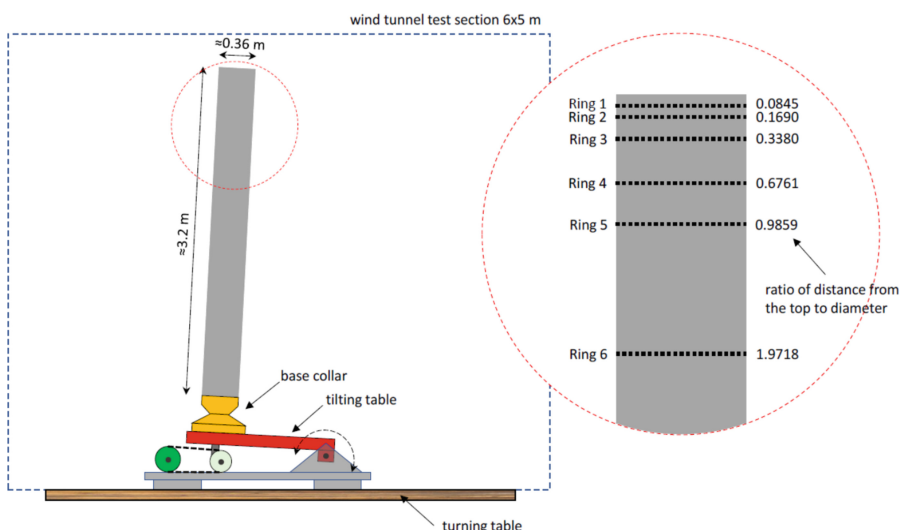


Fig. 1. Sketch of the wind tunnel setup.

Three phases of measurements are carried out to cover different Reynolds number regimes (see Table 1). High-velocity measurements of Phase 2 and Phase 3 require scanners with high-pressure range, reducing to 63 the number of active pressure taps due to the channel availability of such scanners. All tests are performed in uniform flow, low turbulence intensity and with the tilting table turned either off or on, the latter to introduce a vessel-like motion.



Fig. 2. Wind tunnel setup with one isolated cylinder mounted on the tilting table.

In Phase 1 seven pressure scanners from Pressure System Incorporated, model 32RG-010300000, with a pressure range of ± 2500 Pa and a sampling rate of 200 Hz, are used. The output was checked with a pressure calibrator; the sensitivity of each channel was used in the recording software to provide outputs in Pa. In Phase 2 and Phase 3 two pressure scanners from Pressure System Incorporated, model ESP-32HD, with a pressure range of ± 7000 Pa and a sampling rate of 200 Hz are used.

During Phase 1 and Phase 3 accelerations at the top of the cylinder are measured by means of PCB Piezotronics 3 components accelerometer model 356A03, with the sensitivity of each channel directly used by the recording system to provide measurements in m/s^2 . The output was checked with a calibrator from B&K providing a $10\ m/s^2$ acceleration at 159 Hz. The sampling rate is 300 Hz.

2 Results from Analysis of the Pressure Taps

Some results of the measurements taken in Phase 3, Phase 1 and Phase 2.A (Table 1) are presented hereafter with focus on pressure patterns (average and standard deviation) and the corresponding aerodynamic coefficients (average and spectra), limited to the case of setup with one cylinder. In this phase of the experiments (see Table 1), flow velocities from 10 m/s to 70 m/s are explored and three different tilting scenarios are investigated, namely fixed tilting table, 1.04 Hz and 1.40 Hz rolling frequency.

2.1 The Influence of Increasing Wind Speed at Various Distances to the Tip

The evolution of pressure distribution patterns around the cylinder at different heights and Reynolds numbers provides significant insight into the flow behavior. Figure 4

Table 1. Tests performed in the three different phases of the wind tunnel campaign. The notation $a:b:c$ provides the lower bound a and the upper bound c of the interval, and the step b .

Phase	Number of cylinders	Rolling frequency	Angle of attack	Flow velocity	Pressure	Accel
(-)	(-)	(Hz)	(deg)	(m/s)	(-)	(-)
1.A	1	0.00	0.0	22:1:40	yes	yes
1.B	1	0.00	7.2	22:1:38	yes	yes
1.C	1	0.00	43.2	22:1:38	yes	yes
1.D	1	0.00	86.4	22:1:38	yes	yes
1.E	1	1.74	0.0	22:1:38	yes	yes
1.F	1	0.7:0.1:1.5	0.0	38	yes	yes
1.G	1	0.7:0.1:1.5	-10.0	38	yes	yes
1.H	1	0.7:0.1:1.5	-43.2	38	yes	yes
1.I	1	0.7:0.1:1.2	-90.0	38	yes	yes
2.A	1	0.00*)	0.0	5: \approx 5:70	yes	no
3.A	1	0.00	0.0	10:2:70	yes	yes
3.B	1	1.04	0.0	10:2:70	yes	yes
3.C	1	1.40	0.0	40:2:70	yes	yes
3.D	2	0.00	0.0	40:2:70	yes	yes
3.E	2	0.00	7.2	40:4:68	yes	yes
3.F	2	0.80	0.0	40:4:68	yes	yes
3.G	2	0.80	7.2	40:4:68	yes	yes

(*) In this phase the cylinder is directly connected to the wind tunnel floor without the tilting apparatus.



Fig. 3. Detail of the tilting table and of the sensor installation from the top of cylinder.

presents the mean pressure distribution from Phase 3.A (fixed support condition) for Rings 2, 4, and 6 at five Reynolds numbers ranging from 2.59×10^5 to 1.68×10^6 . A clear influence of the cylinder's free end is observed in this pressure distributions. The pressure pattern at Ring 2, positioned close to the top ($d_i/D = 0.1690$), where d_i/D is the ratio distance from the top to diameter, show limited variation with increasing Reynolds number. This suggests that the flow characteristics near the free end are dominated by tip effects rather than the Reynolds number effects. In contrast, at Ring 6, located further from the tip ($d_i/D = 0.19718$), the pressure distribution evolves significantly with Reynolds number, following trends similar to those reported by Achenbach (1968) for sectional models. The transition from subcritical to supercritical flow regimes is clearly visible in the pressure distribution, particularly at positions farther from the tip (Fig. 3).

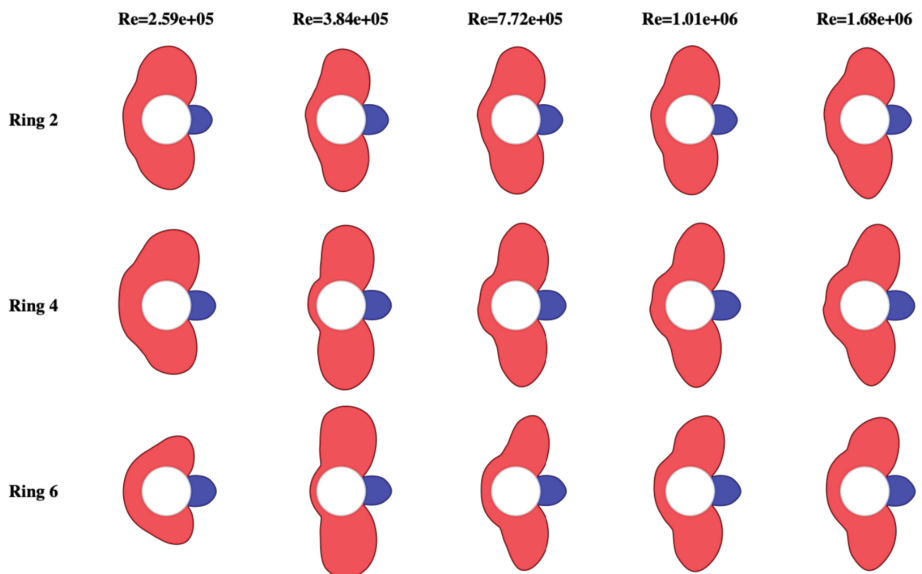


Fig. 4. Mean pressure distribution patterns at different heights and for different Reynolds numbers. For the position of the Rings see the close-up in Fig. 1.

Integration of the pressure measurements form Phases 3.A and 2.A (See Table 1) provides the mean aerodynamic coefficients at different heights along the cylinder. Figure 5 presents the mean drag coefficient and the standard deviation of the lift coefficient as functions of Reynolds numbers for Rings 2,4 and 6. The mean drag coefficient (Fig. 5a) shows a distinct increase when moving toward the top of the cylinder. Ring 2, closest to the free end, exhibits concisely higher mean drag values than Ring 6. Note that Ring 6 is the only one in common with both Phase 3.A and 2.A. This trend aligns with observation reported by Mannini et al. (2023). Ring 6 located approximately two diameters from the top, displays values that closely match those in literature for sectional models (Adachi 1997). The transition from critical to supercritical Reynolds regime (Fig. 5a) in Ring 6 obtained in Phase 2.A seems delayed compared to Phase 3.A. This might be due to an inaccuracy in the estimation of the aerodynamic coefficient due to suppressed pressure

taps in Phase 3.A. The standard deviation of the lift coefficient (Fig. 5b) reveals another interesting phenomenon. The proximity to the cylinder's free end appears to reduce the variability of the lift coefficient's standard deviation with Reynolds number, particularly in the supercritical regime. While Ring 6 shows significant variation across the tested Reynolds number range for both phase 3.A and 2.A. Ring 2 maintains more consistent values after the critical region. Additionally, although not shown in the figures for brevity, the average lift coefficient is not zero in the critical Reynolds number regime, regardless of the ring position. This provides evidence of bi-stable flow phenomena and separation bubbles, as documented in previous literature (Buresti, 2012).

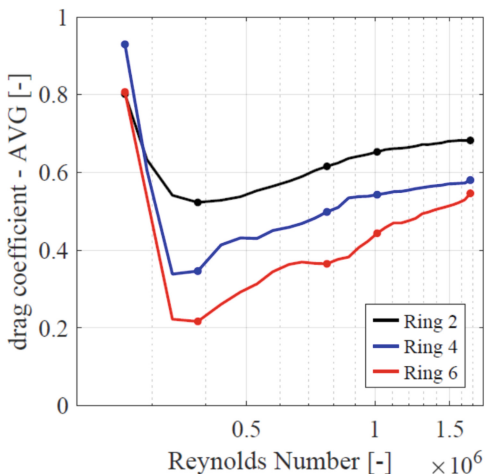


Fig. 5. Mean aerodynamic coefficients at different heights of the cylinder.

Analysis of the fluctuating loads at each height provides insights into the frequency characteristic of vortex shedding, expressed by the Strouhal number. Figure 6 illustrates the changes in Strouhal number with distance from the tip and Reynolds number under different tilting configurations: fixed support (Phase 3.A), 1.04 Hz rolling frequency (Phase 3.B), and 1.40 Hz rolling frequency (Phase 3.C). Also in this case, from PSDF analysis point of view of the lift coefficient, a notable tip effect is observed. The region close to the cylinder summit experiences periodic excitations in the across wind direction at a reduced frequency lower than that predicted by design codes (here a citation of the Eurocode is needed). The Strouhal number approaches the typical value of approximately 0.18 only at a distance of about 1 to 2 diameters from the top. Interestingly, this phenomenon appears unaffected by the tilting movement of the support.

While most aerodynamic coefficient results analyzed in this work come from Phases 2 and 3, a more comprehensive understanding of coherent flow structures was obtained through Principal Component Analysis (PCA) performed on Phase 1 data. Phase 1 measurements provided superior spatial resolution with all 8 rings of pressure taps active (200 taps total), compared to the limited spatial coverage in Phase 2 (2 rings, 25 taps each) and Phase 3 (3 rings, 21 taps each).

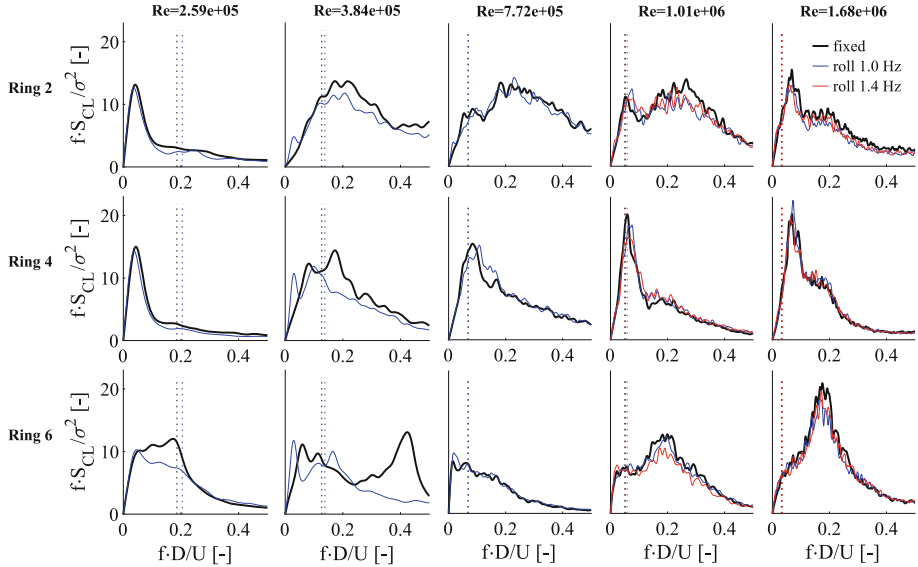


Fig. 6. Changes in the Strouhal number with distance to the tip and Reynolds number, in three tilting configurations. For the position of the Rings see the close-up in Fig. 1. The vertical dashed lines mark the cylinder natural frequency of vibration estimated via acceleration measurements.

Figure 7 shows the first modes of pressure fluctuation derived from the PCA. The results reveal two distinct flow structures: one associated with the cylinder tip and another with mid-span flow-structure interaction. Notable observations include:

1. A clear two-cell structure in the upper portion (2.5-3m height), characterized by alternating positive (red/yellow) and negative (blue) pressure fluctuations, indicating organized vortex structures near the tip.
2. Significant frequency dependence, with pressure fluctuations primarily concentrated in the upper region at lower reduced frequencies ($\text{fred} = 0.050, 0.056$) and extending to lower portions at higher frequencies ($\text{fred} = 0.199$).
3. Confirmation that flow physics up to approximately two diameters from the top is predominantly governed by tip effects, explaining the differences in aerodynamic coefficients between rings near the tip versus those further down.

The PCA results clearly demonstrate how the free-end significantly influences the overall flow characteristics around the cylinder, with important implications for predicting vortex-induced vibrations and aerodynamic loads on structures like wind turbine towers during transportation and installation.

3 Results from Analysis of the Vibrations

The analysis of the evolution of lateral vibration amplitude with the different parameters (wind speed, structural damping, circularity of the cylinder) provides interesting inputs. The operational modal analysis provides modal frequency and modal damping from a

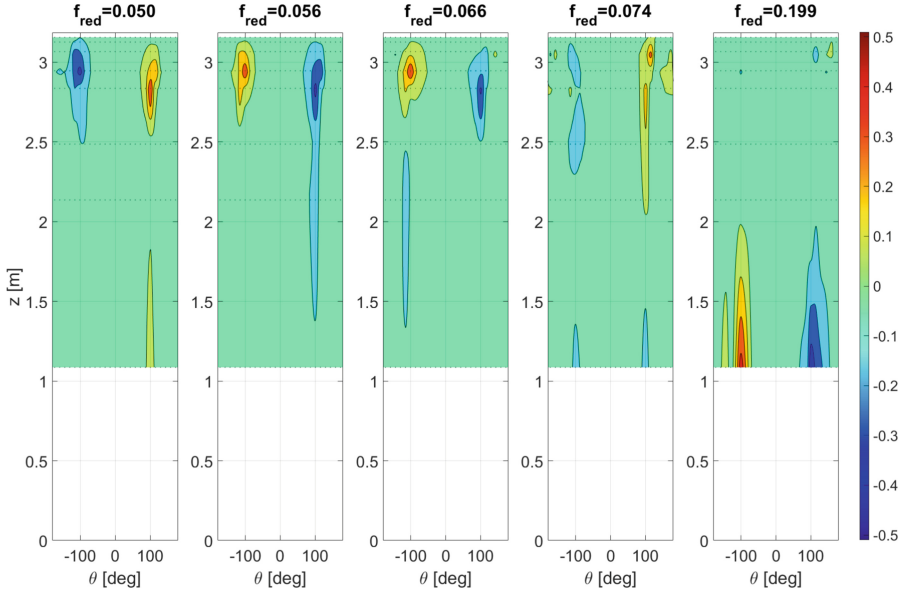


Fig. 7. First mode of the fluctuating part of the pressure coefficient at 40 m/s (Phase 1.A), issued from Dynamic Principal Component Analysis

response signal with an unknown white noise excitation. Applying it to the dynamic response of the cylinder at various wind speeds shows (see Fig. 8) a drop of the modal damping above a threshold close to 15 m/s is observed.

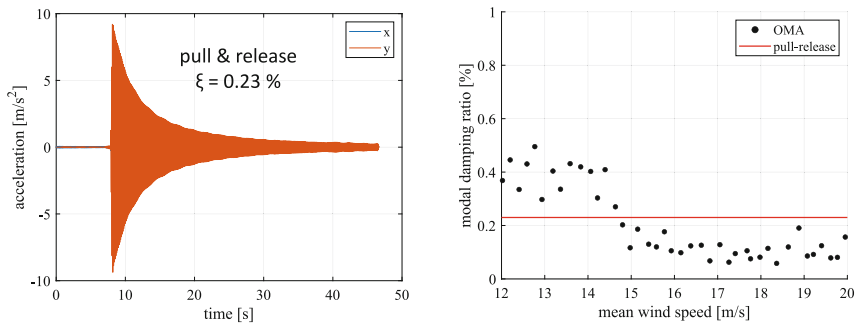


Fig. 8. Acceleration record of a pull and release test (left) and damping estimates via operational modal analysis (OMA) at different wind speeds (right).

The lateral aerodynamic damping in case of turbulent flow, predicted from literature (reflected in the solid blue line in Fig. 9), is expected to increase the total damping by a positive participation; this can be seen at flow speed lower than 15 m/s. However, for speed above this threshold, the dropping of the OMA damping below the mechanical one, suggests the rising of a negative aerodynamic damping. Such a velocity is suspected

to be the critical flow speed for the synchronization of the frequency of vortex shedding with the natural frequency of the cylinder (lock-in). Nevertheless, this point must be widely explored.

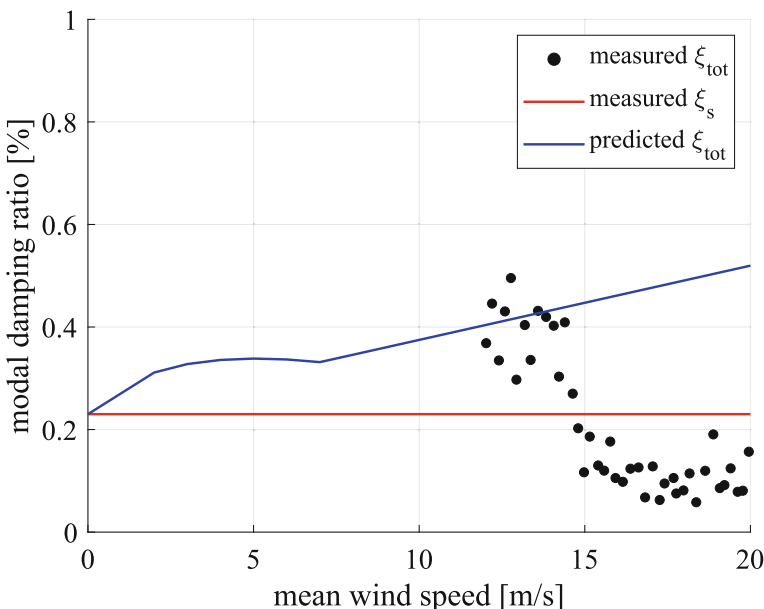


Fig. 9. Comparison of measured damping with predicted one (including aerodynamic damping from literature in case of turbulent flow)

Acknowledgements. This work is part of the transnational access project “ERIES-VORSEA”, supported by the Engineering Research Infrastructures for European Synergies (ERIES) project (www.erries.eu), which has received funding from the European Union’s Horizon Europe Framework Programme under Grant Agreement No. 101058684. This is ERIES publication number C66.

References

- Ellingsen, Ø.M.: Vortex-induced vibrations on industrial chimneys. École doctorale de l’Institut Polytechnique de Paris (EDIPP) (2021)
- Giusti, A., Xhelaj, A., Orlando, A., Torrielli, A., Flamand, O.: Wind tunnel investigation of aerodynamic loads of circular cylinders from subcritical to supercritical Reynolds number regime. In: Proceedings of the 9th European-African Conference on Wind Engineering (EACWE 2025). Trondheim, Norway (extended abstract) (2025)
- Kurniawati, I., Lupi, F., Seidel, M., Niemann, H.-J., Höffer, R.: Vortex shedding load on a full-scale wind turbine tower at transcritical Reynolds numbers. J. Wind Eng. Ind. Aerodyn. **252**, 105821 (2024)

- Livanos, D., et al.: An enhanced analytical calculation model based on sectional calculation using a 3D contour map of aerodynamic damping for vortex induced vibrations of wind turbine towers. *Wind Struct.* **38**, 445–459 (2024)
- Mannini, C., Massai, T., Giachetti, A., Giusti, A.: Aerodynamic loads on groups of offshore wind turbine towers stored on quaysides during the pre-assembly phase. *J. Wind Eng. Ind. Aerodyn.* **242**, 105569 (2023)
- Aerodynamic loads on wind turbine towers arranged in groups with and without helical strakes. Proceedings of the XVII Conference of the Italian Association for Wind Engineering – INVENTO 2022, Milan, Italy, pp. 260–269 (2024)
- Torrielli, A., Giusti, A.: Uncertainties in the response of tower-like structures to wind gust buffeting. *J. Wind Eng. Ind. Aerodyn.* **236**, 105404 (2023)
- Torrielli, A., Orlando, A., Xhelaj, A., Giusti, A., Flamand, O.: Vortex shedding of circular cylinders mounted on a rolling support at different Reynolds number regimes. In: Proceedings of the 9th European-African Conference on Wind Engineering (EACWE 2025), Trondheim, Norway (extended abstract) (2025)
- Achenbach, E.: Distribution of local pressure and skin friction around a circular cylinder in cross-flow up to $Re = 5 \times 10^6$. *J. Fluid Mech.* **34**, 625–639 (1968)
- Buresti, G.: Elements of Fluid Dynamics. Imperial College Press (2012)
- Adachi, T.: Effects of surface roughness on the universal Strohal number over the wide Reynolds number range. *J. Wind Eng. Ind. Aerodyn.* **69–71**, 399–412 (1997)

Open Access This chapter is licensed under the terms of the Creative Commons Attribution 4.0 International License (<http://creativecommons.org/licenses/by/4.0/>), which permits use, sharing, adaptation, distribution and reproduction in any medium or format, as long as you give appropriate credit to the original author(s) and the source, provide a link to the Creative Commons license and indicate if changes were made.

The images or other third party material in this chapter are included in the chapter's Creative Commons license, unless indicated otherwise in a credit line to the material. If material is not included in the chapter's Creative Commons license and your intended use is not permitted by statutory regulation or exceeds the permitted use, you will need to obtain permission directly from the copyright holder.





Wet-Snow Accretion on Overhead Conductors: Experimental Study in a Climatic Wind Tunnel

Francesca Lupi¹ , Erick Ulloa Jimenez², Norbert Hoelscher¹ , Susanne Diburg¹, Jean-Paul Bouchet³ , Bruno Gauducheaum³, Philippe Delpech³ , and Olivier Flamand³

¹ Niemann Ingenieure, Bochum, Germany

Lupi@niemann-ing.de

² Amprion GmbH, Dortmund, Germany

³ Centre scientifique et technique du bâtiment CSTB, Nantes, France

Abstract. The estimation of ice loads is essential for assessing the structural reliability of transmission lines. A probabilistic approach requires the numerical simulation of ice load time histories, derived from meteorological data using empirical models available in the literature, such as the Makkonen model. By analyzing annual extreme values, the risk of structural failure can be quantified for a given probability of occurrence. Ice accretion on conductors can result from various processes, depending on the prevailing meteorological conditions. These processes are typically classified into in-cloud icing, freezing rain, and wet snow accretion. Among these, wet snow accretion is particularly critical due to its relatively high probability of occurrence at altitudes above 600 m, combined with the considerable masses of ice it can generate. To improve the understanding, validate, and extend existing ice load models, a series of experiments was performed on a conductor specimen in the Jules Verne climatic wind tunnel at the CSTB facility in Nantes, France. The experiments focused on wet snow accretion, systematically varying key ambient parameters. The liquid water ratio of snow particles plays a crucial role in determining whether the accretion is light and dry or, conversely, heavy and wet. The first set of experiments investigated the accreted ice mass and shape on a non-rotating conductor for different snow qualities, ranging from drier to wetter snow. Subsequently, the effect of axial rotation of the conductor was examined under the most unfavorable snow condition. Finally, the influence of wind direction on snow accretion was also evaluated and discussed.

Keywords: Wet Snow Accretion · Ice Load Modelling · Climatic Wind Tunnel · Transmission Lines · Overhead Conductors

1 Introduction

Extreme weather events caused by wind and snow have led to several significant structural failures in high-voltage transmission networks. This has raised the critical question of how to reliably assess the actual risk, particularly for existing transmission lines exposed to natural hazards such as wind, snow, and ice. To quantify this risk, an extreme

value statistical analysis can be carried out, provided that ice loads can be realistically estimated based on meteorological data. Theoretical models have been developed in the literature such as the widely used Makkonen model (see [2, 3, 9–11]). However, these models only rely on available meteorological data, which are often limited, incomplete, or do not fully capture the wide range of influencing parameters. Ice load measurements themselves are rare and scattered, due to the inherent uncertainty and scarce availability of measured meteorological parameters. As a result, existing predictive models often provide simplified and largely approximate estimates of ice loads, which may deviate significantly from actual ice events observed in practice.

Recent studies by network operators have brought significant advancements in calculation procedures using long-term weather data [6]. These are based on adaptation of the original Makkonen model to incorporate line-specific influencing factors. Among these, the angle between the overhead line and the prevailing wind direction is a key determining factor of ice loads during icing events. The most uncertain parameter remains the liquid water content. This can be roughly estimated using visibility measurements, which are routinely reported by meteorological stations. However, the uncertainty of such records is extremely high and full-scale validation extremely difficult.

As described in [6], there is a clear correlation between the duration of icing events and the altitude of the location where they occur. As expected, higher elevations tend to experience longer periods of ice accumulation. In Germany, in-cloud icing (often referred to as atmospheric icing) is the dominant process at higher altitudes, whereas wet snow accretion is more common at lower elevations. Freezing rain, on the other hand, requires very specific conditions - typically a temperature inversion near the ground - and can only occur in a limited number of suitably exposed locations. Consequently, its overall incidence is significantly lower compared to in-cloud icing and wet snow accretion.

Extensive research on ice accretion has been conducted in the literature, particularly for bridge cables and wind turbine blades. For bridge cables, a key aspect is assessing the susceptibility of the iced cross-section to galloping. This phenomenon, however, is of secondary importance for transmission lines, primarily due to their bundled conductor arrangement, which significantly increases the stiffness. In the case of isolated lines, galloping could become relevant, but this is typically mitigated during the design phase by locally increasing the mass of the line to prevent aeroelastic instability within the expected range of wind velocities.

Given the extensive coverage of transmission networks at the national scale, prediction accuracy is of primary importance for network operators. Ice load models must not only be conservative, but also as realistic as possible, to ensure that maintenance and retrofitting activities can be prioritized at affordable costs based on realistic and reliable criteria.

In response to these needs, significant efforts have been made in recent years to replicate and investigate the physical processes governing ice accretion on overhead cables in climatic wind tunnels under controlled experimental conditions. Preliminary results from these studies have already been presented in [7, 8].

This paper presents a detailed analysis of the experimental campaign on wet snow accretion conducted on a full-scale conductor specimen in the Jules Verne climatic wind tunnel at the CSTB facility in Nantes, France. First, a brief review of existing predictive

ice models is provided in Sect. 2. The experimental setup and methodology are then described in Sect. 3, followed by a discussion of the results in Sect. 4.

2 Predictive Models for Wet Snow Accretions

The basic equation for ice accretion described in the International Organization for Standardization [5] is:

$$\frac{dM}{dt} = \alpha_1 \cdot \alpha_2 \cdot \alpha_3 \cdot V \cdot LWC \cdot D \quad (1)$$

dM represents the accumulated snow mass per unit length during the time step dt . The parameter α_1 denotes the collision efficiency, i.e., the fraction of snow particles that impact the model compared to the total number of approaching particles. α_2 represents the sticking efficiency, which describes the fraction of snow particles that adhere to the cylinder upon collision, rather than bouncing off. Finally, α_3 denotes the accretion efficiency, indicating the fraction of the sticking particles that contributes to ice accretion, without dripping off the object as liquid water (run-off). V is the wind speed in [m/s], LWC is the snow content in the air in [g/m^3] and D is the diameter of the conductor in [m].

Three main factors govern the rate of wet snow accretion: the precipitation rate (i.e., the snow content in the air, represented by the Liquid Water Content, LWC), the wind speed (V), and the liquid water fraction of the snow (i.e., the Liquid Water Ratio, LWR). In particular, the wind speed affects the density of the accumulated snow. Higher impact velocities of snowflakes result in a more compact and denser snow deposit. The LWR is related to the sticking efficiency α_2 . The most favorable conditions occur when partially melted snowflakes collide with the conductor and adhere to its surface upon impact. At a certain LWR, the adhesive forces of the wet snow reach a maximum. As LWR further increases above this threshold, the physical phenomenon progressively changes to freezing rain.

The primary challenge in developing predictive models for wet snow accretion stems from the fact that key governing parameters - particularly the mass concentration of falling wet snow (LWC) and the liquid water ratio (LWR) of snowflakes - are not directly or routinely measured by meteorological stations [13]. To some extent, these parameters can be inferred from standard weather data, such as precipitation rate, visibility, air temperature, and humidity. However, due to the complexity of the phenomenon and the inherent scarcity and uncertainty of meteorological data, existing models for wet snow accretion remain highly simplified. For instance, one of the most commonly used parameterizations for α_2 is a simple inverse relationship with wind speed, as proposed by Admirat [1]:

$$\alpha_2 = \frac{1}{V} \quad (2)$$

This relationship is physically questionable because it assigns units to one of the α -coefficients, thereby removing the influence of wind speed from the total accretion rate in Eq. (1). However, despite its simplifications, this expression remains a widely

accepted theory for the sticking efficiency of wet snow and is adopted in the international standard for atmospheric icing [5]. Here, the other coefficients α_1 and α_3 are typically set to one for wet snow accretion.

A more advanced approach to modeling wet snow accretion parameters (α_1 , α_2 and α_3) involves direct numerical simulations of particle trajectories. This method has been applied in Vigano [14, 15], where the sticking efficiency is determined as a function of the particle's impact angle on the surface. Additionally, the study highlights the influence of liquid water content on sticking efficiency, as the liquid phase within the particles enhances adhesion.

3 Experiments in the Climatic Wind Tunnel

Wet snow accretion on a conductor specimen is simulated in the CSTB climatic wind tunnel (“Thermal” circuit) in Nantes, France. This facility can reproduce various weather conditions (see, for instance, [12, 14, 15]). For the present experiment, the air temperature is varied between $-10\text{ }^{\circ}\text{C}$ and $-2\text{ }^{\circ}\text{C}$, with a constant wind speed set to 10 m/s. The turbulence intensity of the chamber with only air flow is about 5% [14]. The test section of the thermal unit measures 21 m in length, 10 m in width, and 7 m in height. A snow gun is positioned 10 m upstream of the test location (see Fig. 1) and in a reversed position with respect to the flow direction. Artificial snow is generated by mixing water and air at high pressure (6 to 10 bar). This two-phase mixture is then expelled at high speed (80 to 100 m/s) through an orifice. The injected water droplets (with a median volume diameter of 250 microns [14]) enter the air stream at approximately $+1\text{ }^{\circ}\text{C}$. As soon as they encounter the cold airflow, they begin to freeze. Depending on the air temperature set in each experiment, the particles are partially frozen when they impact the conductor.

Figure 2 shows the test bench with the 2 m long section of a 1:1 real conductor, suspended and pre-stressed using 2 mm diameter, 1.6 m long piano-wires. The diameter and the length of the piano-wires are designed to replicate the torsional stiffness of a typical 300–400 m long span transmission line. To ensure proper horizontality, the conductor's natural sag due to self-weight and manufacturing tolerances is eliminated by applying a prestressing force of 2300 N.

Axial rotation is enabled by a low-friction bearing (Fig. 3, left). The figure also depicts two unidirectional force sensors, positioned at each end of the conductor, measuring horizontal and vertical forces (K6D40 with ranges of 20 N and 50 N, respectively). Additionally, a unidirectional force sensor (ZFA, range 5000 N, not shown in the figure) is used to measure the prestressing. Figure 3 (right) illustrates the Ri-QR24 encoder, which tracks the axial rotation angle when the conductor rotates freely under the influence of eccentric ice accretion.

Table 1 provides an overview of the wind tunnel tests, which were conducted at a constant wind speed of 10 m/s while varying the air temperature. The temperature ranged from $-10\text{ }^{\circ}\text{C}$ (Icing Test 1) to $-2\text{ }^{\circ}\text{C}$ (Icing Test 3). The air temperature in each experiment played a crucial role in determining the freezing behavior of airborne particles. By maintaining a constant wind speed and keeping the snow gun at a fixed distance from the conductor, air temperature remained the sole variable influencing the Liquid Water Ratio (LWR) of the particles and, consequently, the snow's sticking efficiency.

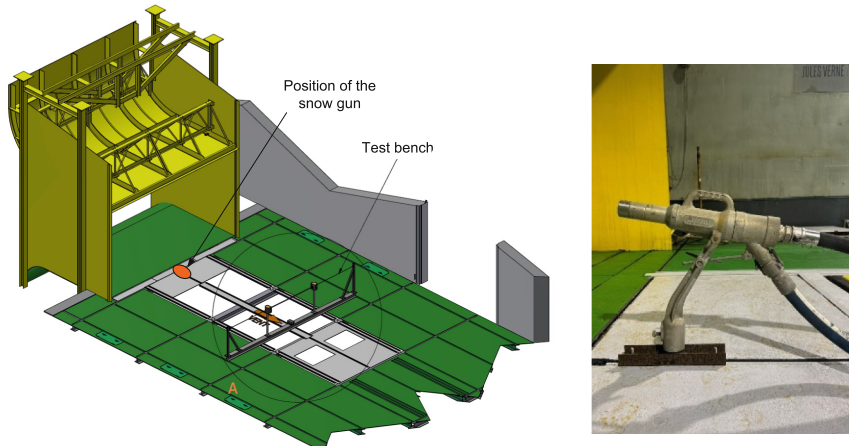


Fig. 1. Climatic wind tunnel, position of the snow gun and of the test bench



Fig. 2. Test bench and specimen of the conductor

The Icing Tests No. 1 and 2 were conducted at low temperatures (-10°C and -8°C), reproducing very dry snow at specimen level. Under these conditions, the Liquid Water Ratio (LWR) was low (approximately 0.1), resulting in minimal accretion (Fig. 4). After one hour, the ice mass per unit length remained below a few hundred grams. In contrast, Icing Test No. 3 was performed at a significantly higher temperature (-2°C), where the snow was so wet that its larger particles were already in a freezing rain state upon impact with the conductor. This was evidenced by the formation of icicles (Fig. 5). Icing Test No. 4 was carried out at -4°C , leading to wet snow accretion. Given the significant difference in snow quality between Icing Test 3 (-2°C) and Icing Test 4 (-4°C), an additional test at an intermediate temperature (-3°C) was conducted (Icing Test 5). This condition proved to be optimal for generating the largest ice accretion. Due to the substantial ice buildup in Icing Test No. 5, the screws failed to hold, causing the conductor to axially rotate. As a result, this test was repeated at the end of the experimental campaign (Icing Test No. 8, see Fig. 6), ensuring that the conductor remained stable throughout the test duration.

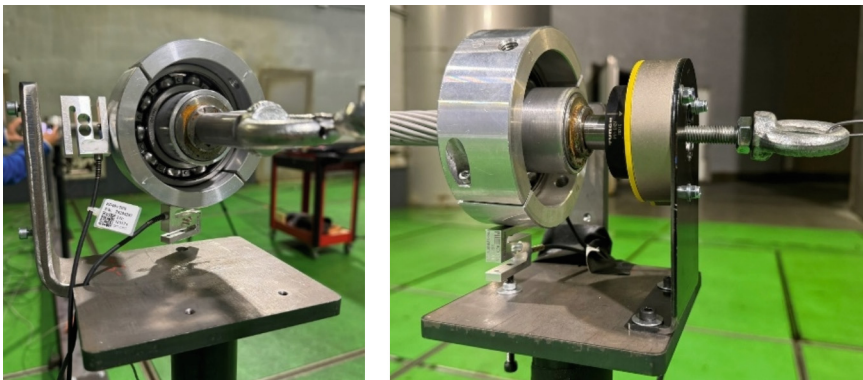


Fig. 3. Low-friction bearing for freely rotating conductor (left) and contact encoder to measure the angle of axial rotation of the conductor (right)

To examine the effect of free rotation, Icing Tests No. 6 and 7 were carried out at -3°C . In all tests, the conductor was positioned perpendicular to the flow (wind direction 90°), except in Icing Test No. 7, where the wind direction was set to 60° (Fig. 7).

4 Results and Discussion

The Liquid Water Ratio (LWR), defined as the ratio of the liquid part in partially frozen snow particles to their total mass, is the key parameter in this investigation. It directly affects the snow's sticking efficiency. The LWR is a dimensionless quantity ranging from 0 to 1. Low LWR values correspond to dry snow, while high values indicate wet, highly adhesive snow. At the upper limit, $\text{LWR} = 1$, the particles consist entirely of supercooled droplets - liquid droplets that remain unfrozen until the impact with the conductor, as observed in freezing rain.

In the wind tunnel, water particles in the liquid state ($\text{LWR} = 0$) are expelled from the snow gun at a temperature slightly above 0°C . These particles are carried by the wind through the cold environment, where they partially freeze in flight. Since both the wind speed (10 m/s) and the flight path length (10 m) are fixed parameters in this investigation, the only factor influencing the degree of freezing before impact is the air temperature. Depending on the air temperature set for each experiment, the particles freeze to varying extents, resulting in a specific LWR at the moment of impact with the model.

Figure 8 illustrates the effect of LWR on the accumulated ice mass per meter over a 1-h period. The LWR values shown in the figure represent the average for each experiment, as listed in Table 1. As expected, the accumulated ice mass is minimal for dry snow ($\text{LWR} \leq 0.15$). With the increasing LWR, the accumulated mass rises rapidly in a nearly linear trend, reflecting higher sticking efficiency. However, at sufficiently high LWR values, the slope of the accumulation curve decreases. This change in slope indicates the onset of run-off effects, which are further confirmed by the visual observation of icicle formation (see Fig. 5).

Table 1. Outline of the wind tunnel tests and results

Icing Test No	Unit	1	2	3	4	5	6	7	8
Wind speed	m/s	10	10	10	10	10	10	10	10
Air temperature	°C	-10.1	-8.0	-2.0	-4.0	-3.0	-3.0	-3.0	-3.0
Wind direction	°deg	90°	90°	90°	90°	90°	90°	60°	90°
Axial rotation	-	fixed	fixed	fixed	fixed	partially rot	rotating	rotating	fixed
Duration	min	60	60	60	60	60	75	75	60
Fx at the end	N/m	0.34	0.04	-7.15	-1.34	-0.86	-2.78	-2.50	-7.91
Fy at the end	N/m	0.70	1.57	42.97	6.10	34.84	27.82	40.68	21.62
LWC	g/m ³	4.2	3.1	1.7	2.8	3.5	2.2	n/a	2.8
LWR - 15 min	-	n/a	n/a	0.49	0.08	0.46	0.39	0.38	0.29
LWR - 30 min	-	n/a	n/a	0.42	0.26	0.37	0.34	0.42	0.37
LWR - 45 min	-	n/a	n/a	0.45	0.11	0.35	0.23	0.30	0.26
LWR - 60 min	-	n/a	0.13	0.44	0.13	0.21	0.18	0.31	0.22
LWR - 75 min	-	n/a	n/a	n/a	n/a	n/a	0.13	0.25	n/a
LWR - mean	-	n/a	0.13	0.45	0.14	0.35	0.25	0.33	0.29
Area of accretion	mm ²	327	394	1097	n/a	3390	3782	5104	2762
Mass 1 h	kg/m	0.072	0.160	4.380	0.622	3.551	2.175	3.233	2.204

The LWR for each experiment is determined in the wind tunnel using thermodynamic principles of heat exchange. A known amount of snow is melted in hot water, and the LWR is calculated by measuring the water temperature before and after melting, applying the equation of thermal equilibrium. The measurement has a significant uncertainty that we estimate at least 10%. This uncertainty arises from several factors. First, it is influenced by the accuracy of temperature measurements and heat losses. Second, the freezing of particles is a dynamic process that evolves throughout the experiment. It has been observed that the LWR of collected ice samples gradually decreases with exposure time. As a result, the LWR measured after 15 min of accumulation might be lower than the

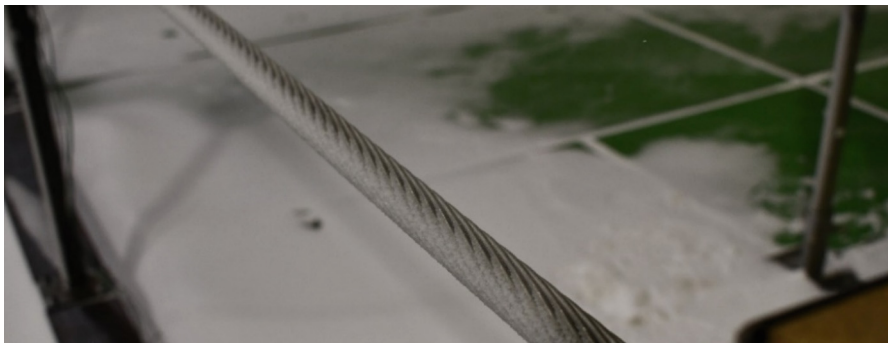


Fig. 4. Icing test 1 – Dry snow



Fig. 5. Icing test 3 – Transition between very wet snow and freezing rain



Fig. 6. Icing test 8 – Wet snow

actual LWR of the particles at the moment they impact the model. Additionally, if ice samples within the same experiment show a progressively lower LWR, this may indicate an increasing fraction of fully frozen ice in the collected samples over time. Lastly, the

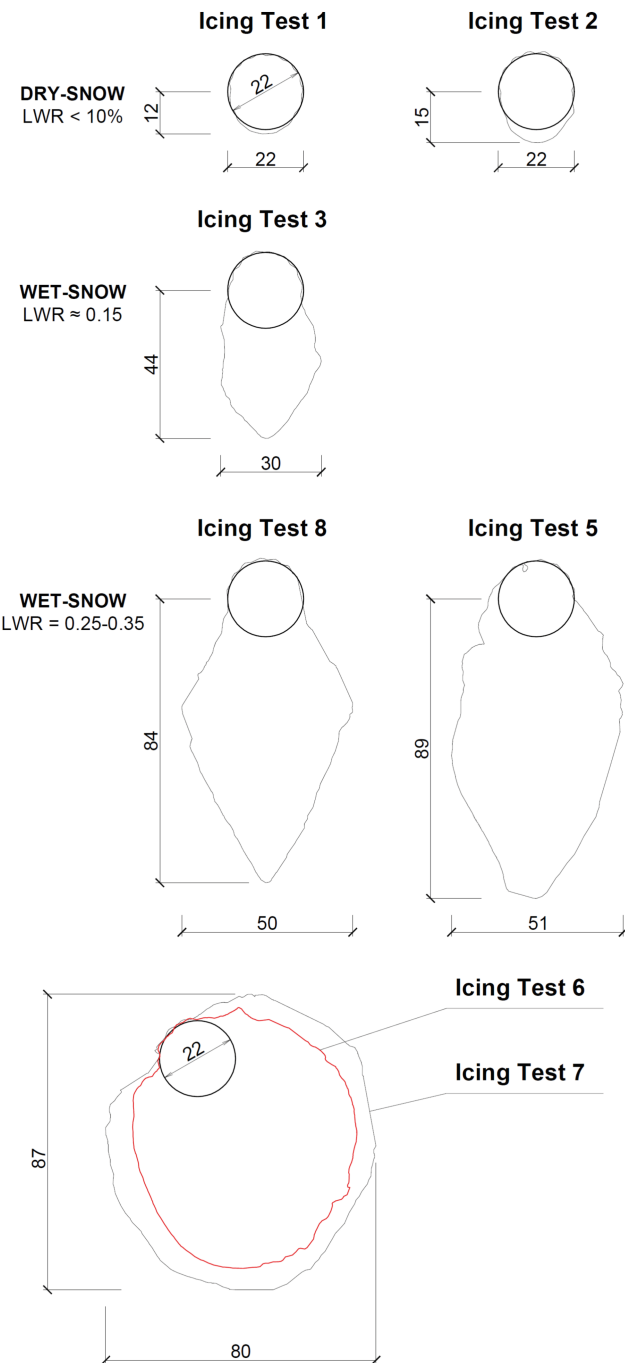


Fig. 7. Cross-sections of iced conductors derived from 3D scanning

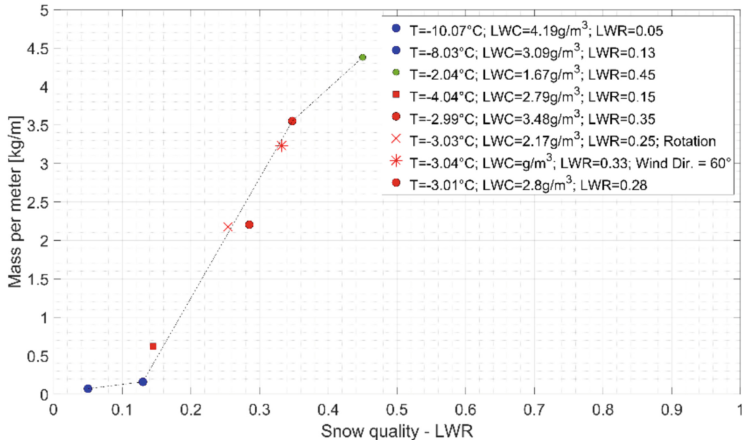


Fig. 8. Accumulated ice mass per meter over a 1-h period.

LWR varies with particle size. The value measured in the wind tunnel should therefore be understood as an average over the particle size distribution.

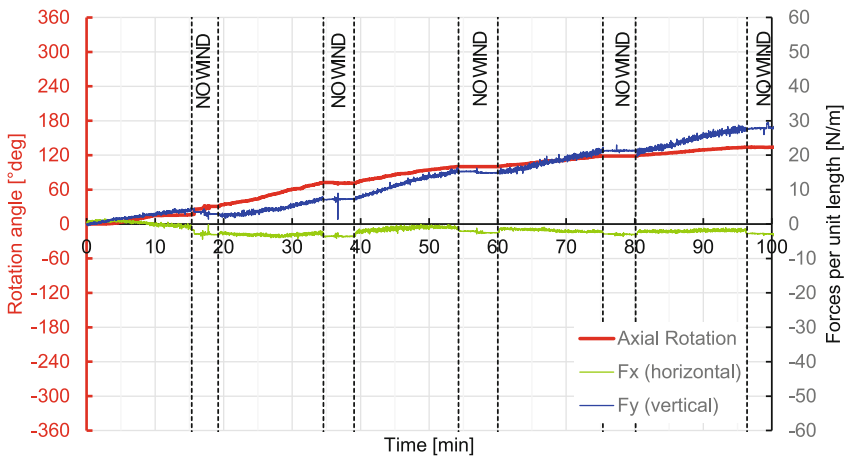


Fig. 9. Forces and rotation angle in Icing Test 6

One of the objectives of the experimental campaign was to investigate ice accretion on a freely rotating conductor. The piano wires of the test bench were designed to provide torsional stiffness comparable, to some extent, to the real values found in 300–400 m span transmission lines. Figure 9 presents the forces and rotation angles recorded during Icing Test 6. The test lasted 75 min, as specified in Table 1, and was divided into five 15-min phases. At the end of each phase, the wind speed was turned off, allowing time for photographic documentation. These pauses were essential, as the vertical force measured during the wind-off intervals corresponds to the self-weight of the iced conductor.

On a non-rotating conductor, ice accretion occurs primarily on the windward side. In contrast, on a conductor free to rotate, the asymmetry of the accumulation (windward) induces a torque and a progressive axial rotation, resulting in a more rounded accretion contour. The experiments demonstrate that this axial rotation increases linearly from the beginning of the test and stops immediately when the wind speed is reduced to zero during the breaks after each 15-min interval. Notably, the conductor remains in its rotated position once the wind stops. This suggests that although aerodynamic forces may contribute to the rotation, the primary driving force is the eccentric self-weight of the ice. Overall, after 75 min of testing, the conductor experienced a rotation of 120° , corresponding to an average rotation rate of approximately 1.6° per minute. As documented in the literature (see [4]), the experiments did not indicate any tendency for the phenomenon to cease. Given a sufficiently long test duration, a complete 360° rotation and a rounded accreted shape would therefore be expected.

5 Conclusions and Outlook

Experiments on wet snow accretion were conducted in the climatic wind tunnel at CSTB. Artificial snow of varying qualities was generated using a snow gun. The key parameter in this study was the Liquid Water Ratio (LWR), defined as the ratio of liquid mass to the total mass of snow particles. It was controlled in the experiments by adjusting the air temperature of the wind tunnel. The results indicate that the accumulated mass over a constant exposure period (1 h) increases almost linearly with rising LWR within the typical range of wet snow. However, at sufficiently high LWR, the slope of the curve decreases, suggesting the onset of run-off effects.

The snow content in the air, quantified as the Liquid Water Content (LWC), was regulated through appropriate snow gun settings and kept constant during the investigation. This parameter serves as a nearly linear time scale factor, accelerating the icing process in the wind tunnel compared to full-scale conditions, thereby enabling in the wind tunnel larger accretions within a shorter time.

Further refinement of the wind tunnel data remains possible. Force sensor measurements exhibit cross-talk effects caused by second-order deformations under load. Therefore, the linear calibration matrix applied in this study can be enhanced to incorporate nonlinear corrections.

For full-scale applications, establishing a relationship between meteorological conditions and snow quality (LWR) is crucial. This would not only help identify the optimal conditions for wet snow accretion but also enable an assessment of its probability of occurrence. Future research will address this aspect.

Another important factor, not yet investigated in this experimental campaign, is the influence of conductor surface temperature on wet snow accretion. The electrical current flowing through the conductor generates heat, which may impact ice formation and shedding.

Last but not least, the effects of wind direction were briefly examined in this experimental campaign. A variation in wind direction from 90 to 60° did not cause a significant change in ice accretion. However, further validation with a broader range of wind directions will be necessary.

Acknowledgements. This work is part of the transnational access project “ERIES-WiST”, supported by the Engineering Research Infrastructures for European Synergies (ERIES) project (www.ries.eu), which has received funding from the European Union’s Horizon Europe Framework Programme under Grant Agreement No. 101058684. This is ERIES publication number C55.

References

1. Admirat, P.: Wet snow accretion on overhead lines. In: Farzaneh, M. (eds.) *Atmospheric Icing of Power Networks*. Springer, Dordrecht (2008). https://doi.org/10.1007/978-1-4020-8531-4_4
2. Ahti, K., Makkonen, L.J.: Observations on rime formation in relation to routinely measure meteorological parameters (1982)
3. Ducloux, H., Nygaard, B.E.: 50-year return-period wet-snow load estimation based on weather station data for overhead line design in France. *Nat. Hazard.* **14**(11), 3031–3041 (2014)
4. Farzaneh, M.: *Atmospheric Icing of Power Networks*. Springer Ed. (2008)
5. ISO 12494, Atmospheric icing of structures, Switzerland (2001)
6. Jimenez, E.U., Steevens, S., Hoelscher, N., Diburg, S.: Enhanced atmospheric icing modelling of high-voltage transmission lines. In: Proceedings of the European African Conference for Wind Engineering EACWE 2025 in Trondheim
7. Jimenez, E.U., et al.: Considerations in replicating in-cloud ice accretion on power lines in climatic wind tunnel testing. In: Proceedings of the European African Conference for Wind Engineering EACWE 2025 in Trondheim
8. Lupi, F., Jimenez, E.U., Matejicka, L., Hoelscher, N., Koss, H.: Considerations in replicating in-cloud ice accretion on power lines in climatic wind tunnel testing. In: Proceedings of the European African Conf. for Wind Engineering EACWE 2025 in Trondheim
9. Makkonen, L.: Estimation of wet snow accretion on structures. *Cold Reg. Sci. Technol.* **17**, 83–88 (1989)
10. Makkonen, L.: Modeling power line icing in freezing precipitation. *Atmos. Res.* **46**(1–2), 131–142 (1998)
11. Makkonen, L.: Models for the growth of rime, glaze, icicles, and wet snow on structures. *Math. Phys. Eng. Sci.* **358**(1776), 2913–2939 (2000)
12. Lubomir, M., Philippe, D., Georgakis Christos T., Olivier, F.: An experimental investigation of ice and snow shedding from bridge cables with and without surface modifications, *Cold Regions Science and Technology*, vol. 220 (2024)
13. Nygaard, B.E.K., Augustsson, H., Somfalvi-Toth: Modelling wet snow accretion on power lines: improvements to previous methods using 50 years observations. *J. Appl. Meteorol. Climatol.* **52**, October 2013
14. Vigano, A.: Modélisation numérique et expérimentale des phénomènes de givrage par accrétion de neige collante. ISAE-ENSMA École Nationale Supérieure de Mécanique et d’Aérotechnique, France (2012)
15. Vigano, A., Delpech, P., Aguinaga, S., Guffond, D., Jacques, B.: Wind tunnel assessment of atmospheric icing and wet snow accretions on structures. In: 6th European and African Conference on Wind Engineering (EACWE) (2013)

Open Access This chapter is licensed under the terms of the Creative Commons Attribution 4.0 International License (<http://creativecommons.org/licenses/by/4.0/>), which permits use, sharing, adaptation, distribution and reproduction in any medium or format, as long as you give appropriate credit to the original author(s) and the source, provide a link to the Creative Commons license and indicate if changes were made.

The images or other third party material in this chapter are included in the chapter's Creative Commons license, unless indicated otherwise in a credit line to the material. If material is not included in the chapter's Creative Commons license and your intended use is not permitted by statutory regulation or exceeds the permitted use, you will need to obtain permission directly from the copyright holder.





Wind Tunnel Tests on a High Rotational Urban Savonius Turbine

Krzysztof Doerffer¹ , Piotr Doerffer¹ , Joanna Grzelak¹ , Józef Kotus² ,
Abdelgalil Eltayesh³ , Luisa Pagnini³ (✉), Giuseppe Piccardo³ ,
and Maria Pia Repetto³

¹ Faculty of Mechanical Engineering and Ship Technology Employment,
Gdańsk University of Technology, 80-233 Gdańsk, Poland

² Multimedia Systems Department, Faculty of Electronics, Telecommunications and
Informatics, Gdańsk University of Technology, 80-233 Gdańsk, Poland

³ Department of Civil, Chemical and Environmental Engineering, University of Genova,
Genova, Italy

luisa.pagnini@unige.it

Abstract. Savonius wind turbines are gaining attention for their low-maintenance design and suitability for small-scale distributed power generation. The THRUST (The High Rotational Urban Savonius Turbine) project focuses on a small diameter Savonius rotor designed to withstand high wind speeds without a braking system. The experimental investigation was conducted in the Giovanni Solari Wind Tunnel at the University of Genoa, under smooth and turbulent flow. In addition to assessing flow conditions, key performance parameters such as torque, voltage, current, rotational speed, and rotor-generated noise were measured in the wind tunnel. Further investigations, including CFD simulations, have allowed to explore these effects in more detail and to interpret the rate of effective wind velocity increase caused by the wind tunnel blockage due to the presence of the wind turbine.

This paper outlines the activities conducted, providing the description of the model, experiments, and measurements. As an example, a selection of results is presented, including power and torque curves, as well as acoustic emission measurements recorded near the rotor. The findings indicate that the Savonius rotor can sustain energy generation even at high wind speeds and turbulence, making it a viable solution for wind energy production in challenging conditions.

Keywords: Savonius Rotor · Wind Tunnel Tests · Small Size Wind Turbines · Turbulence Intensity · Power Curves · Noise Emissions

1 Introduction

Small size wind turbines are becoming a very popular topic due to the increasing interest in distributed power production and renewable energy communities [1, 2]. Unfortunately, during the operating conditions, they may undergo to severe vibrations induced by gusty wind, turbulence and by sudden stops of the machine [3, 4]. These phenomena, besides having a detrimental effect on the energy production, can lead to damages and even

collapses that have the effect of undermining the distributed wind production market [5]. In this context, the simplified maintenance requirements of Savonius rotors offer a great advantage that sustains their appeal in the market for small size installations and makes them ideal for meeting the wind power needs of prosumers [6]. A key advantage is their self-regulating capability: as wind speeds rise, the generated power naturally stabilizes, enabling the rotor to operate safely even in high winds—unlike other turbine types that may require shutdown to prevent damage. This phenomenon occurs naturally, with power output reaching zero at a certain rotational speed (for a tip speed ratio, TSR, of approximately 2).

The proposed research considers a small diameter Savonius rotor wind turbine that is specifically engineered to withstand high rotational wind speed without being provided by any braking system [7]. During very high wind speeds, while other types of wind turbines must be stopped, this Savonius rotor is still operating. In this condition, it supplies limited power but allows producing energy without excessive concern for very high rotational speed. Given the distinctive behavior in extremely high winds and high tip speed ratio power generation, which have not been thoroughly investigated to date, there is a pressing need for detailed measurements at high wind speeds and under various turbulence conditions, including the essential measurement of rotor noise at high rotor speed of rotation.

2 Case Study and Wind Tunnel Set Up

The experimental tests were carried out at the Giovanni Solari Wind Tunnel of the University of Genoa. It is a closed-circuit type operating at atmospheric pressure; the working section is 8.8 m long, with a cross-section of 1.70 (width) \times 1.35 (height) m. The model under investigation consists of a steel Savonius rotor, with a diameter $\Phi = 0.25$ m and a height of 1.0 m, serving as a representative segment of an actual prototype wind turbine. The model is equipped with a torque meter and incorporates essential components such as a 3-phase PMG generator (inner rotor type), a Hall sensor, and an AC/DC current transducer that can be connected to the NI PXI wind tunnel system to measure current parameters and the rotor rpm. A dedicated terminal block facilitates the acquisition of current data. Furthermore, the current transducer communicates with a resistor module capable of applying appropriate loads to the wind turbine.

Tests were conducted under both smooth and turbulence flow conditions. Flow velocities were generated with a wind tunnel rotor propulsion fan frequency ranging from 8 Hz to 40 Hz, leading to wind speed up to 21 m/s (at the inlet), while the rotor's spinning was explored up to 2500 rpm. This comprehensive approach allowed for a thorough examination of the rotor performance across a wide spectrum of operational scenarios. Turbulent flow conditions with intensities I_u of approximately 4% were achieved using a wooden static grid positioned upstream of the model. The grid featured a bar width 15 mm, and mesh size 155 mm, defined as the distance between the centrelines of the bars. For each test, the load on the rotor was varied, measuring wind velocity at the inlet, temperature, torque, voltage, current, rotational speed. Moreover, to establish baseline noise levels within the wind tunnel, measurements were conducted by microphones in different positions and under various conditions. These included the wind tunnel operating with the rotating turbine, with the rotor removed but the mounting supports in place,

and with the tunnel completely empty. Figure 1 illustrates the wind tunnel layout for the tests, showing the position of the wind turbine, the Pitot static tube at the inlet, the grid, and the microphones M1–M4.

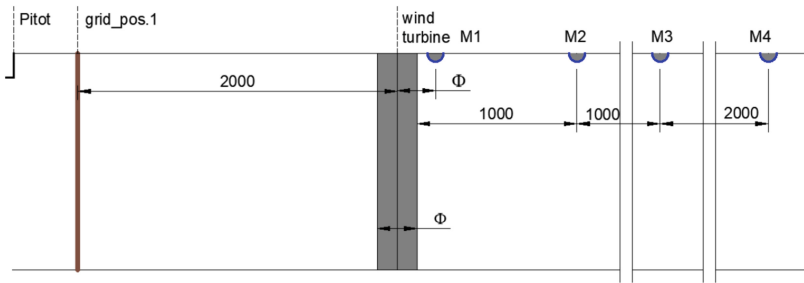


Fig. 1. Wind tunnel test layout (dimensions in mm)

Figure 2a illustrates the steel rotor, the pivotal component of the experiment; Fig. 2b provides a glimpse into the wind tunnel, showcasing the model's placement; Fig. 2c highlights the wooden grid positioned upstream.

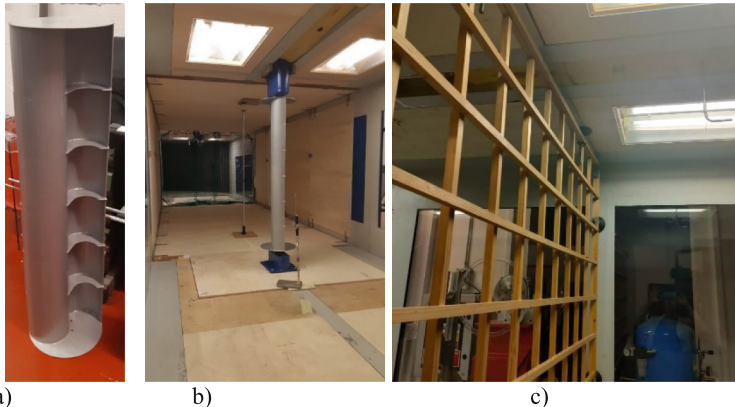


Fig. 2. Savonius rotor (a), model in the wind tunnel with the generator (b); the wooden grid for turbulence generation (c)

3 Wind Tunnel Results

For each test run at a fixed propulsion fan frequency of the wind tunnel, f , experiments were conducted by varying the load applied to the rotor. At each load setting, the wind tunnel velocity—measured by the Pitot tube at the inlet—was stabilized to a steady-state value. Once the turbine reached a steady rotational speed, data was recorded for

one minute. The load on the rotor was then varied, and new measurements were taken after reaching steady-state conditions. Figure 3 reports an example of the measurements of the generated power, P , and torque, T , at different rotational speed ω (in rpm) of the turbine for $f = 24$ Hz in smooth flow and with the wooden grid. In both conditions, the Pitot tube recorded a wind speed $v = 12.3$ m/s. The Reynolds number is calculated as $Re = 3.9 \times 10^4$.

The measured data points establish the relationship between the extracted power and the measured torque versus the corresponding rotational speed of the rotor. The whole set of tests carried out at different wind velocities allows deriving the power curve of the turbine.

Referring to the flow velocity measured at the inlet section, the power coefficient c_p and torque coefficient c_T are obtained:

$$c_p = \frac{P}{\frac{1}{2} \rho v^3 A_s}; c_T = \frac{T}{\frac{1}{2} \rho v^2 R A_s}; \quad (1)$$

where A_s is the turbine swept area, $R = \Phi/2$ is the turbine external radius, ρ is the density of the air. Figure 4 reports the diagrams of c_p and c_T versus the tip speed ratio $TSR = \omega R/v$.

Conversely, conducting experimental investigations of the rotor in a wind tunnel requires careful consideration of the blockage effect. Blockage correction for Savonius rotors [8] typically involves accounting for both solid object blockage and wake blockage. However, assessing these factors can be challenging due to the rotor's motion, which adds complexity to the analysis. Considering that the model frontal area is 0.25 m^2 and the wind tunnel cross section is 2.3 m^2 , the ratio of these surfaces yields a static blockage ratio of $S/C = 11\%$. Following the approach of Pope and Harper [9], the power curve can be corrected considering an increment for the free stream velocity of about 3.5%, while the use of Maskell relationship [10] supplies a correction coefficient of about 16%. The use of one corrective coefficient over another leads to significant variations in the results. CFD analyses, carried out for the investigated set up, have shown that the method by Pope and Harper effectively adjusts the results to match those of an unconfined wind field.

Figure 5 reports the power spectrum density (PSD) of the noise, in smooth flow, recorded by the microphone just behind the rotor (position M1, see Fig. 1) for the static condition in empty wind tunnel (i.e., without the model) and for the wind turbine in operation when it produces the maximum power. In this condition, the turbine rotates at $\omega = 934$ rpm, that corresponds to frequency $1P = 15.6$ Hz. Peaks in the PSD are clearly related to the spinning frequency and its multiples. Figure 6 shows the noise variation during the tests at different tip speed ratio (a), rotational velocity(b) and generated power (c); the diagrams also report values in turbulent flow $I_u = 4\%$.

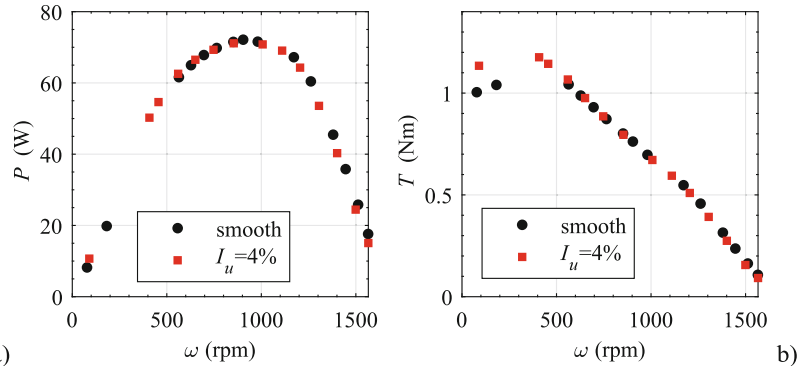


Fig. 3. Power (a) and torque (b) versus rotational speed (a) at different flow conditions for same propulsion fan frequency

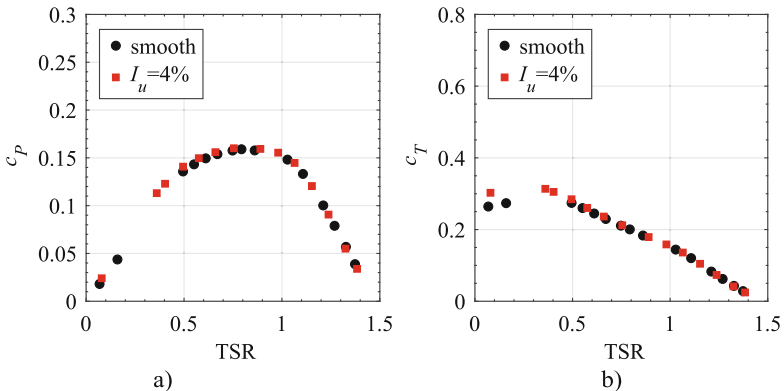


Fig. 4. Power (a) and torque (b) coefficients versus the tip speed ratio; the reference velocity is measured at the wind tunnel inlet.

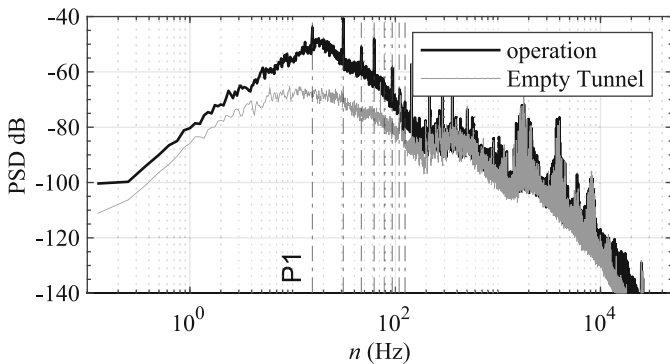


Fig. 5. Noise spectra in smooth flow at a fan frequency of 24 Hz, for the rotating turbine and in the empty wind tunnel.

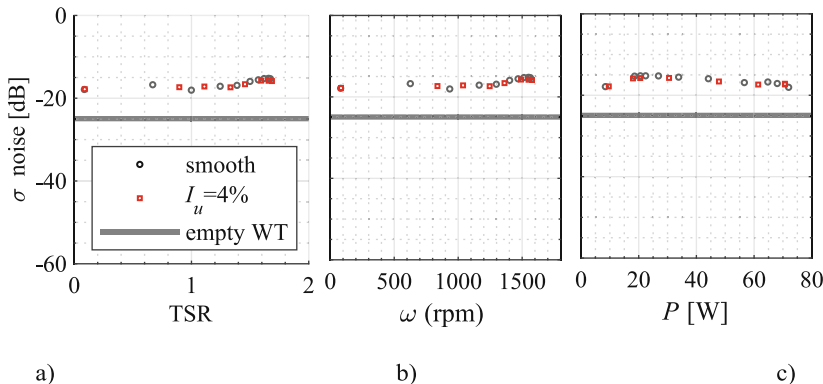


Fig. 6. Noise pressure level for the rotating turbine in smooth flow versus tip speed ratio (a), rotational velocity (b) and mechanical power (c).

Acknowledgements. This work is part of the transnational access project “ERIES-THRUST”, supported by the Engineering Research Infrastructures for European Synergies (ERIES) project (www.ries.eu), which has received funding from the European Union’s Horizon Europe Framework Programme under Grant Agreement No. 101058684. This is ERIES publication number C62.

References

1. Irie, N., Kawahara, N.: Consumer preferences for local renewable electricity production in Japan: a choice experiment. *Renewable Energy* **182**, 1171–1181 (2022)
2. Pagnini, L., Bracco, S., Delfino, F.: De-Simón-Martín M (2024) Levelized cost of electricity in renewable energy communities: uncertainty propagation analysis. *Appl. Energy* **366**, 123278 (2024)
3. Kumar, R., Raahemifar, K., Fung, A.S.: A critical review of vertical axis wind turbines for urban applications. *Renew. Sustain. Energy Rev.* **89**, 281–291 (2018)
4. Pagnini, L., Piccardo, G., Repetto, M.P.: Full scale behavior of a small size vertical axis wind turbine. *Renewable Energy* **127**, 41–556 (2018)
5. Orlando, A., Pagnini, L., Repetto, M.P.: Structural response and fatigue assessment of a small vertical axis wind turbine under stationary and non-stationary excitation. *Renewable Energy* **170**, 251–266 (2021)
6. Dewan, A., Gautam, A., Goyal, R.: Savonius wind turbines: a review of recent advances in design and performance enhancements. *Mater. Today Proc.* **47**(11), 2976–2983 (2021)
7. Doerffer, K., Telega, J., Doerffer, P., Hercel, P., Tomporowski, A.: Dependence of power characteristics on savonius rotor segmentation. *Energies* **14**(10), 2912 (2021)
8. Ross, I., Altman, A.: Wind tunnel blockage corrections: review and application to Savonius vertical-axis wind turbines. *J. Wind Eng. Ind. Aerodyn.* **99**, 523–538 (2011)
9. Pope, A., Harper, J.J.: Low Speed Wind Tunnel Testing. John Wiley & Sons, New York (1966)
10. Maskell, E.C.: A theory of the blockage effects on bluff bodies and stalled wings in a closed wind tunnel. *ARCR and M3400* (1965)

Open Access This chapter is licensed under the terms of the Creative Commons Attribution 4.0 International License (<http://creativecommons.org/licenses/by/4.0/>), which permits use, sharing, adaptation, distribution and reproduction in any medium or format, as long as you give appropriate credit to the original author(s) and the source, provide a link to the Creative Commons license and indicate if changes were made.

The images or other third party material in this chapter are included in the chapter's Creative Commons license, unless indicated otherwise in a credit line to the material. If material is not included in the chapter's Creative Commons license and your intended use is not permitted by statutory regulation or exceeds the permitted use, you will need to obtain permission directly from the copyright holder.





Real Scale Experimental Assessment of Pile Group Dynamic Impedance

Raffaele Di Laora¹(✉) Raffaele Cesaro¹, Emmanouil Rovithis², Luca de Sanctis³, George Anoyatis⁴, Stijn Francois⁴, Eleni Filoglou⁵, Chiara Amendola⁵, Georgia Kroupi⁵, Anastasios Anastasiadis⁵, and Dimitris Pitilakis⁵

¹ Università Della Campania ‘Luigi Vanvitelli’, Napoli, Italy

raffaele.dilaora@unicampania.it

² Democritus University of Thrace, Campus, Greece

³ Università Di Napoli ‘Parthenope’, Napoli, Italy

⁴ KU Leuven, Leuven, Belgium

⁵ Aristotle University of Thessaloniki, Thessaloniki, Greece

Abstract. This work presents ongoing research activities conducted as part of the RESPOND (REal Scale experimental assessment of Pile grOup dyNamic impedance) project, funded under the EU ERIES Transnational Access (TA) initiative.

The project focuses on investigating the dynamic behavior of full-scale pile groups embedded in the well-documented subsoil of the EuroSeistest site, located in the tectonically active Mygdonian basin, 30 km NNE from Thessaloniki, Greece. A 2x2 pile group consisting of four identical bored piles, each with a diameter of 0.60 m and a length of 10 m, was realized. These piles are connected to a 3x3x0.4 m pile cap, serving as the foundation for a 5 m high model structure.

The experimental results have a remarkable value for a reliable design and analysis of structures founded on piles in seismic areas, since soil-structure interaction (SSI) may have a prominent role in the dynamic behaviour of the superstructure. The project is therefore expected to provide a better understanding of fundamental mechanisms associated with dynamic SSI problems, to validate existing formulae for pile group impedances and eventually propose modifications and indications for applications involving moderate non-linearities in the soil.

Keywords: Pile group · field test · dynamic impedance · soil-structure interaction

1 Introduction

Dynamic SSI phenomena are typically distinguished in inertial and kinematic interaction effects [1]. The former result from the development of inertial forces in the vibrating structure associated with the compliance of the foundation and they would not occur in a fixed-base structure. The kinematic interaction, which is more important for embedded structures, stems from the inability of the structure to comply with the free-field deformation pattern induced by a particular ground-motion. The majority of existing

studies and the most commonly adopted procedures in engineering practice employ the so-called sub-structure approach [2–4]), in which the inertial and kinematic interaction mechanisms are rigorously separated from a mathematical standpoint. More specifically, the application of the method is performed in three consecutive steps: (i) calculation of the seismic motion at foundation level, or the Foundation Input Motion (FIM), which may be different from the seismic motion at free-field conditions due to a physical phenomenon termed as kinematic soil-foundation interaction; (ii) computation of the dynamic impedances ('springs' and 'dashpots') associated to swaying, vertical, rocking and cross swaying-rocking oscillation of the foundation; (iii) evaluation of the response of the superstructure supported on springs and dashpots determined in step (ii) and subjected to the FIM calculated in step (i).

Evidently, a crucial ingredient of such method is the determination of the dynamic impedance of the foundation, which regulates the increase in natural period of the structure and, above all, the amount of extra dissipation of energy by radiation of waves from the foundation into the soil medium. To give an idea of the importance of this last aspect, Conti et al. [5] found out by numerical analysis, with reference to a bridge pier resting on a 3x3 pile group, that radiation damping may reduce of 50% the seismic demand on the pier.

The problem of the assessment of the dynamic impedances of pile foundations has been tackled mainly by analytical and numerical means. Formulas and charts are available for single piles in homogeneous soil or for simple stiffness distributions under elastodynamic considerations [6]. However, the performance of such formulae, or of more complex formulations involving numerical analysis, has never been tested with reference to real piles and real soil conditions.

2 Objectives of the Project

The experimental campaign has three main goals: (1) to provide a better understanding of fundamental mechanisms associated with dynamic SSI problems; (2) to compare experimental data with existing analytical formulae for pile group impedances and, eventually, propose modifications and extension to moderate non-linearities in the soil; (3) to verify the importance of pile foundation impedance on the seismic response of the superstructure.

The first goal will be achieved through monitoring accelerations, in the three directions, in a large number of locations within the soil medium and comparing results with classical elastodynamic solutions for low amplitude excitations, corresponding to the low-strain soil stiffness, and finite element analysis employing proper constitutive models for taking into account moderate non-linearities in the soil.

The second goal will be pursued again by analytical and numerical means. It will be checked first the capability of existing formulas to predict impedances for very low strain. Then the capability of an equivalent-linear approach will be verified for moderate non-linearities, eventually proposing rules for using existing formulas with properly modified soil stiffness as function of excitation amplitude, in the same spirit as the approach followed in Iovino et al. [7], Garala et al. [8], Stacul et al. [9], to treat non-linear soil behaviour in kinematic soil-pile interaction. Moderate non-linearities will also

allow a better understanding of the energy dissipation mechanisms, both for the hysteretic part and for the radiation damping; regarding this last issue, it is not clear whether the energy dissipation is ruled mainly by the mobilised soil stiffness or the initial low-strain value, and how soil layering in a real subsoil can modify such mechanism as compared to the simplistic assumption of homogeneous soil.

The third objective is reached by comparison with previous experiments in the same site and same structure yet resting on a shallow foundation. Subsequent paragraphs, however, are indented.

3 Testing Facilities

Since the project is intended to test pile foundations at real scale in the field, i.e. with realistic dimensions and in a natural layered subsoil, the EUROSEISTEST-EUROPROTEAS Research Infrastructure has been selected as host Infrastructure. The real-scale prototype structure of EUROPTEAS is in EUROSEISTEST experimental facility established in the Mygdonian Valley in Northern Greece. EUROPTEAS consists of a simple steel frame with reconfigurable X-bracings founded on a reinforced concrete slab of 3x3x0.4m. Two similar portable reinforced concrete slabs of 9Mg each are placed at the top of the structure representing the superstructure mass. The total height of EuroProteas from the bottom of the foundation slab to the top of the second roof slab is 5.0m while its total mass is approximately 28.5Mg. EuroProteas is a perfectly symmetric structure (Fig. 1) ensuring same bending stiffness in both plane directions. The removable parts of the structure (X-bracings and upper RC slab) allow different configurations of structure's



Fig. 1. EUROPTEAS model Structure.

mass and stiffness, covering a wide range of structural stiffness and natural frequencies between 3Hz and 11Hz.

Soil stratigraphy and dynamic properties in EUROSEISTEST TST site where the model structure has been constructed are well documented by a series of geotechnical and geophysical surveys (Fig. 2). Monitoring capabilities of the Europroteas SSI facility may include more than 80 instruments of various types to monitor structural, foundation and soil response in a particularly dense 3D instrumentation array. Triaxial accelerometers can be mounted on both the superstructure and the foundation slab. Additionally, seismometers can be placed on the ground surface both in the longitudinal and transverse direction of loading up to three times the foundation width to capture the soil response. Long shape-acceleration-arrays (SAAR) are also available to be placed inside the borehole next to the foundation and on the free-field in the direction of loading.

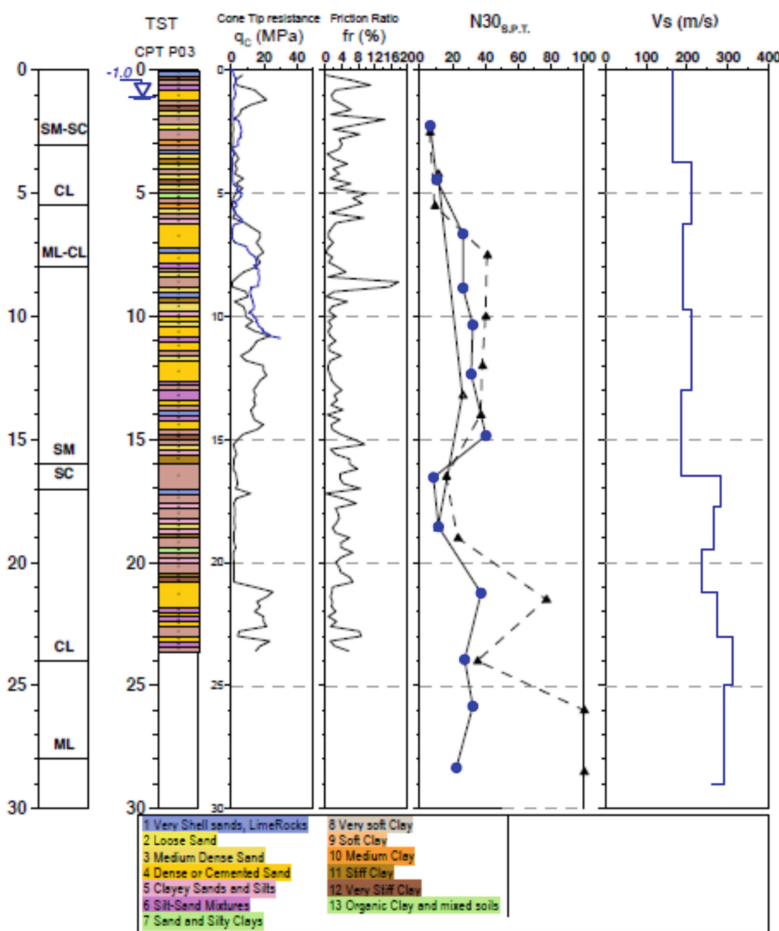


Fig. 2. Soil characterization and field measurements at TST site of EuroSeistest (Series Report 2012).

Forced-vibration tests are also possible through a MK-500U (ANCO Engineers Inc) eccentric mass vibrator owned by the Institute of Engineering Seismology and Earthquake Engineering (EPPO-ITSAK), employed as a source of harmonic excitation. MK-500U is a portable, unidirectional dual counter-rotating shaker that can produce a maximum sinusoidal horizontal force of 50kN and can be operated from 0.1Hz to 20Hz, at frequency steps of 0.1Hz. The shaker is powered by a 2.2kW, 1200rpm electric drive motor controlled by a Toshiba VF-S9 adjustable speed drive.

4 Testing Procedure

The tests carried out so far have been performed in three stages. First, only the foundation, without structure, has been shaken (Fig. 3a). Second, once the structure has been placed on the foundation, the load has been applied on the foundation. Third, the shaker has been moved on the structure mass and thereby the system has been shaken from the top (Fig. 3b).

For the first stage (only foundation) the shaker configuration with the three and four eccentric masses has been used. This is because the load provided by only one or two masses would have been extremely small. Conversely, the second and third stage have been carried out using one, two, three and four masses, given that in this case the load on the foundation can be amplified due to the inertia contribution of the structural mass.

The load consists of sinusoidal forces applied with increasing frequency. For each frequency, the harmonic load has been maintained for one minute, which is largely sufficient to catch the steady-state response.

Further tests conducted later on focused on the response of the single pile, which was tested both for harmonic loading and subsequently subjected to a static vertical and horizontal load test until large displacements.

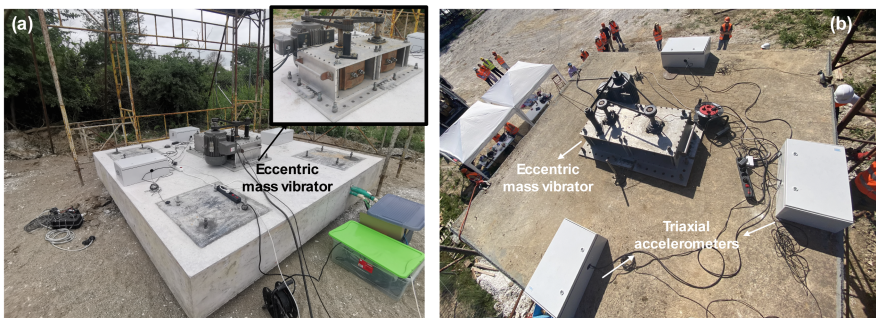


Fig. 3. Part of the forced-vibration tests carried so far with the eccentric mass vibrator mounted on (a) The foundation slab without the superstructure and (b) the superstructure top slab to shake the whole SSI system.

5 Selected Results

At this stage data are being processed and interpreted. Preliminary results are shown in Fig. 4. The computed force is plotted against the imposed vibration frequency in Fig. 4e. Note that the points refer to the actual loading frequencies, which were derived from the FFT transform (Figs. 4a and 4c) of the associated records (Figs. 4b and 4d) from the sensors with the code names 1.1 1.2 and 1.3 (Fig. 4a) placed on the foundation slab. The original signals have been filtered, eliminating the noise corresponding to low

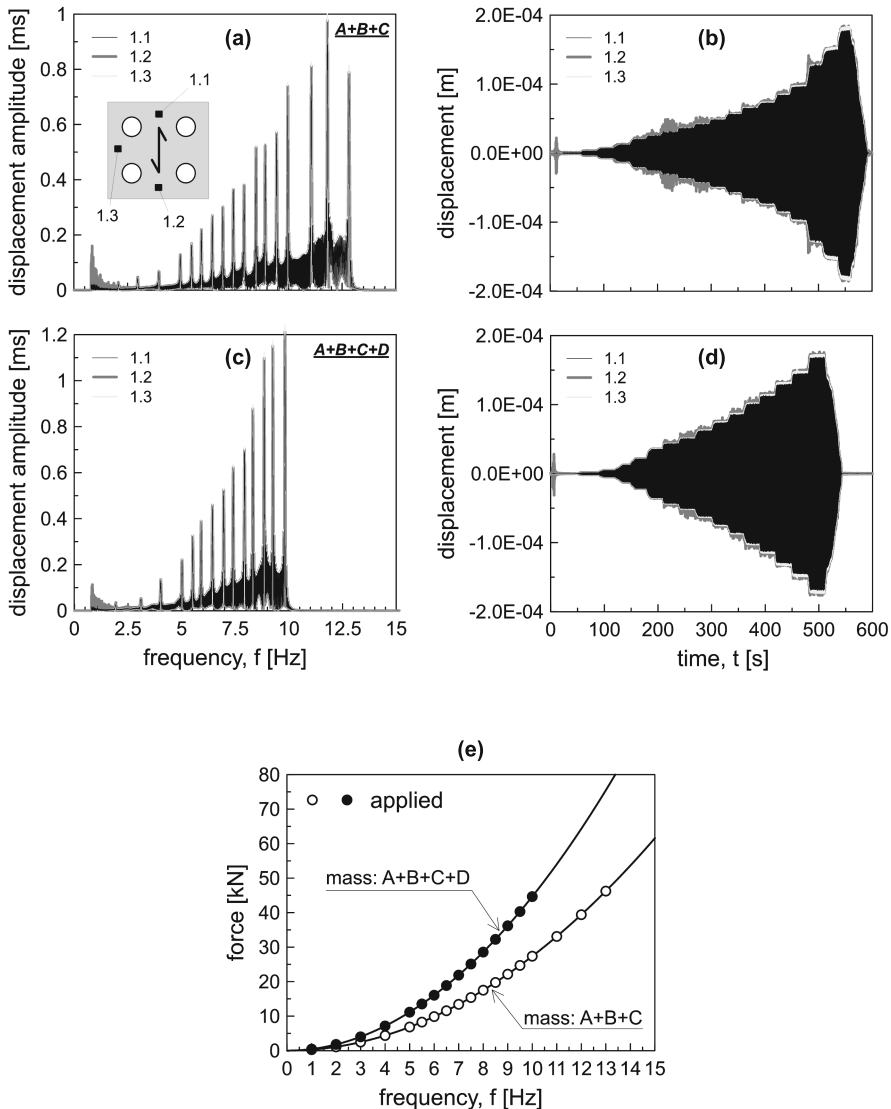


Fig. 4. Selected results.

frequencies. It is noted a good agreement among the three recordings. Also, despite the large force exerted on the pile group cap at high frequencies, the amplitude of the horizontal displacement was recorded low enough to allow for the derivation of the pile group impedances in the linear range, as it was originally planned.

Acknowledgements. This work is part of the transnational access project “ERIES-RESPOND”, supported by the Engineering Research Infrastructures for European Synergies (ERIES) project (www.ries.eu), which has received funding from the European Union’s Horizon Europe Framework Programme under Grant Agreement No. 101058684. This is ERIES publication number C84.

References

1. Mylonakis, G., Gazetas, G.: Seismic soil-structure interaction: beneficial or detrimental? *J Earthq Eng* **4**(3), 277–301 (2000)
2. Kramer, L.S.: *Geotechnical Earthquake Engineering*. Prentice Hall International Series (1996)
3. Gazetas, G., Mylonakis, G.: Seismic soil-structure interaction: new evidence and emerging issues. In: Dakoulas, P., Yegian, M., Holtz, R. (eds.) *Geotechnical Earthquake Engineering and Soil Dynamics*, Vol. II, pp. 1119–1174 (1998)
4. Conti, R., Di Laora, R.: Substructure method revisited for analyzing the dynamic interaction of structures with embedded massive foundations. *J. Geotechnical and Geoenvironmental Engineering* **148**(6) (2022)
5. Conti, R., Di Laora, R., Licata, V., Iovino, M., de Sanctis, L.: Seismic performance of bridge piers: caisson vs pile foundations. *Soil Dyn. Earthq. Eng.* **130**, 105985 (2020)
6. Gazetas, G.: Foundation vibrations, *Foundation Engineering Handbook*. New York-Van Nostrand Reinhold, pp. 553–593 (1991)
7. Iovino, M., Di Laora, R., Rovithis, E., de Sanctis, L.: The beneficial role of piles on the seismic loading of structures. *Earthq. Spectra* **35**(3), 1141–1162 (2019)
8. Garala, T.K., Madabhushi, G.S., Di Laora, R.: Experimental investigation of kinematic pile bending in layered soils using dynamic centrifuge modelling. *Géotechnique* **72**(2), 146–161 (2022)
9. Stacul, S., Rovithis, E., Di Laora, R.: Kinematic soil-pile interaction under earthquake-induced nonlinear soil and pile behavior: an equivalent-linear approach. *J. Geotechnical and Geoenvironmental Eng.* **148**(7), 04022055 (2022)

Open Access This chapter is licensed under the terms of the Creative Commons Attribution 4.0 International License (<http://creativecommons.org/licenses/by/4.0/>), which permits use, sharing, adaptation, distribution and reproduction in any medium or format, as long as you give appropriate credit to the original author(s) and the source, provide a link to the Creative Commons license and indicate if changes were made.

The images or other third party material in this chapter are included in the chapter's Creative Commons license, unless indicated otherwise in a credit line to the material. If material is not included in the chapter's Creative Commons license and your intended use is not permitted by statutory regulation or exceeds the permitted use, you will need to obtain permission directly from the copyright holder.





Seismic Residual Displacements of RC U-Shaped Core Walls: Preliminary Findings

João Pacheco de Almeida^(✉) and Ryan Hoult

Institute of Mechanics, Materials and Civil Engineering, UCLouvain, Belgium
joao.almeida@uclouvain.be

Abstract. The ERIES-ALL4wALL project, “Smart ALLoys for WALLs,” aims to understand and improve the seismic performance of reinforced concrete (RC) building core walls, which are poised to become increasingly vital as the global building stock is expected to double by 2060. This paper presents preliminary results and findings relative to the dynamic testing of two large-scale RC U-shaped core walls, which were tested in the National Laboratory for Civil Engineering (LNEC), in Lisbon. The first unit, UWS1, used conventional steel reinforcement, while the second (UWS2) incorporated largely-debonded iron-based shape memory alloy (FeSMA) rebars. The latter were heated via Joule effect to apply a pre-stress aiming at reducing residual displacements. The units were subjected to alternating uni- and bidirectional ground motions. This paper presents the full time-histories of the wall collar’s relative displacements in both orthogonal directions, along with the corresponding torsional rotations. The article also examines the maximum and at-rest residual displacements, comparing them with those anticipated from quasi-static reverse-cyclic tests. It concludes with a preliminary discussion of unexpected structural behavioral features of UWS2, which are attributed to electrical insulation deficiencies that led to difficulties with the resistive heating system in three of the four wall cross-sectional corners.

Keywords: Reinforced concrete walls · U-shaped walls · Torsion · Residual displacements · Shape memory alloys · Shake table

1 Introduction to the Project ERIES-ALL4wALL

Greater confidence in understanding and simulating reinforced concrete (RC) structures is essential to better define and achieve their target performance. The ERIES-ALL4wALL project focuses on RC buildings with U-shaped core walls, the most common configuration among core wall geometries, which serve as the structural backbone of millions of buildings worldwide. With the global building stock projected to double by 2060 [1], core walls will be crucial for the resilience of the built environment. Additionally, the UN estimates that 2.5 billion more people will be living in cities by 2050, leading to a significant rise in mid- and high-rise structures. RC core walls have long been, and will likely remain, the preferred lateral load-resisting system in building typologies consisting of materials lacking sufficient stiffness or strength. This includes the growing use

of mass timber structures—such as the 25-story Ascent skyscraper, the world's tallest, which features an RC core—along with emerging typologies that incorporate natural or minimally processed materials like tree trunks and bamboo. Furthermore, RC buildings using alternative reinforcement—such as fiber-reinforced polymer (FRP) rebars—are gaining traction, expanding the role of core walls in future construction.

The description and objectives of the project ERIES-ALL4wALL, “Smart ALLoys for WALLs: towards durable structures with long service lives and minimal seismic residual displacements”, funded by the Engineering Research Infrastructures for European Synergies (ERIES; www.ries.eu) Transnational Access program, are provided in the overview by Almeida *et al.* [2]. It also describes the relevance of the project to the ERIES research areas and goals, innovation and impact, and the synergy between seven universities and institutes, complementary in their skills. It includes additionally a summary of the experimental program, the spectrum of numerical simulation approaches employed by the user group, and other associated initiatives—namely, a special issue in the Bulletin of Earthquake Engineering, which is nearing completion, and an international blind prediction competition. More details on the latter can be found in Hoult *et al.* [3].

The present paper focus solely on the presentation of preliminary results obtained from the experimental program of ERIES-ALL4wALL, which consisted in the shake table testing of two half-scale U-shaped wall units, as described in the next section. Despite extensive research on the behavior of RC walls, two closely related topics remain significantly underexplored in experimental studies, and more so for realistic shake table tests: torsional response and residual displacements, which play a crucial role in assessing the post-earthquake repairability of these structures. Thus, both units were subjected to loading designed to induce a bidirectional-torsional response in the walls, as detailed further in the two following sections.

At the time of writing this paper, the authors and the ALL4wALL user group have only recently obtained the measurements results from conventional instrumentation. Therefore, the present paper provides just a preliminary presentation of the main results obtained from the tests of both walls, and some initial findings and comments. A data paper, describing the experimental campaign in detail, as well as the explanation of the test open-access data uploaded to a public repository, can be soon found in Hoult *et al.* [4]. This latter document is currently under preparation, but the corresponding submission for journal publication will have happened by the time of the present ERIES-IW2025 International Workshop. It includes a description of test observations, and the evolution of local damage during the subsequent ground motion runs. Due to space limitations, and the fact that some local results are still being obtained and processed, the present paper limits itself to global engineering demand parameters, skipping many details of the test program.

2 Summary of the Experimental Program

This section provides an overview of the test units and the completed test program. Figure 1(a) presents a 3D representation of both test units, UWS1 and UWS2. Figure 1(b) shows the cross-section and reinforcement detailing of the test units. They differed in the

material used for the vertical reinforcement of the boundary elements: UWS1 incorporated 12 mm diameter ($\Phi 12$) conventional steel reinforcement, designed in accordance with Eurocode 8, as shown on the right side of Fig. 1(b). UWS2 utilized instead $\Phi 10.7$ iron-based shape memory alloys (FeSMA), as illustrated on the left side of Fig. 1(b). The cylinder concrete compressive strengths of the walls at 28 days were, on average, of 27 MPa for UWS1 and 30.3 MPa for UWS2. A ductile longitudinal reinforcing steel was employed for UWS1, with a yield strength varying between 538 and 580 MPa (depending on the rebar diameter), whereas the $\Phi 10.7$ FeSMA rebars had a yield strength of 555 MPa. An extensive characterization of the walls' geometric and mechanical properties will be available in the data paper [4]. The FeSMA rebars were selected with the aim of reducing the residual displacements of the wall. This was based on the underlying working principle that consists in prestressing the wall plastic hinge region, leveraging the unique self-prestressing characteristics of FeSMA upon heating at a specific activation temperature. The latter effect should, in turn, be responsible for the intended wall self-centering and corresponding minimization of the resulting residual displacements. The prestressing of the FeSMA rebars was carried out after the full casting of the wall unit using electrical resistive heating. At the foundation and in the lap-slice region above the first-story slab, the rebars remained clamped to allow the activation process and prevent strain recovery due to heating.

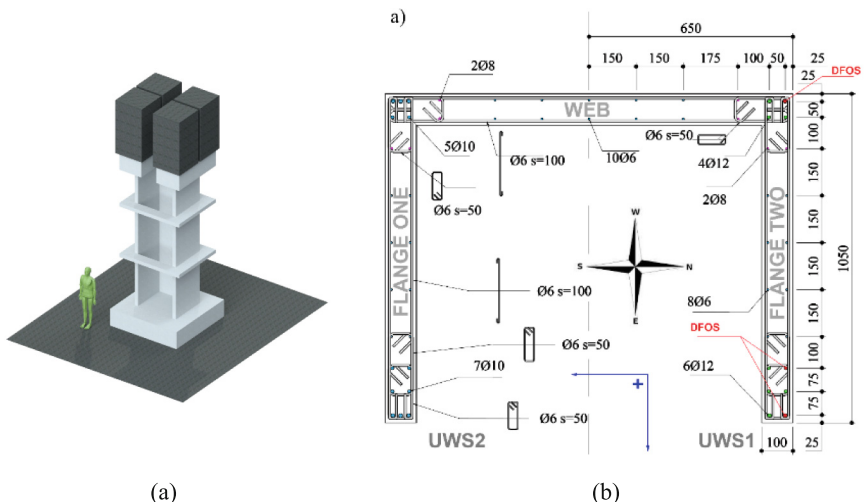


Fig. 1. (a) 3D illustration of the test units (left); (b) wall cross sections detailing for unit UWS1 (right half) and unit UWS2 (left half), with inclusion of reference system in blue (positive in the NS and WE directions).

Unfortunately, despite many precautions during construction, the FeSMA cage was not perfectly electrically insulated from the remaining steel cage, and only limited increase in temperature was achieved. More information and a quick discussion on this relevant issue is provided in Sect. 5. Additionally, to limit inelastic strain demand concentrations at the bottom of the wall and further contribute to elastic recovery and residual

displacement limitations, an unbonded behavior along the height of the FeSMA rebars in the ground story (i.e., below the first-story slab) was sought. Therefore, the FeSMA rebars were shrink-wrapped with two layers, minimizing bond with the surrounding concrete.

Each wall supports a top mass exceeding 28 tons—comprising approximately 3 tons from the wall collar and 25 tons from applied masses. Hoult *et al.* [3] specify the location of the applied mass center relative to the geometric centroid of the wall, which introduces an initial bending moment around the section weak axis.

The ground motions recorded by the station MZ04 during the Central Italy earthquake of October 30, 2016, were applied. The acceleration time histories applied along the West-East and North-South directions of the shake table, with the positive senses indicated in Fig. 1(a), corresponded to the HNN and HNE ground motion components recorded by the MZ04 station, respectively. They are illustrated in Fig. 2(a). The peak ground accelerations are approximately 0.808g and 0.645g. The original ground motions were adapted to consider the Cauchy-Froude similitude law, resampled, cropped, low-pass filtered, integrated in the frequency domain, and windowed as described in Hoult *et al.* [3]. Due to the interaction between the shake table and the specimen, the input acceleration-time histories effectively applied deviated slightly from the ones shown in Fig. 2(a). Figure 2(b) presents the combined scaling factors applied to each of the WE and NS ground motions for each run (i.e., GM0 – GM8). The initial ground motion, GM0, along with all odd-numbered motions (e.g., GM1, GM3, etc.), are applied exclusively in the WE direction. In contrast, the even-numbered ground motions are bidirectional, designed to impose both flexural and torsional demands on the structure; the latter arise due to the offset between the center of mass and the cross-section shear center.

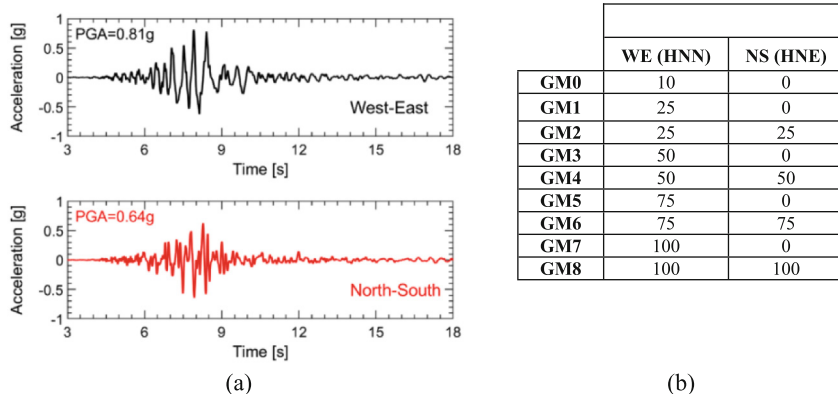


Fig. 2. (a) Acceleration time histories applied to the shake table in the WE and NS directions (scale factor of 100%); (b) Scale factors applied for the consecutive ground motion runs.

3 Wall Collar Displacement and Twist Responses

Due to the dynamic interaction between the units and the shake table, the applied ground motions do not correspond exactly to the time histories shown in Fig. 2(a). Nonetheless, a very good spectral match was achieved. The dynamic responses of the wall units are herein shown based on the measurements obtained with conventional instrumentation. It is noted, however, that a secondary but relevant objective of this project was to explore the application and comparison of advanced optical measurement systems; the reader is invited to refer to the publication by Lo Feudo *et al.* [5], where the evaluation of conventional instrumentation and video tracking of targets (painted circles and crosses, and motion capture markers) is conducted.

Figure 3, Fig. 4, and Fig. 5 show the time history responses for both units, to GM1 through GM8, regarding respectively the following global demand parameters: wall collar relative displacement in the WE direction, wall collar relative displacement in the NS direction, and wall collar twist.

The wall collar relative displacement in the WE direction (Fig. 3) was obtained as the difference between the average measurements of two potentiometers attached to the collar at a height of 4290 mm above the foundation in the WE direction, and a potentiometer measuring the WE displacement of the shake table.

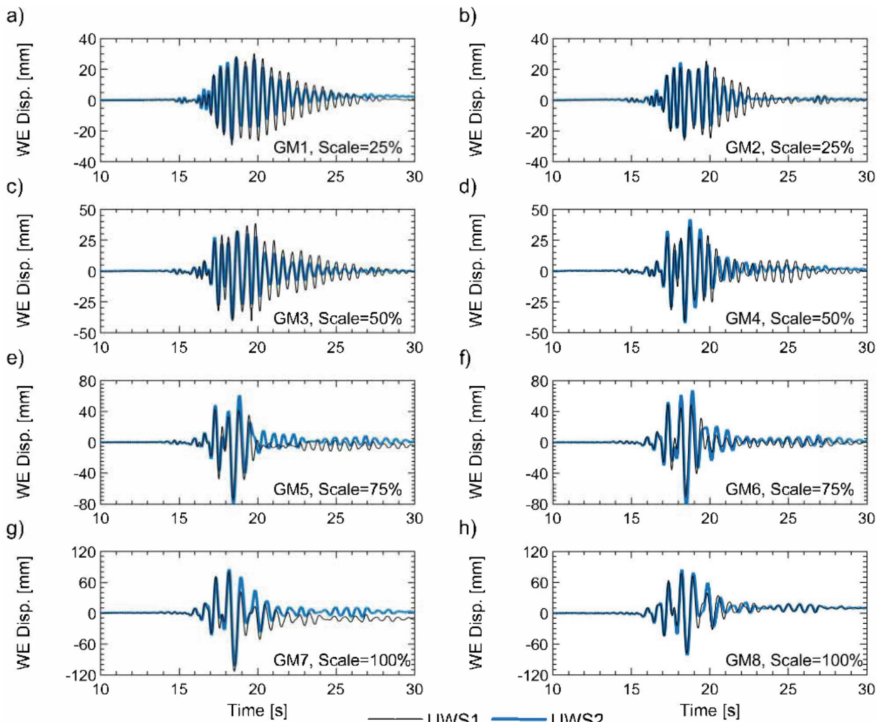


Fig. 3. Relative displacement time histories at the collar of both test units, along the WE direction, for test runs: (a) GM1, through (h) GM8.

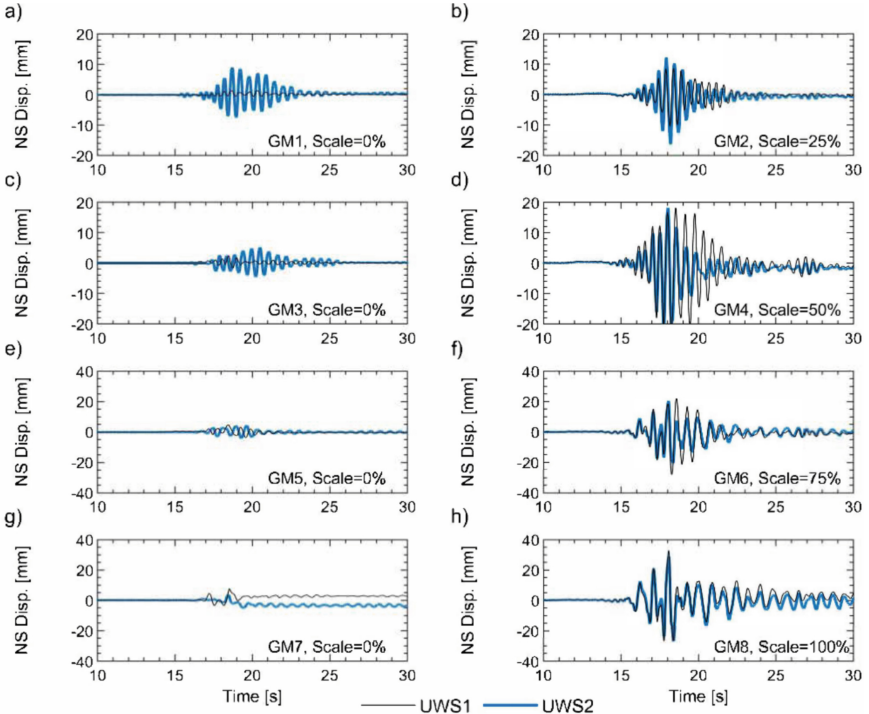


Fig. 4. Relative displacement time histories at the collar of both test units, along the NS direction, for test runs: (a) GM1, through (h) GM8.

A similar approach was applied along the NS direction to obtain the corresponding relative displacement time histories (Fig. 4) from a pair of potentiometers along that direction. The two potentiometers in the WE direction were also used to compute the torsional rotation, or twist, depicted in Fig. 5, considering the distance of 1.2 m between the potentiometers. It is noted that the effect of foundation uplift is included, i.e. results do not depict only contributions from member deformation.

Due to paper length limitations, the analysis of the maximum and residual values of the relative displacements is presented in Sect. 4. Herein, only a small number of salient features of the curves shown in Fig. 3 through Fig. 5 are herein highlighted. Firstly, one can observe a generally similar frequency content of the response, and comparable maximum displacement demands for both walls (see also Sect. 4) when subjected to the ground motions with bidirectional excitation (GM with even numbers), despite some deviations for GM4 and GM6 along the NS direction and twist. It also appears that, on average, damping is not essentially very different for both specimens. However, the previously observed overall similarity in the global response of UWS1 and UWS2 is disrupted by a noticeable difference: when subjected to the lower-intensity unidirectional WE excitations (GM1 and GM3), while UWS1 responded with negligible displacements along the NS direction, as well as torsional rotations, UWS2 showed very significant movements. The latter was unexpected, given the symmetry of the wall cross-section

along WE. The relevance and proposed explanations for this response are provided in Sect. 5.

4 Residual Displacements

This section addresses residual displacements, which is one of the main topics of ALL4wALL presented in the Introduction. In this section, as is customary in this context, displacements are expressed as drifts, i.e. they are normalized by the collar height (h_s). Furthermore, within the framework of structural dynamic behaviour, it is important to distinguish between the maximum residual drift ($\delta_{r,max}$) experienced during the excitation and the residual drift (δ_r) at rest, after the ground motion has stopped. They are illustrated in Fig. 6, wherein the force depicted in the vertical axis of Fig. 6(b) corresponds to the inertial force determined as the product of the acceleration measured at the center of the wall collar times the top mass. The figure also indicates that δ_r at rest is typically much less than $\delta_{r,max}$, due to “shake-down” effects. The dynamic shake-down phenomenon refers to the dynamic response of the structure after its peak drift, during the remainder of the earthquake, and the free vibration phase that follows [6].

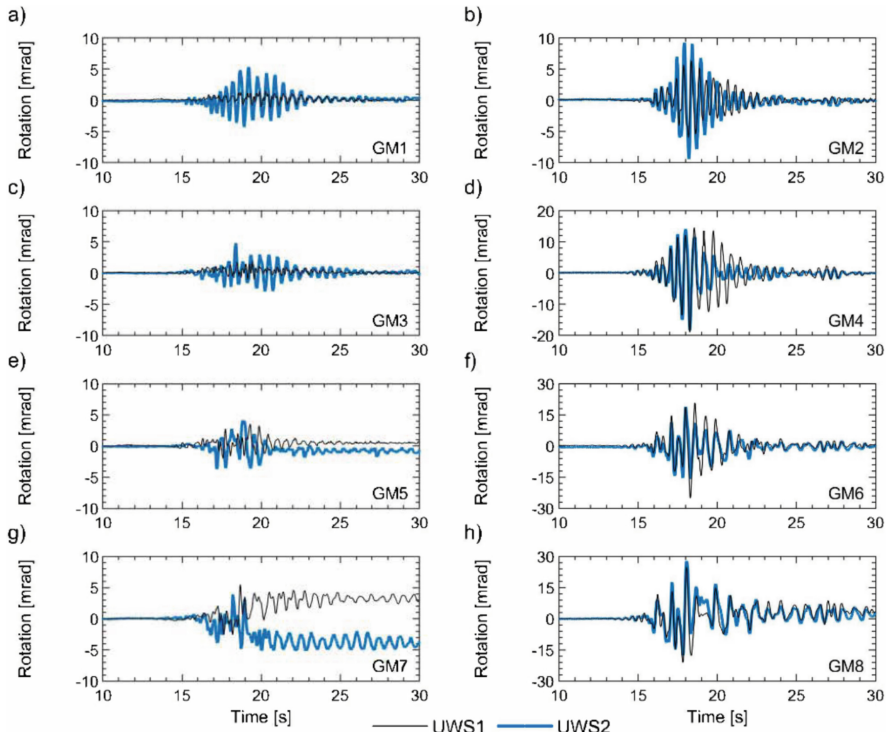


Fig. 5. Twist (torsional rotation) time histories at the collar of both test units, for test runs: (a) GM1, through (h) GM8.

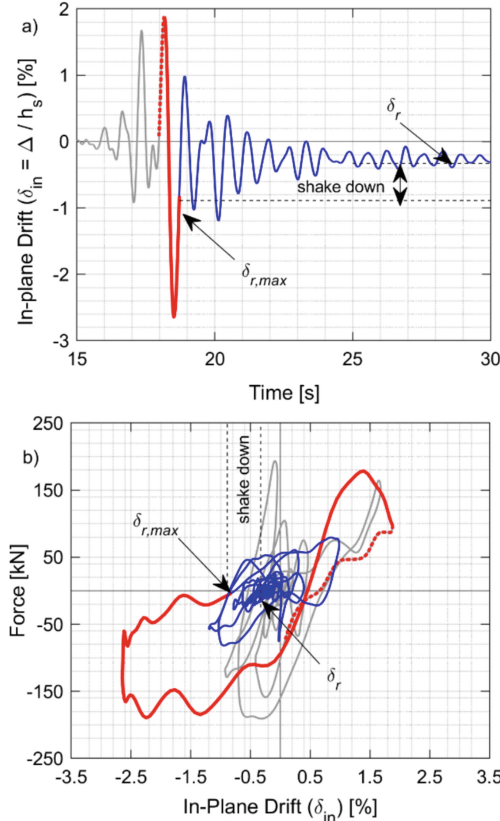


Fig. 6. WE time history response of unit UWS1 under the largest unidirectional ground motion, GM7: (a) drift-time, and (b) inertial force-drift. The “shake down” effects are illustrated as the difference between the maximum residual drift ($\delta_{r,max}$) and the residual drift at rest (δ_r); the in-plane drift (δ_{in}) is the attained in-plane displacement divided by the wall height.

It is important to highlight the difference between the above dynamic residual drifts and the residual drift obtained from reverse-cyclic quasi-static tests, $\delta_{r,max,static}$. The latter has some similarities with $\delta_{r,max}$, to the extent that it corresponds to the drift at which the force becomes null after a peak lateral drift. However, whereas the force indicated in Fig. 6 is an inertial force, the force from quasi-static tests is the nonlinear static resisting force as measured by the load cell of the actuators. In other words, the residual drift from reverse-cyclic quasi-static tests does not account for the effects of viscous forces (since they do not exist), unlike $\delta_{r,max}$.

In a previous study [7], the authors analyzed a large dataset of force-displacement hysteresis from quasi-static tests on (steel-reinforced) RC walls to derive an expression for the residual drift as a function of imposed in-plane drift (δ_{in} , in percent):

$$\delta_{r,max,static} = 0.0022\delta_{in}^2 \quad (1)$$

Equation (1) will be compared with $\delta_{r,max}$, and δ_r from the shake-table ground motion runs. It is noted that δ_r cannot be directly measured in typical quasi-static reverse-cyclic structural tests. Dynamic displacement time histories were analyzed for the ALL4wALL specimens UWS1 (steel-reinforced) and UWS2 (FeSMA-reinforced). Additionally, for completeness, four dynamically tested RC U-shaped wall specimens (WALL0, WALL1, WALL2, and WALL3) with steel reinforcement [8] were also included in the analysis. Figure 7(a) presents the measured $\delta_{r,max}$ (circle markers) and δ_r (square markers) from these dynamic tests, expressed as drift ratios. Only the largest in-plane drift amplitude per ground motion run was considered in calculating $\delta_{r,max}$ and δ_r , resulting in a limited dataset. The (inertial) force data for UWS1 and UWS2 [4] was smoothed using a moving average with a span of 10 data points. This smoothing is important as it influences the calculation of $\delta_{r,max}$, which is determined at zero force. Figure 7(a) also includes the static residual drift estimated using Eq. (1) (dashed black line), which aligns reasonably well with the dynamic $\delta_{r,max}$ data ($r^2 = 0.58$), particularly for larger in-plane drift levels ($\delta_{in} > 1.5\%$). It is noted that past studies addressing residual displacements of bilinear oscillators under ground motions denote $\delta_{r,max,static}$ as the “maximum possible residual displacement based on slow unloading from the peak displacement”, and derived expressions for the latter based on the peak displacement ductility demand and the post-yield stiffness (i.e., the post-elastic stiffness divided by the elastic stiffness) [9].

As expected, δ_r is significantly lower than $\delta_{r,max}$ and approximately follows a linear trend of $0.15\delta_{in} - 0.08$ (with δ_{in} in percent), bound by a lower limit of zero. This suggests that for in-plane drift levels expected from a moderate to large earthquake (i.e., 1.5–2.0%), the at-rest residual drift is approximately 10% of the attained maximum in-plane drift. The negative constant term in the linear expression indicates that there is a range of in-plane drift levels (<0.5%) where negligible δ_r is to be expected because of the essentially elastic (pre-yield) behavior of the wall. It is recalled that plasticity and buckling of the steel bars at the boundary ends of the walls are typically the source of the residual drifts in structural wall buildings [7].

A convenient non-dimensional residual drift ratio ranging from zero to one, first coined by Macrae and Kawashima [9] as the “residual displacement ratio”, is the ratio of δ_r to $\delta_{r,max}$. Figure 7(b) plots this ratio for the same dataset. These data points indicate that, although on average the resting residual drift is approximately 20% of the maximum residual drift experienced, the dispersion is unsurprisingly very large. The same researchers [9] showed that, using bilinear single-degree-of-freedom oscillators, the residual drift ratio strongly depends on the post-yield stiffness and ductility, and less dependent on the soil type and oscillator period. The lower residual drift ratios of UWS1 compared to UWS2 in Fig. 7(b)—except for the most intense ground motions, GM7 and GM8—should be examined within this framework. Another possible contributing factor is the cold-joint wall-foundation interface sliding observed during the dynamic response of UWS1 [4], which was not seen in UWS2. This sliding may have counteracted the wall tilt, effectively reducing the at-rest residual displacements. Increasing damage of UWS1 may have drastically reduced the relevance of base sliding during the largest ground motion, in favor of inelastic flexural deformation modes, which can help explaining the highest residual drift ratio of 0.43 in Fig. 7(b).

It is important to note that, in more recent studies, the residual displacements have been normalised by the peak inelastic displacements and not by the maximum possible residual displacements ($\delta_{r,max,static}$), since the latter approach was found to present some drawbacks [10]. This study points to peak inelastic displacements as a more appropriate intermediate step for estimation of residual displacements, which had also been noted by other researchers [11].

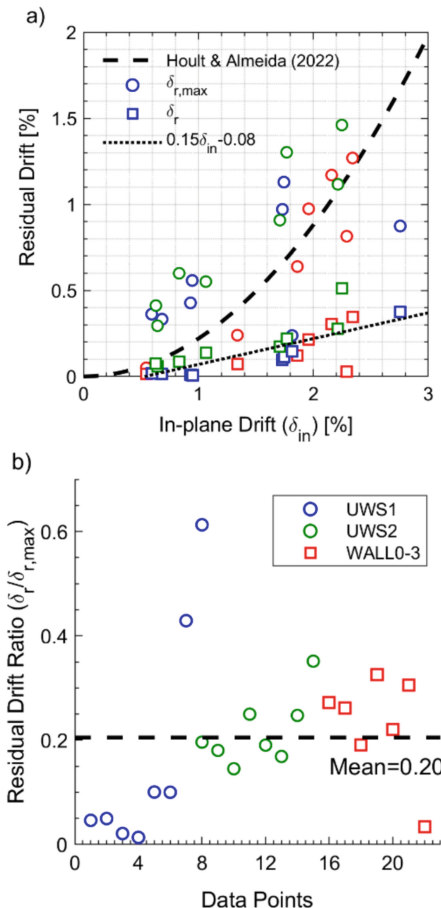


Fig. 7. Residual drifts determined from dynamic tests on U-shaped walls: (a) residual drift (maximum and at rest) as a function of the maximum in-plane drift attained; blue markers are for unit UWS1 in the WE direction, green markers are for unit UWS2 in the WE direction, and red markers are for the test units WALL0–3 [8]; (b) residual drift ratio.

5 Some Preliminary Findings and Discussion

Based on the information presented in the previous section, one general finding relative to the project ERIES-ALL4wALL is that one of its initial goals, namely that of minimizing residual displacements of RC U-shaped walls through an innovative use of iron-based shape-memory alloy rebars in unit UWS2, was not achieved. Additionally, the wall UWS2 depicted an unexpected torsional response, namely when subjected to excitation along the symmetric axis, highlighted in Sect. 3. The present section discusses some of the main possible causes for the above unintended effects, in addition to those already pointed out above (i.e., the shear sliding at the base of UWS1), with a view to possible future improved applications.

It is recalled that the underlying working principle to minimize residual displacements consisted in prestressing the wall plastic hinge region. This required heating the longitudinal FeSMA rebars at the boundary elements of UWS2, which was performed using Joule effect. The target activation temperature was 250°C. Unfortunately, it appears that the FeSMA rebars were not adequately electrically insulated in three of the four corners, despite careful construction. Thus, the electrical resistive heating process did not occur as desired. In fact, the maximum temperature recorded from thermocouples in FeSMA rebars at the UWS2 cross-sectional wall corners were: south-east: 399.2 °C, south-west: 63.5 °C, north-west: 98.1 °C, north-east: 97.8 °C. More details can be found in the data paper [4]. It can be concluded that only partial precompression, centered in the south-east corner, was achieved.

Nevertheless, several positive and promising findings also emerge from the experimental results. In fact, the unexpectedly relevant collar displacements in the NS direction and its significant twisting observed during lower-intensity ground motions applied along the symmetric WE direction of UWS2 confirm the feasibility of effective FeSMA rebar prestressing via Joule heating, with a clear impact on the wall's seismic response. Furthermore, crack pattern analysis [4] suggests that the bond of the FeSMA rebars was effectively minimized (due to shrink-wrapping with two layers), likely contributing to the limitation of inelastic deformations and enhanced elastic recovery of displacement demands. Further research using the optical measurement systems will allow to prove or refute this observation. The authors also admit that, had there been no laboratory safety concerns regarding a potential failure of the wall through an unexpected brittle mode, applying higher-intensity ground motions (i.e., scale factors beyond 100%) could have provided further insights into whether the FeSMA rebars remained predominantly elastic in tension, even despite buckling in compression. This would also have allowed the emergence of more significant residual displacements and a clearer assessment of the performance of the new proposed system.

Acknowledgements. The authors wish to express their sincere gratitude to all the members of the ERIES-ALL4wALL user group, as well as to the team at the NESDE section of the National Laboratory for Civil Engineering, for their remarkable collaborative efforts to successfully carry out these experimental tests, namely (listed in alphabetical order by family name): Alex Bertholet, Paulo Candeias, António A. Correia, Gwendal Cumunel, Catherine Doneux, Yunhyeok Han, Tatjana Isakovic, Antonio Janevski, Stefania Lo Feudo, Andrea Orgnoni, Dan Palermo, Basile Payen, Rui Pinho, Filipe Ribeiro, and Aude Simar.

This work is part of the transnational access project “ERIES-ALL4wALL”, supported by the Engineering Research Infrastructures for European Synergies (ERIES) project (www.eries.eu), which has received funding from the European Union’s Horizon Europe Framework Programme under Grant Agreement No. 101058684. This is ERIES publication number C74.

References

1. UN Environment. Global Status Report 2017: Towards a zero-emission, efficient, and resilient building and construction sector (2017). www.globalabc.org
2. Almeida, J.P., et al.: Shake-table testing of two U-shaped RC walls: overview of the project ERIES-ALL4wALL. In: 18th World Conference on Earthquake Engineering (WCEE2024), Milan, Italy (2024)
3. Hoult, R., Almeida, J.P., Correia, A.A.: Overview and blind prediction from shake table tests of a large-scale RC U-shaped core wall. In: 18th World Conference on Earthquake Engineering (WCEE2024), Milan, Italy (2024)
4. Hoult, R., Correia, A.A., Bertholet, A., Candeias, P., Cumunel, G., Almeida, J.P.: Shake-table tests on two 40-ton reinforced concrete U-shaped walls with uniaxial and bidirectional-torsional response. *Earthquake Spectra* (under submission) (2025)
5. Lo Feudo, S., et al.: Video tracking of targets for vibration measurement of large-scale structures under seismic excitation. *Earthquake Eng. Struct. Dyn.* **54**(8), 2106–2120 (2025)
6. Henry, R.S., Sritharan, S., Ingham, J.: Recentering requirements for the seismic design of self-centering systems. In: Ninth Pacific Conference on Earthquake Engineering, Auckland, New Zealand (2011)
7. Hoult, R.D., Almeida, J.P.: Residual displacements of reinforced concrete walls detailed with conventional steel and shape memory alloy rebars. *Engineering Structures* **256** (2022)
8. Combescure, D., Chaudat, T.H., Moutafidou, A.: Seismic tests of ICONS U-shaped walls – description of the experimental set-up. main results. SEMT/EMSI/RT/99–062. Saclay, France. French Alternative Energies and Atomic Energy Commission (CEA) (1999)
9. Macrae, G.A., Kawashima, K.: Post-earthquake residual displacements of bilinear oscillators. *Earthquake Eng. Struct. Dynam.* **26**(7), 701–716 (1997)
10. Feng, Z., Gong, J.: Study on normalization of residual displacements for single-degree-of-freedom systems. *Earthq. Spectra* **37**(3), 1758–1784 (2021)
11. Liossatou, E., Fardis, M.N.: Residual displacements of RC structures as SDOF systems. *Earthquake Eng. Struct. Dynam.* **44**(5), 713–734 (2015)

Open Access This chapter is licensed under the terms of the Creative Commons Attribution 4.0 International License (<http://creativecommons.org/licenses/by/4.0/>), which permits use, sharing, adaptation, distribution and reproduction in any medium or format, as long as you give appropriate credit to the original author(s) and the source, provide a link to the Creative Commons license and indicate if changes were made.

The images or other third party material in this chapter are included in the chapter's Creative Commons license, unless indicated otherwise in a credit line to the material. If material is not included in the chapter's Creative Commons license and your intended use is not permitted by statutory regulation or exceeds the permitted use, you will need to obtain permission directly from the copyright holder.





Shake Table Testing of Masonry-Infilled RC Frames with Flexible Joints for Seismic-Resilient Structural Performance

Enrico Tubaldi¹(✉), Filip Manojlovski², Aleksandra Bogdanovic², Zoran Rakicevic², Julijana Bojadjieva², Vlatko Sesov², Marko Marinković³, Matija Bošković³, Christoph Butenweg⁴, Matija Gams⁵, Nemanja Krtinić⁵, Fabio Freddi⁶, Daniele Losanno⁷, Prateek Dhir⁸, Hamid Ahmadi⁹, and Alessandro Lotti¹⁰

¹ University of Strathclyde, Glasgow, UK
enrico.tubaldi@strath.ac.uk

² Institute of Earthquake Engineering and Engineering Seismology, University Ss Cyril and Methodius in Skopje, Skopje, Republic of North Macedonia

³ University of Belgrade, Belgrade, Serbia

⁴ RWTH Aachen University, Achen, Germany

⁵ University of Ljubljana, Ljubljana, Slovenia

⁶ University College London, London, UK

⁷ University of Naples, Naples, Italy

⁸ University of Durham, Durham, UK

⁹ TARRC Rubber Research Centre, Hertford, UK

¹⁰ University of Trento, Trento, Italy

Abstract. Masonry infills are critical components of reinforced concrete (RC) frame structures that often sustain significant damage, even during moderate earthquakes. Rubber joints have emerged as a promising solution to enhance their performance. However, further experimental and numerical investigations are required to assess their effectiveness under realistic seismic loading conditions. To address this gap, the H2020 EU-funded FLEJOI project (FLEXible JOInts for seismic-resilient design of masonry-infilled RC frames) was conducted within the ERIES framework. As part of this initiative, two identical RC brick-infilled prototypes were constructed at the Dynamic Testing Laboratory of IZIIS in North Macedonia, each incorporating a distinct rubber joint system. One system was designed to reduce the infill stiffness while introducing damping capabilities, whereas the other aimed to fully decouple the infills from the frame. The prototypes underwent a series of shaking table tests to evaluate their seismic performance. A comprehensive set of sensors was installed to monitor key parameters influencing the seismic response of the structures, infills, and joints. This paper presents an overview of the experimental testing campaign and the data generated. These data will support the calibration and validation of numerical models and serve as a foundation for further studies on the seismic performance of RC frames with masonry infills and rubber joint systems.

Keywords: Shake table tests · Masonry infills · Rubber joints · RC frame

1 Introduction

Reinforced concrete (RC) buildings are among the most common types of construction worldwide. These buildings typically include masonry infill walls, which provide a significant contribution to the building performance [1] and often represent the most vulnerable components of the structure. Infill walls can fail even under low-magnitude earthquakes, resulting in significant direct impacts (such as human casualties and repair costs) and indirect losses (such as downtime). The financial impact of damage to infill walls can be substantial, with studies showing that the cost of repairing infill damage often exceeds the cost of repairing structural components [2]. This underscores the critical need for innovative technologies that can enhance the seismic performance and resilience of buildings while minimizing the consequences of seismic events.

A considerable amount of research has focused on developing technologies to protect masonry infill walls from seismic damage. One common approach involves strengthening the infill walls using various techniques [3, 4]. However, these methods often require strengthening adjacent frame components, making them potentially cost-prohibitive. Recently, alternative strategies have emerged, focusing on the design of engineered infill walls with improved behavior, minimizing their interaction with the structural frame. Many of these strategies aim to increase the infill panel's flexibility and/or isolate it from the surrounding frame using flexible or sliding joints. Among the joint systems developed in the EU-funded INSYSME project [5], rubber joints have proven to be particularly effective due to their adaptable stiffness and energy dissipation properties, which can be customized through the selection of suitable materials and designs.

Experimental tests conducted mainly within the INSYSME project have demonstrated the feasibility of using rubber joints. However, further testing and numerical studies are needed to confirm their effectiveness under more realistic loading conditions and to advance the understanding of their design principles. To address this gap, the H2020 EU-funded project FLEXible JOInts for seismic-resilient design of masonry-infilled RC frames (FLEJOI) was launched under the framework of Engineering Research Infrastructures for European Synergies (ERIES) [6, 7]. The goal of the ERIES-FLEJOI project is to evaluate the effectiveness of two different flexible rubber joint systems designed to protect masonry infills and improve the seismic performance of RC buildings.

The first system under investigation is a compliant joint system, consisting of horizontal joints (developed by TARRC - Tun Abdul Razak Research Centre) integrated into the panel, along with vertical rubber joints placed between the panel and the frame columns [8–11]. The second system, known as INODIS, is a decoupling system with sliding/flexible joints located at the interface between the infill panel and the frame [12–14]. The effectiveness of both systems for infill protection was previously demonstrated under quasi-static loading conditions. The primary objective of this study is to assess the performance of these systems under dynamic loading using shaking table tests.

To this end, two identical infilled RC frame prototypes were constructed at the Dynamic Testing Laboratory of IZIIS in North Macedonia, each equipped with a different rubber joint system. Both prototypes underwent a series of shaking table tests. This article outlines the experimental campaign, providing key information on the properties of the tested prototypes, their construction, instrumentation, testing procedures, and data collected from various sensors. The test results will be used to calibrate and validate

numerical models and will support further research on the seismic performance of RC frames with infills and rubber joints.

2 Experimental Test Models

Two three-dimensional, single-story, one-bay RC frames with masonry infills and rubber joints were constructed and tested at IZIIS Dynamic testing laboratory. These RC frames are identical to those used in the INMASPOL Project, which evaluated the seismic performance of deformable polyurethane joints for infill protection [15]. Each frame measures 2.7 m × 2.7 m in both orthogonal directions, with extended footing beams and a cantilever slab, with a total height of 3.3 m, as shown in Fig. 1. The structural system consists of four square columns (20 cm × 20 cm) and 20 cm wide beams embedded in the 20 cm thick top slab. The columns are reinforced with eight longitudinal bars with 10 mm diameter and double stirrups with 8 mm diameter, while the beams are reinforced with eight longitudinal bars with 10 mm diameter and single stirrups with 8 mm diameter. Both have 5.5 cm concrete covers.

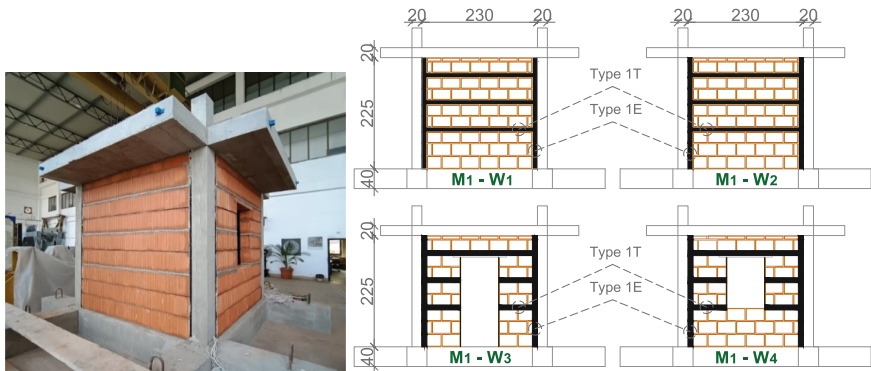


Fig. 1. Model 1 as built (left), wall properties (right).

The first model (Fig. 1) features horizontal rubber strips that divide the panel into four subpanels (Type 1T joints) and vertical rubber strips located between the masonry infill and the RC columns (Type 1E joints). This joint system is designed as a compliant and dissipative mechanism, enhancing the flexibility of the infill walls while also providing energy dissipation capacity. The second model (Fig. 2) incorporates sliding/flexible strips placed along all four sides of the masonry infill (Type 2 joints). This system fully decouples the infill from the RC frame in the in-plane direction while maintaining out-of-plane restraint. To simulate additional mass, both models were loaded with 18 400 kg steel ingots (total 7200 kg).

Figure 3 illustrates the Type 1 and Type 2 joint system. The horizontal joints (Type 1T) were developed by TARRC and consist of a special high-damping rubber compound tailored for this project. The vertical elastomeric joints (Type 1E) were made from recycled rubber provided by Isolgomma and placed at the interface between the masonry infill and the frame columns. The horizontal joints were positioned between two mortar layers, while the vertical joints were adhered to the columns using a silicone adhesive sealant. The Type 2 joint system, designed by Regupol, consists of rubber strips that isolate the infill from the frame, thereby enabling in-plane decoupling. The in-plane separation is achieved through rubber strips with low compressive and shear stiffness, while out-of-plane restraint is ensured by a specialized arrangement of the rubber strips. These strips are divided into three sections: the two outer parts are connected to the infill wall, and the central strip is adhered to the columns. The connection to the top beam (slab) and foundation beam is similarly divided into three segments, with the middle elastomer flanked by two outer elastomers separated by a plastic sheet profile (sliding surface), allowing unrestricted movement between the infill and the RC frame.

The masonry infills were built using Porotherm 20 bricks by Wienerberger, with dimensions $37.5 \times 20 \times 23.8$ cm. The bricks were bonded with 1.5 cm-thick horizontal mortar layers, while the vertical joints remained dry.

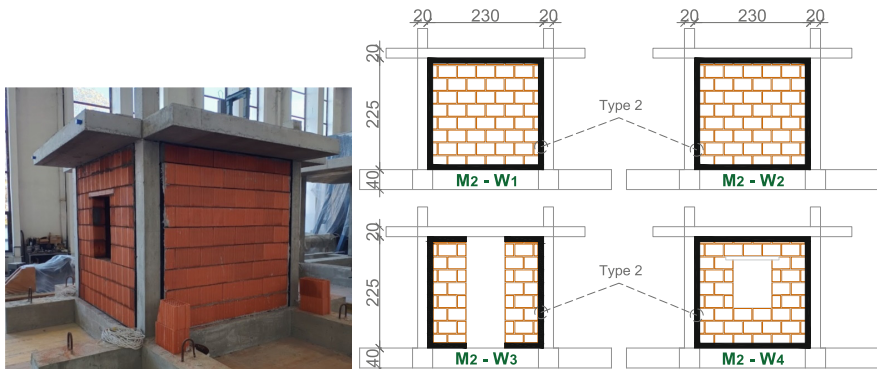


Fig. 2. Model 2 as built (left), wall properties (right).



Fig. 3. Joints Type 1T and 1E (left) and Type 2 (right).

3 Testing Methodology

The experimental test activities included characterization tests of the constituent materials and components and shake table tests of both models to evaluate their dynamic behavior and seismic response to specific earthquake time histories.

During the model construction phase, samples were collected for independent material and component characterization tests. Four concrete cubes ($150 \times 150 \times 150$ mm) were cast during the column construction for both models and tested following the EN 12390–3 standard [16]. The average 28-day compressive strength was 37.37 MPa. Similarly, three mortar cubes of the same dimensions, prepared from the ready-mix mortar used in the infill walls of Model 1, underwent compression tests. The average 28-day compressive strength was 20.5 MPa. For reinforcement, ten samples of 10 mm diameter longitudinal steel bars were tested as per the EN ISO 15630–1 standard [17]. The mean yield strength (f_y) was 578.3 MPa, while the ultimate tensile strength (f_u) averaged 667.3 MPa. Additionally, two brick samples were tested under compression along the rib direction, with thin mortar layers applied between them and the loading plates. Their ultimate load capacities were measured at 435.9 kN and 477.2 kN.

The shaking table tests were conducted in two phases for each model. The comprehensive list of all tests conducted on both models is provided in Table 1 and Table 2. In Phase 1, fully infilled walls were subjected to in-plane loading, aligned with the excitation direction, while walls with openings experienced out-of-plane loading, perpendicular to the excitation. In Phase 2, the models were rotated 90 degrees around the vertical axis, reversing the loading conditions—walls with openings were tested in-plane, whereas fully infilled walls were loaded out-of-plane. The testing program began with low-intensity white noise excitation on the shake table to determine the system's dynamic characteristics. Subsequently, ground motion excitations were applied with progressively increasing intensity levels.

For Model 1, the selected earthquake records included Adana 1998 (M_w 6.3), Erzincan 1992 (M_w 6.6), and Umbria 2016 (M_w 6.2). Model 2 was subjected to the Adana 1998 earthquake (M_w 6.3) and a synthetically generated earthquake based on the Eurocode 8 spectra for Soil Type C. The shaking table tests were performed with increasing intensities of such ground motion records (e.g., 10%, 50%, 100%, as indicated in Table 1 and Table 2). White noise tests were performed at specific points during the seismic sequence to evaluate the variability of the change in dynamic properties. Additionally, modal hammer impact tests were performed before and after the shake table tests to assess changes in the out-of-plane dynamic characteristics of the infill walls using Experimental Modal Analysis (EMA). However, the results of the EMA are out of the scope of this paper.

Table 1. List of performed tests for Model 1 - Phase 1 and 2.

Model 1 – Phase 1		Model 1 – Phase 2	
Test	Type of test	Test	Type of test
1–6	EMA, Impact hammer - wall properties	1–3	EMA Impact hammer - wall properties
7	EMA, ST - wh. Noise 1 - 45 Hz, 0.01g	4	EMA, ST - wh. Noise 1 - 45 Hz, 0.01g
8	Seismic, Adana EQ 10% [0.055g]	5	Seismic, Adana EQ 10% [0.062g]
9	Seismic, Erzincan EQ 10% [0.065g]	6	Seismic, Erzincan EQ 10% [0.065g]
10	Seismic, Erzincan EQ 20% [0.128g]	7	Seismic, Erzincan EQ 20% [0.128g]
11	Seismic, Adana EQ 20% [0.123g]	8	Seismic, Adana EQ 20% [0.132g]
12	Seismic, Adana EQ 50% [0.332g]	9	Seismic, Adana EQ 50% [0.314g]
13	Seismic, Erzincan EQ 40% [0.268g]	10	Seismic, Erzincan EQ 40% [0.267g]
14	EMA, ST - wh. Noise 1 - 45 Hz, 0.01g	11	EMA, ST - wh. Noise 1 - 45 Hz, 0.01g
15–17	EMA, Impact hammer - wall properties	12–14	EMA, Impact hammer - wall properties
18	Seismic, Adana EQ 100% [0.675g]	15	Seismic, Adana EQ 100% [0.728g]
19	EMA, ST - wh. Noise 1 - 45 Hz, 0.01g	16	EMA, ST - wh. Noise 1 - 45 Hz, 0.01g
20	Seismic, Umbria EQ 100% [0.617g]	17	Seismic, Umbria EQ 80% [0.51g]
		18	EMA, ST - wh. Noise 1 - 45 Hz, 0.01g
		19–21	EMA, Impact hammer - wall properties

Table 2. List of performed tests for Model 2 - Phase 1 and 2.

Model 2 – Phase 1		Model 2 – Phase 2	
Test	Type of test	Test	Type of test
1–3	EMA, Impact hammer - wall properties	1	EMA, ST - wh. Noise 1 - 45 Hz, 0.01g
4	EMA, ST - wh. Noise 1 - 45 Hz, 0.01g	2	Seismic, Adana EQ 10% [0.06g]
5	Seismic, Adana EQ 10% [0.065g]	3	EMA, ST - wh. Noise 1 - 45 Hz, 0.01g
6	EMA, ST - wh. Noise 1 - 45 Hz, 0.01g	4	Seismic, Adana EQ 30% [0.17g]
7	Seismic, Adana EQ 20% [0.122g]	5	EMA, ST - wh. Noise 1 - 45 Hz, 0.01g
8	EMA, ST - wh. Noise 1 - 45 Hz, 0.01g	6	Seismic, Adana EQ 40% [0.25g]
9	Seismic, Gener. EQ 30% [0.181g]	7	EMA, ST - wh. Noise 1 - 45 Hz, 0.01g
10	EMA, ST - wh. Noise 1 - 45 Hz, 0.01g	8	Seismic, Adana EQ 50% [0.3g]
11	Seismic, Gener. EQ 60% [0.322g]	9	EMA, ST - wh. Noise 1 - 45 Hz, 0.01g
12	EMA, ST - wh. Noise 1 - 45 Hz, 0.01g	10–12	EMA, Impact hammer - wall properties
13–15	EMA, Impact hammer - wall properties		

3.1 Testing and Instrumentation Setup

The dynamic testing at IZIIS was conducted using a 5.0 m × 5.0 m shake table with five degrees of freedom, supported by two lateral and four vertical MTS hydraulic pistons, and controlled by an MTS Digital Controller 469D. The modal impact hammer used for these tests was the PCB Piezotronics model 086D20, equipped with the softest grey tip.

The instrumentation of the tested models included accelerometers (ACC) from PCB Piezotronics for measuring accelerations, linear potentiometers (LP) from Microepsilon WDS for recording total and relative displacements, linear variable differential transformers (LVDT) from MacroSensors DC750 for displacement measurements, and strain gauges (SG) from KYOWA KFG for capturing strain data. Their exact placement on each model is illustrated in Fig. 4 for Model 1 – Phase 1; Fig. 5 for Model 1 – Phase 2; Fig. 6 for Model 2 – Phase 1; and Fig. 7 for Model 2 – Phase 2. The data acquisition process was carried out using a National Instruments PXI modular system.

Additionally, a digital image correlation (DIC) system was utilized to measure displacement and strain fields on one side of each model, specifically the side subjected to in-plane loading. For Model 1, DIC measurements were taken during selected earthquake runs, whereas for Model 2, all runs were recorded (Fig. 8).

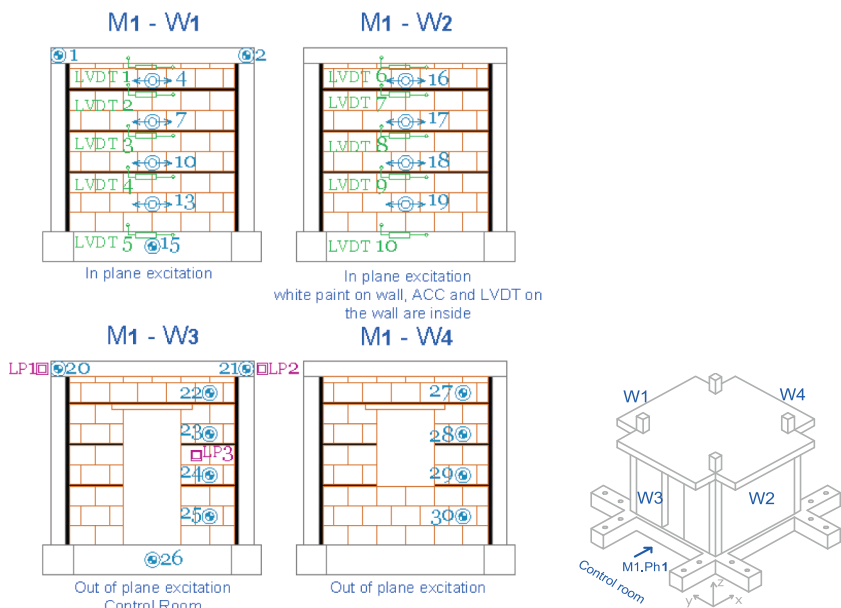


Fig. 4. Instrumentation setup Model 1 – Phase 1.

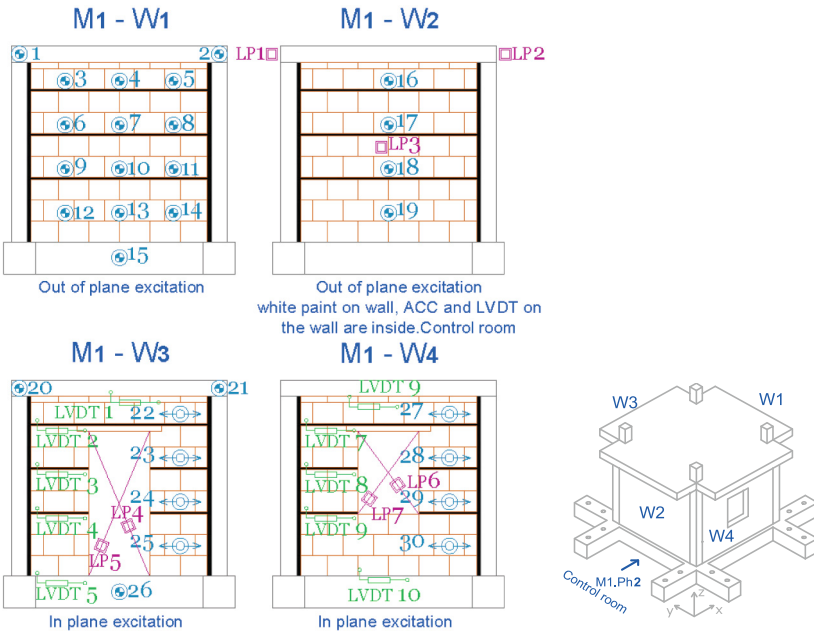


Fig. 5. Instrumentation setup Model 1 – Phase 2.

4 Results and Discussion

This section briefly illustrates the results of the shake table tests conducted on the two models. In particular, Figs. 9, 10, 11, 12 and 13 show the time histories of the accelerations recorded in correspondence of the shaking table and of the top slab under selected seismic inputs. Table 3 summarises the main results observed under the same seismic inputs in terms of peak inter-storey drift ratios (IDR) and top accelerations. It is noteworthy that both prototypes were able to sustain these inputs without experiencing any damage. The first prototype withstood very strong earthquake inputs, corresponding to peak ground accelerations (PGAs) up to 0.728g, without experiencing significant drifts and absolute accelerations, thanks to the stiffness and damping contribution of the Type 1 rubber joint system. A very low peak IDR of 0.69% was attained in phase 1 (full infills subjected to in-plane loading), and a larger one (1.98%) in phase 2, due to the reduced contribution of the infills with opening to the response.

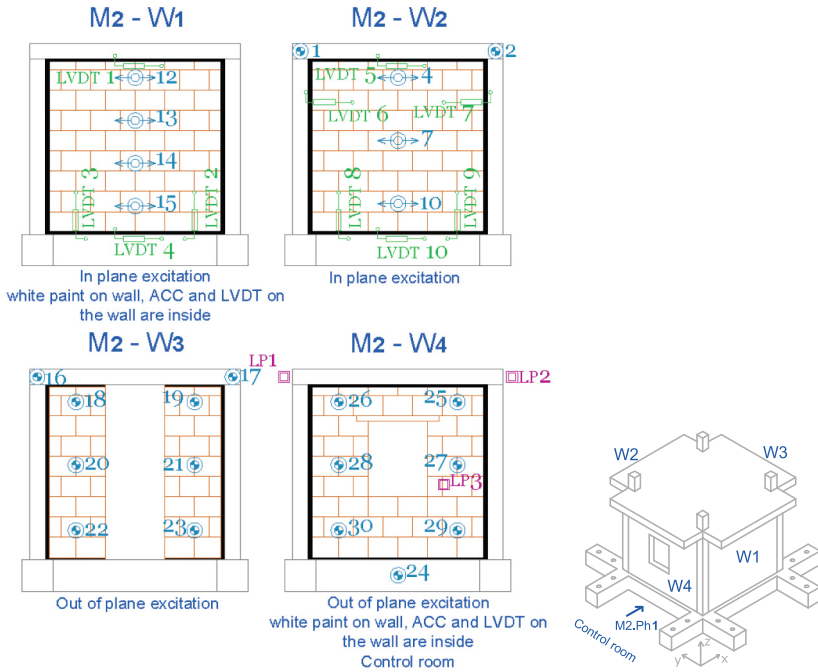


Fig. 6. Instrumentation setup Model 2 – Phase 1.

In testing the second prototype, seismic inputs only up to 0.322g were imposed, because stronger inputs would have resulted in significant damage to the RC frame (while still guaranteeing no damage in the isolated infill panel). The peak IDRs were respectively 2.20% and 2.91% in phase 1 and phase 2.

Figure 13 illustrates some of the results from the digital image correlation (DIC) analysis performed on the videos recorded during some tests. The localization of principal strains in the rubber joints (at the panel-frame interface and also between the masonry subpanels in Model 1) confirms that the joints performed as expected.

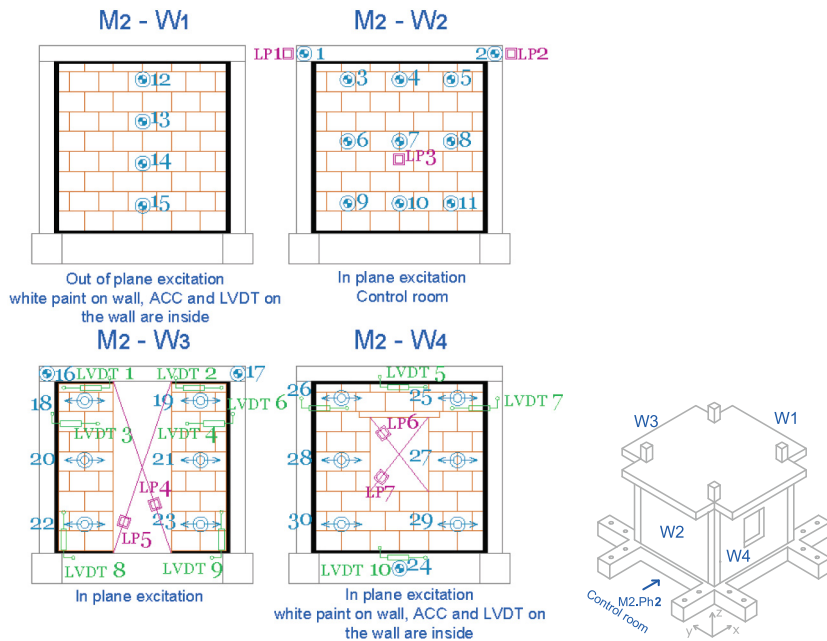


Fig. 7. Instrumentation setup Model 2 – Phase 2.



Fig. 8. DIC setup Model 1 and Model 2.

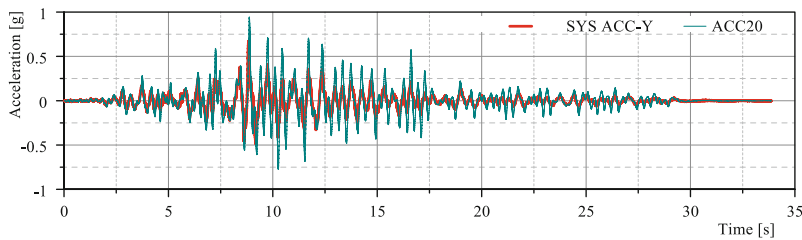


Fig. 9. Model 1 - Phase 1, Adana earthquake 100% [0.675g].

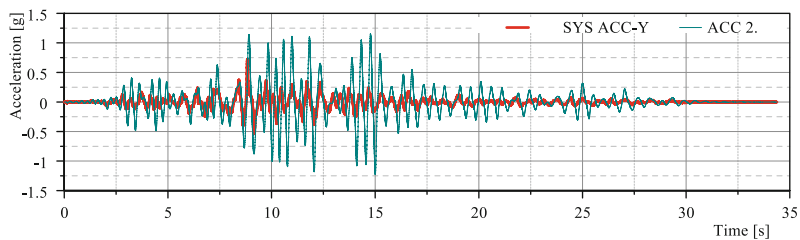


Fig. 10. Model 1 - Phase 2, Adana earthquake 100% [0.728g].

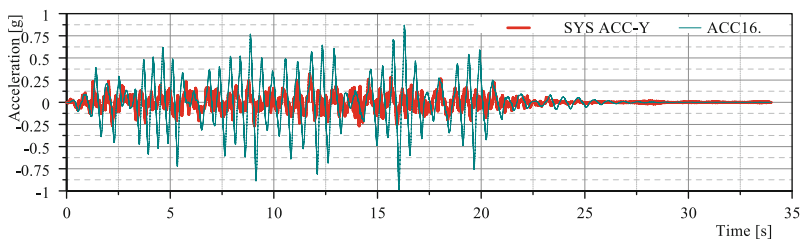


Fig. 11. Model 2 - Phase 1, Generated earthquake 60% [0.322g].

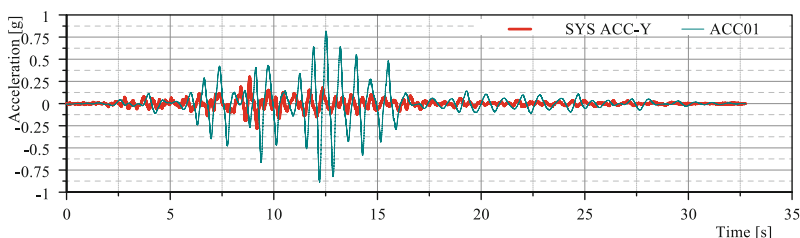
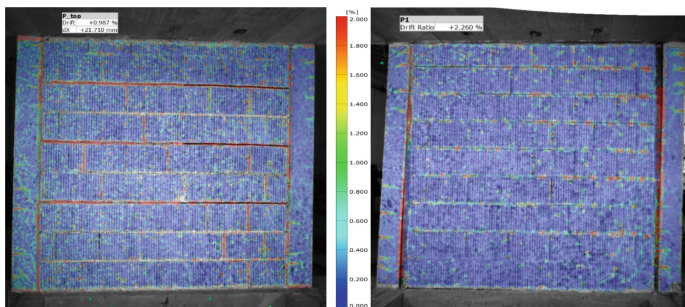


Fig. 12. Model 2 - Phase 2, Adana earthquake 50% [0.300g].

Table 3. Summary of main response parameters for Models 1 and 2 under selected record.

Input/output	Model 1 Phase 1	Model 1 Phase 2	Model 2 Phase 1	Model 2 Phase 2
Input record	Adana 100%	Adana 100%	Generated 60%	Adana 50%
PGA	0.675g	0.73g	0.32g	0.30g
Inter-storey drift	0.69%	1.98%	2.20%	2.91%
Top acceleration	0.93g	1.23g	0.98g	0.89g

**Fig. 13.** Model 1 - Phase 1 - Umbria EQ 100%, left and Model 2 - Phase 1 Generated EQ 60%, right. Major strain plot by DIC. Red denotes higher strains, blue denotes lower strains.

5 Conclusions

This paper has presented the experimental campaign conducted as part of the ERIES-FLEJOI project and some of the preliminary results. The project's primary objective is to further validate the effectiveness of rubber joint technology in reducing the seismic vulnerability of masonry infills and enhancing the earthquake performance of masonry-infilled reinforced concrete (RC) frames. As part of this research, two full-scale RC frame prototypes were tested using the shaking table facility at IZIIS. The first prototype featured a 'compliant system,' incorporating horizontal and vertical rubber joints within the masonry infill to improve flexibility and energy dissipation. The second prototype utilized a 'decoupling system,' where rubber joints were placed only at the interface between the infill and the surrounding RC frame to minimise stress transfer and prevent damage concentration. The results from the shake table tests provided strong evidence of the effectiveness of rubber joint technology. The findings demonstrated that RC frames with these innovative joint systems exhibited significantly improved seismic resilience, with reduced damage and enhanced energy dissipation, even under severe earthquake excitations. These outcomes highlight the potential of rubber joint solutions in earthquake-resistant RC structures, offering a promising approach to mitigating seismic risks in masonry-infilled frames.

Acknowledgements. This work is part of the transnational access project "ERIES-FLEJOI", supported by the Engineering Research Infrastructures for European Synergies (ERIES) project

(www.ries.eu), which has received funding from the European Union's Horizon Europe Framework Programme under Grant Agreement No. 101058684. This is ERIES publication number C60.

References

1. O'Reilly, G.J., Sullivan, T.J.: Probabilistic seismic assessment and retrofit considerations for Italian RC frame buildings. *Bull. Earthq. Eng.* **16**, 1447–1485 (2018)
2. Del Vecchio, C., et al.: Repair costs of existing RC buildings damaged by L'Aquila earthquake and comparison with FEMA P-58 predictions. *Earth. Spec.* **34**(1), 237–263 (2018)
3. Elgawady, M., Lestuzzi, P., Badoux, M.: A review of conventional seismic retrofitting techniques for URM. In: 13th int. brick and Block Masonry Conference, pp. 1–10 (2004)
4. Koutas, L., Bousias, S.N., Triantafillou, T.C.: Seismic strengthening of masonry-infilled RC frames with TRM: experimental study. *J. Compos. Constr.* **19**(2), 04014048 (2015)
5. Da Porto, F., Verlato, N., Guidi, G., Modena, C.: The INSYSME project: innovative construction systems for earthquake resistant masonry infill walls. In *Brick and block masonry*, 1st ed., p. 6 (2016). CRC Press. <https://doi.org/10.1201/9781315374963>
6. European Union's Horizon Europe Framework programme under grant agreement No [101058684] (Engineering Research Infrastructures for European Synergies-ERIES)
7. Tubaldi, E., et al.: Flexible joints for seismic-resilient masonry-infilled RC frames: preliminary analyses for shaking table testing. In: Proceedings of the 18th WCEE, Milan, Italy, 30 June–05 July 2024 (2024)
8. Ahmadi, H., Dusi, A., Gough, J.: A rubber-based system for damage reduction in infill masonry walls. In: Proceedings of the 16th WCEE (2017)
9. Dhir, P.K., Tubaldi, E., Orfeo, A., Ahmadi, H.: Cyclic shear behaviour of masonry triplets with rubber joints. *Constr. Build. Materials.* **351**, 128356 (2022)
10. Dhir, P.K., Tubaldi, E., Ahmadi, H., Gough, J.: Numerical modelling of reinforced concrete frames with masonry infills and rubber joints. *Eng. Struct.* **246**, 112833 (2021)
11. Dhir, P.K., Tubaldi, E., Pantò, B., Caliò, I.: A macro-model for describing the in-plane seismic response of masonry-infilled frames with sliding/flexible joints. *Earth. Eng. Struct. Dyn.* (2022)
12. Marinković, M., Butenweg, C.: Innovative decoupling system for the seismic protection of masonry infill walls in reinforced concrete frames. *Eng. Struct.* **197**, 109435 (2019)
13. Marinković, M., Butenweg, C.: Numerical analysis of the in-plane behaviour of decoupled masonry infilled RC frames. *Eng. Struct.* **272**, 114959 (2022)
14. Milijaš, A., et al.: Experimental investigation on the seismic performance of reinforced concrete frames with decoupled masonry infills considering in-plane and out-of-plane load interaction. *Bull Earthquake Eng.* (2024)
15. Rousakis, T., et al.: Deformable polyurethane joints and fibre grids for resilient seismic performance of reinforced concrete frames with orthoblock brick infills. *Polymers* **12**(12), 2869 (2020)
16. European Committee for Standardization. EN 12390–3: Testing hardened concrete – Part 3: Compressive strength of test specimens. CEN (2009)
17. International Organization for Standardization. EN ISO 15630–1: Steel for the reinforcement and prestressing of concrete – Test methods – Part 1: Reinforcing bars, wire rod and wire. ISO (2010)

Open Access This chapter is licensed under the terms of the Creative Commons Attribution 4.0 International License (<http://creativecommons.org/licenses/by/4.0/>), which permits use, sharing, adaptation, distribution and reproduction in any medium or format, as long as you give appropriate credit to the original author(s) and the source, provide a link to the Creative Commons license and indicate if changes were made.

The images or other third party material in this chapter are included in the chapter's Creative Commons license, unless indicated otherwise in a credit line to the material. If material is not included in the chapter's Creative Commons license and your intended use is not permitted by statutory regulation or exceeds the permitted use, you will need to obtain permission directly from the copyright holder.





Response Analysis of Column-Base Connections in Existing Steel Frames

Luigi Di Sarno^{1,2(✉)}, Mario D'Aniello², Fabio Freddi³, Stathis Bousias⁴,
Jing-ren Wu³, and Reza Khani⁵

¹ University of Liverpool, Liverpool L69 7ZX, UK

luigi.di-sarno@liverpool.ac.uk

² University of Naples Federico II, 80138 Naples, Italy

³ University College London, London WC1E 6BT, UK

⁴ University of Patras, 265 04 Patras, Greece

⁵ University of Tabriz, 51666-16471 Tabriz, Iran

Abstract. The seismic response of existing steel frames is significantly affected by the behaviour of column-base connections. Depending on their design, these connections can exhibit significantly different stiffness, strength, and ductility. While extensive research has been conducted to understand the response of these connections across a wide range of configurations, most studies have focused on uniaxial loading. However, the three-dimensional nature of earthquakes typically subjects these connections to biaxial bending and shear forces. To address this research gap, the ERIES-HITBASE (Earthquake Assessment of Base-Column Connections in Existing Steel Frames) project experimentally investigated the response of exposed column-base connections via bi-directional pseudo-dynamic (PsD) tests. These tests were carried out on a full-scale, three-dimensional steel frame at the Structures Laboratory of the University of Patras, Greece. The steel frame featured two types of column-base connections, *i.e.*, unstiffened and stiffened, representing respectively the base connections of an external moment-resisting frame and an internal gravity frame, respectively. The response of each component of column-base connections was monitored during the PsD-tests to capture their behaviour. This paper presents the preliminary results of numerical simulations conducted for the tested column-base connections. Local and response quantities are investigated, and threshold limits of damage are identified.

Keywords: Existing steel frames · base-column connections · Pseudo-dynamic tests · seismic performance · finite element modelling

1 Introduction

Column-base connections in steel frames typically consist of steel plates welded to the base of columns and anchored to the foundation system. These connections transfer axial forces, shear forces, and, in some cases, bending moments and represent essential components for the stability of the structure. However, several post-earthquake studies [e.g., 1–5] highlighted that, in existing structures, such components are often highly

vulnerable to seismic actions. In this context, there is a need for advanced assessment and retrofitting methods, for which limited guidance is offered in current European codes. For instance, the framework implemented in Eurocode 8-Part 3 [6] for assessing existing steel buildings primarily accounts for beam-to-column connections and lacks explicit guidance for column bases. Additionally, for such connections, there is also a need to establish proper definitions of moment-rotation relationships beyond their peak strength capacities [7, 8] and quantify deformation response for innovative displacement-based design/assessment approaches.

Previous studies have significantly enhanced our understanding of the behaviour of column-base connections across various configurations, including exposed base plate connections [e.g., 9-11] and embedded connections [e.g., 12-14], the latter being commonly used in many European countries for low- to medium-rise steel buildings. However, experimental work in the literature has been limited, with most studies focusing on uniaxial bending [e.g., 7, 15-20], while only a few have considered the effects of biaxial bending [e.g., 21, 22].

To this end, the ERIES-HITBASE project (Earthquake Assessment of Base-Column Connections in Existing Steel Frames) experimentally investigated the behaviour of exposed column-base plate connections. Bi-directional pseudo-dynamic tests (PsD) were conducted at the Structures Laboratory (STRULAB) of the University of Patras, Greece. These tests involved a full-scale specimen sub-structured from a non-seismically designed steel frame, featuring two types of exposed column-base plate connections, one representing moment connections and the other simple connections. This paper introduces the steel frame used as a test specimen and presents the preliminary validation of the finite element (FE) models in ABAQUS that will be used to further expand and generalise the experimental results.

2 Experimental Tests

2.1 Description of Case Study Building

The case study building is a two-storey, three-bay by three-bay steel frame; the geometry is shown in Fig. 1. The building was primarily designed for gravity loads following the European design code Eurocode 3 (EC3) [6], which considered the self-weight of partitions equal to 0.5 kN/m^2 and an imposed load of 3 kN/m^2 . Thus, HEB140 and HEB160 were used for perimeter and internal columns, respectively; such profiles were made of S355 steel. Moreover, the depth of the composite slab was 250 mm, which was made of C20/25 concrete and grade B450C reinforcement. It is worth noting that the bases of the perimeter columns were designed to be fixed connections to simulate the external moment-resisting frames, while those of the internal columns were pinned connections, representing internal gravity frames.

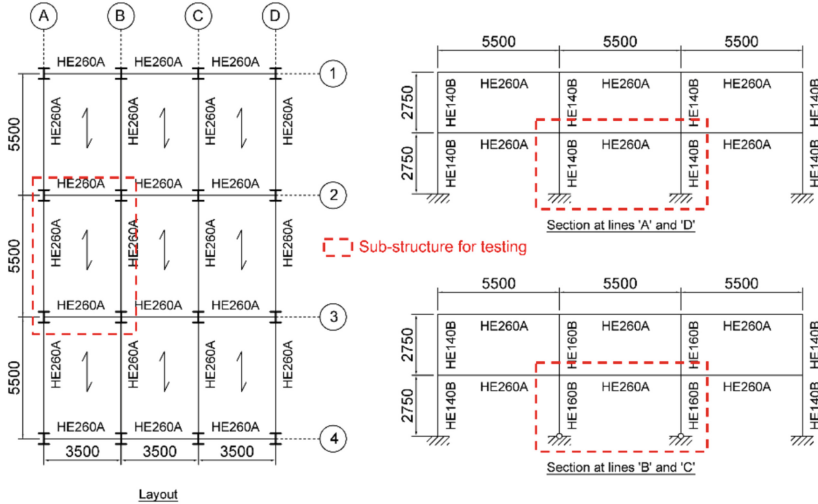


Fig. 1. Layout and section views of the case study steel frame (units in mm).

2.2 Description of the Test Mock-Up

Figure 2 shows the test mock-up, which was extracted from the case study building, as highlighted in Fig. 1. The specimen spans 5.5 m in the longitudinal direction and 3.5 m in the transverse direction and has a storey height of 2.75 m. Beams and columns were made of S355 steel, while the composite slab was made of C20/25 concrete and B450C reinforcement. Concrete footings supporting each column-base connection were also constructed in the lab to investigate the behaviour of column-base plate connections. These footings were made of C20/25 concrete and reinforced with B450C steel bars.

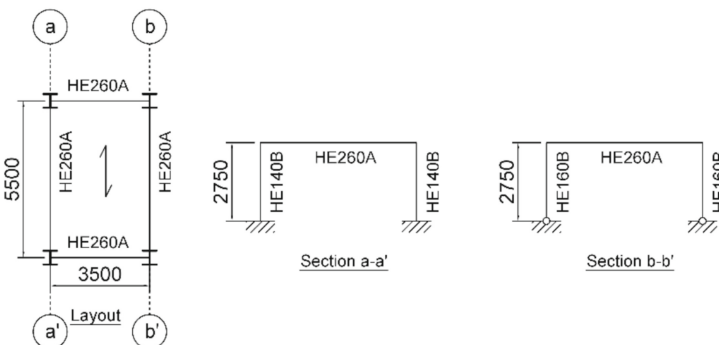


Fig. 2. Test specimen (units in mm).

The specimen had two types of column-base plate connections, one stiffened and the other unstiffened, corresponding to the fixed and pinned connections in the case

study building. Lastly, additional masses totalling 15.76 tons were placed on the slab to simulate the load imposed by the non-structural components and other loads.

2.3 Material Tests

Table 1 summarises the mechanical properties of the materials obtained from characterisation tests. The mean compressive strength of the C20/25 concrete used for the slab and foundation was determined from six samples, yielding values of 32.3 MPa and 34.2 MPa, respectively. The yield strength of the steel profiles ranged from 370 to 431 MPa, while the ultimate strength varied between 487 and 560 MPa. Additionally, the mean compressive strength of the mortar, measured using 50 mm cube samples, was found to be 47.1 MPa.

Table 1. Mean mechanical properties of materials (units in MPa).

	Concrete		Steel				Mortar
	Slab	Foundation	HE 260A	HEB 140	HEB 160	IPE 220	
Mean strength	32.3	34.2	-	-	-	-	47.1
Yield strength	-	-	431	370	431	391	-
Ultimate strength	-	-	549	505	560	487	-

2.4 Pseudo-Dynamic Tests

Figure 3 illustrates the test setup. The PsD-test method of the 3D-frame required the use of a number of actuators to achieve the desired deformation pattern, including translational displacements along the main axes and rotation about the vertical axis. The loading scheme to provide the necessary kinematics involved a pair of actuators acting in tandem along the long direction of the frame (*i.e.*, controllers 1 and 2 in Fig. 3a) and a third actuator operating in the transverse direction (*i.e.*, controller 3 in Fig. 3a). The former controlled the displacement of the frame along the longitudinal axis as well as its rotation, whilst the latter controlled the displacement of the structural system along the transverse axis.

Two diagonally opposite columns of the specimen, *i.e.*, Columns C1 and C3 in Fig. 3c, were densely instrumented. Figure 4 provides an overview of the instrumentation of both column bases, including the type and position of the relevant sensors, which enabled monitoring the key response parameters (*i.e.*, strains and inclination) at several points and sections.

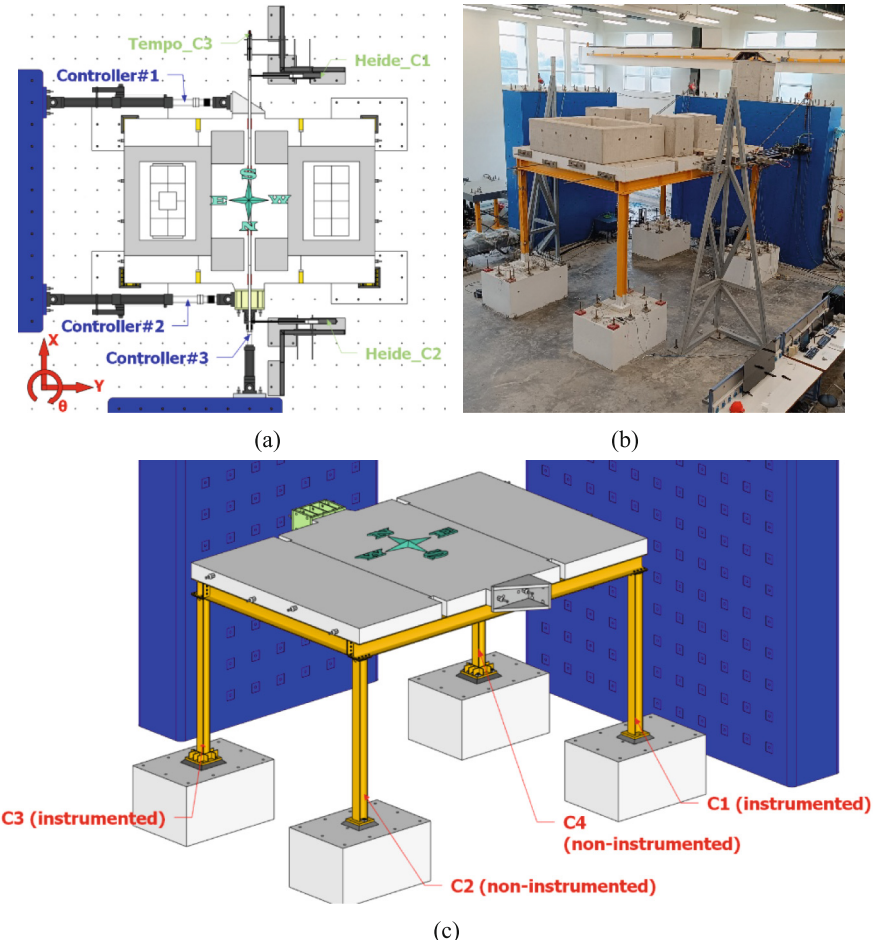


Fig. 3. Test setup: (a) plan view of the control equipment and labelling; (b) photo of the setup; (c) 3D view of the setup and column labelling.

The scope of the tests includes investigating the effects of sequential earthquakes and the influence of cumulative damage on the column-bases on the response of the structure. For this, a pair of natural seismic records was selected and sequentially applied to the structure, accounting for both horizontal components of the earthquakes. The two selected ground motion records referred to the 2016 Central Italy earthquakes and were extracted from the Engineering Strong-Motion Database (ESM) [24]. Preliminary analyses considered various combinations of the specimen axis along which each pair of records and their direction (sign) was applied. These analyses concluded that the most detrimental combination involved applying the record in Fig. 5a along the longitudinal (E-W) specimen (Y) axis, while the record in Fig. 5b applied along the N-S specimen (X) axis.

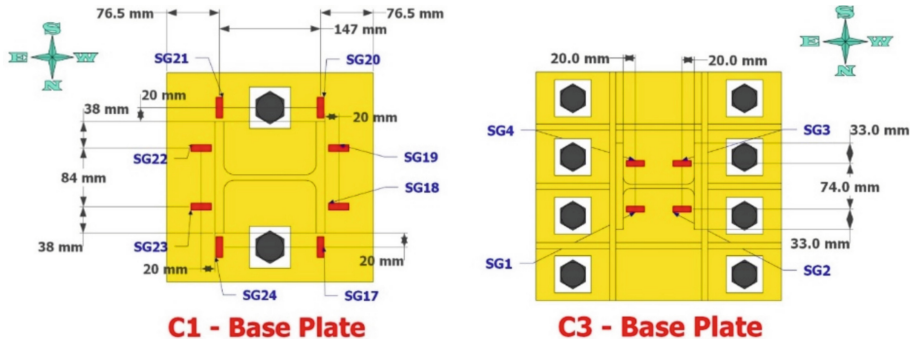


Fig. 4. Instrumentation located at the base plates (units in mm).

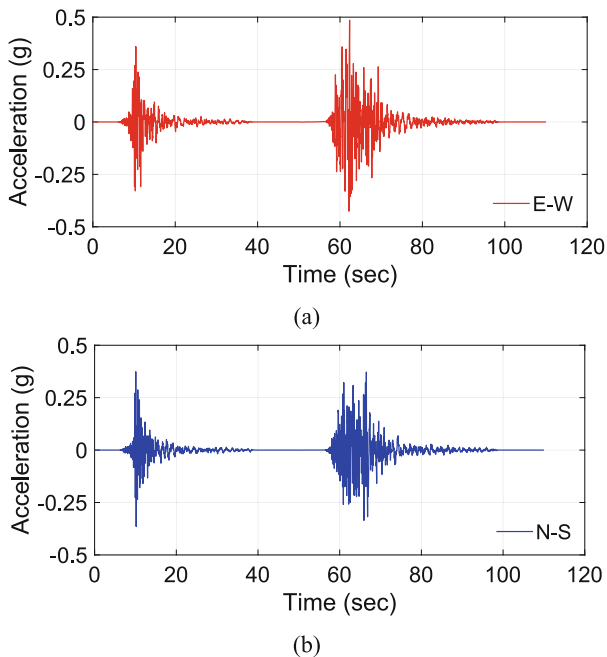


Fig. 5. Ground motion records for (a) longitudinal, Y-direction; (b) transverse, X-direction.

The test matrix of the experimental campaign is summarized in Table 2. Initially, the specimen underwent free vibration tests along both of its main axes to determine its modal properties. Following this, the specimen was subjected to quasi-static cyclic tests along both axes, achieving a maximum floor displacement of 27.5 mm in each direction. Finally, a series of PsD-tests were conducted on the specimen using the pre-selected ground motion records, with incremental scaling factors for the ground motion intensity (SF) ranging from 0.2 to 1.5.

Table 2. Test matrix for the 3D steel frame specimen in the laboratory.

No	Description	Note
1	Free vibration test: Y direction	10-mm pull-back
2	Free vibration test: X direction	10-mm pull-back
3	Quasi-static cyclic test: X direction	max. Displacement: 27.5 mm
4	Quasi-static cyclic test: Y direction	max. Displacement: 27.5 mm
5	Pseudo-dynamic (PsD) tests	Two concurrent sequences of records applied

3 Numerical Simulations

3.1 Description of the FE Model

An advanced 3D-FE model of the tested specimen was built using the ABAQUS software [25] to advance the understanding of the structural response observed in the tests. Figure 6 shows the FE model of the entire specimen, while Fig. 7 shows the modelling details for the connections (*i.e.*, base plates and beam-to-column joints). Bolts and anchor bolts were modelled explicitly to capture the local response of connections. The Concrete Damage Plasticity (CDP) model was used to define the concrete material, while the von Mises criterion was used to simulate the material properties of the steel elements. The composite concrete slab was assumed to behave elastically with a Young Modulus of 33 GPa. This assumption was based on test observations, where no damage or plastic response was detected in the slab. This allowed for a simplified modelling strategy and reduced computational effort during the analysis.

The interactions between the components were simulated by surface-to-surface contacts or tie constraints. For instance, the interaction between the grout and base plate, anchor bolts and plates, holes and anchor bolts, and bolts with beams and plates were modelled via surface-to-surface contact. The tangential behaviour was modelled using a penalty friction formulation, and “Hard” contact was employed for the normal behaviour. The friction coefficient for steel-to-steel was assumed to be 0.3 [26], while 0.1 for concrete-to-steel [27]. Conversely, for other surfaces without potential tangential or normal displacements, such as the slab with beams and welds attached to the plates, tie constraints were implemented. The slab was also tied to the main and secondary beams due to the presence of the studs. All parts were meshed with C3D8R elements. Fixed boundary conditions were assumed at the base of the foundations.

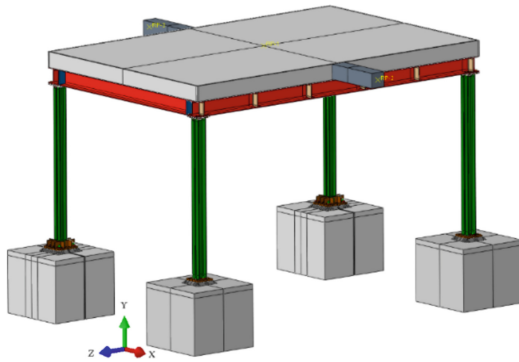


Fig. 6. 3D model of the test specimen in ABAQUS.

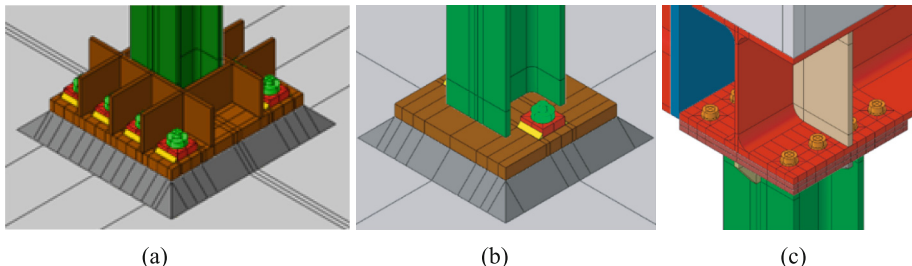


Fig. 7. Details of modelling of connections: (a) stiffened column-base connection; (b) unstiffened column-base connection; (c) beam-to-column connection.

3.2 Model Validation

A displacement-controlled load, with a time-history shown in Fig. 8, was applied along-side in the X direction and imposed in correspondence with Controller 3 (see Fig. 3a). This displacement history aims at simulating the experimental data extracted from the

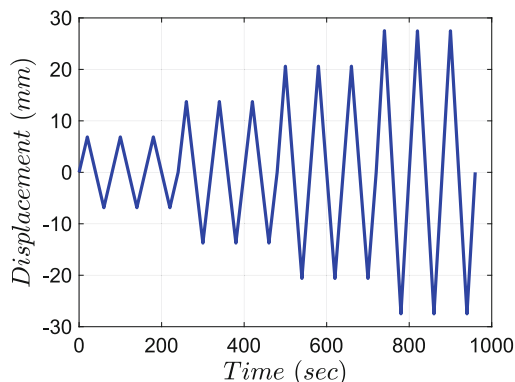


Fig. 8. Loading protocols implemented in the 3D model.

sensor named Tempo_C3 (see Fig. 3a). The resultant force-displacement curve in the X direction obtained from the numerical analyses is then compared with the experimental results, as shown in Fig. 9a. Moreover, Fig. 9b shows the deformed shape of the FE model corresponding to an imposed displacement of 20 mm (*i.e.*, corresponding to the black star in Fig. 9a). It is worth highlighting that the deformation is shown with a scale factor of 5. The results highlight the acceptable accuracy of the numerical model despite some discrepancies.

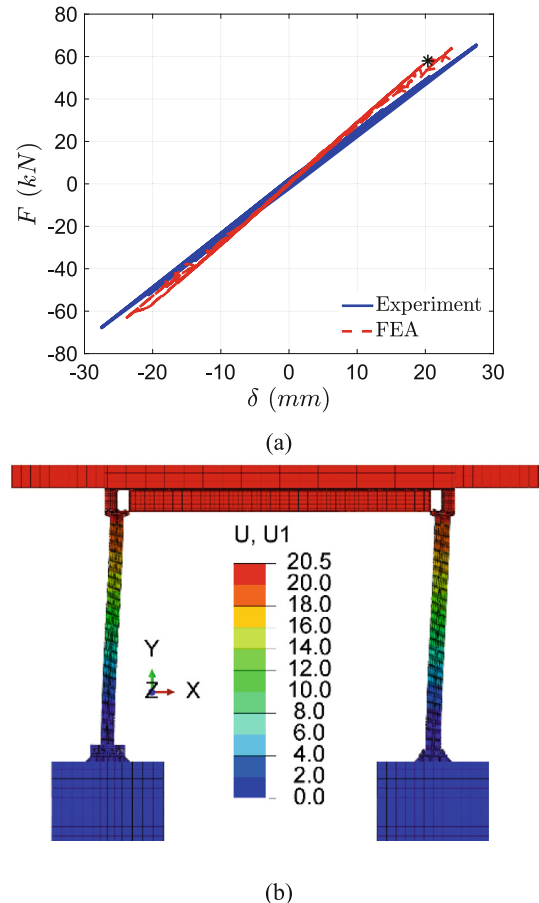


Fig. 9. Results from FE simulation: (a) force-displacement response; (b) deformed shape.

4 Conclusions

This paper summarises the preliminary results of an experimental and numerical study devoted to investigate the seismic response of exposed base-plate connections representative of gravity-load designed steel frames. Full-scale PsD-tests have been carried out on a single-story, one-by-one bay steel frame representing a sub-structure of a non-seismically designed structure. The scope of the tests includes investigating the effects of sequential earthquakes and the influence of cumulative damage on the column-bases on the response of the structures. Preliminary finite element simulations have also been carried out, and the numerical predictions satisfactorily mimic the experimental results. Further calibration will also be carried out to compare the local response at column bases. The calibrated model will then be used to perform numerical parametric analysis to investigate the seismic behaviour of column base connections.

Acknowledgements. This work is part of the transnational access project “ERIES-HITBASE”, supported by the Engineering Research Infrastructures for European Synergies (ERIES) project (www.ries.eu), which has received funding from the European Union’s Horizon Europe Framework Programme under Grant Agreement No. 101058684. This is ERIES publication number C79.

References

1. Mahin, S.A.: Lessons from damage to steel buildings during the Northridge earthquake. *Eng. Struct.* **20**(4–6), 261–270 (1998)
2. Clifton, C., Bruneau, M., MacRae, G., Leon, R., Fussell, A.: Steel structures damage from the Christchurch earthquake series of 2010 and 2011. *Bull. N. Z. Soc. Earthq. Eng.* **44**(4), 297–318 (2011)
3. Okazaki, T., Lignos, D.G., Midorikawa, M., Ricles, J.M., Love, J.: Damage to steel buildings observed after the 2011 Tohoku-Oki earthquake. *Earthquake Spectra* **29**(1_suppl), 219–243 (2013)
4. Di Sarno, L., Paolacci, F., Sextos, A.G.: Seismic performance assessment of existing steel buildings: a case study. *Key Eng. Mater.* **763**, 1067–1076 (2018)
5. Gutiérrez-Urzúa, L.F., Freddi, F., Di Sarno, L.: Comparative analysis of code based approaches for the seismic assessment of existing steel moment resisting frames. *J. Constr. Steel Res.* **181**, 106589 (2021)
6. CEN: EN 1998–3:2005. Eurocode 8: Design of structures for earthquake resistance - Part 3: Assessment and retrofitting of buildings. Comité Européen de Normalisation, Brussels (2005)
7. Latour, M., Piluso, V., Rizzano, G.: Rotational behaviour of column base plate connections: experimental analysis and modelling. *Eng. Struct.* **68**, 14–23 (2014)
8. Latour, M., Rizzano, G.: Full strength design of column base connections accounting for random material variability. *Eng. Struct.* **48**, 458–471 (2013)
9. Latour, M., Rizzano, G.: A theoretical model for predicting the rotational capacity of steel base joints. *J. Constr. Steel Res.* **91**, 89–99 (2013)
10. Fasaei, M.A., Banan, M.R., Ghazizadeh, S.: Capacity of exposed column base connections subjected to uniaxial and biaxial bending moments. *J. Constr. Steel Res.* **148**, 361–370 (2018)
11. You, Y.C., Lee, D.: Effect of anchors on the seismic performance of exposed column-base plate weak-axis connections. *J. Building Engineering* **32**, 101803 (2020)

12. Di Sarno, L., Pecce, M.R., Fabbrocino, G.: Inelastic response of composite steel and concrete base column connections. *J. Constr. Steel Res.* **63**(6), 819–832 (2007)
13. Grilli, D., Jones, R., Kanvinde, A.: Seismic performance of embedded column base connections subjected to axial and lateral loads. *J. Struct. Eng.* **143**(5), 04017010 (2017)
14. Inamasu, H., Kanvinde, A.M., Lignos, D.G.: Seismic design of non-dissipative embedded column base connections. *J. Constr. Steel Res.* **177**, 106417 (2021)
15. Zhou, F., Suita, K., Matsumiya, T., Kurata, M.: Tests on steel column bases with t-stub connections. *J. Structural and Construction Engineering* **69**(581), 117–125 (2004)
16. Lee, D.Y., Goel, S.C., Stojadinovic, B.: Exposed column-base plate connections bending about weak axis: I. numerical parametric study. *International Journal of Steel Structures* **8**(1), 11–27 (2008)
17. Lee, D.Y., Goel, S.C., Stojadinovic, B.: Exposed column-base plate connections bending about weak axis: II. experimental study. *International Journal of Steel Structures* **8**(1), 29–41 (2008)
18. Kanvinde, A.M., Grilli, D.A., Zareian, F.: Rotational stiffness of exposed column base connections: experiments and analytical models. *J. Struct. Eng.* **138**(5), 549–560 (2012)
19. Borzouie, J., MacRae, G.A., Chase, J.G., Rodgers, G.W., Clifton, G.C.: Experimental studies on cyclic performance of column base weak axis aligned asymmetric friction connection. *J. Constr. Steel Res.* **112**, 252–262 (2015)
20. Borzouie, J., MacRae, G.A., Chase, J.G., Rodgers, G.W., Clifton, G.C.: Experimental studies on cyclic performance of column base strong axis-aligned asymmetric friction connections. *J. Struct. Eng.* **142**(1), 04015078 (2016)
21. Cloete, R., Roth, C.P.: Column base connections under compression and biaxial moments: experimental and numerical investigations. *J. Constr. Steel Res.* **184**, 106834 (2021)
22. Seco, L.D., Couchaux, M., Hjaj, M., Neves, L.C.: Column base-plates under biaxial bending moment. *Eng. Struct.* **231**, 111386 (2021)
23. CEN. EN 1993–1–1:2005. Eurocode 3: Design of steel structures. Part 1–1: General rules and rules for buildings. Comité Européen de Normalisation, Brussels (2005)
24. Luzi, L., et al.: The engineering strong-motion database: a platform to access pan-european accelerometric data. *Seismol. Res. Lett.* **87**(4), 987–997 (2016)
25. Dassault Systèmes Simulia. F.E.A. Analysis user's manual 6.14 (2011)
26. CEN. EN 1993–1–8:2005. Eurocode 3: Design of steel structures. Part 1–8: Design of joints. Comité Européen de Normalisation, Brussels (2005)
27. British Standards Institution. Temporary works - Management procedures for the control of temporary works. British Standards Institution, London (2024)

Open Access This chapter is licensed under the terms of the Creative Commons Attribution 4.0 International License (<http://creativecommons.org/licenses/by/4.0/>), which permits use, sharing, adaptation, distribution and reproduction in any medium or format, as long as you give appropriate credit to the original author(s) and the source, provide a link to the Creative Commons license and indicate if changes were made.

The images or other third party material in this chapter are included in the chapter's Creative Commons license, unless indicated otherwise in a credit line to the material. If material is not included in the chapter's Creative Commons license and your intended use is not permitted by statutory regulation or exceeds the permitted use, you will need to obtain permission directly from the copyright holder.





Geographically Distributed Hybrid Testing of a Multi-Storey Timber Structure on Compliant Soil: Pilot Design

Ihsan E. Bal^{1,2} , Eleni Smyrou¹ , Stylianos Kallioras³ , Kamer Özdemir¹ , Tansu Gökçe⁴ , Adam Crewe⁴ , George Mylonakis^{4,9} , Roberto Tomasi⁵ , Angelo Aloisio⁵ , Solomon Tesfamariam⁶ , Stathis Bousias⁷ , Oh-Sung Kwon⁸ , and Anastasios Sextos⁴

¹ Hanze University of App. Sci., Research Centre Noorderruimte, Groningen, Netherlands
i.e.bal@pl.hanze.nl

² Faculty of Science and Engineering, ENTEG, University of Groningen, Groningen, Netherlands

³ Department of Civil Engineering and Architecture (DICAr), University of Pavia, Pavia, Italy

⁴ School of Civil, Aerospace and Design Engineering, University of Bristol, Bristol, UK

⁵ Faculty of Science and Technology, Norwegian University of Life Sciences, As, Norway

⁶ Department of Civil and Environmental Engineering, University of Waterloo, Waterloo, Canada

⁷ University of Patras, Patras, Greece

⁸ Department of Civil and Mineral Engineering, University of Toronto, Toronto, ON, Canada

⁹ Department of Civil and Environmental Engineering, Khalifa University, Abu Dhabi, UAE

Abstract. Timber construction is rapidly advancing in structural engineering due to its benefits, such as light weight, ease of prefabrication, and contribution to societal goals. With an increase in building height, however, knowledge garnered by coupling advance modelling and experimental testing will enable designers to push the boundary further. The ERIES-HYSTERESIS project will use geographically distributed hybrid testing to investigate energy dissipation characteristics and soil-structure interaction (SSI) responses of multi-story buildings constructed with mass timber. Testing large-scale timber structures with SSI considerations poses unique challenges, requiring an innovative hybrid testing methodology. Geographically distributed hybrid simulation involves designing a representative pilot structure and dividing it into subcomponents for simultaneous testing. This paper details the 3D design of the pilot structure, considering constraints required for hybrid testing. SSI is addressed as a critical factor, with the objective of identifying the hierarchy of failure between the soil, the wall-foundation connection and the hold-downs. A balance has been achieved between maintaining a realistic design and ensuring the experimental requirements remain within the capabilities of the involved laboratories.

Keywords: Hybrid Testing · Timber Structures · Soil-structure Interaction · Wind Loads · Earthquake Loads

1 Introduction to the ERIES-HYSTERESIS

Timber construction is rapidly gaining traction in structural engineering due to its notable advantages, such as lightweight properties and ease of prefabrication. Additionally, it aligns with emerging societal concerns, including reducing the carbon footprint of the construction sector, promoting circularity, enhancing energy efficiency, and advancing bio-based building solutions.

The ERIES-HYSTERESIS (Novel HYbrid teSTing of a gEographically distRibutEd multi-Storey tImber Structure) project seeks to leverage geographically distributed hybrid testing to provide experimental insights into the energy dissipation mechanisms and SSI behaviour of buildings using cross-laminated timber (CLT) panels. The findings of the project will significantly contribute to the development of multi-story timber structures in regions subject to strong wind, and moderate to high seismic forces. Given the complexity of the problem and the need for large-scale testing that accounts for SSI, a novel hybrid testing approach is necessary.

Despite increasing interest, the structural behaviour of large, multi-story timber buildings under lateral loads, such as wind and earthquakes, remains insufficiently explored. A critical gap in recent advancements is the lack of experimental validation, particularly in fundamental areas such as hysteretic energy dissipation, deformation capacity, and their interplay with SSI effects. In timber structures, especially, energy dissipation primarily occurs at element-to-element and timber-to-foundation connections, facilitated by energy-dissipating connectors and hold-downs. The effectiveness of these components, and consequently, the damping characteristics of the entire structure, depend largely on the displacement profile, which is significantly influenced by SSI. Therefore, generating experimental data that incorporates both energy dissipation elements and SSI effects is essential for advancing the design of large multi-story timber buildings under lateral loading. However, achieving this within a single testing facility is impractical, as SSI and full-scale structural responses are typically evaluated in separate experimental setups. Combining large-scale SSI test rigs with shake tables or pseudo-dynamic testing configurations is constrained by laboratory space and equipment limitations. ERIES-HYSTERESIS addresses this challenge by segmenting the complex problem into manageable parts and distributing them across multiple specialized testing facilities. By harnessing advancements in computational power and high-speed networking, geographically distributed hybrid testing emerges as a viable solution.

To achieve the goals mentioned above, ERIES-HYSTERESIS will simultaneously utilize the SoFSI (Bristol) and STRULAB (Patras) facilities, alongside European and Canadian partners with extensive experience in geographically distributed hybrid testing and timber structures design.

2 State-of-the-Art in Large Timber Structural Testing

Research on the use of mass timber and CLT for multi-story construction started in countries where timber construction is traditionally widespread while regulations on structural design under horizontal loads are mature enough. Studies in New Zealand, for example, supported by a series of experiments [1], have shown that prestressing technology, when combined with the timber elements, can provide ideal hysteretic damping and re-centering properties under seismic loads.

For addressing the energy dissipation issue at the timber connections, series of experimental and numerical studies have been published, a significant portion of which was co-authored by the partners in the ERIES-HYSTERESIS consortium. Schneider et al. [2] compare experimental and numerical models for timber mechanical connectors under cyclic loading and conclude that energy damage index is a good indicator to be considered in seismic design. Blomgren et al. [3] propose the use of buckling-restrained braces (BRBs) as a lateral load resisting system in timber construction, while Tesfamariam et al. [4] present the concept of damped shear walls for significantly improving the energy dissipation capacity of plywood panel construction. Other energy dissipating devices have been studied in the literature, such as the asymmetric friction connectors [5] and steel cushions [6]. Energy dissipating devices for timber construction have also been extensively tested for seismic retrofitting purposes [7].

In multi-story construction with CLT panels, hold-downs appear as an efficient solution. Tannert and Loss [8] present contemporary and novel hold-down systems such as internal-perforated steel plates fastened with self-drilling dowels, hyper-elastic rubber pads with steel rods, and high-strength hold-downs with self-tapping screws. It has been shown that an efficient design of a hold-down system enables constructing high-rise timber structures, a concept that has been utilized by Teweldebrhan and Tesfamariam [9] and [10]. The TALLWOOD project in the US [11] has been another attempt to collect experimental evidence on the seismic response of tall timber structures, while the SSI component, crucial for identifying the response of the energy dissipating devices, was not considered.

All these recent developments in the state-of-the-art highlight that with an efficient energy dissipation, large multi-story, and high-rise mass timber construction is feasible [12]. The major knowledge gap is, thus, a large-scale testing of the energy dissipation, the interaction of the energy dissipators and connectors with the mass timber system, as well as the possible contribution of the SSI in this interaction. This knowledge gap is particularly important in horizontal loading conditions, such as in common different hazards such as wind and earthquake loads [13]. ERIES-HYSTERESIS will address this gap, by using a geographically distributed hybrid testing approach [14].

3 Design of a 3D Pilot Structure

In the HYSTERESIS project, a 3D pilot structure has been designed based on realistic assumptions. This structure must balance realism with constraints in the testing facilities. The most essential criterion is that it must be suitable for sub-structuring to enable effective experimental studies.

Sub-structuring is a technique that breaks down a complex structure into multiple substructures to facilitate testing and analysis. Instead of testing the entire structure as a single entity, only the critical components are physically tested, while the remaining parts are either numerically simulated or tested separately at different facilities. This approach helps overcome the physical and logistical constraints of full-scale testing. A schematic substructuring workflow is given in Fig. 1.

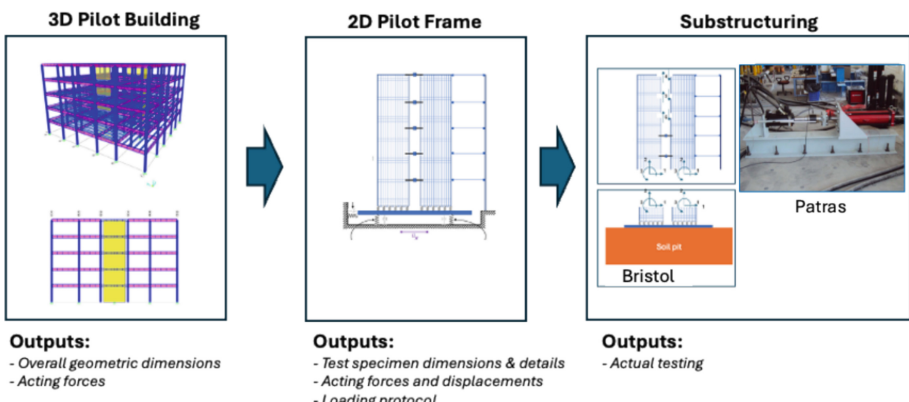


Fig. 1. Schematic workflow steps of geographically distributed hybrid testing; 3D Pilot Design, 2D Pilot Frame Extraction, and Substructuring.

The main sub-structuring criteria for the HYSTERESIS project are as follows:

- 3 degrees of freedom (DOF) to be controlled simultaneously at the SoFSI Lab (Bristol).
- 2 DOF to be controlled simultaneously at STRULAB (Patras).
- The test specimen at SoFSI must fit within the constraints of the soil pit, including its depth, width, and length.
- The foundation of the specimen in the soil pit at SoFSI Lab must allow near-unconstrained soil deformations, which requires:

Sufficient depth of the soil layers beneath the foundation.

Adequate distance between the foundation edges and the soil pit walls to minimize boundary effects.

- The forces and deformations at the sub-structuring interfaces must remain within the force and stroke capacities of the actuators at both laboratories.

By meeting these criteria, the 3D pilot structure will ensure realistic yet experimentally feasible hybrid testing, integrating SSI effects and lateral loading conditions for a comprehensive structural response assessment. The 3D pilot structure chosen for the ERIES-HYSTERESIS is given in Fig. 2.

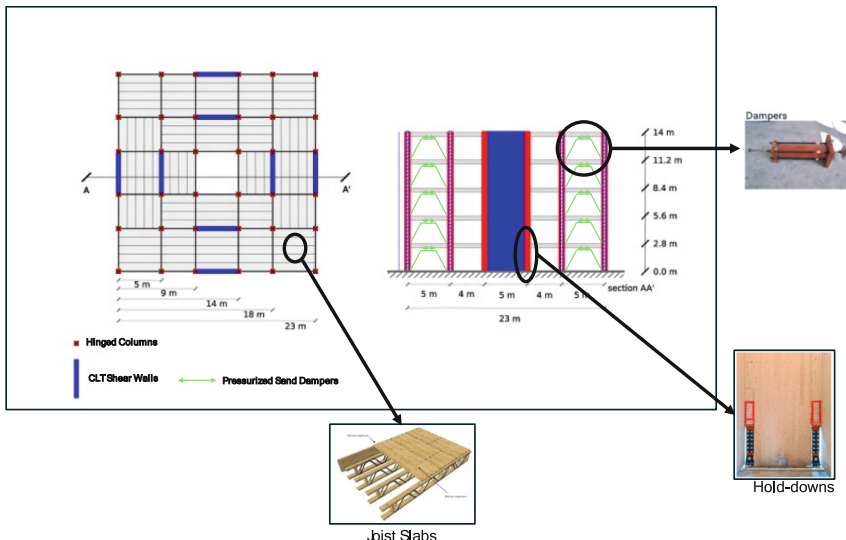


Fig. 2. Plan and elevation of the 3D pilot structure with the structural components, including hinged columns, joist slabs, pressurized sand dampers and CLTs connected with hold-downs.

The 3D pilot structure is assumed to be built in Athens, Greece, where wind and seismic loads are close to average (i.e. not extreme) when the whole Europe is considered. The wind design parameters per Eurocode [15] are as follow:

- Wind Velocity, V_b : 33m/s
- Terrain Category: II (open terrain with low vegetation)
- Orography Factor, $C_o(z)$: 1.0 (amplification of the wind speed due to terrain elevation changes)
- Turbulence Factor, k_1 : 1.0
- Structural Factor, $C_s C_d$: 1.0
- Air Density, ρ : 1.25 kg/m³
- Windward and Leeward Coefficients: 0.8 and 0.5, respectively.

Similarly, the seismic design input parameters are as follow:

- Ground acceleration, $a_g/g = 0.16$
- Spectrum Type: 1
- Soil Type: C
- Soil Factor, S : 1.15
- Spectrum Corner Periods, T_b , T_c and T_d : 0.2, 0.6 and 2.0, respectively

The design spectrum (EN 1998-1, 2004 [15]) used for the seismic design of the 3D pilot structure, as well as the 7 real acceleration records selected and used for the nonlinear time history analyses are given in Fig. 3.

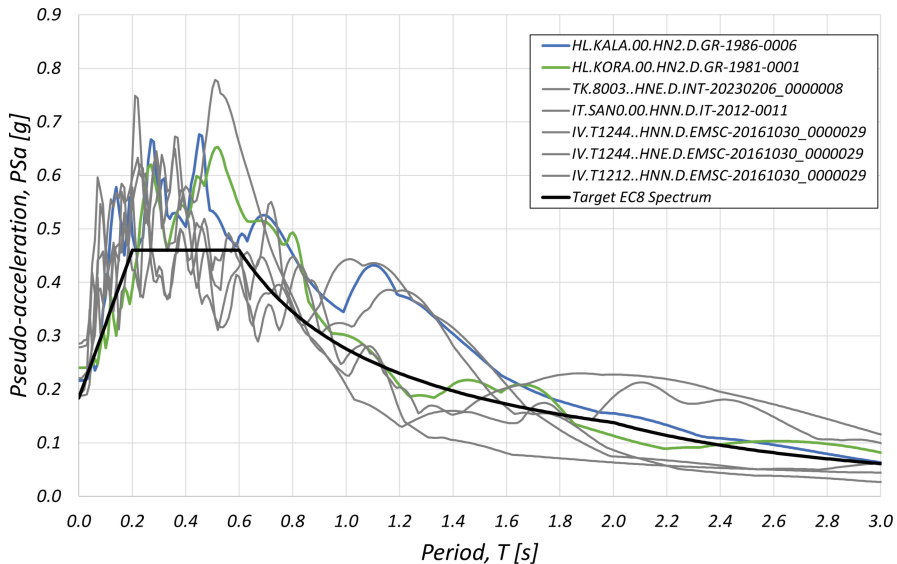


Fig. 3. Design acceleration spectrum and the selected set of records for nonlinear time history analyses.

4 Design Iterations, Nonlinear Model and the Preliminary Test Setup

Since the 3D pilot structure is designed with hinged columns and follows a frame-type layout, the lateral load resistance is primarily provided by symmetrically placed frames, ensuring a well-balanced structural response to lateral forces (see Fig. 2). Given this symmetrical configuration, extracting a single representative frame for detailed lateral load analysis is both practical and sufficient. By isolating this lateral load-bearing frame, a dedicated numerical model is developed using OpenSeesPy [16, 17].

For the computational model, a frame-based representation is adopted, where the timber elements, including cross-laminated timber (CLT) panels and glulam hinged columns, are modeled as elastic elements. In contrast, hold-downs and pressurized sand dampers, which play a crucial role in energy dissipation, are represented as zero-length elements with nonlinear hinge definitions to capture their force-deformation behavior (see Fig. 4). The fundamental period of the system is calculated as 0.52 s, which is a reasonable value given the height and overall mass distribution of the structure.

The design process of the 3D pilot structure is influenced by multiple parameters, each carefully considered to ensure structural feasibility and performance. These parameters have been discussed and refined through several consortium meetings, where feedback and insights were incorporated into the final design decisions. Given the iterative nature of the design process, a parametric modeling approach has been implemented to facilitate rapid adjustments and evaluations. To achieve this, a parametric design file has been created within the Jupyter Python environment, allowing for easy modification of key design variables. The complete workflow of the iterative design process is illustrated in Fig. 5, demonstrating the structured approach to refining the final model.

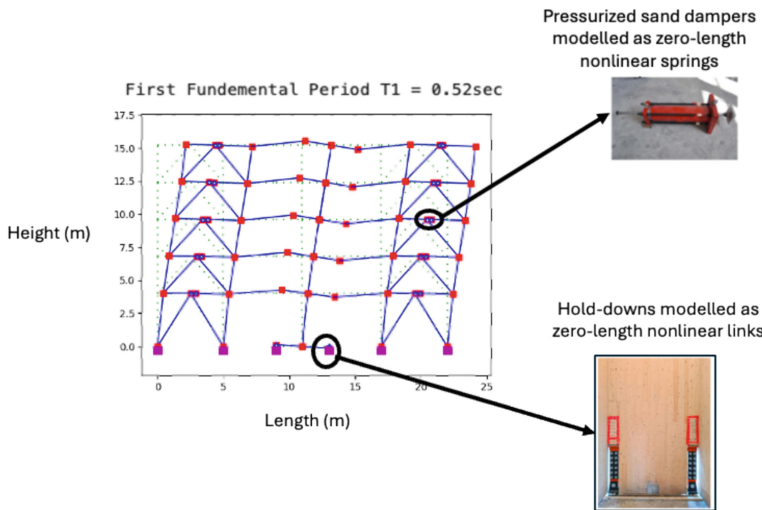


Fig. 4. Numerical model representation of the multi-story timber structure. Pressurized sand dampers are modelled as zero-length nonlinear springs, while hold-downs are represented as zero-length nonlinear links.

Pressurized sand dampers are incorporated as an additional lateral load-resisting system (see references [18–20]) due to their cost-effectiveness, tuneable hysteretic response, and rate-independent energy dissipation. These dampers have already been experimentally tested by the STRULAB (Patras) team, ensuring their effectiveness in dissipating energy under lateral loads. In addition to the sand dampers, recentring hold-downs are integrated into the design as part of the primary lateral load-bearing system. These hold-downs feature a flag-shaped hysteresis loop (Fig. 6), which enables the structure to self-centre after experiencing lateral forces, effectively minimizing residual deformations and preventing permanent damage.

Nonlinear time history analyses were performed on the 2D pilot frame, extracted from the 3D pilot structure. In Eurocode-based seismic design [15], an equivalent elastic approach is typically used, where elastic seismic forces are divided by a behaviour factor (q -factor) to account for the structure's ductility. However, this method does not explicitly capture the inelastic response, energy dissipation, or dynamic interactions among structural components. For ductile timber structures, this factor is $q = 4$, yet the

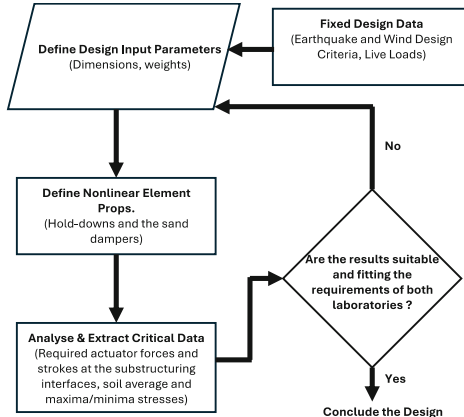


Fig. 5. Iterative design workflow used in the Jupyter Python Notebook.

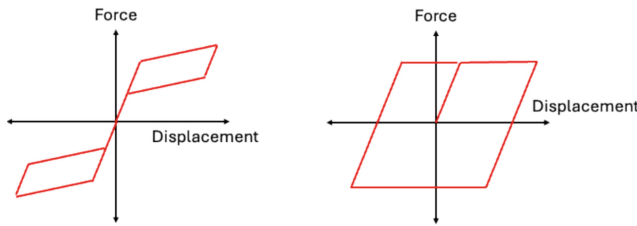


Fig. 6. Schematic force-displacement loops for the re-cantering hold-downs (left) and the pressurized sand dampers (right).

actual force redistribution and damage mechanisms depend on the nonlinear behaviour of connections and dissipative devices.

As a result, the distribution of forces among different nonlinear components, such as hold-downs and dampers, is governed by the overall response of the structure and its dynamic interaction with a given ground motion. This force distribution may deviate significantly from initial design assumptions, particularly due to higher-mode effects and coupled lateral and vertical deformations, potentially influencing structural performance. To ensure accuracy and reliability in the experimental phase, it is essential to verify these nonlinear effects before proceeding with the physical tests.

The results presented in Fig. 7 indicate that the maximum and minimum recorded base shears occasionally exceed the design base shear at several instances. However, when examining the individual responses of each structural element, no significant exceedance of the design forces was observed. This suggests that the 3D pilot structure remains within the expected performance limits, making it suitable for further sub-structuring and hybrid testing.

The discrepancy between the design base shear and the nonlinear time history results can be attributed to the activation of higher mode effects. While the seismic design follows a first-mode approach, where the equivalent static forces are distributed according

to a simplified modal response, nonlinear link elements present in the model introduce complex dynamic interactions, leading to the engagement of higher modes. These higher-mode contributions, which are typically not captured in conventional design methods, influence the base shear fluctuations observed in the time history analyses. Despite this, the absence of significant force exceedance in individual elements provides confidence in proceeding with the next phase of the sub-structuring process.

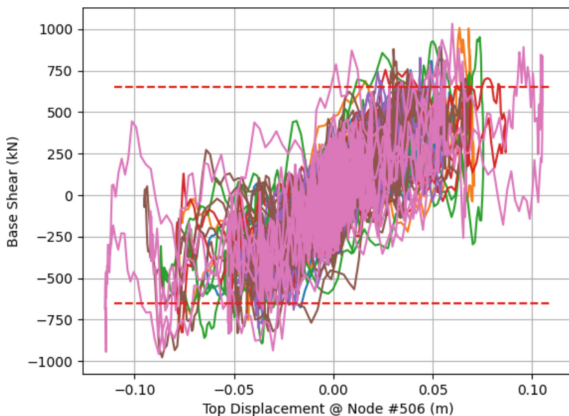


Fig. 7. Base Shear – Top Displacement from the nonlinear time history analyses, monitoring the top node, and comparison to the design base shear (horizontal dashed lines).

Since the designed structure is intended for geographically distributed hybrid testing, several constraints must be carefully addressed. Firstly, both the pressurized sand dampers and the hold-downs selected for the design must be non-rate dependent, ensuring their behaviour remains consistent across different loading speeds. Furthermore, the hybrid testing algorithm requires accurate definition of the initial stiffness of each component in the system.

Two potential critical points in this setup are identified:

- Pressurized sand dampers – Their initial stiffness may be influenced by the applied pressure, affecting their dynamic response.
- SSI – Instability in soil deformations could introduce unexpected variability in the hybrid testing algorithm, potentially compromising the accuracy of the experiment if deformations become excessive.

To mitigate these uncertainties, both the pressurized sand dampers and the SSI conditions must be pre-tested before commencing the full-scale hybrid experiments. This ensures that the numerical assumptions made in the computational model are validated and adjusted if necessary, improving the overall reliability of the testing procedure.

A 3D CAD model of the preliminary test setup for the SoFSI lab has been developed, as shown in Fig. 8. This setup is designed to meet key experimental requirements, with the following main features:

- Control of the CLT wall at the interface between the top of the ground floor and the bottom of the first floor.
- Application of compatibility and equilibrium at this interface by accurately controlling three degrees of freedom (DOF).
- The 3DOF control system consists of i) two vertical actuators responsible for controlling axial deformation and rotation of the control point of the specimen, and ii) one lateral actuator for controlling lateral deformation of the control point of the specimen.

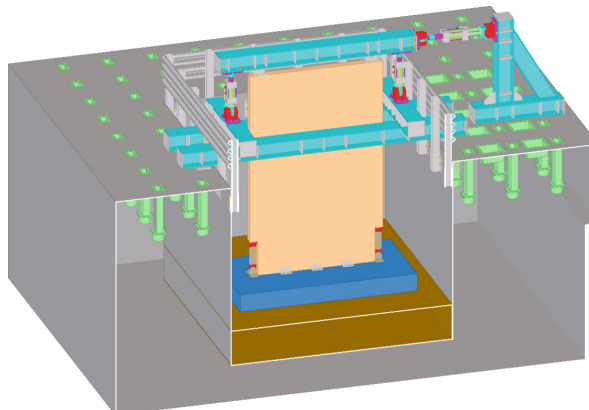


Fig. 8. Preliminary test setup design for the SoFSI Lab, where the specimen of the ground story CLT panel and hold-downs is placed on soil.

At the time of writing this paper, the optimization process for the SoFSI test setup was still ongoing. The primary optimization parameters under consideration include:

- Soil depth beneath the foundation to ensure accurate SSI.
- Foundation and specimen dimensions, carefully chosen to maintain appropriate boundary conditions within the soil pit.
- Optimization of the steel resistance frame, exploring the potential for scaling the specimen while maintaining structural integrity.

This structured setup ensures a well-controlled experimental environment for evaluating soil-structure interaction and dynamic response characteristics under seismic and other lateral loading conditions.

5 Conclusions and Future Work

This study presents the design and preliminary assessment of a geographically distributed hybrid testing approach for evaluating the seismic and wind performance of a multi-story timber structure on compliant soil. The proposed 3D pilot structure, developed within the ERIES-HYSTERESIS project, integrates SSI effects and energy dissipation

mechanisms, such as pressurized sand dampers and recentering hold-downs, ensuring a realistic yet experimentally feasible test configuration. Nonlinear time history analyses conducted on the extracted 2D pilot frame confirmed that the global base shear occasionally exceeds the design values due to higher mode activation, but individual structural components remained within acceptable force limits. These findings validate the sub-structuring approach and provide confidence in proceeding with the experimental phase. Additionally, the parametric design framework implemented in Jupyter Python offers a flexible methodology for iterative optimization, allowing adjustments to key structural parameters before full-scale testing.

The next phase of the project involves the final optimization and validation of the SoFSI and STRULAB test setups, focusing on critical parameters such as soil depth, foundation dimensions, and steel resistance frame scaling. Additionally, pre-testing of pressurized sand dampers and SSI effects will be conducted to refine the numerical assumptions and ensure seamless integration with hybrid testing algorithms. The geographically distributed hybrid testing approach will be executed, leveraging the SoFSI (Bristol) and STRULAB (Patras) facilities for synchronized experimental studies. The outcomes of this research will contribute to the hybrid testing capabilities in European structural test facilities, while fostering advancements in multi-story mass timber construction, particularly in seismic-prone and high-wind regions.

Acknowledgements. This work is part of the transnational access project “ERIES-HYSTERESIS”, supported by the Engineering Research Infrastructures for European Synergies (ERIES) project (www.ries.eu), which has received funding from the European Union’s Horizon Europe Framework Programme under Grant Agreement No. 101058684. This is ERIES publication number C52.

References

1. Palermo, A., Pampanin, S., Buchanan, A., Newcombe, M.: Seismic design of multi-storey buildings using laminated veneer lumber (LVL). In: NZ Society of Earthquake Engineering, Annual National Conference, Wairakei, New Zealand, March 2005 (2005)
2. Schneider, J., Shen, Y., Stiemer, S.F., Tesfamariam, S.: Assessment and comparison of experimental and numerical model studies of cross-laminated timber mechanical connections under cyclic loading. *Const. & Building Mat.* **77**, 197–212 (2015)
3. Blomgren, H.E., Koppitz, J.P., Valdes, A.D., Ko, E.: The heavy timber buckling-restrained braced frame as a solution for commercial buildings in regions of high seismicity. In: WCTE World Conference on Timber Engineering, Vienna, Austria (2016)
4. Tesfamariam, S., Wakashima, Y., Skandalos, K.: Damped timber shear wall: shake-table tests and analytical models. *ASCE J. Struct. Eng.* **147**(6), 04021064 (2021)
5. Aloisio, A., Contento, A., Boggian, F., Tomasi, R.: Probabilistic friction model for aluminium-steel Asymmetric Friction Connections (AFC). *Eng. Struct.* **274**, 115159 (2023)
6. Yüksel, E., et al.: Behaviour of steel cushions subjected to combined actions. *Bull. Earthq. Eng.* **16**(2), 707–729 (2018)
7. Boggian, G., Tardo, C., Aloisio, A., Marino, E.M., Tomasi, R.: Experimental cyclic response of a novel friction connection for seismic retrofitting of RC buildings with CLT panels. *ASCE J. Struct. Eng.* **148**(5), 04022040 (2022)

8. Tannert, T., Loss, C.: Contemporary and novel hold-down solutions for mass timber shear walls. *Buildings* **12**, 202 (2022). <https://doi.org/10.3390/buildings12020202>
9. Teweldebrhan, B.T., Tesfamariam, S.: Performance-based design of tall-coupled cross-laminated timber wall building. *Earthq. Engng Struct. Dyn.* **51**, 1677–1696 (2022)
10. Skandalos, K.: Seismic design and demand assessment of seismically isolated and innovative timber lateral load resisting systems. PhD Thesis, The University of British Columbia (2021)
11. NHERI Tallwood Project. <http://nheritallwood.mines.edu>. Accessed 15 Dec 2022
12. Tesfamariam, S.: Tall timber buildings: Innovative building design and damping considerations. *Struct. Eng. CTBUH J.* **1**, 40–47 (2022)
13. Tesfamariam, S.: Performance-based design of tall timber buildings under earthquake and wind multi-hazard loads: past, present, and future. *Front. Built Environ.* **8**, 848698 (2022)
14. Mojiri, S., Mortavazi, P., Kwon, O.S., Christopoulos, C.: Seismic response evaluation of a five-story buckling-restrained braced frame using multi-element pseudo-dynamic hybrid simulations. *Earthquake Engng Struct Dyn.*, pp. 1–23 (2021)
15. European Committee for Standardization (2004) EN 1998-1: Eurocode 8: Design of structures for earthquake resistance – Part 1: General rules, seismic actions and rules for buildings. CEN, Brussels
16. McKenna, F., Fenves, G.L., Scott, M.H.: Open system for earthquake engineering simulation (OpenSees). Pacific Earthquake Engineering Research Center, University of California, Berkeley (2000). <https://opensees.berkeley.edu>
17. Zhu, M., Zsarnóczay, A., Scott, M.H., McKenna, F., Ryan, K.L.: OpenSeesPy: Python Library for the OPENSEES FINITE ELEMENT FRAMEWORK (2018). <https://openseespydoc.readthedocs.io>
18. Makris, N., Palios, X., Moghimi, G., Bousias, S.: Pressurized sand damper for earthquake and wind engineering: design, testing, and characterization. *J. Eng. Mech.* **147**(4), 04021014 (2021)
19. Kalfas, K.N.: Component testing of cost-effective pressurized sand dampers. In: Proceedings of the 18th World Conference on Earthquake Engineering. International Association for Earthquake Engineering, Tokyo (2024)
20. Kalfas, K.N., Makris, N.: Assessment of the effect of design parameters of pressurized sand dampers from component testing. *J. Eng. Mech.* **150**(1), 04023106 (2024)

Open Access This chapter is licensed under the terms of the Creative Commons Attribution 4.0 International License (<http://creativecommons.org/licenses/by/4.0/>), which permits use, sharing, adaptation, distribution and reproduction in any medium or format, as long as you give appropriate credit to the original author(s) and the source, provide a link to the Creative Commons license and indicate if changes were made.

The images or other third party material in this chapter are included in the chapter's Creative Commons license, unless indicated otherwise in a credit line to the material. If material is not included in the chapter's Creative Commons license and your intended use is not permitted by statutory regulation or exceeds the permitted use, you will need to obtain permission directly from the copyright holder.





Dynamic In-Situ Testing of a 15-Year-Old Friction-Pendulum Base Isolation System

A. Rapone^{1(✉)}, P. M. Calvi², G. Gabbianelli³, T. C. Becker⁴, H. Sucuoğlu⁵,
B. Chalarca³, Igor Lanese⁶, Elisa Rizzo-Parisi⁶, F. Dacarro⁶, and Gerard J. O'Reilly¹

¹ University School for Advanced Studies IUSS Pavia, Pavia, Italy
aldo.rapone@iusspavia.it

² Civil and Environmental Engineering, University of Washington, Seattle, Washington, USA

³ Department of Civil Engineering and Architecture, University of Pavia, Pavia, Italy

⁴ Department of Civil and Environmental Engineering, University of California, Berkeley, CA, USA

⁵ Department of Civil Engineering Middle, East Technical University, Ankara, Turkey

⁶ European Centre for Training and Research in Earthquake Engineering, Pavia, Italy

Abstract. Base isolation systems represent one of the most effective strategies for the seismic protection of buildings and infrastructure, applicable to both new constructions and retrofitting projects. Base isolation has received significant attention over the past few decades that led to remarkable improvements of this technology, resulting in the progressive deployment of better performing devices. Despite these significant advancements, the current understanding of the performance of isolated structures primarily stems from component-level testing of brand-new isolation bearings, while comprehensive studies on the long-term behavior of base isolation systems, particularly involving large groups of isolators in real-world applications, remain limited. The PASFIT project, introduced in this paper, addresses this knowledge gap by conducting extensive dynamic field testing of a 15-year-old base-isolated residential building equipped with 32 single-friction-pendulum bearings.

This unique experimental program offers two key benefits: evaluating the performance of an entire group of base isolators under real-world conditions and providing valuable data for an in-depth analysis of the overall structural response of both the building and the isolation system, particularly in relation to material aging and natural deterioration over time.

This paper presents an overview of the PASFIT project, detailing the efforts undertaken to successfully complete its ambitious experimental activities. Preliminary results are summarized at the end of the paper and contextualized within the broader objectives of quantifying isolation system degradation and validating its long-term reliability.

Keywords: Base isolation · seismic response · aging effects · experimental campaign

1 Introduction

Seismic isolation is one of the most advanced technologies in seismic engineering for protecting buildings and infrastructure from earthquake damage. Unlike traditional seismic design approaches, which focus on strengthening structures and enhancing energy dissipation, seismic isolation aims to minimize the transmission of seismic energy into the building. Isolating a structure involves placing isolation devices, such as elastomeric bearings or friction pendulum systems, between the superstructure and its foundation. These devices are designed to be vertically stiff to support the gravity loads while possessing low horizontal stiffness, to enable the structure to move almost independently of the ground during an earthquake. Despite its numerous advantages, seismic isolation presents some challenges. Examples include group response evaluation and long-term performance characterization. Currently, characterization tests are primarily conducted on brand-new individual isolators in laboratory settings. While these tests can be used to assess key mechanical properties such as stiffness and damping, they do not fully capture the behavior of an entire system of isolators under real-world conditions.

The interaction between multiple isolators, as well as between the isolators and the superstructure, can significantly influence the system's overall response, leading to behavior that differs from that of a single device tested independently. Additionally, base isolation devices are known to degrade over time due to environmental factors such as weather exposure, temperature fluctuations, and wear. Assessing how these conditions alter the mechanical properties of the bearings is crucial to ensuring the long-term effectiveness of the system.

While accelerated aging tests can be conducted in laboratories, they do not always provide an accurate representation of real-world performance. Existing reference values, such as those proposed by Constantinou [1], offer estimates of mechanical property changes up to 30 years after construction based on tests of replaced bearings. However, these remain approximations derived from controlled laboratory conditions rather than in-situ performance data.

Hence, the PASFIT project aims to generate valuable field data essential for addressing these critical challenges. This is achieved through extensive dynamic field testing of a 15-year-old base-isolated building in Central Italy, which was installed as part of the CASE project [2] following the 2009 L'Aquila earthquake. During the testing phase of these isolated buildings, data was collected to determine the properties of the newly installed system. Also, thanks to these data it will be possible to quantify the actual aging of the entire system.

This paper provides an overview of the undertaken activities and highlights preliminary key findings.

2 Case Study Building

The case study building considered in this study, referred to as "Building 20.4", is part of a cluster of four structures developed within the CASE project [2] in Arischia, a small village near L'Aquila, Italy (Fig. 1). Among the unoccupied buildings, potential candidates for testing, Building 20.4 was chosen for its compatible characteristics (e.g.,

weight/mass and overall dimensions) with the available testing equipment (described later). This three-story timber building has an overall height of 12 m and consists of three interconnected blocks linked by two staircase and elevator units, accommodating six apartments per floor. The structure is supported on a 21 m x 45 m reinforced concrete slab, which is elevated above ground level by 32 hollow steel columns. The base isolation system consists of 32 single-curvature friction pendulum bearings (SFPB) manufactured by ALGA [2], with a nominal friction coefficient of 5%. The detailed specifications of these isolation bearings are illustrated in Fig. 2 and Table 1.

The structural mass of the building alone is approximately 600 tons, while the mass of the building-concrete slab assembly increases to around 1500 tons, excluding variable loads. Based on nominal design parameters, the isolated system exhibits a fundamental period of approximately 3 s.

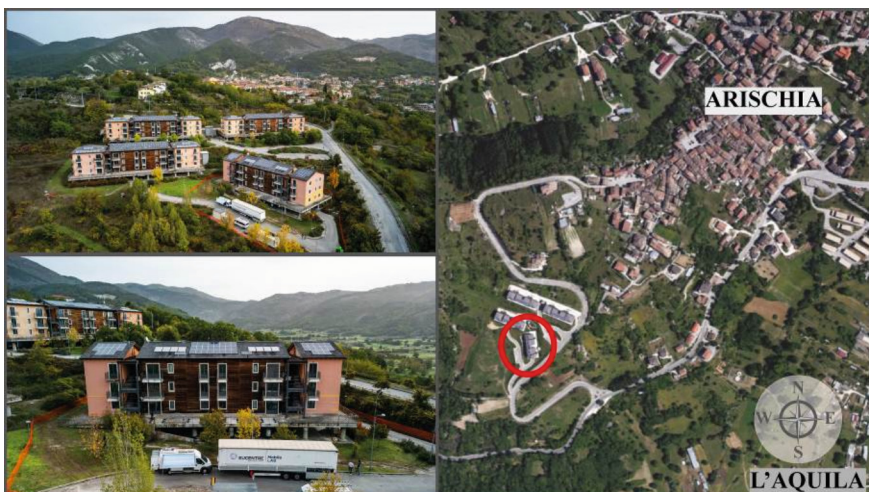


Fig. 1. Case study location

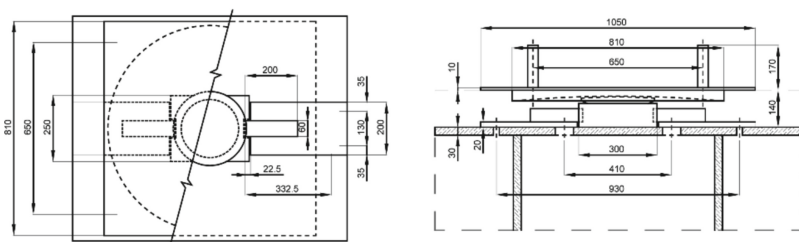


Fig. 2. Geometrical properties of the friction pendulum bearings

Table 1. Nominal specifications of SCSS

Isolators Nominal Values		
L	810	mm
D	800	mm
D _{pad}	250	mm
R _{eq}	3500	mm
μ	5.0	%
d _{max}	260	mm

3 Field Test Setup

3.1 The EUCENTRE's MOBILAB

The EUCENTRE's mobile laboratory, MOBILAB [3, 4], was deployed for the in-situ testing activities. Designed to be fully autonomous and transportable, MOBILAB combines the capabilities of a conventional laboratory with the flexibility required for large-scale, on-site experimental investigations.

The system is equipped with:

- Four hydraulic actuators, each capable of delivering a force of 1000 kN and a displacement of ± 250 mm, in order to simulate dynamic displacements and accelerations (Fig. 3);
- Hydraulic system, including pumps, reservoirs, accumulators, and piping, to ensure constant oil flow in the actuators (Fig. 4);
- Digital controller, which supervises the system, generating and managing signals that coordinate the actuators during the testing phase;
- Power unit, with a power of 600 kW ensures operational independence and efficiency.

The system is capable of simulating dynamic scenarios, such as seismic events, with an oil flow capacity of approximately 6000 l/min. The achievable acceleration is 1.2 g for mobilized weights lower than 150 tons, though this decreases to 0.3–0.4 g for heavier systems. Transportability is ensured by three trailers housing the pumps, accumulators, power unit, and actuators, along with a van for the controller and data acquisition systems, enabling direct deployment to testing sites.

3.2 Design of Self-Reacting Frame

The primary challenge in designing the test setup was determining how to securely anchor the four actuators to the structure. To maximize the available force output, the actuators needed to be positioned horizontally and as closely aligned as possible with the isolation system.

To achieve this, a steel truss structure was designed, capable of anchoring to the columns beneath the isolation system while maintaining sufficient rigidity to prevent deformations caused by actuator forces. Additionally, the system needed to be easily



Fig. 3. The four actuators of MOBILAB



Fig. 4. Scheme of the hydraulic system of MOBILAB, after [4]

assembled on-site and adaptable to the geometric tolerances of the structure. Based on these requirements, the self-reacting frame was developed (Fig. 5).



Fig. 5. Graph of the transmission of push and pull stresses in the self-reacting frame

The self-reacting frame was fabricated using S355 steel and primarily utilized bolted connections to interconnect its various components. The system comprises three adjustable-diameter rings designed to embrace the columns, along with two trusses that connect these rings, effectively transmitting both compressive and tensile forces.

The configuration was designed so that one end of each actuator could be attached to the central ring, while the other end was connected to a reaction plate. This plate was linked to the top reinforced concrete slab using post-tensioned bars, ensuring a stable and effective load transfer mechanism.

Once the reaction system configuration was established, the design process was carried out through advanced numerical analysis, involving multiple iterations. The

components anchored to the columns, including the rings and trusses, were analyzed using SeismoStruct [5] software with a beam-element-based model (Fig. 6). This model guided the design of the primary structural components and the selection of steel plate sections.

To further refine the design, detailed brick models were developed in Abaqus [6] to evaluate both welded and bolted connections, as well as the local stress distribution at the joints with the steel columns, ensuring the system would withstand testing without damage (Fig. 7).

To prevent local failures, all welded connections were executed as full-penetration welds between joined parts and, in some cases, were intentionally overdesigned. Likewise, bolted connections were designed to prevent deformation by incorporating high-strength bolts. An overview of the frame, along with a comparison between the 3D model and the installed structure, is provided in Fig. 8.

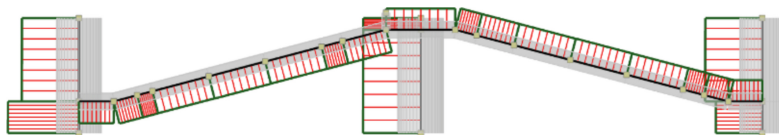


Fig. 6. SeismoStruct preliminary model of self-reacting frame

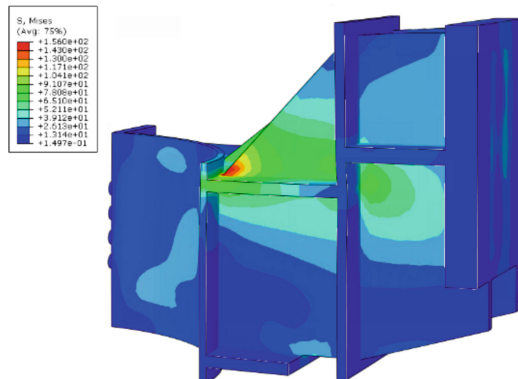


Fig. 7. Abaqus brick model used for local damage evaluation

3.3 Instrumentation Layout for Case-Study

Another critical aspect was the selection of the placement for the mobile laboratory equipment and the instrumentation used for data acquisition during the tests. Particular attention was given to the hydraulic system, as improper positioning could result in an oil pressure loss, primary to test invalidation or, worse, damage to the hydraulic system itself. To minimize the length of hydraulic tubing, the hydraulic system control unit was positioned in front of the building. The actuators and reaction frames were installed in

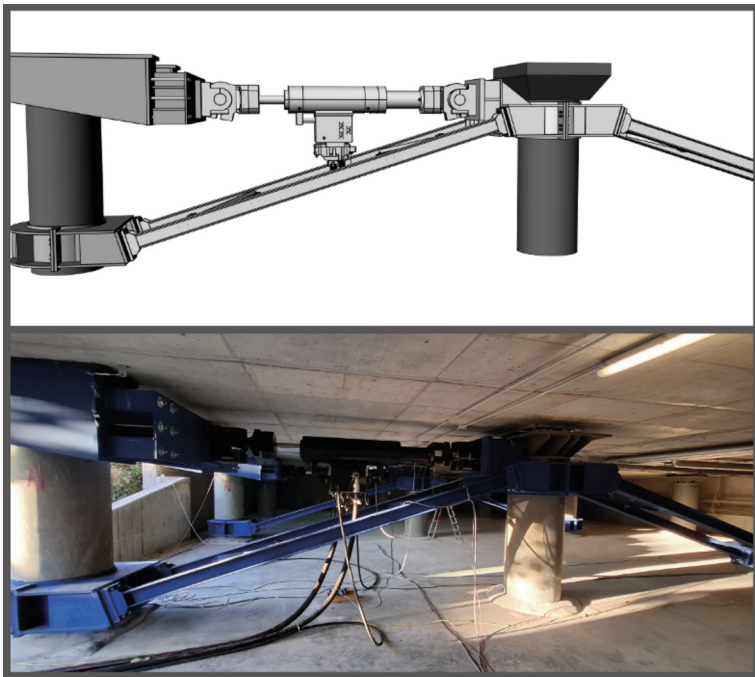


Fig. 8. Comparison between 3D model and the realized self-reacting frame

the four rows of columns located at the center of the building. Given the size of the test specimen, it was necessary to divide the data acquisition and monitoring into two stations. The first station, integrated into the MOBILAB equipment, was used for monitoring the reaction frames and the reinforced concrete slab via transducers (LVDTs) and displacement sensors (Tracers), as shown in Fig. 9. Both types of instruments measure displacement; however, due to space and positioning limits, the tracers were employed specifically to record the vertical displacement of the isolated system. The second acquisition station, located outside the MOBILAB, was entirely dedicated to the reception of data from triaxial accelerometers. These accelerometers were installed in pairs at each floor of the building and on the reinforced concrete slab at two opposite corners. This configuration allowed the determination of potential torsional behaviors of the isolation system or the building itself.

4 Field Testing

The field experiments were conducted in displacement-control, considering 1-to-3 cycle sinusoidal loading histories of varying amplitude and velocity. The test matrix is detailed in Table 2. Four single-cycle tests were performed to replicate a set of analogous experiments carried out in 2009 during the commissioning of a similar building, equipped with identical isolation system and similar building characteristics. As shown in the table, the tests performed have amplitudes ranging from 50 mm to 200 mm and peak velocities

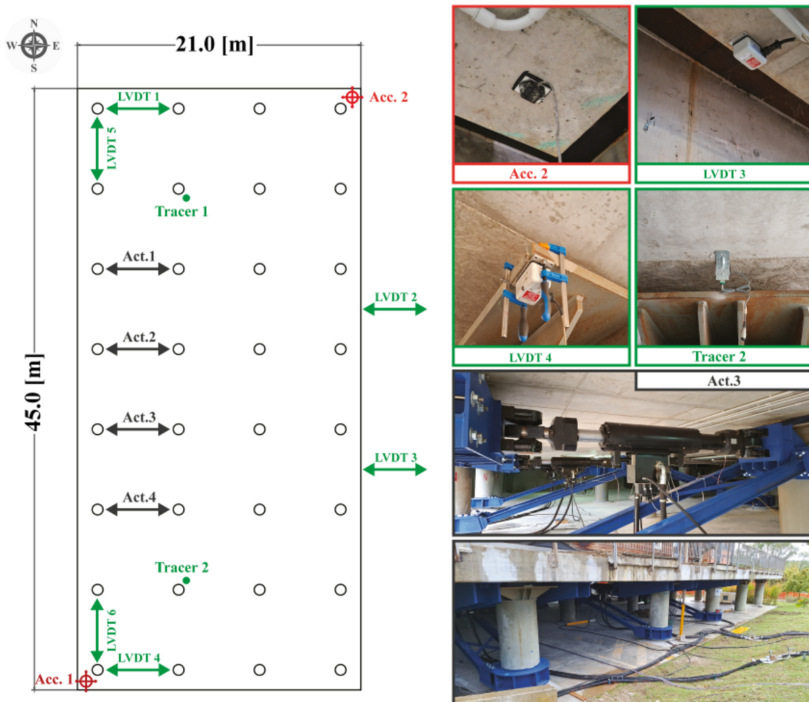


Fig. 9. Actuators and instrumentation setup of isolated slab

during testing from 50 mm/s to 250 mm/s. This variety of sinusoidal cycles allowed for recording the system's response under various induced frequencies.

4.1 Data Analysis

This section provides a brief overview of some of the data collected, although for the most part data processing is still at a very preliminary stage. Some initial comments on the observed response are included, but additional analysis is required before any definitive conclusions can be drawn.

For the purpose of illustration, the force-displacement of a representative test is outlined in (Fig. 11). Overall, the outlined response is consistent with what one would expect to see from a friction pendulum base isolated building, with an initially rigid response, followed by a drop in stiffness occurring in correspondence of the activation of the base isolation devices. The activation load is proportional to the friction coefficient at the sliding interface of the devices (discussed more later), while the post-activation stiffness is proportional to the mass of the building and the curvature of the bearings.

It is noteworthy that despite feeding identical input, different forces were recorded by the individual actuator load cells. This behavior is particularly noticeable in the final stage of the push or pull phase, where force increments are recorded by the actuators to enforce the lock at the maximum amplitude value of the cycle.

Table 2. Input protocols of conducted tests

Test ID	Ampl	Max. Vel	Freq	Load shape	Cycles	Repetitions
	[mm]	[mm/s]	[Hz]			
2	130	50	0.061	sine	1	1
3	130	100	0.122	sine	1	1
4	150	200	0.212	sine	1	1
5	150	250	0.265	sine	1	1
6	50	50	0.159	sine	3	1
7	100	50	0.08	sine	3	1
9	200	50	0.04	sine	3	1
11	50	100	0.318	sine	3	1
12	100	100	0.159	sine	3	1
14	200	100	0.08	sine	3	2
16	50	200	0.637	sine	3	1
17	100	200	0.318	sine	3	1
19	200	200	0.159	sine	3	4
22	100	250	0.398	sine	3	1
23	150	250	0.265	sine	3	4
24	200	250	0.199	sine	3	2

On the same note, non-uniform displacements were recorded by the LVDTs monitoring the horizontal displacement of the concrete slab, indicating that the system experienced torsional movements in addition to horizontal displacements in the direction of the applied loads (Fig. 10). While partly attributable to inherent aspects of the experimental setup, this outcome emphasizes the complexity of the response of an isolated building under real world conditions, compared to the response of a single bearing tested in the laboratory. Clearly, this warrants further investigation.

Noticeable force oscillations can also be detected in the response. While they could be an artifact of the experimental setup, these oscillations are possibly due to the degradation of the sliding surfaces of the isolators, which altered the nominal short-term expected response.

From an initial analysis of the collected data, an increase in the coefficient of friction is also observed, from the nominal value of 5% shown in Table 1, to an average value ranging between 10% and 15%. Figure 12 illustrates the variation of the static coefficient of friction, calculated at the instant when the velocity is zero, and the dynamic friction, calculated at the instant when the velocity is at its maximum.

From the two observed trends, the dynamic friction, after an initial value of approximately 14%, stabilizes around 10%. Conversely, the static friction, after initial lower values, stabilizes at around 14% over time.

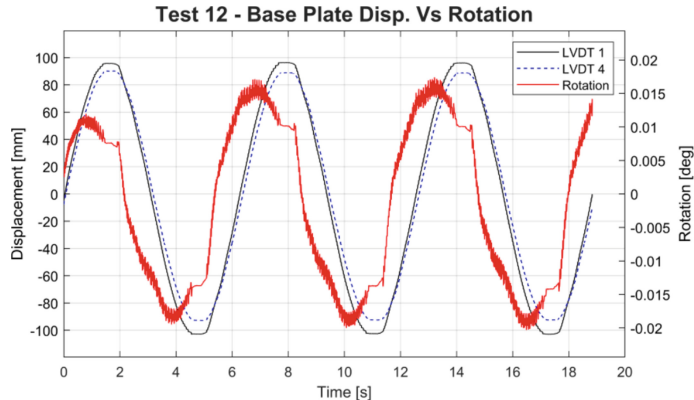


Fig. 10. Displacement and rotation of slab during time in the Test 12

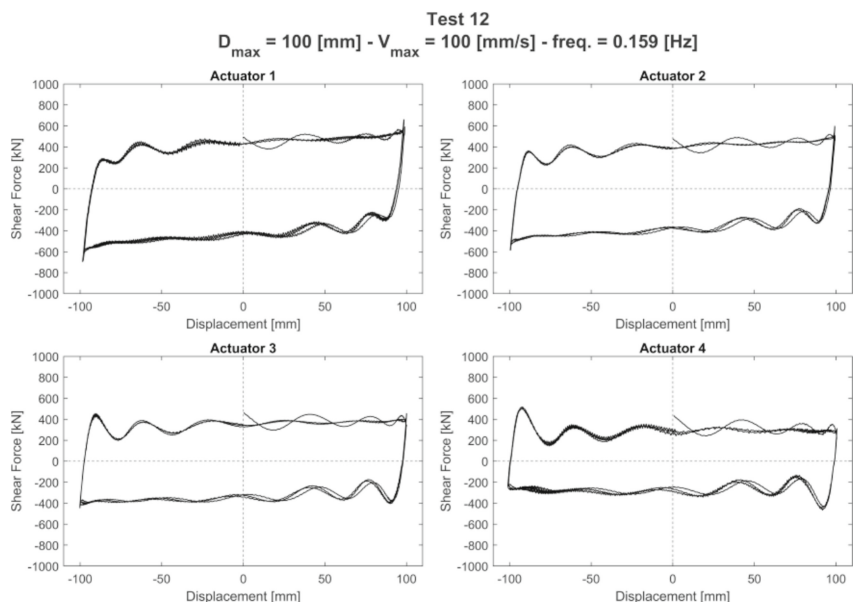


Fig. 11. Force-Displacement plot of actuators during Test 12

Table 3 presents the average values of the coefficients of friction recorded during the tests. The values shown represent the arithmetic mean of the coefficients of friction calculated for each test, grouped by amplitude and peak velocity. The divergence from the nominal values could be a consequence of the bearings' 15 year exposure in the field, but this aspect too will require additional analysis.

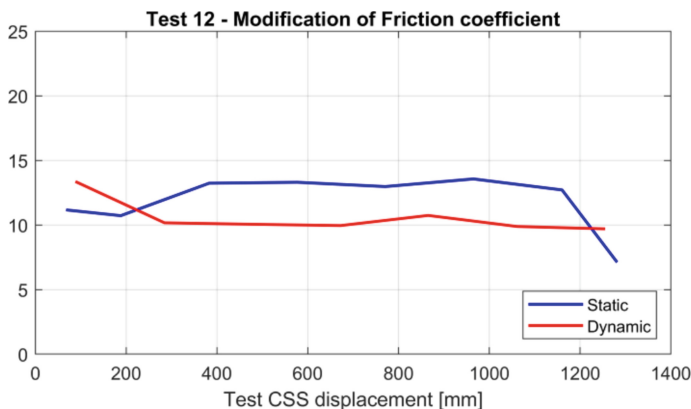


Fig. 12. Variation in the static and dynamic friction coefficient during Test 12

Table 3. Mean value of friction coefficient divided using amplitude and peak velocity

Ampl [mm]	μ [%]	Max. Vel [mm/s]	μ [%]
50	8	50	10
100	10	100	12
150	16	200	13
200	14	250	15

5 Conclusion

This article provided a preliminary overview of the field-testing activities undertaken as part of the PASFIT project. Because of the complexity of the project and the unprecedented extent of field testing conducted, the preparation and planning phases spanned over several months. The development of the self-reacting steel frame presented challenges at multiple stages, from conceptualizing its operating mechanism to creating the technical drawings for the fabrication stage. Conducting tests outside of the laboratory environment also introduced numerous issues. Foremost among these was determining the placement of the mobile laboratory's hydraulic system, whose size imposes limitations both in geometric terms and system performance. Additionally, setting up the instrumentation for data acquisition required detailed analysis to fully understand the behavior of the entire system.

The collected data has only undergone preliminary processing, and additional work is needed before any meaningful conclusions can be drawn. The expectation is that once processed and analyzed, the experimental results will provide valuable insights pertaining to the response of aged base isolators and to the behavior of base isolator groups under real world conditions.

From the initial data analysis presented herein, aspects such as the unintended torsional response and the varying friction behavior have already been detected. It is well-documented in literature [1] that the coefficient of friction varies depending on both temperature and sliding velocity, although available studies are typically focused on individual isolators. The results of this large-scale testing program provide data to monitor the evolution of the friction coefficient for an entire aged isolated system, at varying forcing frequency and velocity. Hence, the anticipation is that this paper will be followed by several others as data processing and data analysis progress, and new insights are gained.

Acknowledgements. This work is part of the transnational access project “ERIES-PASFIT”, supported by the Engineering Research Infrastructures for European Synergies (ERIES) project (www.ries.eu), which has received funding from the European Union’s Horizon Europe Framework Programme under Grant Agreement No. 101058684. This is ERIES publication number C63.

References

1. Constantinou, M., Tsopelas, P., Kasalanati, A., Wolff, E.: Property Modification Factors for Seismic Isolation Bearings (Technical Report No. MCEER-99-0012). Multidisciplinary Center for Earthquake Engineering, Buffalo, NY (1999)
2. Calvi, G.M.: L’Aquila, Il Progetto C.A.S.E.: Complessi antismisici sostenibili ed ecocompatibili. IUSS Press (2010)
3. Bolognini, D., Dacarro, F.: Collaudo del Laboratorio Mobile. Progettazione Sismica 1 (2018)
4. Calvi, G.M., Moratti, M., Dacarro, F., Andreotti, G., Bolognini, D.: Feasibility study for in-situ dynamic testing of structures and geotechnical systems. Eng. Struct. **235**, 112085 (2021). <https://doi.org/10.1016/j.engstruct.2021.112085>
5. SeismoStruct, 2024. SeismoStruct: A Computer Program for Static and Dynamic Nonlinear Analysis of Framed Structures, Seismosoft, official Italian reseller: Mosayk srl
6. ABAQUS: Analysis User’s Manual, Dassault Systemes Simulia, Inc. (2022)

Open Access This chapter is licensed under the terms of the Creative Commons Attribution 4.0 International License (<http://creativecommons.org/licenses/by/4.0/>), which permits use, sharing, adaptation, distribution and reproduction in any medium or format, as long as you give appropriate credit to the original author(s) and the source, provide a link to the Creative Commons license and indicate if changes were made.

The images or other third party material in this chapter are included in the chapter’s Creative Commons license, unless indicated otherwise in a credit line to the material. If material is not included in the chapter’s Creative Commons license and your intended use is not permitted by statutory regulation or exceeds the permitted use, you will need to obtain permission directly from the copyright holder.





Experimental Investigation of Pallet Sliding in Steel Racking Systems via Shake Table Testing

Dimitrios Tsarpalis^{1(✉)}, Dimitrios Vamvatsikos¹, Christos Lachanas¹, Akrivi Chatzidaki¹, Michalis Vassiliou², Kemal Can Struja², Dimitrios Konstantinidis³, Christoph Adam⁴, Nicholas Kyriakides⁵, Athanasia Kazantzi⁶, Konstantinos Bakalis¹, Giuseppe Abbiati⁷, Filippo Delladonna⁸, Giuseppe Fabbri⁹, Luca Sutera¹⁰, Igor Lanese¹¹, and Gerard J. O'Reilly^{1,12}

¹ National Technical University of Athens, Athens, Greece

dimitris93@central.ntua.gr

² ETH Zurich, Zürich, Switzerland

³ University of California, Berkeley, USA

⁴ University of Innsbruck, Unit of Applied Mechanics, Innsbruck, Austria

⁵ Technical University of Cyprus, Limassol, Cyprus

⁶ International Hellenic University, Thermi, Greece

⁷ Aarhus University, Aarhus, Denmark

⁸ SACMA S.P.A, Biella, Italy

⁹ AISEM (Italian Association of Lifting-Handling-Racking), Automha, Italy

¹⁰ Mecalux SA, Madrid, Spain

¹¹ EUCENTRE - European Centre for Training and Research in Earthquake Engin/Ng, Pavia, Italy

¹² IUSS - Istituto Universitario Di Studi Superiori, Pavia, Italy

Abstract. Pallet racking is a long-established material handling solution that optimizes warehouse space through multi-level pallet storage and ensures time efficiency through the absence of any mechanical fasteners between the goods and the supporting steel structure. This however could lead to potentially vulnerable situations since heavy pallets are stored at high load-levels, with only the force of gravity and friction keeping them in place. Recent earthquakes have highlighted these risks, with pallet sliding and fall-offs causing operational disruptions and structural collapses; such failure modes are not adequately addressed by current seismic design codes for racks. The ERIES project RACKSLIDE addresses this knowledge gap through an extensive experimental campaign that investigates pallet sliding on two rack configurations with diverse structural characteristics. Test specimens, that depict small portions of the actual frames, are designed and constructed by industry experts and then installed on an innovative 9 degrees-of-freedom shake table system. By using as input motion, the load-level accelerations, evaluated by numerical modelling of the entire system, the proposed setup allows to assess sliding phenomena on the uppermost levels of high-rise racks. Afterwards, the experimental results are compared with blind predictions from numerical analyses, leveling the ground for future model calibrations and code applications.

Keywords: Pallet Sliding · Steel Racking Systems · Shake Table Testing

1 Introduction

Racking systems form the backbone of modern logistics and goods supply chains, lying at the core of every physical product route from manufacturer to consumer. Rack-supported and rack-containing warehouses come in various shapes and sizes, universally constructed from cold-formed steel frames that range from 4 m to more than 25 m of height. The vast majority stores palletized goods that stay put only by the force of gravity and friction. This is a potentially vulnerable situation that has been severely tested by recent earthquakes (e.g., the Emilia-Romagna event in 2012, Italy), resulting in disruptions of operation and some spectacular collapses.

To date, limited knowledge exists regarding the effect of pallet sliding on racking structures. Dynamic shake-table tests on a simple “pallets-on-beam” setup [1] have showcased that peak sliding could be affected by a range of parameters such as the type of pallet material, the surface finish of the steel beam, the direction and the frequency content of the seismic excitation. However, as the objective of these studies was to investigate the pallet-beam interaction problem, the employed setup comprised only a small segment of the actual racking structure, missing important structural characteristics that are likely to affect sliding, such as the period of vibration, the effect of higher modes, the interaction between levels. The lack of research validation is also evident in the current seismic codes for racks, where no guidelines are currently available for the estimation of content-sliding.

The ERIES project RACKSLIDE brings together 7 universities, 1 association of rack manufacturers, and 5 supporting industrial partners with active interest in researching pallet sliding. The project proposes leveraging the 9DLAB shake table system of EUCENTRE to conduct innovative investigations that will form the state-of-art in the content-structure-sliding interaction problem. The program is carefully designed to comprehensively assess pallet sliding phenomena at various load levels of high-rise racks through a hybrid numerical-experimental approach. Initially, numerical analyses are conducted using appropriately selected ground motions, from which absolute acceleration time histories are derived for each load level. These recorded excitations then serve as input for the two moving platforms of 9DLAB, and the experimental results are subsequently compared with numerical predictions.

At the time of writing, the experimental campaign is ongoing, and the test data have not yet been fully integrated into a database or thoroughly analyzed. Accordingly, this paper focuses on a single rack case study using one ground motion excitation, while the experimental results should be considered preliminary and interpreted with caution.

2 Numerical Analysis on Full System

2.1 Description of Case Study

The case study under consideration comprises a double-depth Automated Rack Supported Warehouse (ARSW), designed by professional engineers within the context of the European project STEELWAR, for installation in the city of Van in Turkey using the following design assumptions: (i) Peak Ground Acceleration, PGA = 0.3g , (ii) importance factor, $\gamma_I = 0.8$, (iii) Soil Type B. ARSWs represent an emerging storage

technology that enables fully automated storage operations while supporting both the stored pallets and the external cladding shell. Compared to traditional rack configurations, these warehouses are designed to accommodate more load levels and a higher pallet capacity, requiring heavier steel profiles and connections. However, the fundamental principles of the racking industry—such as the use of cold-formed thin-walled members and simple hooked or bolted connections—remain applicable.

Along the cross-aisle direction, the system consists of four “macro-columns” of 25.35m height and 2.51m width (Fig. 1a), where each “macro-column” comprises two K-braced upright frames with mirrored bracing patterns. In the down-aisle direction (Fig. 1b), the warehouse consists of 40 storage bays, each 2.15 m long, where each pair of beams carries two pallets. To enhance the latter stiffness in this direction, two stiff bracing towers are placed at one edge and the middle of the warehouse. Automated cranes are used for goods handling, operating in two aisles and 14 load levels: Load levels 1 to 3 are for 1000 kg pallets, 4 to 11 for 800 kg, and 12 to 14 for 600 kg. In total, the system can accommodate approximately 9,000 pallets.

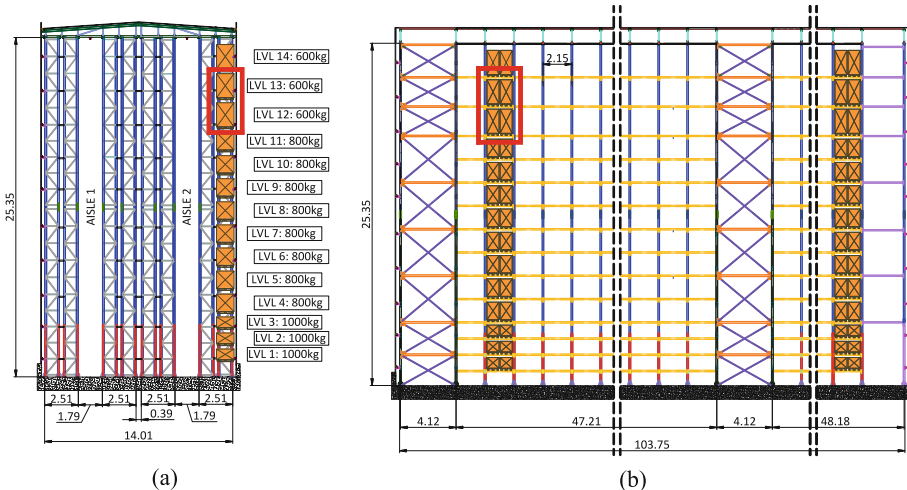


Fig. 1. Geometry of ARSW case study: (a) cross-aisle view and (b) down-aisle view.

2.2 Numerical Modeling of Full System

Two numerical 2D models (one for each principal direction) of the ARSW archetype are realized in the open-source structural analysis software OpenSees [2]. This compromise is necessary since numerical convergence in a fully 3D model is highly challenging due to the thousands of degrees of freedom and the nonlinear friction slider elements that are implemented to simulate the biaxial motion of each pallet. Furthermore, research so far has indicated minor structural interaction between the cross- and down-aisle direction of typical ARSW configuration and that 2D models can provide sufficient accuracy [3].

The uprights are modelled using elastic beam-column elements with P- Δ formulation, while the rest of the members (diagonals, beams, X braces) are simulated with linear elastic beam elements. The beam-to-upright and diagonal-to-upright joints are modelled using zero-length rotational and axial springs, respectively. To capture the relative displacement between the pallets and the supporting rack, the numerical models incorporate the *flatSliderBearing* elements of OpenSees, which explicitly consider the effect of sliding and friction. Specifically, each pallet is modelled as a subsystem consisting of a slider element, a lumped mass equal to the mass of the unit load and dummy rigid elements to model the vertical eccentricity of the unit load and the beam [4]. The slider elements are coupled with a Coulomb friction model, assuming an initial friction coefficient of $\mu = 0.3$.

Even in 2D analyses, a large number of nonlinear sliders (e.g., of the order of 100) can lead to convergence issues and impractical computational times. To address this, additional simplification procedures are followed. In the cross-aisle direction, only one of the four macro-columns are modelled, while the contribution of the roof truss is accounted for by using horizontal axial springs at the top nodes of the uprights. In the down-aisle direction, the individual storage bays are lumped into concentrated masses using the methodology described in [3], effectively reducing the number of friction sliders involved. A comparison between the modes of vibration of the full 3D model and the simplified 2D ones confirm that the lower fidelity models capture the salient dynamic characteristics of the warehouse. Additionally, the modal analysis reveals long structural period along the cross-aisle direction ($T_{CA} = 2.65\text{s}$) due to the weak bracing system formed by the uprights and the diagonals, whereas significantly greater stiffness is observed along the down-aisle direction ($T_{DA} = 1.44\text{s}$), attributed to the presence of the two stiff bracing towers.

2.3 Derivation of Input Excitations

Following the development of the numerical models, a series of nonlinear Response History Analyses (RHAs) is conducted using a set of 30 hazard-compatible ground motion records from the PEER-NGA strong motion database. A Rayleigh damping formulation with $\zeta = 3\%$ is applied, ensuring that the slider elements are excluded from the damping matrix to prevent artificial viscous damping in the system.

For each record, the two horizontal record components (e.g., 0° and 90°) are randomly assigned as input to the 2D models (one per model), after which RHAs are performed. The recorded quantities include the time-histories of absolute accelerations, velocities, and displacements at each load level (served later as input for the shake table system) as well as the sliding displacement of each slider element. Out of the 30 records, only five are ultimately selected for the shake table campaign. The selected records showcase non-negligible pallet sliding at moderate levels of down- or up-scaling (with uniform scaling for both horizontal components of the excitation) while remaining within the 9DLAB limitation in terms of peak accelerations, velocities, and displacements.

The present work focuses on a specific ground motion of the set: ChiChi 1993, station ILA013. At a scale factor of 1.50, which from this point onwards is considered as 100% intensity, the profiles of cross-aisle maximum Peak Floor Acceleration (PFA),

Peak Floor Velocity (PFV), and Peak Floor Displacement (PFD), are shown in Fig. 2a-c, respectively. Moreover, the profile of cross-aisle maximum pallet sliding is shown Fig. 2d. As anticipated, peak responses occur at the topmost levels of the rack, with a recorded PFA of 1.87 g and maximum sliding of 107mm at level 14. Similar trends are observed in the down-aisle direction, which is not shown here for brevity.

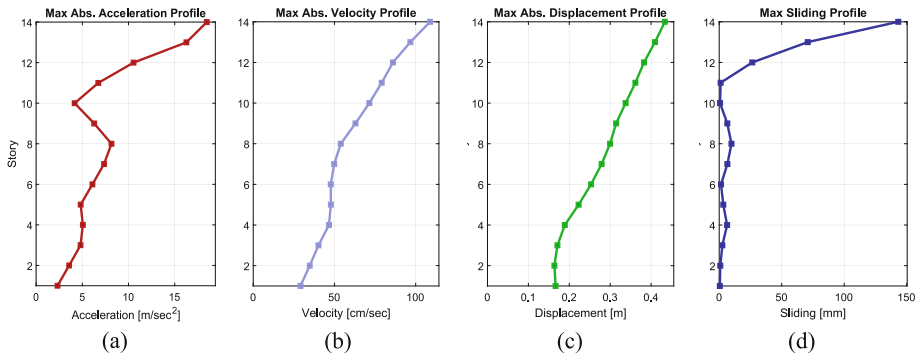


Fig. 2. Cross-aisle profiles of: (a) PFA, (b) PFV, (c) PFD, and (d) pallet sliding for record Chichi 1993, Station ILA013, and scale factor of 1.50 (100% intensity).

3 Description of Test Setup

3.1 Experimental Setup and Instrumentation

Figure 3a illustrates the general layout of the test setup implemented in the 9DLAB shake table system at EUCENTRE. The system consists of two independent moving platforms capable of imposing horizontal and vertical displacements, as well as rotations, providing a total of nine distinct degrees of freedom. However, within the context of the RACKSLIDE experimental campaign, only horizontal displacements are considered.

The specimen (Fig. 3a) is a 1:1 scale replica of a small segment of the warehouse, specifically a single bay and frame of load levels 12 to 14, as indicated by the red box in Fig. 1a-b. It comprises two upright frames, each of two uprights and diagonal elements, as well as three sets of twin pallet beams hooked on the uprights. The bottom two pairs of beams (representing levels 12 and 13) are loaded with pallets, whereas the top pair (level 14) remains unloaded due to height limitations of the shake table system. The specimen height is 4060 mm, manufactured precisely to the available height between the two attachment levels, while the plan dimensions are 2270 mm × 1100 mm. The uprights are bolted via stiff end-plates at their bottom and top to the 9DLAB base table and top platform, respectively. All structural members are made of cold-formed steel sections, with the pallet beam surfaces finished with powder coating, while the diagonals and uprights are zinc-coated.

Two standard EUR-pallets, each weighing 590 kg, are placed on each of the two loaded levels, for a total load of $4 \times 590 \text{ kg} = 2,360 \text{ kg}$. The unit loads are represented

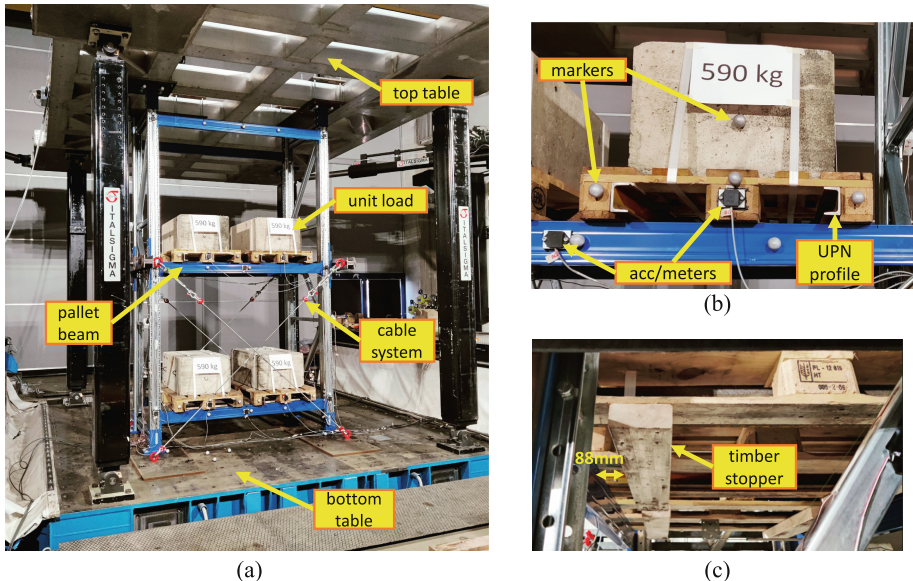


Fig. 3. Experimental setup of testing campaign: (a) general layout, (b) installed instruments, (c) timber stopper and allowable cross-aisle sliding.

by cast concrete blocks, which are fastened to the wooden pallets via plastic straps. To ensure realistic test conditions, used-but-undamaged pallets are selected to replicate the actual pallet-on-beam surface conditions during warehouse operation.

Each EUR-pallet has a length of 1200 mm and is supported by two 50 mm-wide beams with a 1000 mm clear span between them, leaving an average of 100 mm of sliding tolerance along the cross-aisle direction before disengagement at either pallet end. Since pallet fall-off could damage both the supporting rack and laboratory equipment, a slide-off prevention system has been designed to restrict cross-aisle pallet movement within safe ranges. This system includes: (i) two UPN profiles (Fig. 3b) attached to the pallet blocks using self-drilling screws in order to prevent pallet fall-off due to excessive rigid-body rotations and (ii) two timber stoppers (Fig. 3c) to limit cross-aisle sliding displacements to a range of ± 88 mm. In the down-aisle direction, the pallets are free to move as disengagement is prevented by the presence of the uprights.

Non-identical excitations are applied to the two platforms in the cross-aisle direction, based on the time history of absolute accelerations, velocities, and displacements extracted from the RHAs for levels 12 (bottom platform) and 14 (top platform). In the down-aisle direction however, the stiff bracing towers, along with the relatively low seismic forces at the upper part of the structure, result in nearly identical movement of levels 12 and 14. In other words, the structure moves almost like a rigid body with negligible interstorey drift. Therefore, identical excitations are applied to both platforms in the down-aisle direction. To ensure that also the middle load level (representing level 13 of the warehouse) moves along with the two platforms, an external bracing system is installed (Fig. 3a), consisting of two pairs of tensioned cables. The cables not only

maintain synchronized movement of the load levels but also provide a more realistic representation of the high structural stiffness along the down-aisle direction due to the presence of the bracing towers.

The instrumentation plan includes an advanced optical tracking system, consisting of optical cameras with a precision of ± 0.3 mm positioned outside the shake table, and markers (Fig. 3b) placed on the two platforms, the rack, and the pallets. This configuration allows for real-time monitoring of the motion of the steel beams and pallets, which enables the calculation of sliding displacements and rotations. Additionally, an accelerometer is installed on each pallet to record the time-history of absolute accelerations experienced by the unit load, allowing for detection of the acceleration threshold at the onset of sliding. Finally, strain gauges are attached to the uprights and the diagonal members to ensure that no plastic deformations occur in the steel members during the sliding tests.

3.2 Numerical Modelling of Test Specimen

Subsequently, a 3D model of the test specimen is realized in OpenSees, as illustrated in Fig. 4. The uprights, diagonals, and pallet beams are simulated using the same assumptions as those applied in the 2D models of the full system. To reduce numerical complexity, the cables are modelled as elastic beam elements without initial bow-like imperfections or tension-only behaviour. During reverse loading, only two of the four cables are in tension and thus active. To approximate the actual lateral stiffness they provide, their cross-section area is numerically reduced to 50% of the actual one.

The methodology that incorporates simulating the sliding motion of a pallet as a subsystem of dummy stiff elements, concentrated masses and friction sliders, is extended herein to 3D space. Each EUR-pallet is supported at six contact points with the steel beams, each modelled by a friction slider element. The two central support points carry 50% of total pallet weight, resulting in a normal force of $50\% \cdot 6\text{kN} / 2 = 1.5\text{kN}$ per slider surface. The four corner support points share the remaining 50% of the weight, leading to a normal force of 0.75kN per slider.

The numerical subsystem used to achieve the described load distribution is depicted on the right part of Fig. 4. Dummy horizontal and vertical rigid elements transfer the forces from the three concentrated masses (of total weight of 6.0kN) to the six sliders. To prevent relative deformations between the six support points while still allowing for rigid body rotations of the pallet, a rigid diaphragm constraint is imposed to these points.

Since the two platforms experience different input excitations along the cross-aisle direction, a Multi-Support Excitation Pattern is employed, allowing different prescribed motions at various structural supports. In terms of numerical model setup, the key difference between the conventional Uniform Excitation and the Multi-Support approach is that the former applies input excitation as imposed accelerations, whereas the latter uses imposed displacements. Additionally, the Multi-Support method is more prone to numerical instabilities, thus requiring smaller analysis time steps.

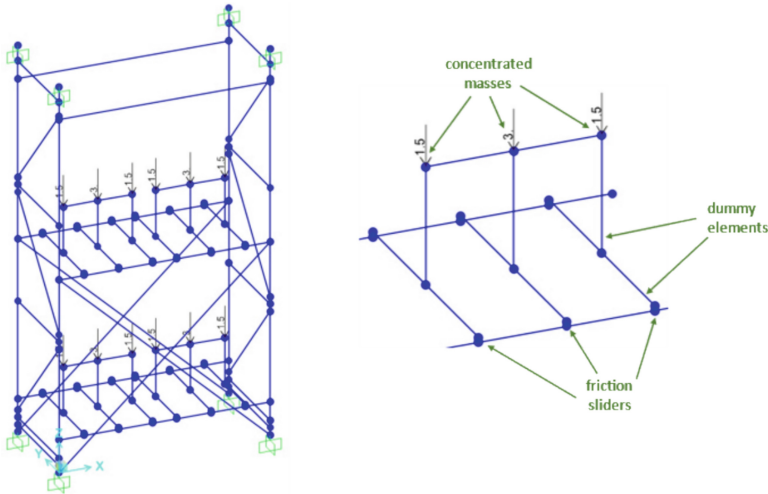


Fig. 4. Numerical 3D model of test specimen.

4 Shake Table Tests

4.1 Testing Series

The testing series for the ground motion under consideration is summarized in Table 1, along with the dynamic properties of the input excitation at the top table, expressed in terms of PFA, PFV, and PFD. A total of seven uniaxial shake table tests (Tests #1 to #7) are conducted using only the cross-aisle component of excitation, starting from a 10% scale and increasing incrementally up to 110%. Subsequently, six biaxial tests (Tests #8 to #13) incorporate both cross- and down-aisle components of motion, ranging from 30% to 110% scale. Finally, two additional uniaxial cross-aisle tests at 30% and 50% scale (Tests #14 and #15) serve as validation checks to ensure that sliding displacements remain consistent with those observed in the initial Tests #2 and #3, confirming that the pallet-to-beam surfaces have not been significantly damaged over consecutive testing.

If significant pallet sliding (i.e., greater than 3mm in any direction) is observed during a test, the shake table system halts operation, allowing lab technicians to manually reposition the pallets to their original positions. Additionally, after each test, strain gauge data is analyzed to verify that no failure has occurred in the steel members of the test specimen.

To optimize the duration of each dynamic test, the input signals have been trimmed to retain only the critical portion where pallet sliding occurs, limiting the total duration to 30 s. Since this trimming process introduces nonzero initial conditions, a windowing function is applied to ensure a smooth transition from rest to full excitation. Preliminary numerical analyses indicate negligible differences in sliding displacements and pallet accelerations between the original and modified signals.

Table 1. Summary of shake table tests and dynamic characteristics of input signals.

Test no	Direction of motion	Scale	PFA [g]		PFV [cm/s]		PFD [mm]	
			CA	DA	CA	DA	CA	DA
1	1D	10%	0.19	—	9.1	—	34	—
2		30%	0.56	—	27.2	—	103	—
3		50%	0.93	—	45.4	—	171	—
4		70%	1.31	—	63.5	—	240	—
5		90%	1.68	—	81.7	—	308	—
6		100%	1.87	—	90.7	—	342	—
7		110%	2.05	—	99.8	—	377	—
8	2D	30%	0.56	0.26	27.2	25.2	103	94
9		50%	0.93	0.43	45.4	42.0	171	156
10		70%	1.31	0.60	63.5	58.8	240	219
11		90%	1.68	0.77	81.7	75.6	308	281
12		100%	1.87	0.86	90.7	83.9	342	312
13		110%	2.05	0.94	99.8	92.3	377	344
14	1D	10%	0.19	—	9.1	—	34	—
15		30%	0.56	—	27.2	—	103	—

4.2 Uniaxial Tests

Before conducting the experimental tests, a series of RHAs were performed on the previously developed 3D numerical model of the test specimen, using different assumptions for the friction coefficient (μ). Prior research [5] suggests that the static friction coefficient (μ_s), which governs resistance before sliding onset, typically averages around 0.50 for pallet-on-beam surfaces. However, no comprehensive studies have yet established the dynamic friction coefficient (μ_d) for these surfaces, which governs resistance during sliding and is generally lower than μ_s . Additionally, more advanced friction models that account for velocity- or pressure-dependent behavior remain underdeveloped in this context. Given these uncertainties, a simplified Coulomb friction model was adopted for this preliminary study, assuming a single friction coefficient (i.e., $\mu = \mu_s = \mu_d$) with values ranging from 0.30 to 0.55.

Figure 5 compares the observed maximum pallet sliding displacements (red stars) with numerical predictions (rectangles, color-coded by friction coefficient). The first two tests, conducted at 10% and 30% scale factors, did not result in noticeable sliding and are therefore omitted from the graphs. The observed cross-aisle sliding displacements (left graph) closely match the model with a friction coefficient of $\mu = 0.35$. In contrast, the model using $\mu = 0.50$ (i.e. close to typical values of μ_s) significantly underestimates sliding—predicting nearly half of the observed displacement—suggesting that static friction alone may not fully describe pallet sliding behavior. On the other hand, no

sliding was observed in the down-aisle direction, as expected since no input acceleration is applied along this axis.

An additional key observation, also evident in the numerical sliding profiles (Fig. 2d), is that pallets resting on the upper beam pair exhibit greater sliding than those on the lower pair. This reinforces the idea that top storage levels pose the highest risk for pallet slide-off.

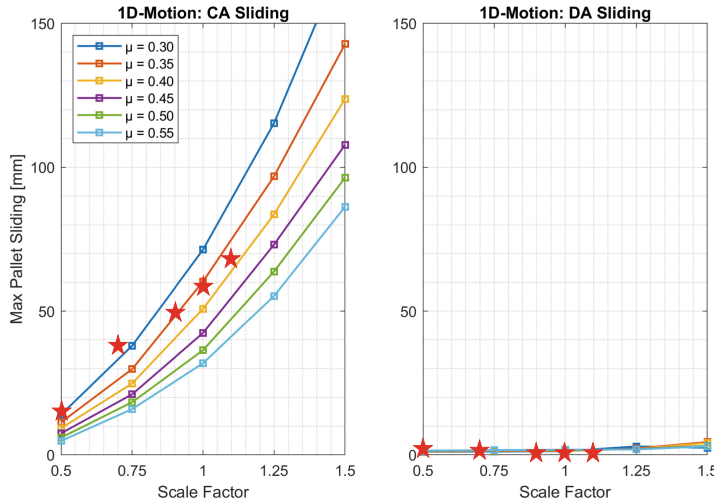


Fig. 5. Comparison of predicted and observed sliding displacements in uniaxial tests.

4.3 Biaxial Test

After completing the uniaxial tests, biaxial tests were performed, and the results obtained through comparing the predicted and observed sliding displacements are shown in Fig. 6. In the cross-aisle direction, the observed displacements again align well with the numerical predictions for a friction coefficient of 0.35, while the model using $\mu = 0.50$ continues to underestimate them. A key observation is that biaxial motion increases sliding in the cross-aisle direction, even though the input signal along this axis remains unchanged. For example, at 110% intensity, Test #7 in the uniaxial case resulted in a maximum cross-aisle displacement of 65 mm, whereas Test #12 in the biaxial case reached 75 mm.

In the down-aisle direction (shown in the right graph of Fig. 6), the maximum observed sliding displacements were greater than the predicted ones, even exceeding those from the model with μ value as low as 0.30. However, these larger displacements were only observed on the top-right pallet (Fig. 7a), while sliding of the top-left pallet was closer to the predictions of the numerical model. This variability highlights how friction behavior can differ, even under seemingly similar conditions (same material, same beams, similar usage). Interestingly, all pallets tended to slide toward the center of the beam, which was likely caused by the small bending angles in the beam, resulting from its flexural curvature.

At the end of the biaxial tests, noticeable surface wear was observed on the beams (Fig. 7b) due to the repeated sliding and repositioning of the pallets. To check if the surface wear had any significant impact on the friction performance, two uniaxial tests were repeated at low intensity at the end of the testing series. The results showed no major differences from the original tests, indicating that the wear did not significantly affect the friction. Additionally, off-table static friction tests conducted after the dynamic tests showed μ_s values around 0.55.

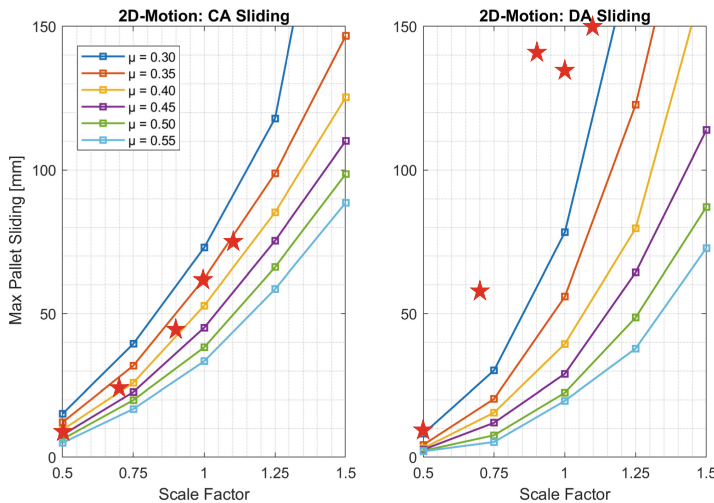


Fig. 6. Comparison of predicted and observed sliding displacements in biaxial tests.



Fig. 7. Final pallet positions after biaxial test #12: (a) down-aisle sliding and (b) surface wear on the steel beams.

5 Conclusions

This paper presented part of an innovative experimental campaign aimed at providing key insights into the pallet sliding problem in racking systems. The tests were conducted using the 9DLAB system of EUCENTRE, which consists of two independent

moving platforms capable of simulating seismic excitations at the upper floors of high-rise structures. The methodology followed a hybrid numerical-experimental approach, beginning with a series of RHAs to extract the time history of accelerations, velocities, and displacements at different load levels. Subsequently, a series of uniaxial and biaxial tests were performed on a test specimen representing the upper load levels of an ARSW archetype structure. The following key conclusions can be drawn:

- The static friction coefficient alone may not fully capture pallet sliding behaviour.
- Despite using beams from the same batch and pallets of similar age and usage, one pallet experienced greater sliding, especially in the down-aisle direction, highlighting variability in friction.
- Down-aisle motion can amplify the cross-aisle sliding displacements.
- Greater sliding occurred at pallets resting on the upper beams compared to bottom ones, consistent with the numerical predictions.

Acknowledgements. This work is part of the transnational access project “ERIES-RACKSLIDE”, supported by the Engineering Research Infrastructures for European Synergies (ERIES) project (www.ries.eu), which has received funding from the European Union’s Horizon Europe Framework Programme under Grant Agreement No. 101058684. This is ERIES publication number C58.

References

1. Castiglioni, C.A., Drei, A., Kanyilmaz, A., Mouzakis, H.P.: Earthquake-Induced pallet sliding in industrial racking systems. *J. Build. Eng.* **19**, 122–133 (2018)
2. OpenSees Homepage. <https://opensees.berkeley.edu/>
3. Tsarpalis, D., Vamvatsikos, D., Vayas, I., Delladonna, F.: Simplified modelling for the seismic performance assessment of automated rack-supported warehouses. *J. Structural Eng.* **147**(11) (2021)
4. Tsarpalis, D., Vamvatsikos, D., Vayas, I.: Seismic assessment approaches for mass-dominant sliding contents: the case of storage racks. *Earthquake Eng. Struct. Dynam.* **51**(4), 812–831 (2021)
5. Castiglioni, C.A., Drei, A., Carydis, P., Mouzakis, H.P.: Experimental assessment of static friction between pallet and beams in racking systems. *J. Build. Eng.* **6**, 203–214 (2016)

Open Access This chapter is licensed under the terms of the Creative Commons Attribution 4.0 International License (<http://creativecommons.org/licenses/by/4.0/>), which permits use, sharing, adaptation, distribution and reproduction in any medium or format, as long as you give appropriate credit to the original author(s) and the source, provide a link to the Creative Commons license and indicate if changes were made.

The images or other third party material in this chapter are included in the chapter's Creative Commons license, unless indicated otherwise in a credit line to the material. If material is not included in the chapter's Creative Commons license and your intended use is not permitted by statutory regulation or exceeds the permitted use, you will need to obtain permission directly from the copyright holder.





Project RecycleSlab - Structural Behaviour of Recycled Aggregate Reinforced Concrete Flat Slabs with Drop Panels Under Seismic and Cyclic Actions

António Ramos^{1(✉)}, Carla Marchão², Dario Coronelli³, Duarte Faria⁴, Fausta Fiorillo³, Gianpaolo Rosati³, Jaroslav Halvoník⁵, João Pacheco de Almeida⁶, Jorge de Brito⁶, Luca Martinelli³, Marco Lamperti⁷, Miguel Fernandez Ruiz⁸, Monica Lavagna³, Robert Vollum⁹, and Rui Marreiros²

¹ CERIS, NOVA School of Science and Technology, Lisbon, Portugal
ampm@fct.unl.pt

² NOVA School of Science and Technology, Lisbon, Portugal
³ Politecnico di Milano, Milan, Italy

⁴ MFIC Ingénieurs Civils SA, Morges, Switzerland
⁵ Faculty of Civil Engineering, Slovak University of Technology in Bratislava, Bratislava, Slovakia

⁶ CERIS, Instituto Superior Técnico, University of Lisbon, Lisbon, Portugal

⁷ European Commission, Joint Research Centre (JRC), Ispra, Italy

⁸ Universidad Politécnica de Madrid, Madrid, Spain

⁹ Imperial College London, London, UK

Abstract. This paper presents the RecycleSlab research project, where a large-scale experimental test is being prepared. The specimen is a two-story building with flat slabs with drop panels, cast with concrete made with coarse recycled concrete aggregates (CRCAC), and will be tested under combined gravity and lateral loads. In this paper, the test setup is described in terms of structural design, test protocol, specimen dimensions and materials characterization. In addition, the research project will explore the effectiveness of innovative digital surveying techniques for the assessment of seismic damage in flat slab structures. For that purpose, the specimen will be measured in 3D before and after testing using laser scan technology with the aim of creating digital models. The testing of the full-scale two-story flat slab structure will be carried out at the ELSA laboratory of the European Commission's Joint Research Centre.

Keywords: Flat Slab · Punching · Concrete · Coarse Recycled Concrete Aggregates · Seismic Action; Circular Economy

1 Introduction

The structural application of flat slabs is widely prevalent in office, commercial, and residential buildings worldwide. However, their structural performance under seismic loads is not well understood, particularly in the slab-column connection area, where

the combined effects of high gravity loads and earthquake-induced stresses make it a critical zone. One of the most critical aspects of flat slab design is their resistance to punching shear failure. Such failures are brittle and sudden, making their prevention through proper design essential. Although punching failure is a localized issue, it can trigger progressive collapse and, in some cases, even lead to the complete failure of the structure. The loss of a slab-column connection increases stress in adjacent connections, raising the likelihood of further failures.

From a mechanical perspective, incorporating CRCA (Coarse Recycled Concrete Aggregate) is expected to negatively impact punching shear capacity. This is because CRCA is weaker than Coarse Natural Aggregate (CNA), and CRCAC (Concrete with CRCA) tends to develop larger crack widths than Natural Aggregate Concrete (NAC) [1]. Both factors reduce aggregate interlock, which plays a crucial role in shear and punching resistance. Shear design proposals for CRCAC [1] have confirmed this effect and were considered in Annex N (*Recycled aggregate concrete structures*) of the second-generation EN 1992 standard [2]. However, no similar study has been conducted for punching shear due to the limited availability of experimental data.

A recent State-of-the-Art review [3] highlights that research on the punching behavior of flat slabs remains scarce and has primarily been conducted using unrepresentative test specimens. Most available test results stem from very thin slab specimens, limiting an accurate assessment of shear resistance. This could lead to unsafe design, due to material and structural size effects, as well as shear span ratios that are not typical in actual structural applications. The paper [3] strongly recommends further testing, particularly on slabs with realistic thicknesses and representative dimensions in relation to the maximum aggregate diameter, to enhance the understanding of CRCAC's punching shear behavior, given that this phenomenon is highly influenced by size effects. Besides that, no flat slabs subjected to earthquake induced displacements, or other types of horizontal cyclic actions, were studied.

Also, testing of multi-story reinforced natural aggregate concrete slab specimens remains limited [4]. In North America, some studies have been conducted on scaled reinforced concrete slabs [5] and post-tensioned slabs [6]. In Europe, tests have been performed on a three-story waffle slab supported by columns [7] and a two-floor flat slab structure [8, 9, 10] at the JRC ELSA facility. The latter study contributed to the development of a new formulation for assessing the drift capacity of flat slab structures [9].

To the authors' knowledge, no additional tests on floor assemblages with thick slabs designed for both gravity and lateral loads have been conducted in Europe. Large-scale multi-story structure testing is essential due to its representative scale, the ability to analyze load redistribution within floors, and the opportunity to evaluate the overall structural response in terms of ductility and energy dissipation.

2 Research Significance

This paper presents the experimental program proposed within the RecycleSlab research project—*Structural Behaviour of Recycled Aggregate Reinforced Concrete Flat Slabs with Drop Panels under Seismic and Cyclic Actions*—conducted under the ERIES project

(HORIZON-INFRA-2021-SERV-01–07) and funded by the Horizon Europe Framework Programme. The project aims to investigate the behaviour of large-scale flat slab floors with drop panels, constructed using CRCAC, under combined gravity and lateral loads. The ultimate goal is to contribute to the development of a European Seismic Code Regulation for such structures. This initiative will mark the world's first pseudo-dynamic and cyclic tests on CRCAC flat slabs, with proposed methodologies for structural assessment to be incorporated into future design codes.

Construction and demolition waste (CDW) accounts for more than one-third of the total waste generated in the European Union (EU27). Additionally, the construction aggregates industry is the world's largest non-energy extractive sector. As a result, recovering CDW as recycled aggregates for concrete aligns with the European Union's Circular Economy Action Plan, offering a sustainable solution for the construction industry. Given that concrete is the second most used material globally after water, the potential benefits of this approach are substantial. However, in many regions, recycled aggregates are predominantly landfilled or downcycled, such as in backfilling operations or in road construction.

The scientific community has extensively studied the material behaviour of concrete made with CRCA, identifying its key resistance mechanisms and confirming its viability as a structural material. Despite this, CRCAC is not widely produced on a large scale in most regions [11]. This is primarily due to scepticism among clients, contractors, and designers, driven by the lack of large-scale demonstrations of CRCAC's structural performance and the absence of comprehensive testing for specific structural elements. Consequently, clear design guidelines covering all relevant resistance mechanisms and structural components remain unavailable.

Flat slabs, a widely used and resource-efficient structural solution, exemplify this challenge. Slabs account for the largest portion of the total concrete volume in a building, making them an ideal candidate for CRCAC applications. However, research on the punching behaviour of CRCAC flat slabs under gravity loads is limited, restricting their practical implementation. Moreover, no studies have examined the seismic performance of CRCAC flat slabs, which is particularly critical in regions with moderate to high seismic activity. The lack of knowledge regarding their behaviour under both gravity and seismic loads, along with the absence of demonstrative examples, hinders the broader adoption of CRCAC. This highlights the pressing need for further research in this area.

Testing a drop-panel solution aligns with the UN's Sustainable Development Goals, particularly in reducing material consumption and associated CO₂-equivalent emissions. Over the past decades, flat slabs made of conventional concrete have been the predominant structural choice for buildings and parking garages. While they offer architectural benefits due to their flat soffit, they can be highly inefficient in material usage, leading to unnecessary environmental impact.

In a recent paper about sustainability in the construction industry [12] the authors conclude that for moderate to large spans, flat slabs exhibit significantly higher environmental impact, whereas drop-panel solutions lead to much lower emissions, while maintaining comparable economic and functional performance. This difference arises from the structural efficiency of drop panels, where material is placed only where needed,

optimizing resource use. Additionally, when used efficiently, reinforced concrete structures have environmental impacts comparable to or even lower than other construction materials, such as timber or composite solutions. This underscores the importance of rational material use in achieving sustainable construction practices.

As the project aims to analyse and demonstrate a structurally and resource-efficient flat slab system, an environmental assessment will be conducted using a comparative life cycle assessment (LCA). This LCA will evaluate the environmental impacts of producing the tested prototype (constructed with CRCAC and drop panels) against a conventional flat slab system made with natural aggregate concrete, designed to exhibit similar structural behaviour but without drop panels. The comparison will be based on a truly equivalent functional unit, the flat slab system itself. This ensures a fair assessment of both systems as complete flat slab structures. This analysis will quantify the potential reduction in the carbon footprint achieved through the incorporation of drop panels and recycled aggregates, highlighting their environmental benefits.

Additionally, the research project will explore the effectiveness of advanced digital surveying techniques for assessing seismic damage in flat slab structures. The physical prototype will be captured in 3D both before and after testing using laser scanning technology, enabling the creation of detailed digital models for further analysis.

This research prioritizes public safety, economic efficiency, and the sustainability of the construction industry. Its goal is to enhance understanding of the seismic response of reinforced concrete flat slab structures made with CRCA. The group involved in this research comprises several European Universities and Research Centres, led by CERIS - Civil Engineering Research and Innovation for Sustainability, with team members from Nova School of Science and Technology and Instituto Superior Técnico from University of Lisbon, together with the Politecnico di Milano, the Imperial College London, the Slovak University of Technology in Bratislava and the Universidad Politécnica de Madrid, along two industry partners, Holcim (Itália) SpA and c5Lab - Sustainable Construction Materials Association, in collaboration with the Joint Research Centre of the European Commission. The experimental tests will be carried out at the ELSA laboratory of the European Commission's Joint Research Centre in Ispra, Italy.

3 Experimental Programme

3.1 Test Specimen

The two-story building specimen will feature two CRCAC flat slab floors with a three-by-two span configuration. The spans will measure 4.5 m and 5.0 m in the longitudinal direction and 4.5 m in the transverse direction, with a story height of 3.2 m (Fig. 1). The columns will have square cross-sections, with side dimensions of 0.4 m for internal columns, 0.35 m for edge columns, and 0.3 m for corner columns. Steel load cells will be installed at the mid-height of the columns during construction to measure internal forces. This experimental technique has been recently implemented at JRC ELSA and has undergone further developments [8, 9, 10].

The specimen's foundation will be a reinforced concrete beam grid (in order to move the specimen inside/outside the laboratory and to fasten the specimens to the laboratory's

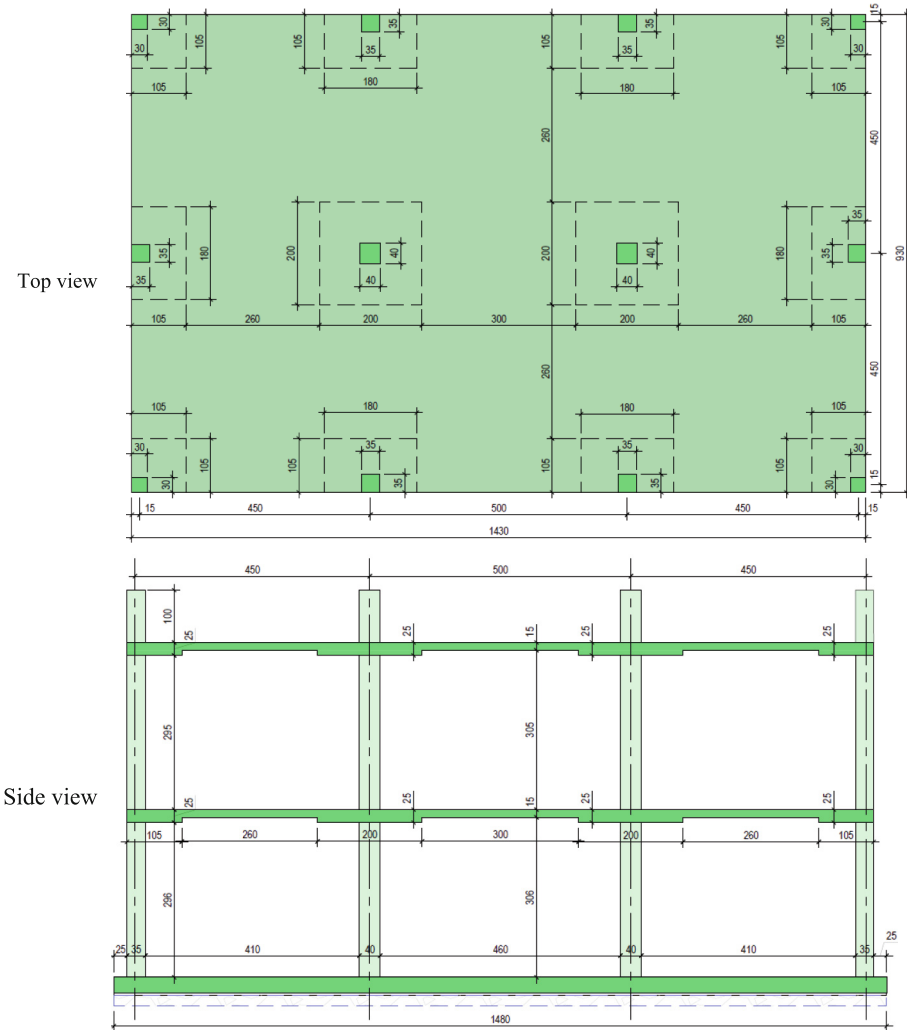


Fig. 1. Building geometry (dimensions in cm).

strong floor). The JRC ELSA Reaction wall has dimensions that allow testing the 6.4 m high, 14.3 m long and 9.3 m wide, two floors flat slab building proposed.

3.2 Materials

The reinforcement to be used will be B500 of ductility class C. At the columns, the splicing will be done using rebar couplers from Peikko.

The concrete was developed and produced by the industrial user partner Holcim (Itália) SpA. The aim was to have a C30/37 strength class, with a replacement ratio of 50% of the coarse aggregates (>4 mm), which translates to around a total 29% substitution

ratio for all the aggregates. The cement used was 42.5R Type II/B-LL from Holcim, and the plasticizer was Mapei Dynamon. Table 1 presents the concrete composition. During the concrete development, the concrete compressive strength was assessed through tests on 15 cm concrete cubes (Table 2).

Table 1. Concrete composition.

Cement (kg/m ³)	Water (l/m ³)	Sand 0/10* (kg/m ³)	Recycled Gravel 8/18 (kg/m ³)	Plasticizer (l/m ³)
360	160	1289	520	2,88

* Sand 0/10 contains 40,4% of aggregates > 4mm

Table 2. Compressive concrete strength.

Age (days)	3	7	28
f _{cm,cube} (MPa)	28,1	35,1	41,2

3.3 Structural Design

The building was designed for a dead load corresponding to the self-weight of the structural elements plus an allowance for the self-weight of non-structural elements of 3 kN/m². The live load was taken as 2 kN/m² assuming $\psi_2 = 0.30$ (for assessment of the quasi-permanent loading). The design earthquake action was taken as a 0.6% horizontal drift ratio.

The structural analysis was performed with ANSYS and SAP2000, to double check the design and to cover usual deviations in modelling of this type of structures, notably of the slab-column connection regions. All structural elements were modelled elastically to determine the internal force distribution. Lateral actions were applied as imposed displacements on the slabs corresponding to the specified drift level. To account for variations in stiffness between the slabs and columns throughout the loading process, two different stiffness scenarios were analysed: SS1 - all elements with constant (bulk) values of the stiffness and dimensions. This model shall cover the response before any cracking occurs or if the loss of stiffness between the slab and the columns are comparable; SS2 - the modulus of elasticity of the columns was reduced to 50%, and to 25% for the slabs, to determine the internal forces of the columns and slab-column connections, for a more realistic scenario concerning the earthquake action. This large reduction of the slabs' stiffness can be justified by the work of [13], where several flat slab-column connections under combined gravity and horizontal cyclic loading were analysed, and the experimental connection stiffness varied from 12% to 17% of the elastic stiffness.

Although not needed from the design, it was decided to have a floor containing shear reinforcement (first floor), using shear studs. The shear reinforcement layout considered can be observed on Fig. 2. Initially the second floor, with similar longitudinal reinforcement, will not contain shear reinforcement, but provisions for a possible retrofitting using post-installed shear reinforcement were made, to be installed before the last experimental phase. The idea is to have information on the behaviour of flat slabs with or without shear reinforcement, a subsequently, and if possible, to study a strengthening/retrofitting technique applicable to this type of structures.

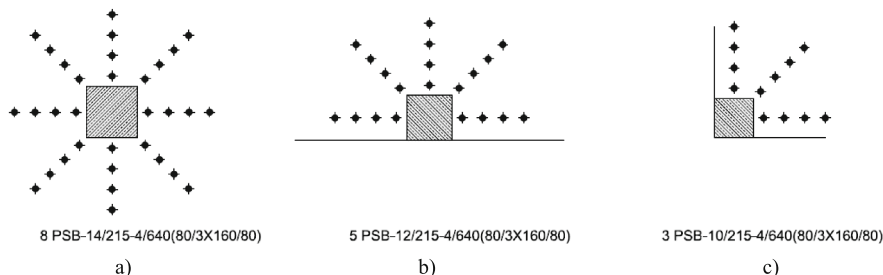


Fig. 2. Shear reinforcement on the first floor (Peikko PSB): a) central column; b) edge column; c) corner column.

3.4 Loading and Testing Program

To achieve all objectives of this research program the experimental campaign is divided in two sets of tests. First, and to appraise the seismic behaviour of flat slabs with ductile shear walls under a seismic action, two pseudo-dynamic tests will be carried out, for two levels of seismic motion: one for the serviceability limit state (SLS) and another for the ultimate limit state (ULS). Two numerical shear walls (the shear walls are only considered in the numerical model used to control the pseudo-dynamic tests) will be considered.

Subsequently quasi-static cyclic loading tests will be performed, without the numerical shear walls. The floors will be tested under combined gravity and lateral cyclic loading, with increasing horizontal displacements to near-failure conditions. The test sequence is planned to achieve progressive and controlled damage of slab-column connections.

The gravity loading will be the self-weight and supplementary weight provided by the use of water tanks placed on the slabs, to simulate the quasi-permanent load considered ($3,6 \text{ kN/m}^2$) (see Fig. 3).

Horizontal loading will be applied by two hydraulic jacks per floor, with a capacity of 1000 kN each. These actions will be applied in “shear-keys”, with prestressed unbonded connections to the side of the slabs at mid-span, in order to minimize the interference of this application in the behavior of the building.

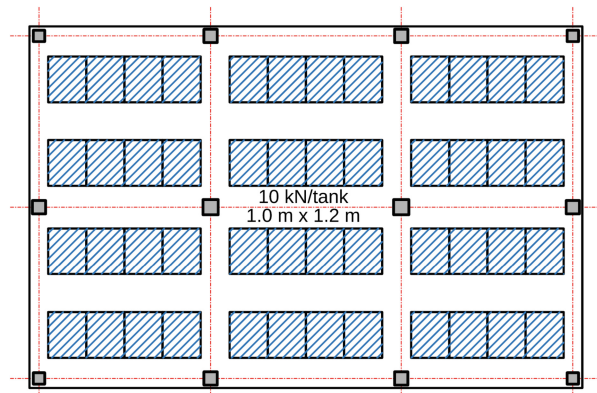


Fig. 3. Water tanks placement – supplementary weight.

3.5 Data Acquisition and Instrumentation Plan

Attending the uniqueness and scale of the planned experimental tests, a careful planning of the data acquisition system was carried out. During the planned test phases several measurements are going to be performed, in order to collect information about the behaviour of this type of structures under seismic and horizontal cyclic loading.

Two 1000 kN hydraulic actuators will be used at each floor to apply the horizontal forces. All actuators are equipped with a load cell mounted on the piston rod, to measure the force transferred to the structure. Horizontal displacements will be taken at the far end of the specimen, with respect to the reaction wall, using two displacement transducers per floor, in order to also monitor torsion.

In order to assess the evolution of crack widths along the slab's thickness during testing, small holes in the slabs near the columns, obtained by placing a small plastic tube before casting, are going to be instrumented with LVDT fastened to the bottom face of the slab, with the target glued on the top face of the slab, at the other end of the hole. Also, inclinometers will be used to assess the slab's rotation near the slab-column connections.

For assessing the internal forces at the columns a special steel device (load cell), placed at the mid-height of the columns during the construction of the building. Three types of these devices will be produced and calibrated. Similar devices were already used in the SlabStress Project [8, 9, 10], but an improved version was developed for the current project.

The building specimen will undergo 3D surveying to evaluate the potential and effectiveness of advanced digital surveying techniques for assessing seismic damage in flat slab structures. Laser scanner measurements will be conducted both before and after testing, allowing for the creation of pre- and post-test digital models. These models can be examined, measured, compared, and analyzed at any time to accurately identify and assess damage.

3.6 Life Cycle Assessment

The project includes a life cycle assessment (LCA) conducted in accordance with relevant standards (EN 15804:2012 + A2:2019 [14], ISO 14044:2006 [15], and ISO 14040:2009 [16]) to evaluate the environmental impacts of the flat slab system from cradle to gate. This assessment covers the entire production process, including raw material procurement, transportation to the production site, and slab manufacturing.

The LCA will be comparative, incorporating different scenarios to analyze various assumptions and their environmental implications: Flat slab without drop panels and natural aggregates; Flat slab with drop panels and natural aggregates; Flat slab without drop panels and with recycled aggregates; Flat slab with drop panels and with recycled aggregates. Different transport distances of the raw materials used for concrete production will be considered.

The objective of this LCA is to: a) Assess the environmental benefits of using drop panels, particularly in reducing the volume of concrete required for the flat slab, thereby decreasing clinker consumption; b) Identify optimal conditions for the use of CRCA by conducting sensitivity analyses (e.g., evaluating different transport scenarios) to determine when CRCA result in a lower carbon footprint compared to natural aggregates; c) Demonstrate the impact of different functional unit choices (such as comparing a complete structural system versus one cubic meter of concrete) on life cycle impact assessments and overall findings.

The choice of the functional unit - the structural element itself - represents a significant contribution to the state of the art. Most environmental impact comparisons between NAC and CRCAC typically focus on: a) The procurement of coarse aggregates, without accounting for necessary adjustments in concrete mix design when using CRCA; b) The production of 1 m³ of concrete, considering mix design changes but overlooking the impact of CRCA on concrete properties; c) The production of 1 m³ of concrete normalized by compressive strength, which remains inadequate since CRCA influences various concrete properties in different ways. In designing the flat slab system, both elastic and long-term slab deflections must be considered, and the concrete mix will be tailored to achieve comparable durability properties. This approach ensures a truly equivalent functional unit, allowing for a more accurate comparison of the environmental impacts of CRCAC and NAC.

4 Final Remarks

This paper presents a large-scale test setup of a CRCAC flat slab building with drop panels, subjected to seismic and cyclic loading. This groundbreaking experimental study is expected to generate significant interest among the scientific and engineering communities, as well as the broader public, by demonstrating the potential of CRCAC in structural applications. The findings will be shared with academia and industry professionals, with a strong focus on disseminating design guidelines to practitioners.

Beyond its technical contributions, this research has a notable social impact by enabling the design of safer structures using sustainable materials. Additionally, the selection of efficient structural systems will encourage engineers to optimize resource use, thereby reducing the environmental footprint of construction. A key benefit of this

project is its contribution to minimizing the extraction of natural resources and decreasing construction waste accumulation, which will have a meaningful impact, particularly in European countries.

Acknowledgements. This work is part of the transnational access project “ERIES- RecycleSlab” (Structural Behaviour of Recycled Aggregate Reinforced Concrete Flat Slabs with Drop Panels under Seismic and Cyclic Actions), supported by the Engineering Research Infrastructures for European Synergies (ERIES) project (www.ries.eu), which has received funding from the European Union’s Horizon Europe Framework Programme under Grant Agreement No. 101058684. This is ERIES publication number C67.

References

1. Pacheco, J., de Brito, J., Chastre, C., Evangelista, L.: Uncertainty of shear resistance models: influence of recycled concrete aggregate on beams with and without shear reinforcement. *Eng. Struct.* **204**(1), 109905 (2020)
2. European Committee for Standardization (2023), FprEN 1992–1–1 (2023). Eurocode 2: Design of concrete structures - Part 1–1: general rules and rules for buildings, bridges and civil engineering structures, CEN
3. Ramos, A.; et al.: A review of punching behavior of slab–column connections with recycled coarse aggregate concrete. *Structural Concrete* 2024. (<https://doi.org/10.1002/suco.202400435>)
4. Coronelli, D., Muttoni, A., Pascu, I.R., Ramos, A.P., Netti, T.: A state of the art of flat-slab frame tests for gravity and lateral loading. *Struct. Concr.* **21**(6), 2764–2781 (2020). <https://doi.org/10.1002/suco.202000305>
5. Moehle, J.P., Diebold, J.W.: Experimental study of the seismic response of a two-story of a flat-plate structure. University of California, Berkeley (1984)
6. Kang T.H.-K., Wallace J.W.: Shake table tests of reinforced flat plate frames and post-tensioned flat plate frames. In: 13th World Conference on Earthquake Engineering, Vancouver, B.C., Canada (2004)
7. Zaharia, R., et al.: Pseudodynamic earthquake tests on a full-scale RC flat-slab building structure. European Commission Joint Research Centre, 119 pp (2006)
8. Coronelli, D., et al.: Testing of a full-scale flat slab building for gravity and lateral loads. *Eng. Struct.* **243**, 112551 (2021)
9. Muttoni, A., et al.: Deformation capacity evaluation for flat slab seismic design. *Bull. Earthq. Eng.* **20**, 1619–1654 (2022)
10. Ramos, A.P., et al.: Seismic performance of strengthened slab-column connections in a full-scale test. *J. Earthquake Eng.* **27**(9), 2299–2318 (2022). <https://doi.org/10.1080/13632469.2022.2112320>
11. Pacheco, J., de Brito, J., Lamperti-Tornaghi, M.: Use of recycled aggregates in concrete – Opportunities for upscaling in Europe. Luxembourg, Publications Office European Union, (2023). <https://doi.org/10.2760/144802.JRC131294>
12. Regulez Pérez, B., Faria, D.V., Todisco, L., Fernández Ruiz, M., Corres Peiretti, H.: Sustainability in construction: the urgent need for a new ethics. *Struct. Concr.* **24**(2), 1893–1913 (2022). <https://doi.org/10.1002/suco.202200406>
13. Isufi, B., Pinho Ramos, A., Lúcio, V.: Post-earthquake performance of slab-column connection with punching shear reinforcement. *J. Earthquake Eng.* **26**(3), 1171–1193 (2020). <https://doi.org/10.1080/13632469.2020.1713924>

14. EN15804:2012+A2:2019 (2012). Sustainability of construction works. Environmental product declarations. Core rules for the product category of construction products, CEN
15. ISO-14044 (2006). Environmental management - Life cycle assessment - Requirements and guidelines. Genève, Switzerland, ISO: 58
16. ISO-14040 (2009). Environmental management - Life cycle assessment - Principles and framework. Genève, Switzerland, ISO: 20

Open Access This chapter is licensed under the terms of the Creative Commons Attribution 4.0 International License (<http://creativecommons.org/licenses/by/4.0/>), which permits use, sharing, adaptation, distribution and reproduction in any medium or format, as long as you give appropriate credit to the original author(s) and the source, provide a link to the Creative Commons license and indicate if changes were made.

The images or other third party material in this chapter are included in the chapter's Creative Commons license, unless indicated otherwise in a credit line to the material. If material is not included in the chapter's Creative Commons license and your intended use is not permitted by statutory regulation or exceeds the permitted use, you will need to obtain permission directly from the copyright holder.





ERIES-RESTORING: REtrofitting of STOne MasonRy Using INnovative Grid-Based Composites

Madalena Ponte¹(✉), Larisa Garcia-Ramonda², Igor Lanese³, Gerard J. O'Reilly⁴, Elisa Rizzo-Parisi³, Francesco Graziotti¹, Luca Pelà², Andrea Penna¹, Guido Magenes¹, Rita Bento⁵, and Gabriele Guerrini¹

¹ Departement of Civil Engineering and Architecture (DICAr), University of Pavia, Pavia, Italy
madalena.ponte@unipv.it

² Department of Civil and Environmental Engineering, Universitat Politècnica de Catalunya, Barcelona, Spain

³ European Centre for Training and Research in Earthquake Engineering (EUCENTRE), Pavia, Italy

⁴ University School for Advanced Studies (IUSS), Pavia, Italy

⁵ CERIS, Instituto Superior Técnico, Universidade de Lisboa, Lisbon, Portugal

Abstract. This paper discusses the effectiveness of Composite Reinforced Mortars (CRM) and Fiber-Reinforced Mortars (FRM) as seismic retrofit of existing stone masonry buildings. A large experimental campaign was conducted within the ERIES-RESTORING project, involving vertical compression, diagonal compression, and quasi-static cyclic tests. Undressed stone masonry specimens under different retrofit configurations, compatible with historical masonry, were studied: bare masonry, CRM applied on one side, CRM applied on two sides, and FRM applied on two sides. The CRM retrofit consisted of a glass-FRP mesh embedded in natural hydraulic-lime mortar and the FRM retrofit of a mortar with polymeric fibers. For the vertical and compression tests, three masonry wallets were tested for each retrofit configuration, excluding the FRM that was not tested under this type of loading. Instead, for the testing of the in-plane cyclic behavior, full-size piers were subjected to a constant axial stress level and double-fixed boundary conditions. Two different pier aspect ratios were investigated to study the flexural and shear behavior. The FRM retrofit was tested only under quasi-static cyclic shear-compression loading and was applied directly to both sides of a single pier with an aspect ratio inducing flexural behavior. The experimental results, including damage mechanisms, lateral strength, and deformation capacity, can be referred to for calibrating advanced numerical models and conducting parametric studies on geometric, material, and loading conditions. Lastly, the outcomes of this project will contribute to the validation of analytical models and the development of design guidelines and code requirements for these retrofitting techniques on historical masonry.

Keywords: Composite Reinforced Mortars · Fiber-Reinforced Mortars · Quasi-Static Cyclic Shear-Compression Tests · Seismic Retrofit of Existing Buildings · Stone Masonry

1 Introduction

The protection of the built cultural heritage is an important step towards the preservation of the past culture and history of countries, but also of the future, leading to greater sustainability. Most Mediterranean countries present a high density of historical masonry buildings in stone masonry, that require effective and durable retrofitting techniques. Ence, solutions like Composite Reinforced Mortars (CRM), Fabric Reinforced Cementitious Matrices (FRCM), and Fiber Reinforced Mortars (FRM) have shown good results and have been more recently used due to their compatibility with historic structures and the use of lime-based mortars ([1, 2]). However, much has still to be studied on these retrofit solutions, since most of them are not yet standardized, lacking guidelines for their design and experimental results on their effectiveness on masonry structures.

The work presented in this paper is a large experimental campaign, part of the ERIES project, in a collaborative effort led by the Universidade de Lisboa (Portugal) alongside the University of Pavia (Italy), Universitat Politècnica de Catalunya (Spain), EUCENTRE Foundation, IUSS Pavia (Italy), and initial contributions from ETH Zurich (Switzerland). The experimental program included a vertical compression, diagonal compression, and quasi-static cyclic shear-compression testing campaign. The specimens were made of undressed stone masonry, and four configurations were tested: unreinforced (bare), retrofitted with CRM on one side, retrofitted with CRM on two sides, and retrofitted with FRM on two sides. Moreover, for the quasi-static cyclic shear-compression tests two different height/length aspect ratios were studied on full-scale specimens, one to force flexural behavior and the other shear.

The goal of the campaign was to evaluate the performance of CRM and FRM in enhancing the seismic behavior of masonry. The results will be used to validate analytical models and contribute to the development of design guidelines.

2 Characterization of Constituent Materials

Calcareous sandstone rocks from the province of Bergamo, Italy, were used as masonry units and were characterized by a mean density of 2580 kg/m^3 , mean compressive strength of 149 MPa perpendicular and 144 MPa parallel to the sedimentation layers, and mean tensile strength of 19 MPa. The mortar adopted for the masonry construction was a weak hydraulic lime mortar mix designed specially to represent the overall properties commonly found in historical masonry structures in the Mediterranean countries. For compatibility purposes between the substrate and the strengthening, natural hydraulic lime was also included in the CRM retrofit mortar mix. Tensile and compressive strength were retrieved from 160 x 40 x 40 mm prisms after 28 days of curing [3], obtaining, respectively, 0.17 MPa and 0.81 MPa on mortar used for the masonry construction, 5.84 MPa and 22.55 MPa on mortar used for CRM retrofitting, and 6.91 MPa and 47.02 MPa on mortar used for FRM retrofitting. The CRM retrofit was applied using Glass-FRP (GFRP) meshes characterized by mean tensile strengths of 74 kN/m and 86 kN/m in the weft and warp directions, respectively, and an ultimate strain of 1.5% in both directions. The mesh presents a total fiber weight of 400 g/m^2 and is spaced 120 mm apart in the weft and 80 mm apart in the warp directions. The GFRP mesh was

mechanically fixed to the substrate by helicoidal steel connectors made of stainless steel AISI 304 with a nominal diameter of 10 mm.

3 Specimen Description

Masonry specimens were built to be tested under three different types of loading, vertical compression (VC), diagonal compression (DC), and quasi-static cyclic shear-compression (SC). The type of masonry and construction techniques adopted were the same for all three tests and were made in order to replicate the construction commonly found in historical ancient buildings in the Mediterranean countries.

The masonry was characterized as double-leaf natural stone masonry with irregular horizontal courses and roughly dressed sedimentary rock blocks (Fig. 1). The total nominal thickness of the masonry walls was 300 mm with mortar and stone fragments infilling the interspace of the stone leaves. Through stones were only used at the walls' edges. The CRM and FRM retrofit presented a total thickness of about 30 mm, with a nonuniform mortar layer thickness that depended on the irregularity of the masonry surface (Fig. 1c-d). The layers of the retrofit solutions were connected mechanically to the surface through helicoidal connectors that were embedded into about $\frac{3}{4}$ of the specimen thickness when the retrofit was applied only on one side, and passed through both masonry leaves when the retrofit was applied on both sides. In both cases, the connectors also provided transverse passive confinement to the masonry. The connectors were applied together with polymeric discs to help spread the locally concentrated stresses. A density of about five connectors per square meter of façade was considered for each specimen.

Vertical compression tests were carried out on nine wallettes under different retrofit configurations, with three wallettes per type of retrofit: bare masonry (V_URM), CRM applied on one side (V_CRM1), and CRM applied on both sides (V_CRM2). The wallettes were saw-cut from a long wall (Fig. 1a), after 28 days of curing, excluding the edges to avoid the confining effects of through stones necessary for the wall construction. The wallettes presented dimensions of 120 x 80 x 30 cm, by adapting the regulations of EN 1052-1 [4] that are specified for brick block dimensions instead of irregular stones. The CRM retrofit was applied after the wallettes were saw-cut into their dimensions, with the warp of the mesh in the horizontal direction.

Diagonal compression tests were carried out on nine wallettes under different retrofit configurations, with three wallettes per type of retrofit: bare masonry (D_URM), CRM applied on one side (D_CRM1), and CRM applied on both sides (D_CRM2). The wallettes were also saw-cut from a long wall, following the same procedure as for the VC tests wallettes. The wallettes presented dimensions of 100 x 100 x 30 cm, following the specifications of ASTM (2015) [5]. The CRM retrofit was applied after the wallettes were saw-cut into their dimensions, without considering a preferential direction for the warp and weft.

Quasi-static cyclic shear-compression tests were carried out on seven full-scale walls under different retrofit configurations: bare masonry (URM), CRM applied on one side (CRM1), CRM applied on both sides (CRM2), and FRM applied on both sides (FRM2). Two different aspect ratio (height/length) configurations were studied for URM, CRM1

and CRM2: slender specimens ($h/l = 1.5$) representing piers between window openings (Fig. 1b), and squat specimens ($h/l = 0.69$) simulating solid walls or walls with widely spaced openings. The FRM retrofit was applied only for the slender configuration. The slender specimens were identified as “SL_(type of retrofit)” and the squat ones as “SQ_(type of retrofit)”. The slender specimens included portions of the adjacent top and bottom spandrels for a proper anchorage of the retrofit; on the other side, for the squat specimens, the mesh was anchored on additional top and bottom RC beams that were designed, together with a system of threaded bars and steel profiles, to prevent rocking or sliding of the masonry pier regarding the foundation and spreader beam. The CRM retrofit was applied for the slender specimens with the warp of the mesh in the horizontal direction and the squat specimens in the vertical direction to force the squat specimens to fail in shear and the slender ones in flexure. Mesh overlaps of at least 300 mm were carried out when necessary.

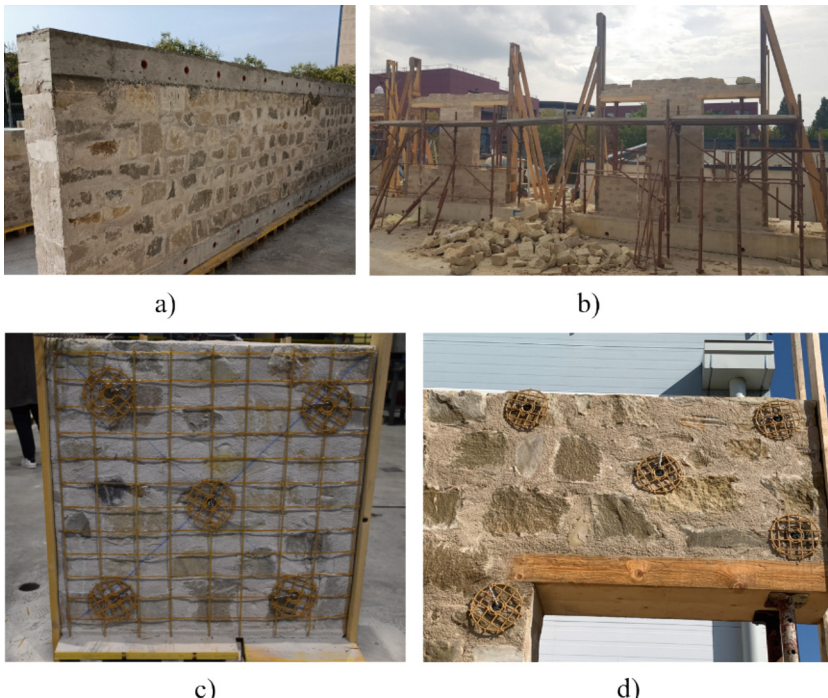


Fig. 1. a) Finished look of the masonry long wall for VC tests, b) construction of slender piers for quasi-static cyclic shear-compression tests, c) CRM retrofit application on specimen for diagonal compression tests, and d) FRM retrofit application on specimen for quasi-static cyclic shear-compression tests.

4 Vertical Compression Tests

4.1 Test Set-Up and Testing Protocol

A centered axial force was applied on the wallette by a force-controlled universal testing machine and was distributed uniformly by the RC beams. The upper and lower faces of the beams in contact with the machine were regularized with gypsum. The load was applied at a controlled rate with loading and unloading cycles of amplitudes 1/6, 1/3, and 1/2 of the expected strength with respective durations of the ramps of 210, 420, and 630 s. After these cycles, the specimens were loaded monotonically to failure. At zero and maximum values, the load was kept constant for 10 s before the unloading or reloading phase to stabilize the stress state. Eight 50-mm-stroke potentiometers were deployed: two vertical and one horizontal potentiometer, positioned in each main façade of the wallette to measure in-plane strains (Fig. 2a); while one horizontal potentiometer was placed on each side façade along the wallette thickness (Fig. 2b). The mounting rods of the potentiometers were positioned in stones, avoiding mortar joints, and, for the case of the retrofitted specimens, a sufficiently large hole on the retrofit was made.

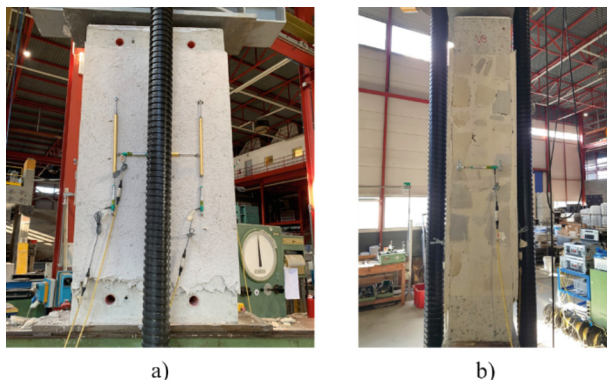


Fig. 2. Vertical compression test set-up: a) front and b) side views.

4.2 Results

Compressive stress-strain curves were obtained for each specimen, as presented in Fig. 3 for specimen V_URM_1. The compressive strength of the masonry, f_c , was evaluated by dividing the maximum vertical force resisted by the specimen, P , by the nominal cross-section area of the specimen, given by $A_n = 800 \times 300 \text{ mm}^2$. Considering that for low-stress levels, the material behaves as isotropic, homogeneous, and linear elastic, the elastic parameter, Young's modulus, E , was defined between 10% and 33% of the measured compressive strength by calculating the slope of the secant between these points, as shown in Fig. 3b.

The values of E and f_c are presented in **Table 1**. The compressive strength of the masonry retrofitted with CRM on one side increased by 1.25 times and with CRM on

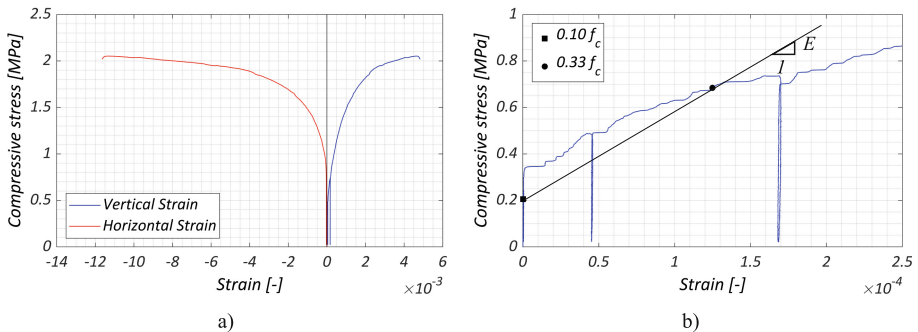


Fig. 3. Vertical compression test response of V_URM_1: a) vertical and horizontal strain, and b) zoom on vertical strain in the initial phase.

Table 1. Vertical compression test results.

	Bare masonry		CRM on one side		CRM on two sides	
	f_c [MPa]	E [GPa]	f_c [MPa]	E [MPa]	f_c [MPa]	E [MPa]
Average	1.98	3.47	2.49	3.46	2.85	4.76
C.o.V	6.6%	27.2%	1.8%	24.5%	6.9%	21.2%

two sides by 1.5 times, regarding the bare masonry. On the other hand, the E presented the same value when retrofitted on only one side and an improvement factor of 1.4 when retrofitted on both sides.

5 Diagonal Compression Tests

5.1 Test Set-Up and Testing Protocol

An axial force centered on the diagonal of the wallette was applied to the specimen by a force-controlled universal testing machine. The two corners in contact with the machine were regularized with gypsum. The load was applied at a controlled rate with loading and unloading cycles of amplitudes 1/6, 1/3, and 1/2 of the expected strength with respective durations of the ramps of 100, 200, and 300 s. After these cycles, the specimens were loaded monotonically to failure. At zero and maximum values, the load was kept constant for 10 s before the unloading or reloading phase to stabilize the stress state. Eight 50-mm-stroke potentiometers were deployed to measure the vertical and horizontal deformations. One vertical and one horizontal potentiometers were positioned in each main façade of the wallette, within the middle half, to measure in-plane strains (Fig. 4). The mounting rods of the potentiometers were positioned in stones, avoiding mortar joints, and, for the case of the retrofitted specimens, a sufficiently large hole on the retrofit was made.

5.2 Results

Compressive stress-strain curves were obtained for each specimen, as presented in Fig. 5 for specimen D_URM_1. The shear strength of the masonry, τ_{max} , was evaluated according to the ASTM and RILEM standards [5, 8] by dividing the maximum vertical force resisted by the specimen, P , by the nominal cross-section area of the specimen, given by $A_n = 1000 \times 300 \text{ mm}^2$. To compute the shear strength of the structure like this, it is assumed a pure shear stress state at the center of the panel, with the principal stress direction coinciding with the two diagonals of the wall.

The shear modulus G was calculated from the shear strength, following the same method as in the calculation of E from the vertical compression tests, as shown in Fig. 5b. However, the actual stress distribution is not purely uniform, as shown by Frocht [9]. Analytical and numerical methods improve the accuracy of principal stress estimation at the pier's center, allowing for a more precise calculation of masonry tensile strength by comparing it to the τ_{max} with a ratio of 0.5 to 0.707. Here, the latter was considered.

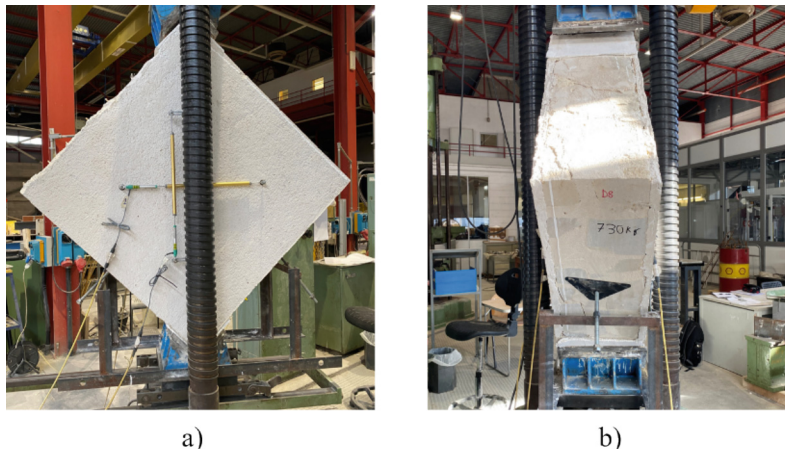


Fig. 4. Diagonal compression test set-up: a) front and b) side views.

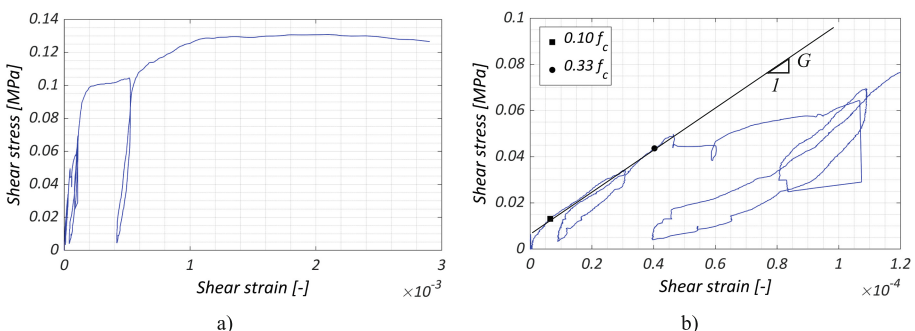


Fig. 5. Diagonal compression test response of D_URM_1: a) shear strain, and b) zoom on shear strain in the initial phase.

The values of G , τ_{max} and f_t are presented in Table 2. The tensile strength of the masonry retrofitted with CRM on one side increased by 2.5 times and with CRM on two sides by 4.0 times, regarding the bare masonry. On the other side, reliable conclusions cannot be made regarding G since potentiometers were not able to record significant deformations on three of the retrofitted specimens.

Table 2. Diagonal compression test results.

	Bare masonry		CRM on one side		CRM on two sides	
	f_t [MPa]	G [GPa]	f_t [MPa]	G [MPa]	f_t [MPa]	G [MPa]
Average	0.09	1.10	0.23	1.12	0.37	1.58
C.o.V	2.2%	53.8%	3.4%	52.9%	8.9%	- %

6 Quasi-Static Cyclic Shear-Compression Tests

6.1 Test Set-Up and Testing Protocol

A system of two strong-walls and a strong-floor, available at the EUCENTRE laboratory, was used for the test set-up (Fig. 6a-b). The RC foundations of the piers were fastened to the strong-floor with pos-tensioned bars. Two vertical servo-hydraulic actuators attached to the top RC spreader beam imposed a constant axial load of 20% of the masonry's compressive strength and a double-bending boundary condition. Additionally, the out-of-plane displacements of the pier top were prevented. The horizontal actuator applied the first sets of cycles in force control up to less than half the predicted lateral strength, calculated as proposed in Ponte et al. (2024) [6]. Then, displacement-controlled cycles were applied until reaching near-collapse conditions due to severe damage, strength degradation, or instability to the vertical load. Push-and-pull cycles of any amplitude were repeated three times. The specimens were instrumented with 40 displacement transducers to monitor the specimen displacements and eventual ones between the specimen and the test set-up.

6.2 Results

The retrofitted specimens tested under quasi-static cyclic shear-compression presented distinct enhancement in structural behavior depending on their geometry and retrofit configuration. For both aspect ratios, the specimens present a clear trend in the efficacy of the retrofit regarding strength and deformation capacity, with different variations of failure mode. The envelope force-displacement curves of the tested specimens are presented in Fig. 7 and Fig. 10b.

Squat masonry walls exhibited a shear failure mode characterized by diagonal cracking with significant damage at the intersection, as shown in Fig. 8. From the capacity

curves, it was concluded that squat piers benefited most from CRM applied symmetrically, which doubled the lateral load-bearing capacity and increased the displacement capacity at 20% strength loss, ultimate displacement, by 1.5 times regarding the bare masonry (SQ_URM). This increase in displacement capacity allowed the ultimate drift to move from the 0.5% ultimate drift coded for URM masonry piers failing in shear [7] to a value of 0.7%. Moreover, applying the CRM on only one side resulted in smaller improvements. The load-bearing capacity increased by a factor of 1.4, and the ultimate displacement by a factor of 1.2, with the ultimate drift improving to 0.6%. Therefore, symmetrically strengthening the masonry specimens led to a 30% additional increase in load-bearing and displacement capacity compared to asymmetrical strengthening.

On the other side, the slender masonry specimens exhibited a hybrid or flexural failure mode, shown in Fig. 9, as predicted by the analytical calculations in [6]. In fact, the bare masonry specimen presented initially a rocking mechanism that transitioned in the final loading cycles into a shear failure mode with diagonal cracking. However, unlike the squat specimens, where masonry wedges delimited by the diagonal cracks were expelled, the slender piers still carried the load through the diagonal struts without significant accumulation of crack opening.

According to the capacity curves, CRM on both sides of slender specimens increased the lateral load-bearing capacity by approximately 1.5 times, similar to the squat specimens, and the ultimate displacement by 3.0 times, with an exceptional improvement. The latter meant that the 1.0% drift limit prescribed by the current building codes for masonry piers failing in flexure [7] was increased by 3 times. In comparison, when the CRM was applied to only one side, there was a lower increment of the load-bearing capacity of 1.2 times and the ultimate displacement of 1.4 times, corresponding to an ultimate drift of 1.4%. Symmetric strengthening with CRM on slender walls resulted in a 20% higher load capacity and a double improvement in displacement capacity compared to the single-sided application, highlighting the importance of symmetric reinforcement, especially for deformation capacity.

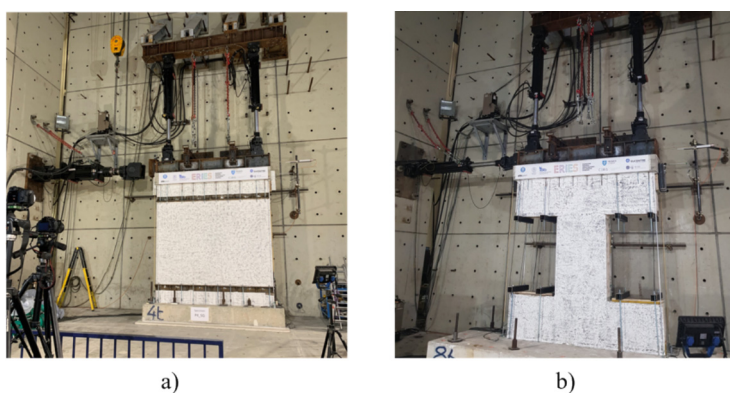


Fig. 6. Quasi-static cyclic shear-compression tests test set-up: a) squat specimen, b) slender specimen.

Near the end of the tests, all retrofitted specimens exhibited delamination of the retrofit layer from the substrate and rupture of the GFRP mesh. The delamination, probably aggravated by the irregularity of the stone masonry, could possibly be lessened by increasing the number of connectors. Slender specimens with CRM also developed a sliding shear interface at the base of the pier at the end of the test (Fig. 9b-c), and masonry crushing.

The application of the FRM retrofit system on both sides of the masonry was also studied for slender piers. The mechanism of collapse was similar to the slender pier retrofitted with CRM on both sides, as shown in Fig. 10a. Moreover, despite the FRM solution presenting a higher stiffness and a slightly lower strength (enhancement factor of 1.4 regarding bare masonry), with the peak load at a lower displacement, the ultimate displacement was the same for both retrofit solutions, corresponding to an ultimate drift value of 3.0%. This suggests that both CRM and FRM retrofitting techniques effectively enhance the in-plane behavior of slender walls, with CRM providing a slightly greater strength enhancement.

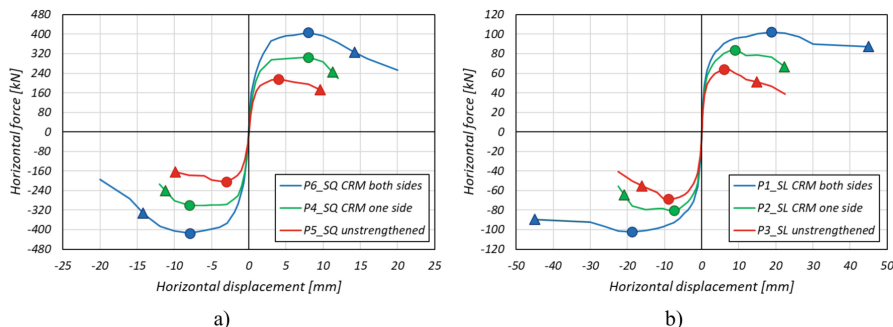


Fig. 7. Force-displacement envelope curves: a) squat and b) slender specimens.

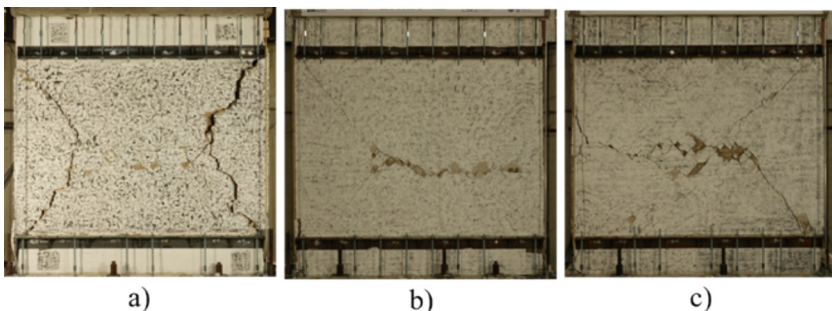


Fig. 8. Final crack pattern: a) SQ_URM, b) SQ_CRM1 (retrofitted side), c) SQ_CRM2.

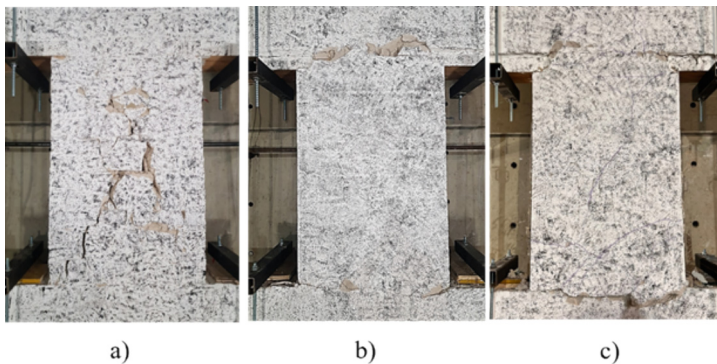


Fig. 9. Final crack pattern: a) SL_URM, b) SL_CRM1 (retrofitted side), c) SL_CRM2.

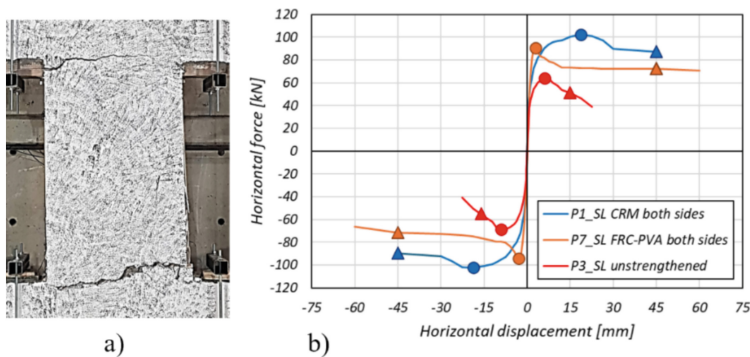


Fig. 10. SL_FRM2 results: a) Final crack pattern, b) force-displacement envelope curve.

7 Concluding Remarks

This paper presents an overview of the ERIES-RESTORING project, demonstrating the effectiveness of CRM and FRM retrofitting in enhancing structural performance under vertical compression, diagonal compression, and quasi-static cyclic shear-compression. Specifically, the compressive strength of bare masonry increased by a factor of 1.25 with CRM on one side and 1.5 with CRM on both sides; while the tensile strength exhibited a more substantial improvement, increasing by factors of 2.5 and 4.0, respectively. Moreover, for full-scale piers failing in shear, CRM on one side increased the lateral strength by 1.4 times, while CRM on both sides resulted in a twofold increase. In contrast, for slender piers failing in flexure, the lateral strength increased by a factor of 1.2 for CRM on one side and 1.5 for CRM on both sides. In terms of ultimate displacement capacity, slender piers showed significant improvements, with increasing factors of 1.4 for CRM on one side and 3 for CRM on both sides. For squat piers, the increase in ultimate drift capacity was more modest, with factors of 1.2 and 1.6 for CRM on one side and CRM on both sides, respectively. Additionally, a slender specimen retrofitted with FRM on two sides exhibited a 1.4-fold increase in lateral strength and a 3-fold increase in ultimate

drift, demonstrating a performance comparable to CRM on both sides. These findings will help develop guidelines for the design of CRM and FRM retrofit of masonry and numerical models.

Acknowledgements. This work is part of the transnational access project “ERIES-RESTORING”, supported by the Engineering Research Infrastructures for European Synergies (ERIES) project, funded within the European Union’s Horizon Europe Framework Programme under Grant Agreement No. 101058684. This is ERIES publication number C65. The authors would like to acknowledge the help provided by the staff of the EUCENTRE Foundation and of DICAr/UniPV, the material support by Laterlite S.p.A., the financial support by the European Union – NextGeneration EU through the postdoctoral grant Margarita Salas, the financial support by the Foundation for Science and Technology (FCT) through the CERIS project UIDB/04625/2025, and the financial support by DPC-ReLUIS project (2024–2026) through WP5 “Integrated and sustainable interventions for existing buildings” and WP10 “Masonry constructions” funded by the Italian Department of Civil Protection. Luca Pelà acknowledges the support received from the AGAUR - ICREA Acadèmia Research Program by the Department of Research and Universities of the Catalan Government.

References

- Guerrini, G., Bruggi, A., Urso, S., Quaini, M., Penna, A.: Cyclic shear-compression tests on two stone masonry piers strengthened with CRM and FRCM. *Procedia Structural Integrity*, Elsevier B.V. 2214–2221 (2022). <https://doi.org/10.1016/j.prostr.2023.01.283>
- Garcia-Ramonda, L., Pelà, L., Roca, P., Camata, G.: Cyclic shear-compression testing of brick masonry walls repaired and retrofitted with basalt textile reinforced mortar. *Compos Struct* 283 (2022). <https://doi.org/10.1016/j.compstruct.2021.115068>
- European Committee for Standardization: EN 1015–11 - Methods of test for mortar for masonry - Part 11: Determination of flexural and compressive strength of hardened mortar. Belgium, Brussels (2007)
- European Committee for Standardization: EN 1052–1: Methods of test for masonry - Part 1: Determination of compressive strength. Belgium, Brussels (1999)
- ASTM International (2015) E519–15 - Standard Test Method for Diagonal Tension (Shear) in Masonry Assemblages. ASTM International, West Conshohocken, PA, USA
- M. Ponte et al.: Preliminary results of the ERIES-RESTORING project: RETrofitting of STOne masonRy using INnovative Grid-based composites. In: 8th World Conference on Earthquake Engineering, Milan, July (2024)
- Ministero delle Infrastrutture e dei Trasporti,: DM 17/01/2018 - Aggiornamento delle ‘Norme Tecniche per le Costruzioni’ (in italiano). Italy, Rome (2018)
- RILEM. Recommendation for Testing and Use of Construction Material. RILEM TC 76-LUM. Diagonal tensile strength of small wall specimens, pp. 488–489 (1994)
- Frocht, M.M.: Recent advances in photoelasticity and an investigation of the stress distribution in square blocks subjected to diagonal compression. *Trans. ASME, Appl. Mech. Division* 53 (1931)

Open Access This chapter is licensed under the terms of the Creative Commons Attribution 4.0 International License (<http://creativecommons.org/licenses/by/4.0/>), which permits use, sharing, adaptation, distribution and reproduction in any medium or format, as long as you give appropriate credit to the original author(s) and the source, provide a link to the Creative Commons license and indicate if changes were made.

The images or other third party material in this chapter are included in the chapter's Creative Commons license, unless indicated otherwise in a credit line to the material. If material is not included in the chapter's Creative Commons license and your intended use is not permitted by statutory regulation or exceeds the permitted use, you will need to obtain permission directly from the copyright holder.





The Resume Project: Numerical Analyses and Laboratory Test

Antonio Formisano^{1(✉)}, Emilia Meglio¹, Vlatko Sesov², Aleksandra Bogdanovic², Julijana Bojadjieva², Zoran Rakicevic², Antonio Shoklarovski², Filip Manojlovski², Angela Poposka², Toni Kitanovski², Dejan Ivanovski², Marco Domaneschi³, Raffaele Cucuzza³, Valentina Villa³, and Giuseppe Carlo Marano³

¹ Department of Structures for Engineering and Architecture, University of Naples Federico II, Naples, Italy
antoform@unina.it

² Ss. Cyril and Methodius University in Skopje Institute of Earthquake Engineering and Engineering Seismology-IZIIS, Skopje, Macedonia

³ Department of Structural, Building and Geotechnical Engineering, Politecnico di Torino , Torino, Italy

Abstract. Europe faces significant challenges due to seismic activity, which frequently leads to extensive damage, particularly in seismically active regions such as Italy. Recent destructive earthquakes have underscored the urgent need for innovative strategies to improve the seismic resilience and energy efficiency of existing buildings. The RESUME project addresses these challenges by proposing an integrated approach to seismic and energy retrofitting. Its innovative methodology combines structural reinforcement with thermal insulation improvements, targeting reinforced concrete (RC) structures originally designed only for vertical loads.

A key feature of the project is the development of a “dry seismic coat,” composed of cork panels paired with a composite timber-aluminum alloy exoskeleton. This system enhances both the seismic and energy performance of retrofitted buildings by simultaneously improving strength, stiffness, and thermal insulation.

This article presents the implementation and preliminary results of shaking table tests conducted at the IZIIS Laboratory in Skopje. These tests involved infilled and retrofitted three-dimensional RC frames subjected to simulated seismic loads. The experimental program was designed to assess critical aspects such as: (1) the effectiveness of the retrofitting system in enhancing seismic safety, (2) the comparative energy performance of the system relative to conventional insulation methods, (3) the feasibility of a combined seismic-energy vulnerability assessment methodology for RC buildings.

Thus, the present paper details the design, setup, and execution of the tests, focusing on the experimental setup, specimen construction and instrumentation, and loading protocol development. Preliminary results are also presented highlighting the retrofitting system’s capacity to improve seismic behavior, while also indicating potential gains in energy efficiency, paving the way for further research outcomes.

Keywords: Aluminum alloy · Timber · Existing Building · Integrated Retrofit · Lightweight Exoskeleton

1 Introduction

The increasing awareness of seismic vulnerability and energy inefficiency in elderly buildings has placed urgent attention on the need for comprehensive retrofitting strategies, particularly in earthquake-prone regions. Many obsolete masonry and reinforced concrete structures, constructed before modern seismic standards were established, pose significant consequences in the event of an earthquake. As a result, ensuring structural safety while simultaneously improving energy performance has become a key priority in both research and policy discussions. Italy and several other European countries have witnessed the devastating effects of seismic events on outdated buildings, highlighting the need for innovative retrofitting solutions. In parallel, the growing emphasis on sustainability, coupled with rising energy costs, has reinforced the necessity of integrating energy-efficient solutions with seismic strengthening measures. Studies have demonstrated that combined retrofitting approaches not only enhance a building's resilience and thermal performance but also offer greater economic feasibility compared to isolated interventions [1].

To address these challenges, various retrofitting methods have been explored, incorporating both seismic strengthening and energy-efficient materials. Hybrid approaches include the use of fiber-reinforced mortars alongside insulation layers [2] or laminated timber paneling that not only improves structural integrity but also contributes to aesthetic enhancement [3]. Among the many available techniques, a widely adopted solution involves applying external reinforcements to building facades, combined with thermal insulation panels. Over the years, different configurations of this system have been developed, including cast-in-place reinforced concrete walls [4], timber-cement composite panels with integrated seismic resistance and timber-fiber insulation properties [5], as well as cold-formed steel frames with diagonal cross-bracing for enhanced lateral stability [6].

This study aims to advance the field of combined seismic and energy retrofitting by evaluating the performance of an innovative exoskeleton system composed of laminated timber and aluminum bracings or panels. The research follows a structured methodology, beginning with numerical simulations to determine the most effective reinforcement configuration. The optimal solution, whether bracing elements or panels, will then be experimentally validated through shaking table tests conducted at the IZIIS Laboratory in Skopje.

The experimental phase involves two identical 1:3 scale reinforced concrete structures with the same geometric and mechanical characteristics. One specimen which serve as a baseline without reinforcement, is already tested and the achieved results are herein presented. The second specimen will incorporate the optimized exoskeleton system based on numerical assessments. By comparing their seismic and energy performance, this research aims to provide insights into the feasibility, effectiveness, and practical implementation of this integrated retrofitting solution for existing RC structures.

2 Test Specimen

2.1 Unreinforced Infilled RC Structure

The test structure selected for reinforcement is a 1:3 scale prototype of a basic reinforced concrete (RC) frame, originally designed following outdated construction standards that do not account for seismic loads. This structure is intended to replicate older buildings that lack adequate earthquake-resistant features, making it a suitable candidate for evaluating the effectiveness of retrofitting strategies. Figure 1 depicts the geometrical characteristics of the unreinforced RC structure.

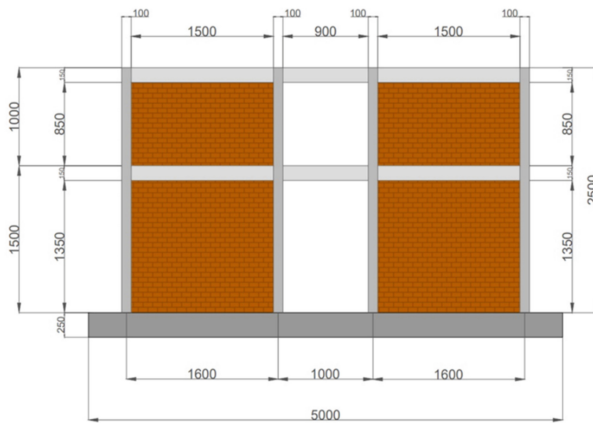


Fig. 1. Unreinforced RC structure: geometrical properties.

The framework consists of two parallel longitudinal frames, spaced 1.4 m apart, and connected transversely only through the RC slab, without additional transverse beams. Each frame has three spans, giving the entire structure a total length of 4.2 m. The building model includes two stories, with the ground floor measuring 1.5 m in height and the upper floor 1 m. Hollow brick infill walls are placed exclusively in the end spans along the longitudinal direction.

The foundation system consists of a 25 cm thick reinforced concrete slab, providing uniform support for the frame. The beam elements have rectangular cross-sections of 10 × 15 cm, while the columns measure 10 × 10 cm. In both beams and columns, longitudinal reinforcement bars are positioned only at the corners, with 8 mm diameter bars. Stirrups are 4 mm in diameter and spaced at 10 cm intervals. The concrete used in the structure has a compressive cubic strength of 20 MPa, corresponding to class C16/20, which is characteristic of lower-strength concrete used in older buildings.

This experimental model provides a realistic representation of inadequate RC structures, allowing a detailed investigation into the impact of retrofitting measures on both seismic and energy performance. The three-dimensional configuration of the unreinforced RC structure is depicted in Fig. 2.

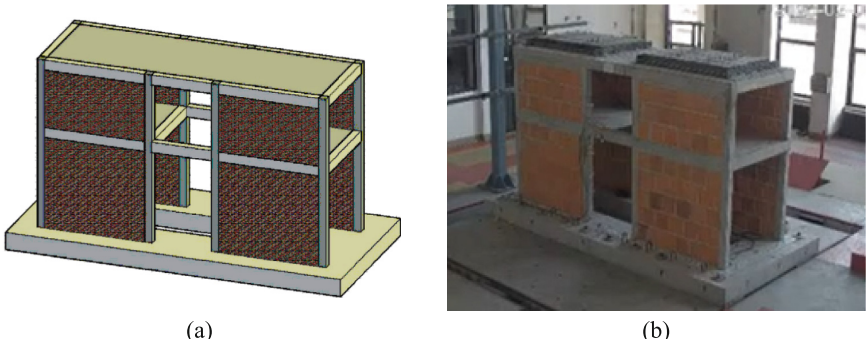


Fig. 2. Unreinforced RC structure: three-dimensional drawing (a) and real tested specimen (b).

2.2 RC Structure Reinforced with the Dry Seismic Coat

The numerical analysis focuses on evaluating two distinct external exoskeleton solutions, both incorporating aluminum alloy and laminated timber as primary structural materials. These systems are designed to enhance the seismic resistance of existing structures while simultaneously improving energy efficiency. Both configurations share a common structural framework, consisting of timber frames connected using galvanized steel plates and screws. The exoskeleton is anchored to the original structure via steel pins positioned at the beam-column joints, ensuring a strong yet adaptable connection.

The two solutions investigated differ in the design of their seismic-resistant elements, which are made of aluminum alloy components:

- X-Bracing Configuration – This solution employs concentric X-shaped aluminum braces.
- Shear Panel Configuration – Instead of bracing, this version integrates thin aluminum panels acting as shear walls.

The exoskeletons are installed on all exterior faces of the structure, except for the central span along the longitudinal direction, which remains open for inspection and monitoring during laboratory testing.

The aluminum elements are secured to the timber frame using galvanized steel angles, and they include connectors for attaching insulation panels. These insulation panels are made of recycled cork, offering both environmental sustainability and thermal efficiency. The aluminum components, including the diagonal braces and shear panels, have a uniform thickness of 2 mm and are composed of AW6060 aluminum alloy. Meanwhile, the timber frames are constructed from Gl28 h laminated timber.

Further construction details, including the exoskeleton assembly scheme and the two configurations, are illustrated in Fig. 3, highlighting the integration between the reinforcement system and the existing RC frame.

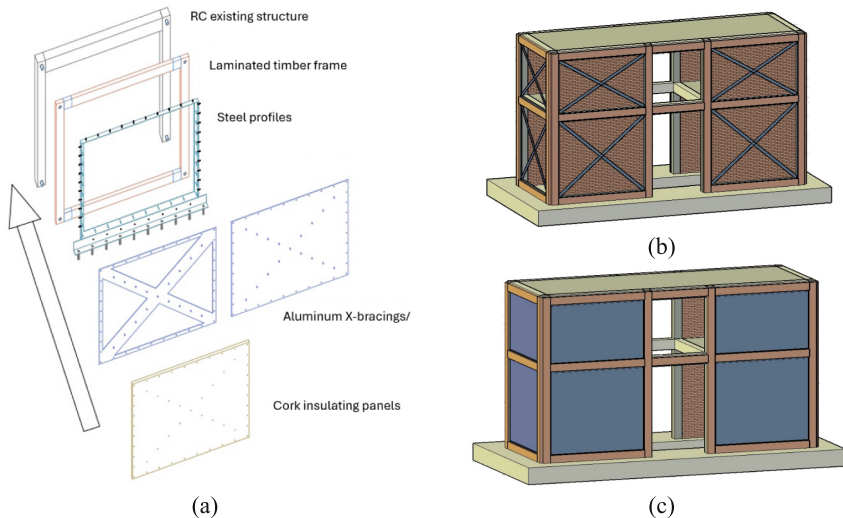


Fig. 3. Reinforced RC structure: exoskeleton assembly scheme (a), X-bracings configuration (b) and shear panel configuration (c).

3 Numerical Models

The 1:3 scale reinforced concrete (RC) structure was modeled using ProSap v.22, a structural analysis software developed by 2SI (Ferrara, Italy). To evaluate the effects of retrofitting, a modal analysis was conducted to identify the structure's vibration modes before and after reinforcement, followed by nonlinear static (pushover) analyses to determine the most efficient exoskeleton configuration for laboratory testing. In the pushover simulations, the infill walls were represented as equivalent struts, in accordance with established modeling techniques [7]. The seismic hazard level was assigned based on a location in L'Aquila, Abruzzo, Italy, with a topographic category of T1 and a soil classification of A, consistent with the Italian seismic code [8].

The first model was developed to reproduce the current state of the building, namely the unreinforced RC structure with infill walls (Fig. 4a). For the numerical representation of the exoskeleton solutions, two distinct reinforcement approaches were implemented:

- X-Bracing Configuration (Fig. 4b) – The actual diagonal braces were explicitly modeled in the structural analysis.
- Shear Panel Configuration (Fig. 4c) – The aluminum panels were simulated using ten equivalent diagonal elements, with their thickness matching that of the aluminum panel and widths determined using the strip model method [9].

The modal analysis of the three structural configurations (current state, X-bracing, and aluminum panel) revealed no significant qualitative changes in vibration mode sequences. The first vibration mode remained translational in the transverse (Y) direction, the second was torsional, and the third was translational in the longitudinal (X) direction. However, the reinforcement system significantly reduced the structure's natural period in its fundamental vibration modes, indicating increased stiffness (Fig. 5).

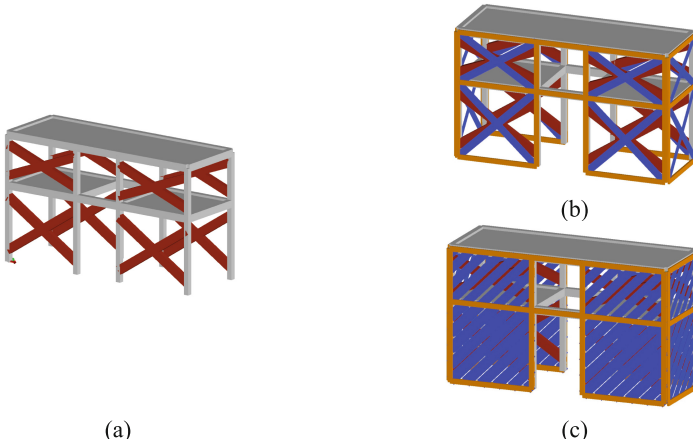


Fig. 4. Numerical models: current state (a), X-bracings configuration (b) and shear panel configuration (c).

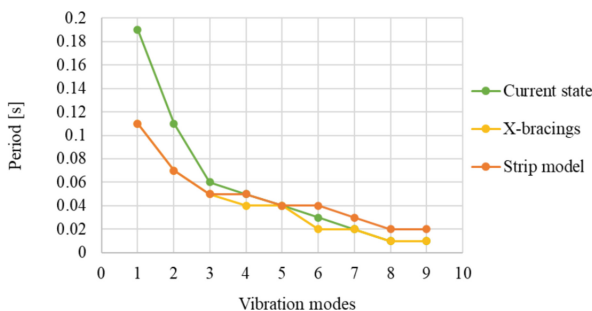


Fig. 5. Modal analysis: vibration periods mode 1.

Additionally, a reduction in maximum displacements and inter-story drift was observed, with the aluminum panel solution (strip model) exhibiting the most pronounced improvements (Fig. 6).

The results of the pushover analysis in terms of capacity curves of the structure, both before and after reinforcement, are presented in Fig. 7. The outcome shows notable increases in strength and stiffness due to the application of the dry seismic coat. The most significant stiffness and strength gains were observed in the transverse Y direction, where no infill walls were present. Moreover, the aluminum panel solution (strip model) demonstrated superior structural performance compared to the X-bracing system, achieving a greater increase in strength and lateral stiffness.

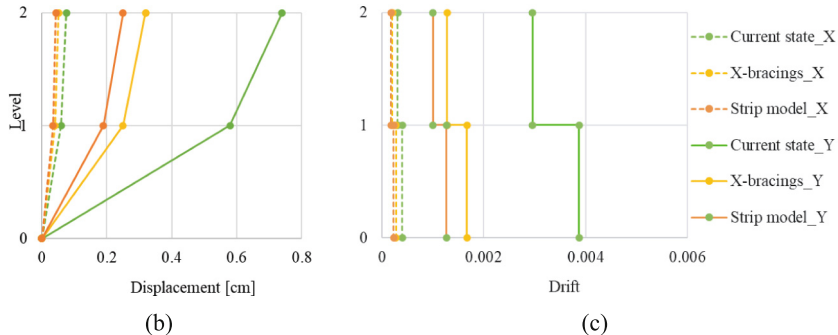


Fig. 6. Modal analysis: maximum displacements (b) and inter-story drift (c).

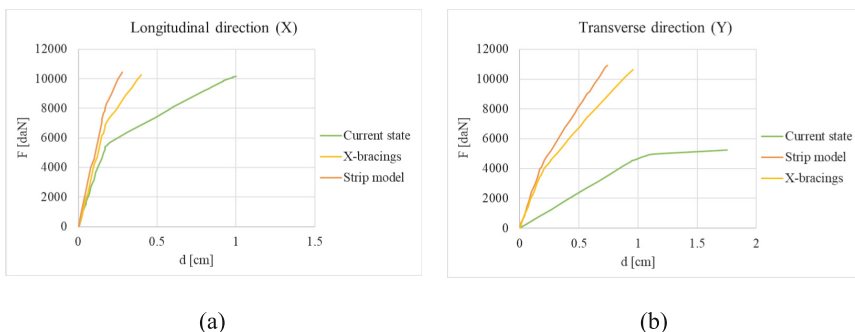


Fig. 7. Capacity curves of the pushover analysis: longitudinal direction (a) and transverse direction (b).

4 Selection of the Optimal Configuration

Overall, the implementation of the retrofitting strategies led to substantial improvements, as evidenced by both the modal and pushover analyses. The most pronounced impact of the exoskeleton was observed in the transverse (Y) direction, where the absence of infilled walls initially resulted in lower lateral stiffness.

However, clear benefits were also recorded in the longitudinal (X) direction, where infill walls were located at the end spans, further contributing to the system's overall effectiveness.

The quantitative assessment of these improvements is provided in Table 1, which summarizes the percentage variations in dynamic properties relative to the original, unreinforced structure. Additionally, Table 2 presents the percentage increases in strength and stiffness for both exoskeleton configurations relative to the original structure, as obtained from the pushover analysis.

Table 1. Modal analysis: percentage variation of dynamic properties compared to the unreinforced structure.

Configuration	Period	Max displacement		Drift	
		X	Y	X	Y
Brace	-42.1%	-31.6%	-56.8%	-32.1%	-56.8%
Strip	-42.1%	-42.1%	-66.2%	-42.0%	-66.2%

Table 2. Pushover analysis: percentage variation of strength and stiffness compared to the unreinforced structure.

Configuration	Max Force		Stiffness	
	X	Y	X	Y
Brace	+ 1.1%	+ 103%	+ 28%	+ 344%
Strip	+ 3.6%	+ 108%	+ 60%	+ 377%

These findings confirm that both retrofitting strategies significantly enhance the structural stiffness and stability of existing RC buildings. However, the aluminum panel configuration consistently demonstrated superior performance compared to the X-bracing system. Due to its greater effectiveness, the aluminum panel solution was selected for application on the RC specimen to be tested on the shaking table, ensuring the best performance in the experimental phase.

5 Experimental Test

As part of the experimental investigation, two models have been constructed: Model X and Model Y, both with identical geometric and mechanical characteristics. The testing is structured into three phases to analyze the effectiveness of the exoskeleton system as a seismic strengthening method.

- Phase 1: Model Y is subjected to increasing seismic loads until the expected deformations and damage levels are reached.
- Phase 2: An exoskeleton system is installed on the already damaged Model Y to evaluate its ability to enhance the seismic performance of the structure.
- Phase 3: Model X is tested with the exoskeleton system applied before the experimental testing, allowing for a direct comparison between a model strengthened prior to loading and one reinforced after sustaining damage.

At this stage, only Phase 1 has been completed. The following section presents the activities carried out during this phase.

The shake table used for dynamic testing at IZIIS measures 5.0 m by 5.0 m and has five degrees of freedom. It is supported by two lateral and four vertical MTS hydraulic pistons, controlled by an MTS Digital Controller 469D. The instrumentation of the tested models included accelerometers (ACC) - PCB Piezotronics, linear potentiometers (LP) – Microepsilon WDS, linear variable differential transformers (LVDT) – MacroSensors DC750, and strain gauges (SG) – KYOWA KFG, measuring accelerations, total and relative displacements, and strains, respectively. The data acquisition was performed using the National Instruments PXI modular system.

Specifically, 12 accelerometers were installed at different heights in two horizontal directions. Additionally, four linear potentiometers were placed at the slab level. A total of 10 LVDTs were used, of which two were positioned between the model and the shake table, while eight were placed around the column-beam connection. Furthermore, 30 strain gauges were installed, 24 of which were installed on the reinforcement bars in the columns at different heights, and six were attached to the concrete of the columns.

The testing program began with low-intensity white noise shake table tests to determine the dynamic characteristics of the system. Subsequent tests involved ground motion excitations with amplitudes scaled to progressively increasing intensity levels. The considered seismic inputs for the first model included the Adana 1998 earthquake (Mw 6.3), the Umbria 2016 earthquake (Mw 6.2), and a synthetically generated earthquake based on the Eurocode 8 spectra for Soil C. Figure 8 presents the time history of the maximum intensity seismic input applied during Phase 1. A full list of all tests performed on Model Y during Phase 1 is provided in Table 3.

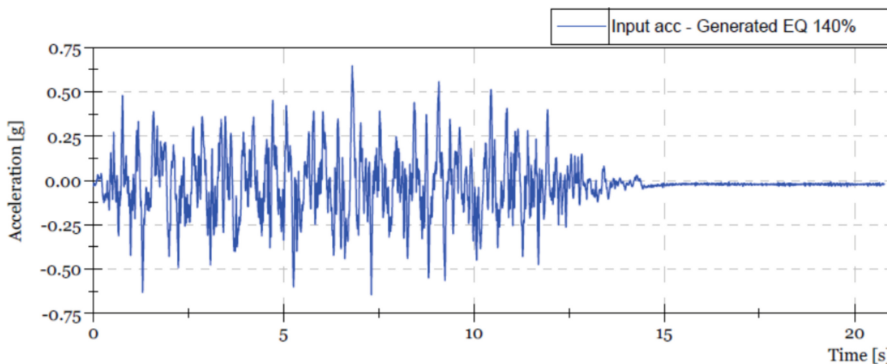


Fig. 8. Model Y – Phase 1. Input acceleration time history.

Table 3. Simulated earthquakes on Model Y.

Test No	Type of excitation	Characteristics of the excitation	Input acc.[g]
1	White noise	$f = 1 - 45 \text{ Hz}; t = 300\text{s}$	0.01
2	White noise	$f = 1 - 45 \text{ Hz}; t = 300\text{s}$	0.02
3	White noise	$f = 1 - 45 \text{ Hz}; t = 300\text{s}$	0.05
4	EQ1: Adana	15%	0.1
5	EQ2: Generated EQ	18%	0.1
6	EQ3: Umbria	10%	0.1
7	EQ2: Generated EQ	27%	0.15
8	EQ2: Generated EQ	50%	0.3
9	White noise	$f = 1 - 45 \text{ Hz}; t = 300\text{s}$	0.05
10	EQ2: Generated EQ	75%	0.45
11	White noise	$f = 1 - 45 \text{ Hz}; t = 300\text{s}$	0.05
12	EQ2: Generated EQ	100%	0.6
13	White noise	$f = 1 - 45 \text{ Hz}; t = 300\text{s}$	0.05
14	EQ2: Generated EQ	100%	0.6
15	White noise	$f = 1 - 45 \text{ Hz}; t = 300\text{s}$	0.05
16	EQ2: Generated EQ	120%	0.72
17	White noise	$f = 1 - 45 \text{ Hz}; t = 300\text{s}$	0.05
18	EQ2: Generated EQ	140%	0.84
19	White noise	$f = 1 - 45 \text{ Hz}; t = 300\text{s}$	0.02

After the last test, severe damage was observed on the bare frame, with visible cracks, and approximately 80% of the infill on the ground floor collapsed. The natural frequency of the model decreased by about 80% from the beginning to the end of the testing. Figure 9 illustrates the model before and after testing.



Fig. 9. Model Y – Phase 1, Before and After Testing

6 Conclusions

The research presented in this study underscores the significant potential of the RESUME project's integrated approach for seismic and energy retrofitting of existing RC structures. Through a combination of numerical modeling and experimental test, the effectiveness of the dry seismic coat system—composed of laminated timber and aluminum alloy elements paired with cork insulation panels—has been investigated. The numerical analyses, particularly the modal and pushover simulations, demonstrated that both proposed configurations—the X-bracing and aluminum shear panel systems—improved the dynamic and structural performance of a typical reinforced concrete frame designed without seismic criteria. Among these, the aluminum panel configuration outperformed the bracing system, yielding the most notable reductions in natural vibration periods, maximum displacements, and inter-story drifts. Quantitatively, this solution led to an over 40% decrease in dynamic response parameters and increases in lateral strength and stiffness exceeding 100% in transverse direction, with stiffness improving by as much as 377%, highlighting the critical role of the exoskeleton where infill walls were initially absent.

The experimental campaign involves the execution of shake table tests to validate the outcomes obtained through numerical simulations. In the first phase, testing was carried out on Model Y, which had no prior reinforcement. This specimen was subjected to progressively intensified seismic inputs until it sustained significant damage, including visible cracking and the near-total collapse of the ground floor infill walls. By the end of the testing phase, the structure's natural frequency had decreased by approximately 80%, indicating a dramatic loss of stiffness and structural integrity. These results clearly highlight the vulnerability of outdated reinforced concrete frames under seismic loading and emphasize the urgent need for effective retrofitting strategies. Future work will involve installing and testing the exoskeleton system on both intact and previously damaged structures, specifically Model X and Model Y, during Phase 2 of the experimental program.

Acknowledgements. This work is part of the transnational access project “ERIES-RESUME”, supported by the Engineering Research Infrastructures for European Synergies (ERIES) project (www.ries.eu), which has received funding from the European Union’s Horizon Europe Framework Programme under Grant Agreement No. 101058684. This is ERIES publication number C76.

References

1. Pertile, V., Stella, A., De Stefani, L., Scotta, R.: Seismic and energy integrated retrofitting of existing buildings with an innovative ICF-based system: design principles and case studies. *Sustainability* **13**(16), 9363 (2021)
2. Bournas, D.: Concurrent seismic and energy retrofitting of RC and masonry building envelopes using inorganic textile-based composites combined with insulation materials: a new concept. *Compos. Part B-Eng.* **148**, 166–179 (2018)
3. Margani, G., Evola, G., Tardo, C., Marino, E.M.: Energy, seismic, and architectural renovation of RC framed buildings with prefabricated timber panels. *Sustainability* **12**(12), 4845 (2020)
4. Ecosystem. <https://www.ecosism.com/moduli/geniale/>. Accessed 24 Oct 2024
5. Betonwood. <https://www.betonwood.com/>. Accessed 24 Oct 2024
6. Meglio, E., Formisano, A.: Seismic design and analysis of a cold-formed steel exoskeleton for the retrofit of an rc multi-story residential building. *Appl. Sci.* **14**(19), 8674 (2024)
7. Al-Chaar, G.: Evaluating Strength and Stiffness of Unreinforced Masonry Infill Structures. US Army Corps of Engineers, Engineer Research and Development Center (2002)
8. Ministry of Infrastructure and Transport. Technical Standards for Construction. In Official Gazette; Number 42 of 20 February 2018; Ministry of Infrastructure and Transport: Rome, Italy, 2018 (In Italian)
9. Formisano, A., Mazzolani, F.M., De Matteis, G.: Numerical analysis of slender steel shear panels for assessing design formulas. *Int. J. Struct. Stab. Dyn.* **7**(02), 273–294 (2007)

Open Access This chapter is licensed under the terms of the Creative Commons Attribution 4.0 International License (<http://creativecommons.org/licenses/by/4.0/>), which permits use, sharing, adaptation, distribution and reproduction in any medium or format, as long as you give appropriate credit to the original author(s) and the source, provide a link to the Creative Commons license and indicate if changes were made.

The images or other third party material in this chapter are included in the chapter's Creative Commons license, unless indicated otherwise in a credit line to the material. If material is not included in the chapter's Creative Commons license and your intended use is not permitted by statutory regulation or exceeds the permitted use, you will need to obtain permission directly from the copyright holder.





Design and Analysis of Large-Scale Tests of a Self-centring Seismic-Resilient Steel MRF

Elena Elettore¹ Ali Roumieh¹ Fabio Freddi¹ Massimo Latour² Antonella B. Francavilla³ Sabatino Di Benedetto² Fernando Gutiérrez-Urzúa^{1,4} Ludovica Pieroni¹ Barbara Simpson⁵ Andrea R. Barbosa⁶ Shahab Ramhormozian⁷ Damian N. Grant⁸ Gianvittorio Rizzano² Filipe L. Ribeiro⁹ and Antonio A. Correia⁹

¹ University College London, London, UK

e.elettore@ucl.ac.uk

² University of Salerno, Salerno, Italy

³ Pegaso University, Naples, Italy

⁴ AtkinsRéalis, Epsom, UK

⁵ Stanford University, Stanford, USA

⁶ Oregon State University, Corvallis, USA

⁷ Auckland University of Technology, Auckland, New Zealand

⁸ Arup, London, UK

⁹ National Laboratory for Civil Engineering (LNEC), Lisbon, Portugal

Abstract. Conventional seismic design methods rely on structural inelastic hysteretic response to dissipate seismic energy. This approach often results in extensive damage and substantial direct and indirect losses following high-intensity earthquakes, thereby affecting the overall resilience of communities. To address this issue, modern earthquake engineering is facing an extraordinarily challenging era in providing affordable, high-seismic-performance structures able to minimise both seismic damage and repair time. To this end, the ERIES SC-RESTEEL (Self-Centring seismic-RESilient sTEEL structures) project examines the structural response, reparability, resilience, and performance recovery of low-damage self-centring steel Moment-Resisting Frames (MRFs) equipped with friction devices and post-tensioned bars with disc springs at column bases and beam-to-column joints. Shaking table tests will be conducted at LNEC (Laboratório Nacional de Engenharia Civil) in Lisbon, Portugal, to investigate the performance of a large-scale 3-storey steel MRF. Key objectives include evaluating the seismic performance of the structure, its reparability strategy, and the performance after repairs. This paper presents the test specimen design, advanced Finite Element analyses of various joint configurations, and the preparatory work for the tests. The findings offer valuable insights into the expected experimental outcomes.

Keywords: Self-Centring · Steel Moment-Resisting Frames · Seismic Resilience · Reparability · Finite Element Analyses

1 Introduction

Earthquakes are destructive natural hazards, causing extensive structural damage and significant economic losses. Conventional seismic design methods (e.g., Eurocode 8 [1]) rely on structural damage to dissipate seismic energy and meet the life safety requirements. While this approach achieves its primary objective of protecting the occupants, it often results in severe damage, high repair costs and extended downtime.

To overcome these drawbacks, modern earthquake engineering faces an extraordinarily challenging task of providing seismic-resilient structures that can minimise both seismic damage and repair time, thereby allowing for limited socio-economic losses after severe earthquakes. Well-established solutions include the use of supplemental damping [2–5] and base isolation systems [6, 7]. Other strategies also aim to reduce residual deformations [8–13] and have recently gained recognition for their distinct advantages. In steel Moment Resisting Frames (MRFs), a promising solution involves integrating dissipative devices (e.g., Friction Devices (FDs)) and Self-Centring (SC) systems (e.g., Post-Tensioned (PT) bars) in Beam-to-Column Joints (BCJs) [14, 15] and Column Bases (CBs) [16–21]. These systems reduce structural damage and limit residual deformations, enhancing repairability and recovery time [22]. Although several studies on such SC structures have been conducted in recent years, demonstrating their advantages, there remains a significant need for advanced research to inform policy-making and building codes, thereby promoting their application in practice.

Previous studies investigated the use of SC-CBs [18–21], and performed large-scale Pseudo-Dynamic (PsD) tests to investigate the seismic performance and repairability of the system [22]. These studies demonstrated the benefits of the SC-CBs in minimising residual drifts and the effectiveness of the repair method. However, several open issues still need to be addressed. For example, one challenge related to the use of SC-BCJs is the potential frame expansion due to the rocking behaviour of beams, potentially inducing damage in the slab and compromising the self-centring capability of the joints [15]. Additionally, past studies [14] demonstrated that the placement of SC-BCJs could be optimised to limit structural complexity. Moreover, while proof-of-concept studies are widely available for such innovative systems, large-scale shaking table tests remain quite limited [e.g., 23, 24].

Within this context, the ERIES SC-RESTEEL (Self-Centring seismic-RESilient sTEEL structures) project aims to advance knowledge on such structural configurations by experimentally investigating the seismic performance, repairability, and effective placement of SC devices. The research involves large-scale shaking table tests on a 3-storey steel MRF equipped with both SC-BCJs and SC-CBs at LNEC in Lisbon, Portugal, as well as component tests on subassemblies at the STRENGTH Laboratory of the University of Salerno, Italy.

The solution features SC-BCJs and SC-CBs together with a splice introduced at the beam's midspan to mitigate the frame expansion effect. The shaking table tests aim to evaluate the response under real earthquake scenarios. In particular, they will allow: 1) to analyse the impact-induced local damage at rocking interfaces and its effect on system damping (which the PsD tests only simulated numerically); 2) to assess the influence of the vertical component of the ground motion on the self-centring capacity of the CBs;

3) to quantify repairability metrics, e.g., repair time and performance of the repaired structure across multiple scenarios.

This paper presents the test specimen design, the advanced Finite Element (FE) analyses of various BCJ subassembly configurations in ABAQUS [25], the non-linear dynamic analyses on the 3-storey structure in OpenSees [26] considering three different configurations for the joint distribution and the preparatory work for the tests.

2 Test Specimen

2.1 Design of the Test Specimen

The specimen for the shake table tests is illustrated in Fig. 1a. The internal MRF is intended to provide the lateral capacity, while the external frames are designed for gravity loads only. The inter-storey heights are equal to 1.92 m at the first storey and 1.80 m at higher storeys. The longitudinal and transverse bays have span lengths of 3.50 m and 2.00 m, respectively. The specimen has been extracted from a prototype structure characterised by 3 storeys and 3 bays in both directions and scaled based on the material and acceleration scaling identity, with a scaling factor equal to $\lambda = 0.6$.

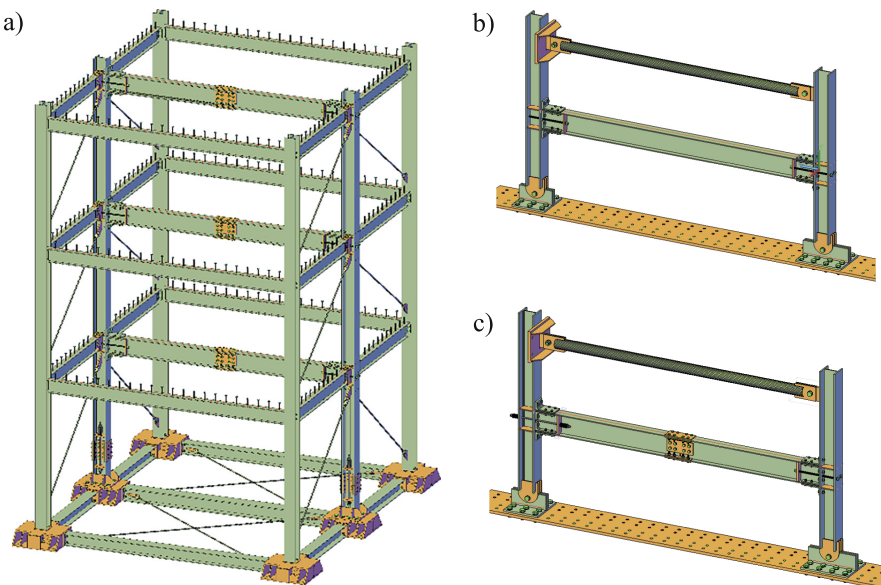


Fig. 1. a) 3D Large-Scale Test Specimen; b) and c) Test Sub-assemblies.

The design was carried out in accordance with the Eurocode 8 provisions [1]. The design earthquake at the Ultimate Limit State (ULS) is defined considering the Type 1 elastic response spectrum with a PGA = 0.35g and soil type D. The Collapse Limit State (CLS) is assumed to have an intensity equal to 150% of the ULS. The behaviour factor

based on the Eurocode 8 for MRFs in Ductility Class High (DCH) is assumed as $q = 6.5$. The inter-storey drift limit for the Damage Limit State (DLS) is assumed to be 1% for non-structural elements fixed in a way such as not to interfere with structural deformations. The assumed floor system is a HI BOND A55/P600 steel-concrete composite floor with a total height of 110 mm. The floor masses of the specimen to carry out the test are equal to 11.76 and 10.31 tonnes at intermediate floors and the roof, respectively. Hence, the total mass of the specimen is equal to 33.82 tonnes, which is compatible with the specific equipment available at the research infrastructure (<40 tonnes). Beam and column cross-sections of the MRF are IPE240 and HEB180, while the profiles of the gravity frames are IPE180 and HEA160, respectively. All the profiles are of steel grade S355. The MRF is equipped with BCJs and CBs in two different configurations, *i.e.*, with and without PT bars. For the sake of clarity, hereinafter, the joints without PT bars are referred to as Low-Damage (LD) joints (LD-BCJs and LD-CBs), while joints with PT bars are referred to as Self-Centring (SC) joints (SC-BCJs and SC-CBs).

The specimens of the component tests are shown in Fig. 1b and c. These tests aim to characterise the response of the BCJ subassemblies and evaluate the effectiveness of the proposed solution in mitigating the frame expansion effect. These subassemblies are extracted from the second storey of the 3-storey structure. Two configurations will be tested: *i*) BCJs implemented with a continuous beam (Fig. 1b) and *ii*) BCJs where a splice allowing axial displacements is included at midspan (Fig. 1c). Each frame subassembly will be tested in both LD and SC configurations.

2.2 Design of the Beam-to-Column Joints (BCJs) and Column Bases (CBs)

Figure 2 illustrates the BCJ with and without PT bars, *i.e.*, the SC-BCJ in Fig. 2a and the LD-BCJ in Fig. 2b. In both configurations, the connection is equipped with FDs, which dissipate the seismic input energy through the alternate slippage of the surfaces in contact. The FDs consist of properly coated steel friction shims and steel cover plates clamped with pre-loadable bolts. The self-centring system is composed of PT bars symmetrically placed with respect to the column's depth and arranged in series with a system of disc springs, ensuring an adaptable stiffness-resistance combination. Slotted holes are included at the beam's flanges to accommodate the target rotation (*i.e.*, 0.04 rads). In the case of the SC-BCJs, the moment-rotation behaviour is the typical flag-shape curve, where M_1 is the moment at the gap opening. Conversely, in the case of LD-BCJ, the moment-rotation behaviour is a hysteretic rectangular curve where M_{slip} is the slippage moment of the FDs.

Figure 3 illustrates the CB connection with and without PT bars, *i.e.*, the SC-CB in Fig. 3a and the LD-CB in Fig. 3b. Similar to the BCJ, in both configurations, the column base is connected by a combination of FDs and a SC system composed of PT bars and disc springs. The mechanism and moment-rotation behaviour of both CBs is similar to the BCJ.

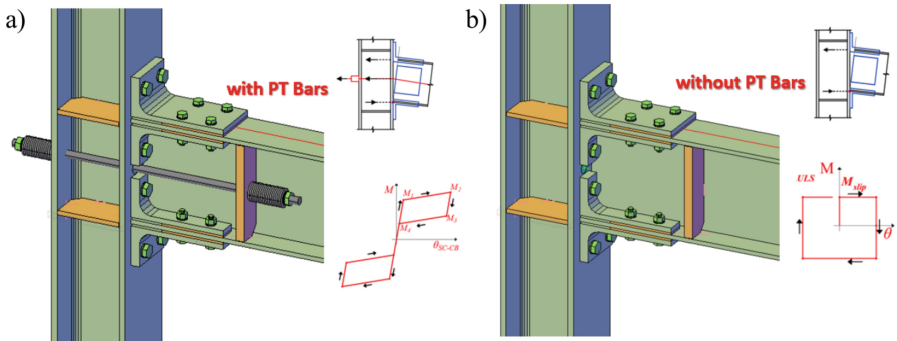


Fig. 2. 3D view & moment rotation behaviour for: a) SC-BCJ; b) LD-BCJ.

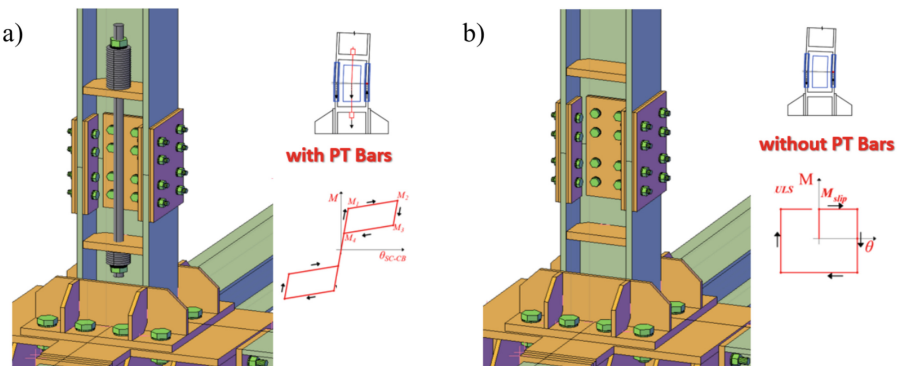


Fig. 3. 3D view and moment rotation behaviour of: a) SC-CB; b) LD-CB.

3 Experimental Programme

Table 1 summarises the proposed test programme. Phase 1 of the programme investigates the local behaviour of materials and components, including steel coupons, friction shims, and PT-bars with disc springs. Phase 2 includes quasi-static tests on the BCJ subassemblies, both with and without the central splice, considering both the LD- and SC-BCJs. The tests will be performed using cyclic loading with increasing amplitudes up to a target rotation of 0.04 rad, according to AISC 341-16 [27]. Phase 3 investigates the dynamic response and seismic performance of the 3-storey structure through shaking table tests. These tests will be performed considering different layouts of the SC joints' placement along the height of the structure and a set of ground motion records with increasing intensities from the DLS to the CLS. Such tests will evaluate the seismic performance, SC capacity, and repairability of the structure. Each test will be preceded by characterisation tests, such as white noise tests, to estimate damping ratios and natural periods. Phase 4 of the programme evaluates the performance of the repaired structure under repeated records and the influence of the vertical component of the ground motion.

Wire transducers and accelerometers are used at each level to measure horizontal displacements and accelerations. Additionally, the local response of the structure and its

components are assessed through strain gauges and Linear Variable Differential Transformers (LVDTs). LVDTs also allow for tracking the opening and closing of the gap in the splice mechanisms. Load cells and strain gauges are installed to monitor tensile forces and deformations in the PT bars along with the test. Finally, advanced sensors (*i.e.*, <https://tokbo.it>) are used in bolts and PT bars to monitor the force variation.

Table 1. Experimental programme.

Phase	Description
1	Material and components characterisation tests, coupon tests, double lap-shear friction joints, and tests on PT bars with disc springs
2	Subassemblies cyclic tests, with and without splice, with LD- and SC-BCJs, and considering different levels of PT bars prestressing
3	Shaking table tests of the 3-storey large-scale test specimen with different placements of the self-centring joints
4	Additional tests with and without vertical ground motions and repeated tests for reliability assessment

4 Finite Element Analysis

4.1 Finite Element Analysis of the Subassemblies

Figure 4a shows the ABAQUS model developed to simulate the tests on the subassemblies and provide insights to inform experimental testing design. For the sake of brevity, only the configuration with a splice at midspan is represented. The FE models have been developed using a procedure similar to the one used in Elettore *et al.* [21].

To comprehensively analyse the response of the connection, the numerical study was conducted in sequential phases. Initially, the isolated SC-BCJ was subjected to a monotonic loading. Subsequently, the two different configurations of the single-bay frame (with and without splice) were examined under the same monotonic conditions and successively under cyclic loading.

Figure 4b shows the comparison of the axial force evolution in the beam between the two frame configurations: with and without splice. The results demonstrate the suitability of the proposed solution in avoiding the frame expansion and the consequent increase of the axial force in the beam. Figure 5 shows the comparison of the monotonic and cyclic moment-rotation responses of the different models. Figure 5a shows a consistent slippage moment, corresponding to the activation of the FDs, among the three different configurations. The results also show the detrimental effect deriving from the frame expansion. This results in an axial force increase in the beam and, consequently, in a moment hardening response, leading to plastic deformations in the beam and column web. Similarly, Fig. 5b illustrates the cyclic moment-rotation response of the SC-BCJs with and without splice. The results show a slightly better self-centring capability for

the frame with splice. The benefits are limited in this configuration but are expected to be more pronounced in other configurations with different forces in the PT bars and FDs, as well as multiple bays. These preliminary results highlighted the importance of the splice in reducing damage, ensuring self-centring capability, and ensuring a more controlled and predictable structural response.

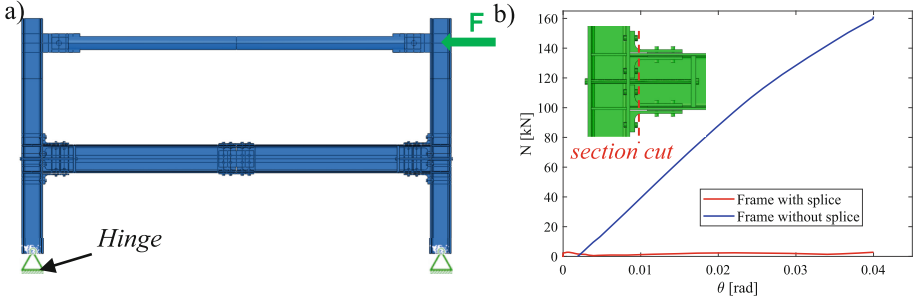


Fig. 4. ABAQUS model and results: a) Frame configuration with splice; b) Axial force comparison between the two frame configurations.

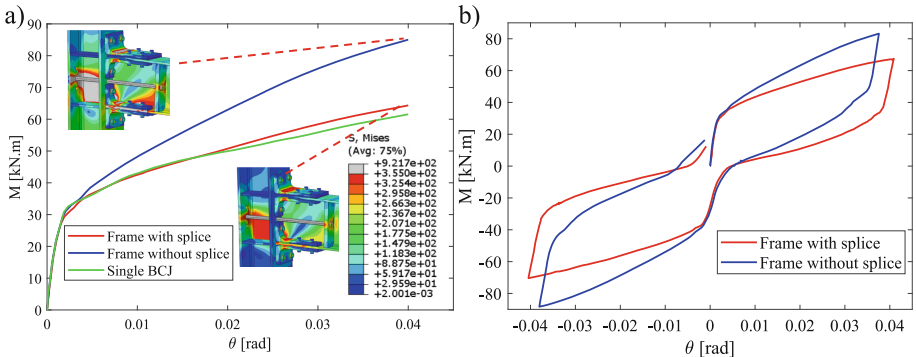


Fig. 5. Comparison in the response of SC-BCJ: a) Monotonic moment-rotation behaviour; b) Cyclic moment-rotation behaviour

4.2 Finite Element Analysis of the 3-Story Frame

2D non-linear FE models are developed in OpenSees [26] (Fig. 6). Three different models have been developed considering different configurations of the joints. In particular: 1) the MRF equipped with LD-BCJs and LD-CBs (*i.e.*, LD-MRF); 2) the MRF with LD-BCJs and SC-CBs (*i.e.*, LD-MRF-CB); and 3) the MRF with SC-CBs and SC-BCJs (*i.e.*, SC-MRF). Numerical simulations are conducted to investigate and compare the seismic performance of the structures equipped with different connection typologies and to verify their compatibility with the test equipment's capacities. The LD- and SC-BCJ modelling strategies are shown in Fig. 6b and c and are consistent with Pieroni *et al.* [14]. On the

other end, the LD- and SC-CB modelling strategies are shown in Fig. 6d and e, and are consistent with Elettore *et al.* [20].

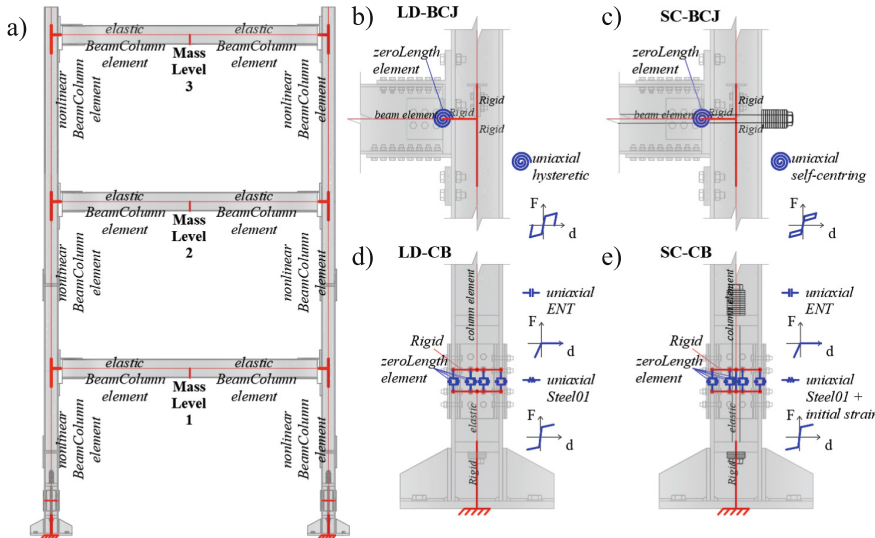


Fig. 6. 2D OpenSees Modelling of: a) MRF; b) LD-BCJ; c) SC-BCJ; d) LD-CB; e) SC-CB.

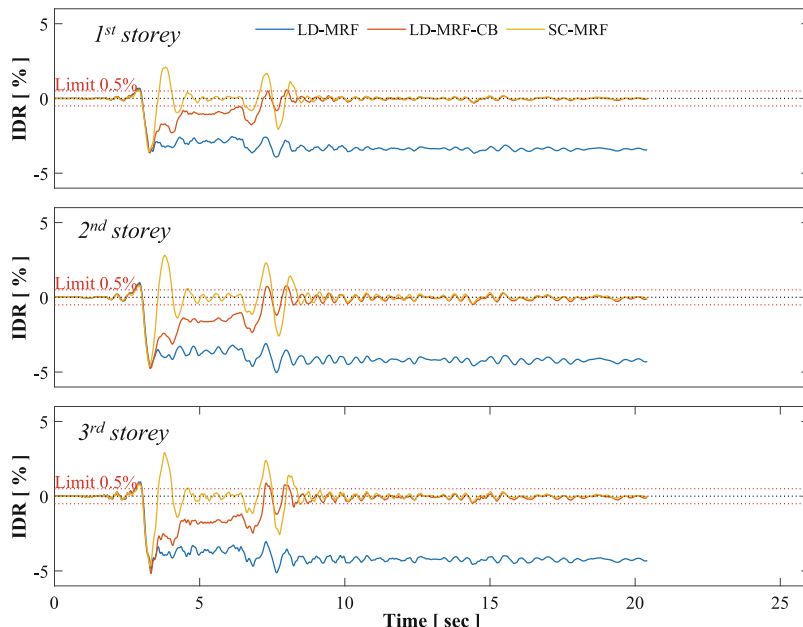
The three models have an almost identical natural vibration period $T_1 = 0.43$ s. A large set of ground motion records was originally considered for the record selection. This set was restricted to 5 records, as reported in Table 2. In all cases, the records were scaled in time by a scaling factor of $\lambda^{1/2} = 0.6^{1/2} = 0.77$ to match the specimen scaling criteria. Moreover, their acceleration intensity was scaled at the ULS and at the CLS intensities (*i.e.*, $S_{a,ULS}(T_1) = 1.182g$ and $S_{a,CLS}(T_1) = 1.773g$). All ground motion input records were verified to ensure compliance with the shake table's requirements in terms of Peak Ground Displacement (PGD), Peak Ground Velocity (PGV) and overturning moments for all intensities of interest.

Figure 7 shows the results of the non-linear time-history analyses for a single ground motion record, *i.e.*, Northridge-01. The comparison of the time histories of the Inter-storey Drift Ratios (IDRs) among the three configurations at the CLS intensity demonstrates that, as expected, frames with self-centring connections (*i.e.*, the LD-MRF-CB and SC-MRF) exhibit a significant reduction in the residual IDRs at all storeys, confirming the effectiveness of the solution. The SC-MRF structure results in a completely self-centring response with almost zero residual IDRs for both seismic intensities. Additionally, despite having SC joints only at the base, the LD-MRF-CB exhibits a significant reduction in residual drifts at all storeys, in all cases below the reparability limit of 0.5%. Conversely, this limit is never satisfied for the LD-MRF, which experiences larger residual IDRs of approximately 4% for the CLS.

Table 2. Selected ground motions evaluated at the CLS complying with shake table capacity.

Earthquake	Horizontal			Vertical	
	PGA [g]	PGV [mm/s]	PGD [mm]	PGV [mm/s]	PGD [mm]
Northridge-01	0.92	476.40	111.41	191.95	49.91
Ferndale-891	0.81	469.79	71.94	81.34	16.67
Niigata, Japan	1.12	527.45	114.27	164.95	85.15
Chi-Chi-2951	0.80	382.58	164.27	174.81	107.75
Ferndale-905	0.74	423.51	51.52	298.79	56.75
Limit of Shake Table	-	600.00	200.00	400.00	200.00

Such numerical analyses strongly supported the record selection, identifying records that, while ensuring compliance with the shake table's requirements, allow exploring the seismic response considering different ground motions' characteristics.

**Fig. 7.** Comparison of the Inter-storey Drifts Ratios (IDRs) time histories among the three configurations for a single ground motion record (Northridge-01) at the CLS.

5 Conclusions

The present paper illustrates the preliminary numerical work conducted for the design of the experimental campaign of the ERIES-SC-RESTEEL (Self-Centring seismic-RESilient sTEEL structures) project. The project examines the structural response, repairability, resilience, and performance recovery of low-damage self-centring steel Moment-Resisting Frames (MRFs), including friction devices and post-tensioned bars with disc springs at Column Bases (CBs) and Beam-to-Column Joints (BCJs). The experimental campaign includes a series of shaking table tests on a large-scale 3-storey steel structure considering different Self-Centring (SC) joint placements, configurations and properties. The shaking table tests will be conducted at LNEC in Lisbon, Portugal, while additional tests on subassemblies will be carried out at the STRENGTH Laboratory of the University of Salerno, Italy. Finite Element (FE) models were developed in ABAQUS for the subassemblies. The results highlighted the importance and effectiveness of the proposed solution in mitigating frame expansion effects, hence reducing damage to the connection and promoting the self-centring response. Additionally, numerical models of the 3-storey frame were developed in OpenSees, and non-linear dynamic analyses were performed to investigate the performance of the structure considering three distributions of self-centring and/or low-damage joints. The outcomes offer useful insights for the design of shaking table tests and for the prediction of the expected experimental results. The results confirmed the effectiveness of the SC connections in reducing the residual deformations. Moreover, the numerical study allowed defining the preliminary set of records to be used in the shaking table tests.

Acknowledgements. This work is part of the transnational access project “ERIES-SC-RESTEEL”, supported by the Engineering Research Infrastructures for European Synergies (ERIES) project (www.ries.eu), which has received funding from the European Union’s Horizon Europe Framework Programme under Grant Agreement No. 101058684. This is ERIES publication number C68.

This research is also partially supported by the UK Research and Innovation Institution (UKRI) in the framework of the project R4STEEL “Post-earthquake Functional Recovery, Resilience, Repairability and Reversibility of STEEL Structures” (Grant Number EP/Z003156/1).

References

- EN 1998–1, Eurocode 8: Design of structures for earthquake resistance – Part 1: General rules, seismic actions and rules for buildings, European Committee for Standardization
- Symans, M.D., et al.: Energy dissipation systems for seismic applications: current practice and recent developments. *J of Struct Eng* **134**(1), 3–21 (2008)
- MacRae, G.A., Clifton, G.C., Mackinven, H., Mago, N., Butterworth, J.W., Pampanin, S.: The sliding hinge joint moment connection. *Bull of The New Zealand Society for Earthq Eng* **43**(3), 202–212 (2010)
- Francavilla, A.B., Latour, M., Rizzano, G., Nigro, F., Piluso, V.: Experimental assessment of the hysteretic response of resilient low-damage friction joints with different Belleville disk springs configurations. *Soil Dyn & Earthq Eng* **180**, 108617 (2024)

5. Gutiérrez-Urzúa, L.F., Freddi, F.: Influence of the design objectives on the seismic performance of steel moment resisting frames retrofitted with buckling restrained braces. *Earthq. Eng. Struct. Dyn.* **51**(13), 3131–3153 (2022)
6. Grant, D.N., Fenves, G., Whittaker, A.: Bidirectional modelling of high-damping rubber bearings. *J of Earthq Eng* **8**(1), 161–185 (2004)
7. Calvi, P.M., Calvi, G.M.: Historical development of friction-based seismic isolation systems. *Soil Dyn & Earthq Eng* **106**, 14–30 (2018)
8. Ricles, J., Sause, R., Garlock, M., Zhao, C.: Post-tensioned seismic-resistant connections for steel frames. *J of Struct Eng* **127**(2), 113–121 (2001)
9. Christopoulos, C., Filiatrault, A., Uang, C.-M., Folz, B.: Posttensioned energy dissipating connections for moment-resisting steel frames. *J of Struct Eng* **128**(9), 1111–1120 (2002)
10. Blomgren, H.-E., et al.: Full-scale shake table testing of cross-laminated timber rocking shear walls with replaceable components. *J of Struct Eng* **145**(101), 04019115 (2019)
11. O'Reilly, G.J., Goggins, J.: Experimental testing of a self-centring concentrically braced steel frame. *Eng. Struct.* **238**, 111521 (2021)
12. Lettieri, A., de La Peña, A., Freddi, F., Latour, M.: Damage-free self-centring link for eccentrically braced frames: development and numerical study. *J of Constr Steel Res* **201**, 107727 (2023)
13. Simpson, B.G., Rivera, T.D.: Simplified modal pushover analysis to estimate first- and higher-mode force demands for design of strongback-braced frames. *J of Struct Eng* **147**(12), 04021196 (2023)
14. Pieroni, L., Freddi, F., Latour, M.: Effective placement of self-centering damage-free connections for seismic-resilient steel MRFs. *Earthq Eng & Struct Dyn* **51**, 1292–1316 (2022)
15. Deng, K., Pan, P., Wu, S.: Experimental study on a self-centering coupling beam eliminating the beam elongation effect. *Struct Des Tall and Spec Build* **25**(6), 265–277 (2015)
16. Freddi, F., Dimopoulos, C.A., Karavasilis, T.L.: Rocking damage-free steel CB with friction devices: design procedure and numerical evaluation. *Earthq Eng & Struct Dyn* **46**(14), 2281–2300 (2017)
17. Freddi, F., Dimopoulos, C.A., Karavasilis, T.L.: Experimental evaluation of a rocking damage-free steel CB with friction devices. *J of Struct Eng* **146**(10), 1–20 (2020)
18. Latour, M., Rizzano, G., Santiago, A., Da Silva, L.: Experimental response of a low-yielding, self-centering, rocking CB joint with friction dampers. *Soil Dyn & Earthq Eng* **116**, 580–592 (2019)
19. Zhang, R., et al.: Seismic performance of a low-damage rocking column base joint along weak axis. *J of Build Eng* **67**, 106056 (2023)
20. Elettore, E., Freddi, F., Latour, M., Rizzano, G.: Design and analysis of a seismic resilient steel MRFs equipped with damage-free self-centering CBs. *J of Constr Steel Res* **179**, 106543 (2021)
21. Elettore, E., Freddi, F., Latour, M., Rizzano, G.: Parametric finite element analysis of self-centering column bases with different structural properties. *J of Constr Steel Res* **199**, 107628 (2022)
22. Elettore, E., Freddi, F., Latour, M., Piluso, V., Rizzano, G.: Pseudo-dynamic testing, repairability, and resilience assessment of a large-scale steel structure equipped with self-centering column bases. *Earthq. Eng. Struct. Dyn.* **53**(9), 2756–2781 (2024)
23. Wang, Y., Zeng, B., Zhou, Z., Huang, L., Yao, J.: Shaking table test of a three-story frame with resilient variable friction braces. *J. Constr. Steel Res.* **192**, 107252 (2022)
24. Pampanin, S., et al.: Triaxial shake table testing of an integrated low-damage building system. *Earthq Eng & Struct Dyn* **52**(10), 2983–3007 (2023)
25. ABAQUS/Standard and ABAQUS/Explicit – Version 2017. ABAQUS Theory Manual, Dassault Systems (2016)

26. Mazzoni S., McKenna F., Scott M.H., Fenves G.L.: OpenSEES: Open System for earthquake engineering simulation. Pacific Earthquake Engineering Research Centre (PEER), University of California, Berkley, California (2009). <http://opensees.berkeley.edu>
27. ANSI/AISC 341–16 Seismic Provisions for Structural Steel Buildings, American Institute of Steel Construction (2016)

Open Access This chapter is licensed under the terms of the Creative Commons Attribution 4.0 International License (<http://creativecommons.org/licenses/by/4.0/>), which permits use, sharing, adaptation, distribution and reproduction in any medium or format, as long as you give appropriate credit to the original author(s) and the source, provide a link to the Creative Commons license and indicate if changes were made.

The images or other third party material in this chapter are included in the chapter's Creative Commons license, unless indicated otherwise in a credit line to the material. If material is not included in the chapter's Creative Commons license and your intended use is not permitted by statutory regulation or exceeds the permitted use, you will need to obtain permission directly from the copyright holder.





Seismic Retrofitting of RC Buildings Using Cross-Laminated Timber Panels: Insights from the ERIES-STRONG Project

Ivan Giongo¹(✉) , Francesco Graziotti^{2,3} , Nikolaos Stathas⁴ , Stathis Bousias⁴ , Francesco Smiroldo¹, Andrea Bartolotti¹, Nicolò Damiani^{2,3} , Albino Angelis⁵, and Dmytro Dizhur⁶

¹ Department of Civil, Environmental and Mechanical Engineering, University of Trento, Trento, Italy

ivan.giongo@unitn.it

² Department of Civil Engineering and Architecture, University of Pavia, Pavia, Italy

³ European Centre for Training and Research in Earthquake Engineering (EUCENTRE), Pavia, Italy

⁴ Department of Civil Engineering, University of Patras, Patras, Greece

⁵ XLAM DOLOMITI S.r.l, Castelnuovo, Italy

⁶ PYTHON Fixings Ltd, Auckland, New Zealand

Abstract. Timber, with strength-to-weight and modulus-to-strength ratios comparable to steel, is increasingly utilized in seismic retrofitting due to its versatility, sustainability, and rapid installation potential. However, concerns exist regarding its capacity to respond effectively to seismic events, particularly the risk of delayed activation compared to existing structural damage. Timber retrofits high deformability, largely attributed to the ductility of metal connections, enables significant displacements without compromising stability. Nonetheless, challenges arise when timber systems interact with brittle materials, such as in retrofits of reinforced concrete (RC) and masonry buildings, questioning the conventional ultimate limit state.

This study examines the application of cross-laminated timber (CLT) panels for retrofitting RC buildings, as part of the Sustainable Timber Retrofit Of reinforced coNcrete buildinGs (STRONG) project conducted at STRULAB, University of Patras, within the ERIES framework. A two-storey RC frame with masonry infill, representative of 1950–1970 Mediterranean construction practice, was retrofitted using a CLT-based technique (RC-TP) and tested under lateral cyclic loading up to ultimate conditions. The intervention prioritized life safety and global stability over damage containment during high-intensity events. This paper outlines the design criteria and experimental results, highlighting the potential of CLT panels to enhance seismic performance while ensuring structural stability.

Keywords: Seismic retrofit · Cross-laminated timber (CLT) · Masonry infilled RC frames · Experimental tests · Finite element analysis

1 Introduction

Medium-rise reinforced concrete (RC) frame buildings with masonry infills constitute a significant portion of the built environment in many countries. However, their seismic vulnerability has been widely recognized following past earthquake events, which have highlighted the structural deficiencies of these systems, particularly when subjected to lateral loading [1–3]. Many of these buildings were originally designed considering only gravity loads, neglecting both seismic actions and the structural role of masonry infills [4]. While infills contribute to lateral stiffness and reduce inter-story drifts, their presence leads to increased seismic demands due to shorter fundamental periods [5] and can introduce detrimental effects, such as torsional responses and soft-story mechanisms when irregularly distributed [6, 7]. Furthermore, local interactions between the infills and the RC elements may cause brittle failures in the frame, significantly affecting ductility and energy dissipation capacity [8, 9].

To mitigate these vulnerabilities, various retrofit strategies have been explored. Common local interventions include external jacketing with reinforced concrete, steel, fibre-reinforced polymers (FRP), or fibre-reinforced cementitious matrices (FRCM), while global strengthening approaches often involve exoskeletons, bracing systems, shear walls, or seismic isolation [10–12]. While these solutions have demonstrated effectiveness, they often present challenges related to high costs, long construction times, and disruptions to building occupancy.

In recent years, timber has gained increasing attention as a viable alternative for seismic retrofitting. With strength-to-weight and stiffness-to-strength ratios comparable to steel, timber offers advantages in terms of sustainability, prefabrication, and rapid installation. However, concerns remain regarding its ability to provide immediate structural response during seismic events, particularly in cases where activation delay could compromise the existing frame's integrity. The high deformability of timber-based systems, largely due to the ductility of metal fasteners, allows for significant displacements while preserving structural stability. Nonetheless, when combined with brittle materials, such as masonry-infilled RC frames, these systems challenge conventional performance-based design criteria.

This study investigates the application of cross-laminated timber (CLT) panels as a seismic retrofit solution for existing RC buildings. The research is part of the Sustainable Timber Retrofit of Reinforced Concrete Buildings (STRONG) experimental campaign, conducted at the STRULAB facility of the University of Patras within the framework of the ERIES (Engineering Research Infrastructures for European Synergies) project. A two-story, two-bay RC frame with masonry infills, representative of mid-20th century Mediterranean construction, was retrofitted using a CLT-based strengthening technique (RC-TP) and subjected to cyclic lateral loading up to ultimate conditions. This paper discusses the design criteria of the retrofit intervention, which prioritizes life safety and structural stability over damage limitation in high-intensity seismic scenarios.

2 The Retrofit Intervention

The RC-TP (Reinforced Concrete–Timber Panels) retrofit system improves the seismic performance of masonry-infilled RC frames by enhancing lateral strength and deformability. It involves replacing selected infill wythes with cross-laminated timber (CLT) panels mechanically connected to the RC frame. Typical cavity infills consist of a strong outer wythe (solid clay bricks) and a weak inner wythe (hollow clay or concrete blocks). The outer wythe, forming a stiff diagonal strut under seismic loads, increases shear demand on the RC frame, risking brittle column failures. In previous studies (e.g., Smiroldo et al., 2023 [13]), the RC-TP retrofit strategy was tested by removing both wythes and fully replacing the infill with a CLT panel.

This experimental campaign represents the first implementation of an alternative RC-TP variant, where only the external strong wythe is removed, while the internal weak wythe is preserved. This configuration is expected to provide multiple advantages. Firstly, retaining the weak wythe minimizes disruptions to building occupants, reducing downtime and increasing the feasibility of the intervention in operational buildings. Secondly, the low strength and stiffness of the remaining infill are unlikely to induce detrimental frame-infill interactions, thereby avoiding the formation of undesired brittle failure mechanisms. Lastly, this retrofit approach capitalizes on the weak-column strong-beam configuration commonly found in gravity-load-designed RC buildings. By leveraging the inherent strength reserves of the beams, the intervention enhances lateral load resistance while mitigating premature brittle failures due to excessive column shear demand.

The retrofit system consists of installing a CLT panel within the RC frame, secured by a rectangular timber subframe. The panel's strong direction is oriented vertically to support vertical loads in case of severe damage to the RC elements during earthquakes. The subframe is mechanically anchored to the RC frame using concrete screws designed to remain elastic under design-level seismic demands, ensuring integral movement with the structure. The CLT panel is connected to the subframe via dissipative shear connections using perpendicular, partially threaded screws. These fasteners govern force transfer and dissipate energy through controlled plastic deformation, promoting a ductile response while preventing brittle failures in the RC frame. A small gap between the CLT panel and the RC frame edges ensures load transfer occurs exclusively through the connectors, enhancing energy dissipation. The experimental campaign aims to assess the seismic effectiveness and feasibility of this modified RC-TP strategy for widespread application in existing RC buildings.

A detailed description of the numerical model used for predicting the behaviour of the specimens is provided in Bartolotti et al. (2024) [14]. In the As-Built (MI) configuration, masonry infills are modelled as concentric equivalent struts based on the model by Liberatore et al. (2018) [15], with adjustments for openings using established strength and stiffness reduction factors [16]. In the Retrofitted configuration, the CLT panel is modelled with orthotropic elastic shell elements, while panel-to-subframe connections are represented by multi-linear plastic links calibrated from experimental data [13].

3 Structural Design Philosophy

The experimental campaign involves testing two full-scale, two-story, two-bay RC frame specimens from the elastic range up to ultimate conditions. One specimen (S1) represents the as-built (unreinforced) configuration, while the second specimen (S2) corresponds to the retrofitted configuration. The geometry and material properties of the RC elements remain identical in both configurations, ensuring that the only difference between S1 and S2 lies in the retrofit intervention itself.

3.1 As-Built Reference Specimen

The as-built specimen (S1) was designed to represent mid-20th-century Mediterranean RC buildings, a typology that experienced rapid growth during the post-war period. In this era, RC frames with masonry infill walls became the dominant construction method across Southern Europe. For example, in Italy, the number of RC buildings rose dramatically from 77,122 in 1945 to 1,057,267 in 1970, reflecting a twelvefold increase in just 25 years (ISTAT, 2011) [17]. Similar trends were observed in other Mediterranean countries, demonstrating the widespread adoption of this construction technique.

To ensure historical accuracy, Italian building codes and construction practices from the period were used as references, specifically the Regio Decreto Legge (RDL) of 1939 [18] and the Ministerial Circular No. 1472 of 1957 [19]. However, an analysis of original project documentation revealed that code prescriptions were not always strictly followed, mainly due to material shortages, cost-cutting measures, and the absence of rigorous structural inspections.

For both numerical modelling and experimental testing, the materials selected align with those most commonly used in RC construction during this period. The concrete mix followed historical prescriptions, with a minimum compressive strength of 120 kg/cm^2 at 28 days, as per the RDL 1939 and Circular 1957. The reinforcement steel consisted of plain bars, type AQ42, as documented by Verderame et al. (2011) [20]. However, for the actual construction of the specimens, the most probable material properties for existing buildings were adopted, including a mean concrete compressive strength of $f_{cm} = 14.5 \text{ MPa}$, based on the findings of Cristofaro et al. (2012) [21], and a yield strength of $f_{ym} = 322.4 \text{ MPa}$ for the reinforcement steel, as determined using Stil software (ReLUIS – Stil [22]).

The as-built structure was designed solely for gravity loads, in accordance with common mid-century engineering practices, where seismic considerations were often neglected in ordinary building design. Simulating the original design approach based on historical codes and project documentation led to a weak-column/strong-beam configuration, which is a key factor influencing its seismic performance. The columns emerge as the most vulnerable structural elements, raising concerns about potential brittle shear failures during lateral loading.

To ensure consistency when assessing the as-built and retrofitted configurations, collapse mechanisms and cross section strengths were evaluated following modern Eurocode provisions. The analysis conducted using the most probable materials for the period revealed that the ratio between the shear stress associated to the column flexural

failure and its shear strength was = 0.79. This ratio was taken as a reference to determine the target concrete compressive strength, ensuring that the hierarchy of collapse mechanisms remained unchanged even when using the materials available for specimen fabrication. A key challenge emerged, in fact, when sourcing reinforcement bars: only plain bars with a yield strength of $f_{ym} = 220$ MPa were available. Although this value is within the acceptable range for AQ42 steel from the 1950–1970 period (with a lower bound of 211.9 MPa, according to structural analysis software), it is significantly lower than the expected 322.4 MPa. Given the yield strength of 220 MPa for the reinforcement steel, the required target concrete compressive strength was found to be $f_{cm} = 8$ MPa.

The reinforcement layout for the RC frame elements was designed based on typical assumptions for mid-20th-century residential buildings (Fig. 1). The frame was assumed to be located at the ground floor of a three-story residential building, with a vertical load of 200 kN applied at the top of each column, consistent with standard load distributions for buildings of this period. The top beam of the frame was subjected to loads transmitted by the floor slab and the overlying masonry infill, assuming an influence length of 3 m. The resulting distributed load acting on the beam was estimated at 16.5 kN/m.

In accordance with construction practices of the time, shear forces were resisted by both stirrups and bent-up bars, following a widely adopted reinforcement strategy in RC construction during the mid-to-late 20th century. This design ensured an effective distribution of shear forces, utilizing both transverse reinforcement and longitudinal bars shaped to enhance resistance. However, it is well known that bent-up bars lose their shear resistance capacity in cases of shear force reversal, which may occur under seismic loading.

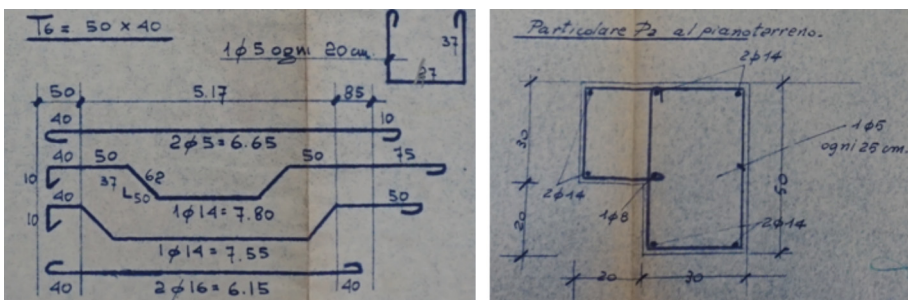


Fig. 1. Example of typical reinforcements in buildings from 1950–1970

To address this issue, the original design relied on the presence of sustained vertical loads on the beam, which inherently provided a margin of safety against shear force reversals. However, since the experimental setup did not allow for the direct application of distributed loads on the beam, the reinforcement layout was modified accordingly. Specifically, the stirrup spacing was adjusted, increasing the density of transverse reinforcement to compensate for the absence of an applied distributed load, thereby ensuring that the margin of safety remained unchanged (Fig. 2.).

This adaptation faithfully reproduces realistic service conditions, while also optimizing the experimental setup. By adjusting stirrup spacing, the study ensures that internal

force distributions remain consistent with those expected under real building conditions, allowing for an accurate evaluation of structural performance under seismic loading.

The mechanical properties of the masonry infill walls were defined based on data available from the literature [13]. The as-built configuration included a double-wythe cavity wall, composed of an internal weak wythe made of hollow clay blocks and an external strong wythe made of solid clay bricks. In the retrofitted configuration, only the internal weak wythe was retained, while the external wythe was removed and replaced with the RC-TP system. This distinction is critical, as it influences the interaction between the infill and the RC frame, particularly under lateral loads.

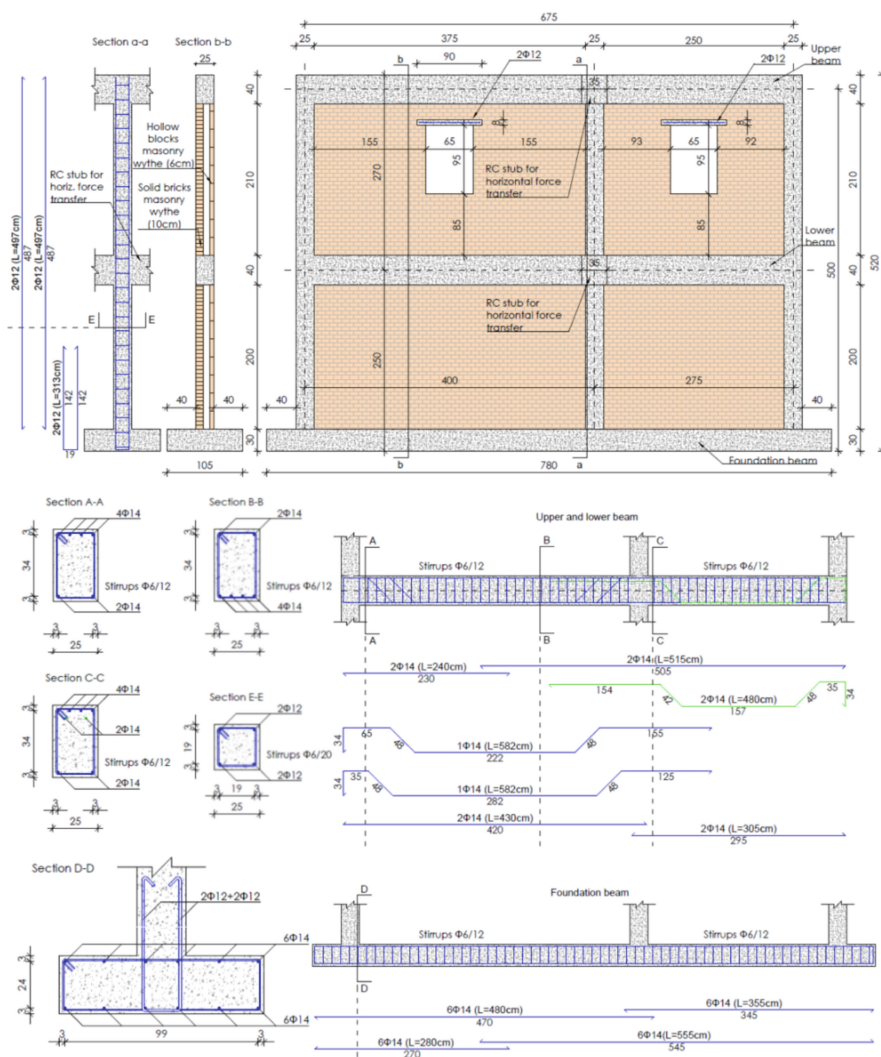


Fig. 2. Details of the as-built specimen S1

3.2 The Retrofit Strategy

Previous studies [23] have shown that placing fasteners on the column side can increase the lateral strength of the frame, but it can also lead to a significant rise in shear demand on the columns. To mitigate this effect, the panel-to-subframe fasteners ($\phi 10$, 160 mm long partially threaded screws [24]) were placed exclusively on the beam side, ensuring that the seismic load transfer does not excessively amplify shear forces in the columns.

The spacing of the fasteners between the CLT panel and the subframe along the beam was carefully designed to balance two key factors: reducing the spacing enhances the lateral strength of the frame, but at the same time, it increases shear demand on the beams. Therefore, the fastener layout along the beam was calibrated to prevent exceeding the shear capacity of the beams while ensuring an effective load transfer mechanism. Additionally, to account for the distribution of forces along the height of the frame, a larger fastener spacing was adopted at the first floor compared to the ground floor, following the expected force distribution along the structure.



Fig. 3. Specimen S2 ready for testing

To optimize the retrofit configuration, an advanced finite element analysis was conducted to evaluate the performance of different fastener spacing layouts between the CLT panel and the subframe. The study considered several spacing configurations, including a 10 cm spacing at the ground floor combined with a 15 cm spacing at the first floor (R1), a 10 cm spacing at the ground floor with a 20 cm spacing at the first floor (R2), and a 15 cm spacing at the ground floor together with a 20 cm spacing at the first floor (R3). The numerical results showed that the last configuration provided the best balance between increased lateral strength and delayed brittle failure mechanisms (Fig. 4). Specifically, this layout resulted in an estimated 50% increase in lateral strength compared to the unreinforced frame, while also enhancing the deformation capacity of the system and reducing the risk of premature failure. Based on these numerical findings, the selected retrofit configuration for the experimental phase incorporated a 15 cm fastener spacing at the ground floor and a 20 cm spacing at the first floor, ensuring an optimal trade-off

between structural resistance and ductility. Figure 3 shows Specimen 2 fully assembled, moments before the testing started.

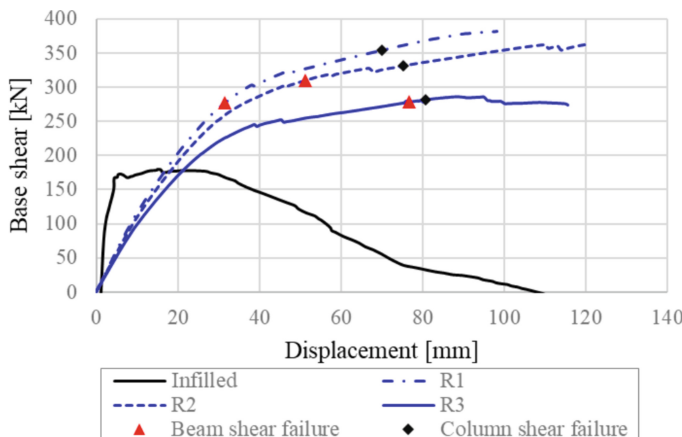


Fig. 4. Numeric simulations: pushover curve comparison

4 Material Characterization and Retrofit Design Updating

A preliminary experimental testing campaign was conducted to characterize the mechanical properties of materials and connections, providing essential data for refining the numerical models and updating the retrofit strategy accordingly. These tests included compression tests on concrete cubes ($f_{c,c}$), tensile tests on reinforcing bars ($f_{y,b}$) and stirrups ($f_{y,s}$), flexural ($f_{f,mr}$) and compression tests ($f_{c,mr}$) on mortar prisms, compression tests on bricks ($f_{c,br}$) and blocks ($f_{c,bl}$), compression tests on masonry prisms (bricks $f_{c,br,ms}$, blocks $f_{c,bl,ms}$), shear tests on masonry triplets (bricks $f_{v,br,ms}$, blocks $f_{v,bl,ms}$), and pull-out ($f_{w,TC}$) and cyclic/monotonic pushout (elastic stiffness k_{TC} , yielding force $f_{vy,TC}$, maximum force $f_{vu,TC}$) tests on timber-to-concrete connections (Fig. 5).



Fig. 5. Selected photos from the preliminary material testing: fasteners pull-out tests; masonry shear tests; block compression tests

The results of the preliminary tests are summarized in tabular form (Table 1).

Table 1. Material properties

	$f_{c,c}$	$f_{y,b}$	$f_{y,s}$	$f_{f,mr}$	$f_{c,mr}$	$f_{c,br}$	$f_{c,bl}$	$f_{c,br,ms}$	$f_{c,bl,ms}$	$f_{v,br,ms}$	$f_{v,bl,ms}$	$f_{w,TC}$	k_{TC}	$f_{v,y,TC}$	$f_{v,u,TC}$
Nº Test	12	6	3	18	36	8	8	3	3	3	3	31	3	3	4
Mean	15.6 MPa	278.7 MPa	323.1 MPa	1.8 MPa	3.8 MPa	8.5 MPa	24.8 MPa	7.4 MPa	1.4 MPa	0.6* MPa	0.4** MPa	51.4 kN	1.9 kN/mm	7.6 kN	18.4 kN
CV [%]	7.4	7.6	0.6	23.5	33.9	26.6	17.3	19.3	10.9	22.2	34.0	4.2	19.4	17.7	8.2

* Test performed with a constant compression equal to 0.2 MPa

** Test performed with a constant compression equal to 0.1 MPa

The updated mechanical properties of the existing materials involve a significant increase in the capacity of the frame in the “as-built” configuration compared to the initially assumed values (Reference Specimen described in Sect. 3.1). Nevertheless, these characteristics remain consistent with the typical range of material properties used in constructions built between 1950 and 1970. In this context, it was considered appropriate not to prioritise an extreme increase in load-bearing capacity (e.g., by introducing connections along the columns), but rather focusing the intervention on enhancing the system’s deformation capacity and overall ductility. The proposed configuration was therefore revised to reflect the actual characteristics of the existing frame.

One of the key adjustments involved refining the connection modelling between the RC frame and the timber subframe. Specifically, the behaviour of the panel-to-frame connection link was modified to account for the elastic stiffness of timber-to-concrete (TC) connectors, which were modelled as springs in series (in the original model such connection was assumed as rigid). This adjustment was applied exclusively in the shear direction, parallel to the panel edges, ensuring a realistic representation of the connection’s deformability. In contrast, in the direction orthogonal to the panel edges, the extraction and compression behaviour was assumed to be rigid, preserving the original link properties in this direction.

To enhance the reversibility of the intervention and minimize environmental impact, the connection between the RC frame and the timber subframe was designed as a dry joint (made with two rows of 340 mm long equally spaced screw fasteners with a shank diameter of 8 mm [25]), avoiding the use of resins or adhesives. This approach allows for the potential removal of the retrofit system without causing damage to the existing structure, while also simplifying the end-of-life disassembly of the intervention. To ensure the effectiveness of the retrofit, this connection was designed to be sufficiently rigid and to have overstrength relative to the panel-to-subframe connection, preventing premature failure at the interface.

The spacing of the TC fasteners was determined based on the above-mentioned testing and data provided by the manufacturer. The design criteria dictated that the shear demand on the connection should remain below the shear yield limit, while the extraction demand should not exceed the withdrawal threshold. Based on these verifications, an initial spacing of 14 cm at the first floor and 18 cm at the second floor was adopted.

The higher-than-expected strength of the masonry infill panels, as observed in the material characterization tests, necessitated a revision of the panel-to-subframe connector spacing. In particular, the spacing was reduced from 15 cm to 12.5 cm at the first floor and from 20 cm to 18 cm at the second floor. Furthermore, supplementary screws were installed at the corners of the CLT panels: three per corner at the ground floor level and two per corner at the upper floor level. This modification was implemented without altering the expected failure mechanism of the system. The higher strength of the stirrups, which increased from the expected 220 MPa to 325 MPa based on preliminary tensile tests, resulted in a higher shear capacity of beams and columns, ensuring that the structural response remained consistent with design assumptions.

The refinements introduced in the numerical modelling and retrofit layout ensure that the RC-TP system effectively improves the lateral resistance and ductility of the retrofitted structure, while also maintaining a balance between strength and deformation capacity. The updated design parameters were subsequently incorporated into the final retrofit strategy, ensuring an optimized structural performance under seismic loading.

5 Test Results and Model Updating

Figure 6 shows the experimental response of specimens S1 and S2 in terms of base shear versus total drift (Dr). It also presents the predictions from the numerical models, which were updated by incorporating the actual material properties measured in the tests described in the previous section. The as-built specimen S1 reached a maximum base shear of 398 kN at approximately 0.5% drift, followed by a softening branch up to $Dr = 1.2\%$, at which point the test was stopped due to the infill walls at the top storey being on the verge of collapse. The retrofitted specimen S2, which involved the removal of the strong external wythe and the application of RC-TP strengthening, showed a 24% increase in capacity, reaching 492 kN at a much larger drift of approximately 2%, when the test was stopped for safety reasons. The pushover responses predicted by the numerical models for both the as-built and retrofitted configurations are represented by the blue curves, which match the experimental data with sufficient accuracy.

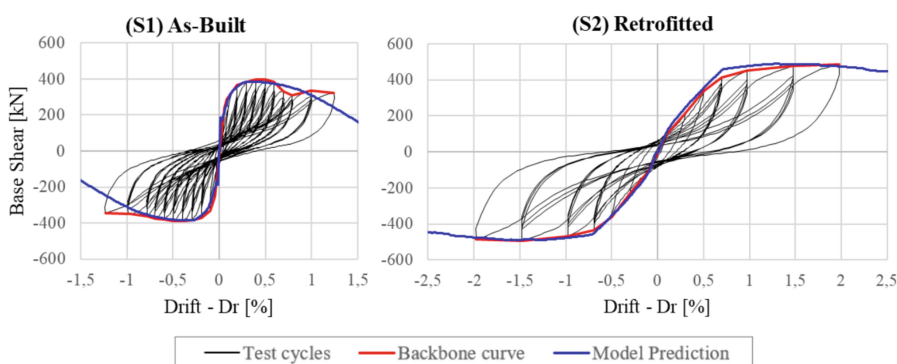


Fig. 6. S1 and S2 specimens: test results and numerical predictions

6 Concluding Remarks

This study presented the development, modelling, and experimental validation of a cross-laminated timber (CLT)-based retrofit strategy (RC-TP) for improving the seismic performance of existing RC frames with cavity infill walls. The work was carried out within the Sustainable Timber Retrofit Of reinforced coNcrete buildinGs (STRONG) experimental campaign, hosted at the University of Patras as part of the ERIES (Engineering Research Infrastructures for European Synergies) project. The proposed intervention, applied for the first time while retaining the internal masonry wythe, proved effective in enhancing both lateral strength and deformation capacity. The integration of material characterization into the numerical modelling process enabled accurate prediction of global behavior, which was confirmed by the experimental results. The findings highlight the potential of the RC-TP system as a sustainable and minimally invasive retrofit solution for gravity-load-designed RC buildings.

Acknowledgements. This work is part of the transnational access project “ERIES-C73”, supported by the Engineering Research Infrastructures for European Synergies (ERIES) project (www.ries.eu), which has received funding from the European Union’s Horizon Europe Framework Programme under Grant Agreement No. 101058684. This is ERIES publication number C73.

The 2024–2026 ReLUIS-DPC Project framework (funded by the Italian Emergency Management Agency, DPC) is also gratefully acknowledged for the support given to the research. XLAM Dolomiti Spa and PYTHON® Fixings are thanked for providing their products.

References

1. Sezen, H., Whittaker, A.S., Elwood, K.J., Mosalam, K.M.: Performance of reinforced concrete buildings during the August 17, 1999 Kocaeli, Turkey earthquake, and seismic design and construction practise in Turkey. *Eng. Struct.* **25**(1), 103–114 (2003)
2. Decanini, L.D., De Sortis, A., et al.: Performance of reinforced concrete buildings during the 2002 Molise. Italy. *Earthquake Spectra* **20**(S1), S221–S255 (2004)
3. Verderame, G.M., De Luca, F., Ricci, P., Manfredi, G.: Preliminary analysis of a soft-storey mechanism after the 2009 L’Aquila earthquake. *Earthquake Eng Struct Dyn* **40**(8), 925–944 (2011)
4. Masi, A.: Seismic vulnerability assessment of gravity load designed R/C frames. *Bull. Earthq. Eng.* **1**(3), 371–395 (2003)
5. Asteris, P.G., Repapis, C.C., Cavalieri, L., Sarhosis, V., Athanasopoulou, A.: On the fundamental period of infilled RC frame buildings. *Struct. Eng. Mech.* **54**(6), 1175–1200 (2015)
6. Gong, M., Zuo, Z., Wang, X., Lu, X., Xie, L.: Comparing seismic performances of pilotis and bare RC frame structures by shaking table tests. *Eng. Struct.* **199**, 109442 (2019)
7. Choudhury, T., Kaushik, H.B.: Seismic fragility of open ground storey RC frames with wall openings for vulnerability assessment. *Eng. Struct.* **155**, 345–357 (2018)
8. De Luca, F., Morciano, E., Perrone, D., Aiello, M.A.: MID 1.0: masonry infilled RC frame experimental database. Italian concrete days, Rome, Italy; 27–28 October (2016)
9. Xu, H., Brodsky, A.: “Multi-platform simulation of infilled shear-critical reinforced concrete frames subjected to earthquake excitations.” *Bull. Earthquake Eng.* 1–26 (2022)

10. Gkournelos, P.D., Triantafyllou, T.C., Bournas, D.A.: Seismic upgrading of existing reinforced concrete buildings a state-of-the-art review. *Eng. Struct.* **240**, 112273 (2021)
11. Di Lorenzo, G., Colacurcio, E., Di Filippo, A., Formisano, A., Massimilla, A., Landolfo, R.: State-of-the-art on steel exoskeletons for seismic retrofit of existing RC buildings. *Int. J.* **37**, 1 (2020)
12. Labo, S., Passoni, C., Marini, A., Belleri, A.: Design of diagrid exoskeletons for the retrofit of existing RC buildings. *Eng. Struct.* **220**, 110899 (2020)
13. Smiroldo, F., Kallioras, S., Sommacal, G., Bournas, D., Piazza, M., Giongo, I.: Full-scale testing of masonry-infilled RC frames retrofitted with cross-laminated timber panels. *Eng. Struct.* **294**, 116789 (2023). <https://doi.org/10.1016/j.engstruct.2023.116789>
14. Bartolotti A., Smiroldo F., Giongo I., 2024, “Nonlinear Dynamic Study on Existing Masonry-Infilled Concrete Frames Retrofitted with Timber Panels”. *STRUCTURES*, v. 2024, 69, (2024), p. 1–13. - <https://doi.org/10.1016/j.istruc.2024.10732>
15. Liberatore, L., Noto, F., Mollaioli, F., Franchin, P.: In-plane response of masonry infill walls: comprehensive experimentally-based equivalent strut model for deterministic and probabilistic analysis. *Eng. Struct.* **167**, 533–548 (2018). <https://doi.org/10.1016/j.engstruct.2018.04.057>
16. Hossamaldeen, M., Romão, X.: Effect of openings on the seismic vulnerability assessment of masonry infilled reinforced concrete frames. *Eng. Struct.* **205**, 110078 (2020)
17. ISTAT. 154°Censimento della Popolazione e delle Abitazioni. 2011. (In Italian)
18. R.D.L. 16 NOVEMBRE 1939 N°2228–2232 (Suppl. Ord. alla Gazz. Uff. del 18 aprile 1940 n°92) Norme per l'esecuzione delle opere in conglomerato cementizio semplice od armato. (In Italian)
19. CIRCOLARE 23 MAGGIO 1957 N°1472, Armature delle strutture in cemento armato. (In Italian)
20. Verderame, G.M., Ricci, P., Esposito, M., Sansiviero, F.C.: Le caratteristiche meccaniche degli acciai impiegati nelle strutture in ca realizzate dal 1950 al 1980. XXVI Convegno Nazionale AICAP (2011). (In Italian)
21. Cristofaro, M.T., D'Ambris, A., De Stefano, M., Pucinotti, R., Tanganeli, M.: Studio sulla dispersione dei valori di resistenza a compressione del calcestruzzo di edifici esistenti. *Il Giornale delle Probe non Distruttive, Monitoraggio, Diagnostica* **2**, 32–39 (2012). (in Italian)
22. ReLUIS - Stil Software. STIL: Software for material characterization in historical RC buildings. <https://www.reluis.it/stil/>
23. Smiroldo, F., Giongo, I., Piazza, M.: Use of timber panels to reduce the seismic vulnerability of concrete frame structures. In: *Engineering Structures*, vol. 244, p. 112797 (2021). <https://doi.org/10.1016/j.engstruct.2021.112797>
24. ETA 11/0190. Würth self-tapping screws: Screws for use in timber constructions. DIBt; 2018
25. <https://www.pythonfixings.co.nz/>

Open Access This chapter is licensed under the terms of the Creative Commons Attribution 4.0 International License (<http://creativecommons.org/licenses/by/4.0/>), which permits use, sharing, adaptation, distribution and reproduction in any medium or format, as long as you give appropriate credit to the original author(s) and the source, provide a link to the Creative Commons license and indicate if changes were made.

The images or other third party material in this chapter are included in the chapter's Creative Commons license, unless indicated otherwise in a credit line to the material. If material is not included in the chapter's Creative Commons license and your intended use is not permitted by statutory regulation or exceeds the permitted use, you will need to obtain permission directly from the copyright holder.





Out-of-Plane Shake-Table Tests on Unreinforced Masonry Gables Considering Different Roof Configurations

Nicolò Damiani^{1,2(✉)}, Marta Bertassi³, Satyadhrik Sharma⁴, Marco Smerilli², Michele Mirra⁴, Igor Lanese², Elisa Rizzo-Parisi², Gerard J. O'Reilly^{2,3}, Francesco Messali⁴, and Francesco Graziotti^{1,2}

¹ Department of Civil Engineering and Architecture (DICAr), University of Pavia, Pavia, Italy
nicolo.damiani@unipv.it

² European Centre for Training and Research in Earthquake Engineering (EUCENTRE), Pavia, Italy

³ University School for Advanced Studies IUSS Pavia, Pavia, Italy

⁴ Faculty of Civil Engineering and Geosciences, University of Technology of Delft (TU Delft), Delft, The Netherlands

Abstract. Low-rise masonry buildings worldwide frequently feature unreinforced masonry (URM) walls coupled with various pitched roof configurations supported by masonry gables. Past earthquakes have highlighted the vulnerability of these components to out-of-plane seismic loads due to their high slenderness, insufficient roof connections, and exposure to amplified accelerations while being subjected to minimal overburden due to their location at the upper part of buildings. This study presents key insights from the experimental campaign of the ERIES-SUPREME project, aimed at enhancing the understanding of the out-of-plane seismic behavior of masonry gables. Incremental dynamic tests were performed on three full-scale URM gables, simulating both induced and tectonic earthquake scenarios until collapse, using two shake tables. Differential motions at the top and bottom tables reproduced the interaction of the gables with three different roof diaphragm configurations, each introducing a unique filtering effect on the seismic input. The outcomes of the experiments can be used for refining existing numerical modelling strategies as well as contribute to developing improved tools for the seismic assessment of URM gables.

Keywords: Differential input motions · Gable walls · Incremental dynamic shake-table tests · Roof stiffness · Out of plane · Unreinforced Masonry

1 Introduction

Unreinforced masonry (URM) structures form a significant portion of the building stock in many areas worldwide. These structures often exhibit a relevant seismic vulnerability, mainly attributable to the poor material mechanical properties, and to the lack

of adequate detailing to prevent local failures such as wall out-of-plane (OOP) overturning. This vulnerability has been documented in post-earthquake damage surveys reported in numerous studies [1–4]. These structures are prevalent in seismically active regions, including areas affected by both natural and induced seismicity. Typical low-rise masonry buildings consist of URM walls with different timber roof configurations, generally supported by masonry gables. Post-earthquake damage surveys and experimental evidence [5, 6] recognized masonry gables as structural elements significantly vulnerable to OOP failures. Their vulnerability is mostly attributed to their high slenderness, weak connections to the roof structure, and location at the top of the building where seismic amplification is typically most pronounced. This location exposes them to amplified seismic excitation compared to the motion at the ground, while they are subjected to minimal vertical overburden loads. Nonetheless, experimental and numerical investigations on the seismic response of URM gable walls remain limited in the literature [7, 8], with most studies focusing on walls with rectangular geometries [9–15], leaving a gap in the understanding of the gable behavior under seismic loading.

To address this gap, this paper presents a dynamic full-scale shake-table testing campaign on three full-scale URM gables to investigate their seismic behavior until complete collapse. The tested gable specimens and their material properties are first described. Although the roof was not explicitly included in the experiments, the effect of its stiffness on the gable response is accounted for by applying differential input motions through two shake tables: one at the gable base and another at its top. A detailed description of the experimental setup is then provided. Input motions representative of both induced and tectonic seismicity were applied to the shake tables and are described alongside the incremental dynamic testing sequence. Finally, the main experimental results are presented, comparing the response of the three gables interacting with roofs of varying stiffness. All experimental data, and the associated instrumentation schemes, are openly available for download at <https://doi.org/https://doi.org/10.60756/euc-1avy7q49> [16].

2 Description and Mechanical Characterization of the Masonry Specimens

2.1 Specimen Geometry

The test specimens of the experimental campaign consisted of three identical full-scale URM gable walls, which were built on a composite steel-concrete foundation. Each specimen had a length of 6 m and height of 3 m. The gables were built using clay bricks, with average dimensions of $230 \times 105 \times 55$ mm, resulting in a gable thickness of 105 mm. The gables consisted of 45 courses of bricks, and all mortar joints were 10-mm-thick (Fig. 1).

Moreover, five joist pockets were realized to accommodate the timber beams of the roof, with a cross-section of 100×200 mm. These beams were used to transfer the vertical load representative of the roof diaphragm weight, resulting in an overburden of 0.07 MPa at the mid-height of the gable. Hence, a vertical load of 4.5 kN was applied through each timber beam, resulting in a total vertical load of 22.5 kN, simulating half

the weight of a typical timber roof diaphragm, consistent with the geometry of the tested gable specimen. These beams were also used to apply lateral loads along the height of the specimen, as further discussed in the following sections.

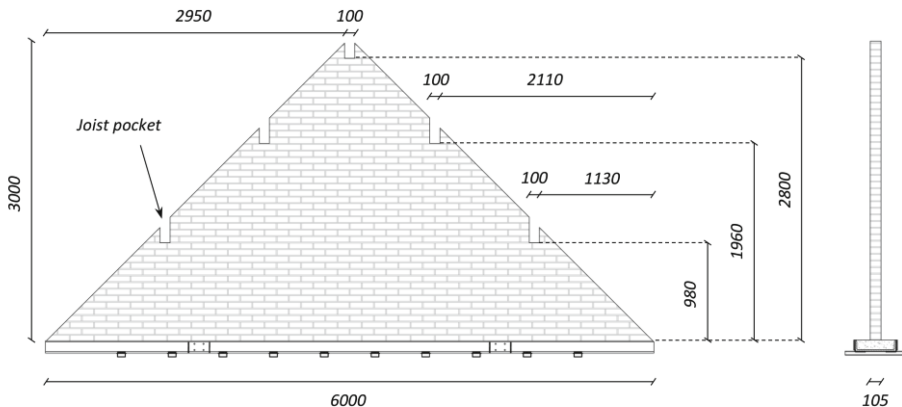


Fig. 1. Full-scale masonry gable specimen details and pictures. Units of mm.

The experimental tests were conducted without steel anchors between the timber joists and masonry gables. This approach simulated a “worst-case” scenario, where timber-to-masonry connections relied entirely on friction, providing a lower-bound estimate of the gable seismic resistance.

2.2 Summary of Material Mechanical Properties

The tested gable specimens were accompanied by complementary material characterization performed on unit, mortar, and masonry as a composite material. All material characterization tests were performed at the “Giorgio Macchi” Material and Structural Testing Laboratory of the Department of Civil Engineering and Architecture (DICar) of the University of Pavia (Italy), on specimens that reached 28 days of maturation.

The characterization included the compressive (f_c) and flexural strength (f_t) of mortar, the compressive (f_u) strength of bricks, the compressive strength (f_m) of masonry perpendicular to bed joints, and secant elastic modulus (E_m) calculated between 10 and 33% of f_m , the bond strength (f_w) of masonry, the initial shear strength (f_{v0}) and friction coefficient (μ). All tests were performed following the latest applicable European norms [17–21]. Furthermore, to characterize the response of masonry bed joints under torsional shear stress ($f_{v0,tor}$, μ_{tor} evaluated assuming a linear elastic hypothesis), a dedicated test was performed [22]. The density of masonry (ρ_m) was determined from the average weight of the tested gables. Table 1 summarizes experimental mean values and coefficient of variation (C.o.V.) for the investigated mechanical properties.

Table 1. Summary of unit, mortar and masonry mechanical properties.

Material properties	Symbol	Units	Mean	C.o.V
Mortar compressive strength	f_c	[MPa]	0.68	0.26
Mortar flexural strength	f_t	[MPa]	0.20	0.50
Unit/brick compressive strength	f_u	[MPa]	42.57	0.09
Masonry compressive strength	f_m	[MPa]	7.44	0.10
Masonry elastic modulus	E_m	[MPa]	4072	0.11
Masonry initial shear strength	f_{v0}	[MPa]	0.19	–
Masonry friction coefficient	μ	[–]	0.51	–
Masonry bond strength	f_w	[MPa]	0.21	0.48
Masonry initial shear strength (torsional)	$f_{v0,tor}$	[MPa]	0.42	–
Masonry friction coefficient (torsional)	μ_{tor}	[–]	1.15	–
Masonry density	ρ_m	[kg/m ³]	1883	–

3 Testing Layout and Setup

3.1 Testing Layout

Three dynamic shake-table tests on full-scale masonry gables were performed at the 9D LAB of the EUCENTRE facilities in Pavia, Italy. This advanced seismic testing system features a dual shake-table configuration, including a top and bottom table capable of applying differential input motions covering nine degrees of freedom. This setup enables reproducing interstorey displacements occurring during earthquakes. The 9D LAB, with its 4.8×4.8 m dimensions, was large enough to accommodate the full-scale gable walls but not an entire roof diaphragm. To account for the influence of roof stiffness on the OOP seismic response of the gables, variations in the input motion imposed on the top shake table were introduced. In particular, three different configurations for the roof structure were considered: (i) Gable1-STIFF, representing a stiff roof diaphragm, where the top shake table replicated the motion of the bottom table; (ii) Gable2-SEMFLEX, representing an intermediate case, where the top motion was linearly amplified relative to the base motion; and (iii) Gable3-FLEX, simulating a flexible roof diaphragm, where the motion at the top was significantly amplified and phase-shifted relative to the base motion.

3.2 Testing Setup

The experimental setup, depicted in Fig. 2, consisted of a dual shake-table configuration, including a top and bottom table capable of applying differential input motions. The test setup included a loading frame, composed of shaped profiles, that transferred accelerations along the gable height through five horizontal loading arms hinged to the frame. Timber beams were screwed to the steel arms to replicate the presence of timber joists typically found in real roof structures. The five horizontal loading arms also

allowed applying the vertical loads to the gable specimens through five springs, one for each loading arm. These loads were applied to the gable specimens by pulling down the horizontal steel arms through steel bars in series with the springs (Fig. 3).

It is worth to note that the loading frame was hinged at both the bottom and top shake tables to avoid introducing additional OOP stiffness and strength to the gable specimen, whose foundation was fixed to the bottom shake table. A stiff instrumentation frame, anchored to the bottom shake table, completed the test setup serving as support and a fixed reference for the instruments.

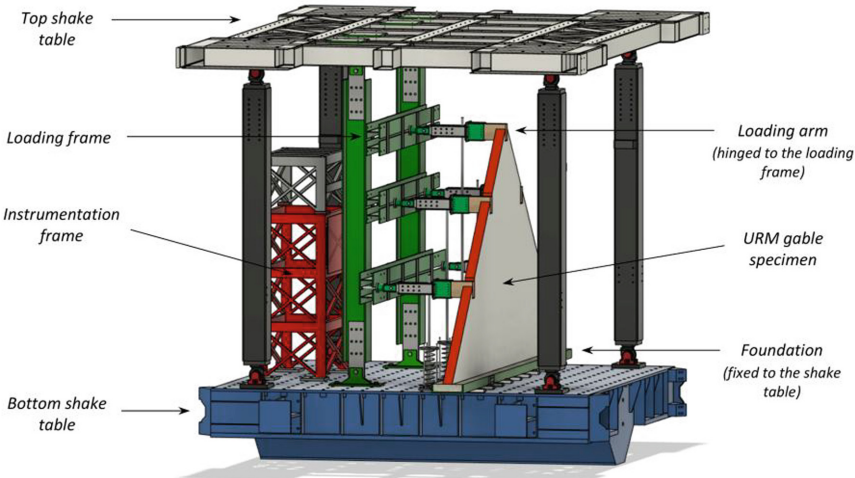


Fig. 2. Three-dimensional view of the shake-table testing setup of the 9D LAB.

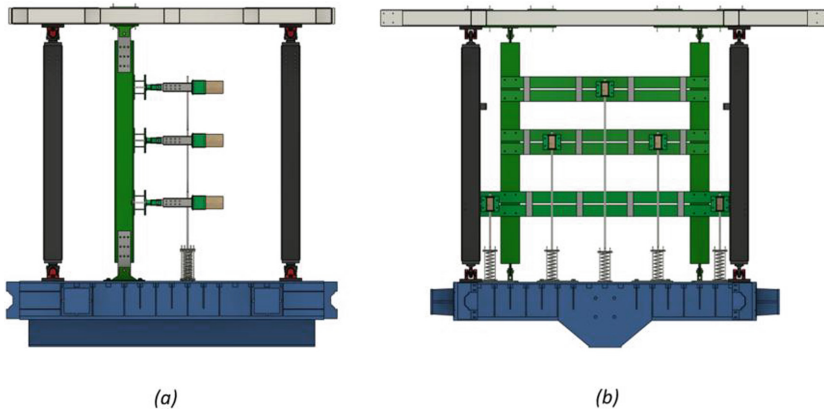


Fig. 3. Lateral (a) and front (b) views of the installed loading frame.

A key feature of this experimental setup is its ability to precisely control the boundary conditions of each masonry gable, ensuring that its seismic response remains independent

of the loading frame. As illustrated in Fig. 4, during the shake-table test, the gable specimen is expected to rotate by pivoting at its base, altering the support conditions of the timber beams. Consequently, rather than being evenly distributed across the full gable thickness, the vertical load applied through the pre-compressed springs results concentrated at a single point. However, since this load remains perpendicular to the bottom shake table, it has minimal impact on the gable specimen out-of-plane seismic response.

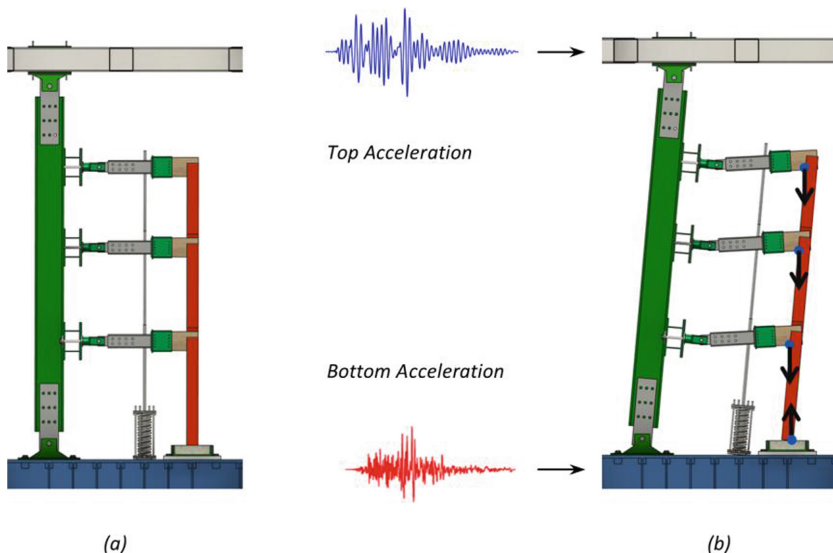


Fig. 4. Representation of the vertical load application during the test: (a) undefomed configuration of the specimen and loading frame; (b) deformed configuration of the specimen and loading frame under differential seismic input.

4 Instrumentation, Input Signals, and Testing Protocols

4.1 Instrumentation and Data Acquisition

The instrumentation installed on each gable included accelerometers, potentiometers, wire potentiometers, and a 3D optical acquisition system. The positioning of the instruments was determined based on the expected deformed shapes and cracking patterns. Accelerometers were installed on the gable specimens to record acceleration-time histories, with additional units placed on the loading and instrumentation frames, as well as on the specimen foundation. Potentiometers were used to measure the elongation or shortening of springs and the relative displacements between the timber beams and the masonry. Wire potentiometers, attached to both the loading and instrumentation frames, were used to record displacements of the gable specimens. Finally, the optical monitoring system was employed to measure displacements on the free surface of the gable, opposite to the loading frame.

4.2 Input Signals

The 9D LAB setup enabled the application of distinct input motions at the bottom and top shake tables, simulating the influence of roof diaphragm in-plane stiffness. Two alternative floor motion (FM) scenarios were considered: FM1, representing induced seismicity, and FM2, associated with tectonic seismicity. For the induced scenario, numerical analyses were performed on a finite element model of a typical URM building from the Groningen region in the Netherlands. The building was assessed in its as-built conditions with a flexible timber roof, and in two alternative retrofitted configurations: one with a rigid concrete roof and another incorporating a timber-based retrofit intervention resulting in a semi-flexible roof. In the tectonic seismicity scenario, recorded data from the 2016 Central Italy earthquake, collected at the attic level of a monitored masonry building, were utilized. In this case, the interaction between the gable and the roof was modeled using an elastic single-degree-of-freedom system. Further details on input signal selection can be found in [23].

Figure 5 presents the induced and tectonic input signals at the bottom (i.e., attic floor) and top (i.e., ridge beam) levels of the gable, along with the corresponding elastic response spectra for a 5% viscous damping ratio.

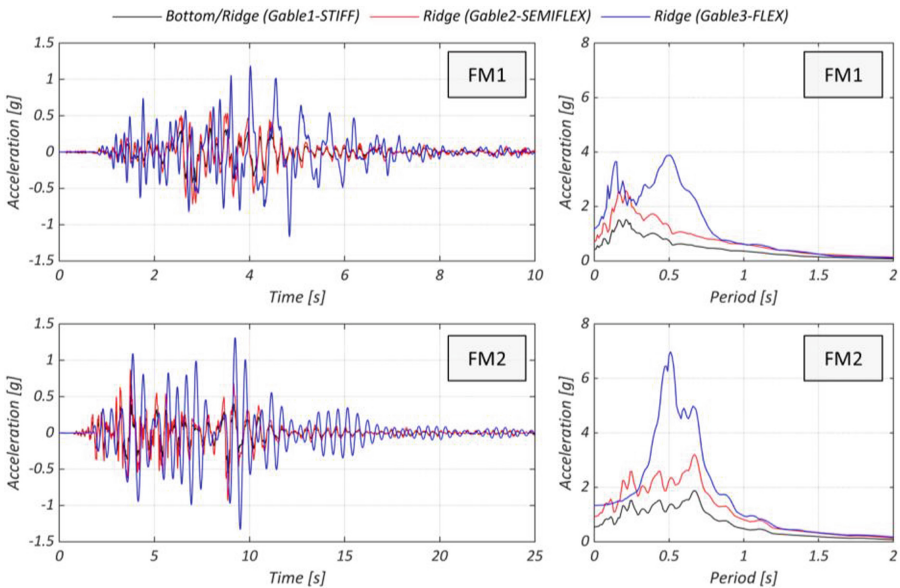


Fig. 5. Summary of acceleration time histories (left) and elastic response spectra (right).

4.3 Testing Protocols

The incremental dynamic test (IDT) for each gable specimen was conducted using both input signals: first the induced (FM1), followed by the tectonic (FM2), with a scaling factor (SF) linearly adjusted based on the bottom input signal. The parameters presented in Table 2, Table 3, and Table 4 include *PBA* (peak base acceleration), *PRA*

(peak ridge acceleration) and Δ_d (ridge beam displacement relative to the bottom shake table). Each of these values is reported both as the nominal (i.e., target theoretical) value corresponding to the input signals in Fig. 5 and as the experimentally recorded value. Moreover, the maximum displacement of a control point on the gable, $\max(d_{ctrl})$, is included. The location of the control point varied with the progression of damage. During the initial tests, before the collapse mechanism was activated, the control point was set at the barycenter of the gable. In later tests, as collapse mechanisms developed, it was relocated to the horizontal crack responsible for failure, which was specific to each gable. When this point was not directly instrumented, its location was determined through trigonometric calculations. Furthermore, all displacement calculations exclude any rigid displacement of the loading frame.

For Gable1-STIFF (Table 2), the nominal Δ_d was zero. However, this condition could not be replicated experimentally due to the difficulty in achieving perfectly simultaneous movement of the bottom and top shake tables. To proceed with the IDT, the tectonic record was scaled up to gable collapse to explore not only higher earthquake motion intensities but also signals with different frequencies and longer durations. It should be noted that for Gable3-FLEX, an additional shake-table test at 100% FM1 was conducted after Test #9 (i.e., the 100% FM2 run) to evaluate its ability to withstand an induced seismic motion after sustaining damage from tectonic motion.

Table 2. Testing sequence of Gable1-STIFF.

Test #	SF	Nom. PBA [g]	Rec. PBA [g]	Nom. PRA [g]	Rec PRA [g]	Nom. Δ_d [mm]	Rec Δ_d [mm]	$\max(d_{ctrl})$ [mm]	
1	FM1	10%	0.04	0.05	0.04	0.13	0	1.7	0.2
2		20%	0.08	0.08	0.08	0.19	0	1.6	0.4
3		30%	0.13	0.12	0.13	0.26	0	2.6	0.4
4		50%	0.21	0.19	0.21	0.39	0	4.6	0.5
5		75%	0.32	0.28	0.32	0.49	0	7.1	0.6
6		100%	0.42	0.37	0.42	0.61	0	8.9	0.7
7	FM2	50%	0.27	0.29	0.27	0.44	0	7.2	0.7
8		75%	0.41	0.43	0.41	0.53	0	10.5	0.8
9		100%	0.55	0.57	0.55	0.71	0	13.0	1.0
10		125%	0.69	0.69	0.69	0.84	0	16.4	1.3
11		150%	0.82	0.86	0.82	0.96	0	19.3	1.5
12		175%	0.96	1.03	0.96	1.19	0	23.3	1.9
13		200%	1.10	1.17	1.10	1.34	0	25.5	2.1
14		250%	1.38	1.51	1.38	1.64	0	31.8	5.5
15		300%	1.65	1.88	1.65	1.86	0	38.1	48.9
16		350%	1.93	1.80	1.93	2.56	0	34.8	collapse

Table 3. Testing sequence of Gable2-SEMIFLEX.

Test #		SF	Nom. PBA [g]	Rec. PBA [g]	Nom. PRA [g]	Rec PRA [g]	Nom. Δ_d [mm]	Rec Δ_d [mm]	max(d_{ctrl}) [mm]
1	FM1	10%	0.04	0.05	0.08	0.16	2.5	2.0	0.03
2		20%	0.08	0.08	0.16	0.29	5.1	4.4	0.1
3		30%	0.13	0.12	0.23	0.36	7.6	6.7	0.2
4		50%	0.21	0.20	0.39	0.45	12.7	10.6	0.3
5		75%	0.32	0.28	0.58	0.62	19.0	15.3	0.5
6		100%	0.42	0.38	0.78	0.81	25.3	19.9	0.7
7	FM2	50%	0.27	0.28	0.43	0.62	21.3	16.6	0.5
8		75%	0.41	0.42	0.64	0.93	31.9	24.1	0.8
9		100%	0.55	0.57	0.85	1.26	42.5	41.1	2.8
10		125%	0.69	0.71	1.06	1.46	53.2	50.5	4.9
11		150%	0.82	0.86	1.28	1.86	63.8	59.9	8.7
12		175%	0.96	1.00	1.49	2.15	74.4	71.2	29.9
13		200%	1.10	1.04	1.70	3.31	85.1	88.5	88.6

Table 4. Testing sequence of Gable3-FLEX.

Test #		SF	Nom. PBA [g]	Rec. PBA [g]	Nom. PRA [g]	Rec PRA [g]	Nom. Δ_d [mm]	Rec Δ_d [mm]	max(d_{ctrl}) [mm]
1	FM1	10%	0.04	0.05	0.12	0.31	5.7	5.9	0.3
2		20%	0.08	0.09	0.24	0.53	11.4	12.1	0.6
3		30%	0.13	0.13	0.36	0.55	17.0	16.0	0.8
4		50%	0.21	0.20	0.60	0.84	28.4	26.7	1.2
5		75%	0.32	0.28	0.90	1.10	42.6	39.8	2.3
6		100%	0.42	0.36	1.20	1.33	56.8	52.8	3.2
7	FM2	50%	0.27	0.28	0.65	0.79	41.1	40.4	2.4
8		75%	0.41	0.43	0.97	1.28	61.6	57.0	3.8
9		100%	0.55	0.57	1.30	1.91	82.2	85.9	30.2
10		125%	0.42	0.36	1.20	1.33	56.8	53.9	18.5
11		150%	0.69	0.70	1.62	2.34	102.7	107.5	33.4
12		175%	0.82	0.85	1.95	2.56	123.3	112.2	collapse

5 Incremental Dynamic Response

The main outcomes of the full-scale shake-table experiments are presented in Fig. 6 in terms of seismic capacity curves, for each gable specimen (Gable1-STIFF, Gable2-SEMFLEX, Gable3-FLEX). These curves depict the maximum displacement of the control point ($\max(d_{ctrl})$) versus the peak base acceleration (PBA), at each input scaling level.

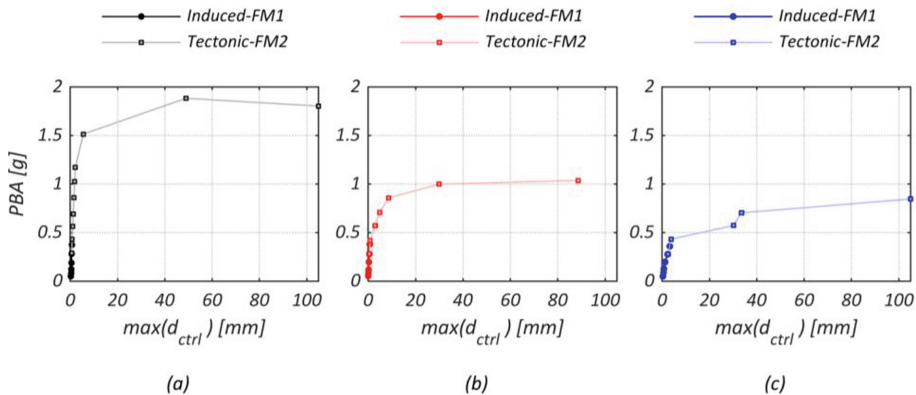


Fig. 6. Capacity curves for: (a) Gable1-STIFF, (b) Gable2-SEMFLEX, and (c) Gable3-FLEX.

Gable1-STIFF (Fig. 6a) exhibited an initial elastic behavior from Test #1 through Test #13, while a notable change in stiffness occurred in Test #14. Gable 2-SEMFLEX (Fig. 6b) remained seemingly elastic until Test #9, while collapse occurred at Test #13, corresponding to a scale factor of 200%. Finally, Gable 3-FLEX displayed elastic behavior until Test #8, but by Test #9, a shift in slope became apparent.

The influence of roof flexibility on the seismic response of URM gables is evident when comparing all three capacity curves. Gable3-FLEX demonstrated significantly lower seismic capacity and substantially greater flexibility, indicating higher vulnerability compared to the other configurations.

6 Conclusions

This paper presented an extensive experimental investigation into the out-of-plane (OOP) seismic behavior of unreinforced masonry (URM) gables through a full-scale shake-table testing campaign. The research was conducted at the EUCENTRE 9D LAB (Pavia, Italy), using an innovative dual shake-table configuration that simulated the interaction between URM gables and different roof diaphragm configurations. The primary aim behind this was to evaluate the seismic response of these structural elements and understand the influence of varying roof stiffness levels on their failure mechanisms.

The results, in terms of incremental dynamic response, demonstrate that roof diaphragm stiffness plays a key role in governing the seismic performance of URM

gables. The experimental results indicate that Gable1-STIFF, representing a stiff roof diaphragm, exhibited the highest resistance to OOP loading, minimizing differential displacements. Gable2-SEMIFLEX, simulating a semi-flexible roof, showed intermediate behavior, with lower resistance and earlier crack formation compared to the stiff configuration. Gable3-FLEX, representing a flexible roof diaphragm, had the lowest acceleration capacity, emphasizing the effects of reduced roof stiffness on gable wall stability. These findings confirm that flexible roof diaphragms amplify OOP displacements and increase masonry gable vulnerability.

This research advances seismic risk mitigation strategies for low-rise masonry structures. The insights gained provide a benchmark for improving code-based guidelines, building design, and retrofitting strategies in earthquake-prone regions worldwide.

Acknowledgements. This work is part of the transnational access project “ERIES-SUPREME”, supported by the Engineering Research Infrastructures for European Synergies (ERIES) project (www.ries.eu), which has received funding from the European Union’s Horizon Europe Framework Programme under Grant Agreement No. 101058684. This is ERIES publication number C64. Additional funds required beyond the scope of the ERIES grant for the realisation of the project were provided by the partner “TNO: Netherlands Organisation for Applied Scientific Research/Nederlandse Organisatie voor Toegepast Natuurwetenschappelijk Onderzoek”.

References

1. Ingham, J., Griffith, M.: Performance of unreinforced masonry buildings during the 2010 Darfield (Christchurch, NZ) earthquake. *Aust. J. Struct. Eng.* **11**(3), 207–224 (2010)
2. Dizhur, D., et al.: Performance of masonry buildings and churches in the 22 February 2011 Christchurch earthquake. *Bull. N. Z. Soc. Earthq. Eng.* **44**(4), 279–296 (2011)
3. Penna, A., Morandi, P., Rota, M., Manzini, C.F., Da Porto, F., Magenes, G.: Performance of masonry buildings during the Emilia 2012 earthquake. *Bull. Earthq. Eng.* **12**, 2255–2273 (2014)
4. Sorrentino, L., Liberatore, L., Liberatore, D., Masiani, R.: The behaviour of vernacular buildings in the 2012 Emilia earthquakes. *Bull. Earthq. Eng.* **12**, 2367–2382 (2014)
5. Graziotti, F., Tomassetti, U., Kallioras, S., Penna, A., Magenes, G.: Shaking table test on a full scale URM cavity wall building. *Bull. Earthq. Eng.* **15**, 5329–5364 (2017)
6. Kallioras, S., Correia, A.A., Graziotti, F., Penna, A., Magenes, G.: Collapse shake-table testing of a clay URM building with chimneys. *Bull. Earthq. Eng.* **18**(3), 1009–1048 (2019)
7. Candeias, P.X., Costa, A.C., Mendes, N., Costa, A.A., Lourenço, P.B.: Experimental assessment of the out-of-plane performance of masonry buildings through shaking table tests. *Int. J. Archit. Herit.* **11**(31), 31–58 (2016)
8. Tomassetti, U., Correia, A.A., Graziotti, F., Penna, A.: Seismic vulnerability of roof systems combining URM gable walls and timber diaphragms. *Earthquake Eng. Struct. Dynam.* **48**, 1297–1318 (2019)
9. Griffith, M.C., Lam, N.T.K., Wilson, J.L., Doherty, K.: Experimental investigation of unreinforced brick masonry walls in flexure. *J. Struct. Eng.* **130**(3), 423–432 (2004)
10. Penner, O., Elwood, K.J.: Out-of-plane dynamic stability of unreinforced masonry walls in one-way bending: Parametric study and assessment guidelines. *Earthq. Spectra* **32**, 1699–1723 (2016)
11. Giaretton, M., Dizhur, D., Ingham, J.M.: Dynamic testing of as-built clay brick unreinforced masonry parapets. *Eng. Struct.* **127**, 676–685 (2016)

12. Graziotti, F., Tomassetti, U., Penna, A., Magenes, G.: Out-of-plane shaking table tests on URM single leaf and cavity walls. *Eng. Struct.* **125**, 455–470 (2016)
13. Sharma, S., Tomassetti, U., Grottoli, L., Graziotti, F.: Two-way bending experimental response of URM walls subjected to combined horizontal and vertical seismic excitation. *Eng. Struct.* **219**, 110537 (2020)
14. Tomassetti, U., Grottoli, L., Sharma, S., Graziotti, F.: Dataset from dynamic shake-table testing of five full-scale single leaf and cavity URM walls subjected to out-of-plane two-way bending. *Data Brief* **24**, 103854 (2019)
15. Sharma, S., Grottoli, L., Tomassetti, U., Graziotti, F.: Dataset from shake-table testing of four full-scale URM walls in a two-way bending configuration subjected to combined out-of-plane horizontal and vertical excitation. *Data Brief* **31**, 105851 (2020)
16. Sharma, S., et al.: Experimental data from out-of-plane shake-table tests on unreinforced masonry gables. *Earthq. Spectra* (2025)
17. European Committee for Standardization (CEN): Methods of test for mortar for masonry. Part 11: Determination of flexural and compressive strength of hardened mortar. European Standard EN 1015-11, Brussels, Belgium (2006)
18. European Committee for Standardization (CEN): Methods of test for masonry units. Part 1: Determination of compressive strength. European Standard EN 772-1, Brussels, Belgium (2006)
19. European Committee for Standardization (CEN): Methods of test for masonry. Part 1: Determination of compressive strength. European Standard EN 1052-1, Brussels, Belgium (1998)
20. European Committee for Standardization (CEN): Methods of test for masonry. Part 5: Determination of bond strength by the Bond Wrench method. European Standard EN 1052-5, Brussels, Belgium (2005)
21. European Committee for Standardization (CEN): Methods of test for masonry units. Part 3: Determination of initial shear strength. European Standard EN 1052-3, Brussels, Belgium (2007)
22. Sharma, S., Graziotti, F., Magenes, G.: Torsional shear strength of unreinforced brick masonry bed joints. *Constr. Build. Mater.* **275**, 122053 (2021)
23. Mirra, M., Damiani, N., Sharma, S., Graziotti, F., Messali, F.: Definition of differential seismic input motions for out-of-plane dynamic testing of unreinforced masonry gable walls considering different roof configurations. *Structures* **79**, 109419 (2025). <https://doi.org/10.1016/j.istruc.2025.109419>

Open Access This chapter is licensed under the terms of the Creative Commons Attribution 4.0 International License (<http://creativecommons.org/licenses/by/4.0/>), which permits use, sharing, adaptation, distribution and reproduction in any medium or format, as long as you give appropriate credit to the original author(s) and the source, provide a link to the Creative Commons license and indicate if changes were made.

The images or other third party material in this chapter are included in the chapter's Creative Commons license, unless indicated otherwise in a credit line to the material. If material is not included in the chapter's Creative Commons license and your intended use is not permitted by statutory regulation or exceeds the permitted use, you will need to obtain permission directly from the copyright holder.





3D Shaking Table Tests of a Full Scale 2-Storey Building with Fiber-Reinforced Elastomeric Isolators

Daniele Losanno^{1(✉)}, S. Prakash¹, P. Medaglia¹, F. Parisi¹, Dimitrios Konstantinidis², Enrico Tubaldi³, Hamid Ahmadi⁴, A. Strauss⁵, D. De Domenico⁶, Dimitrios Vamvatsikos⁷, Christos Lachanas⁷, Michalis Vassiliou⁸, Filipe L. Ribeiro⁹, and Antonio A. Correia⁹

¹ University of Naples Federico II, Naples, Italy

daniele.losanno@unina.it

² University of California, Berkeley, CA, USA

³ University of Strathclyde, Stratchlyde, Scotland

⁴ Tun Abdul Razak Research Centre (TARRC), Hertford, UK

⁵ University of Natural Resources and Life Sciences, Vienna, Austria

⁶ University of Messina, Messina, Italy

⁷ National Technical University of Athen, Athens, Greece

⁸ ETH, Zurich, Switzerland

⁹ LNEC, Lisboa, Portugal

Abstract. During the last two decades fiber-reinforced elastomeric isolators (FREIs) emerged as a promising option to reduce both the cost and weight of rubber bearings. The project ERIES-FREISUST (Fiber-Reinforced Elastomeric Isolators for seismic resilient structures with SUSTainable Solutions) aims to demonstrate the reliability of FREIs in limiting damage to structural and non-structural components and contents. Two FREI systems were designed for a full-scale 2-story reinforced concrete (RC) infilled frame, differing in standardization and cost levels, namely a Virgin-rubber Carbon-fiber FREI (VC-FREI) and a Reclaimed-rubber Polyester-fiber FREI (RP-FREI). These isolation systems were installed in unbonded configuration at the base of the building and tested at the ST3D shaking table facility of Laboratorio Nacional de Engenharia Civil (LNEC), Lisbon, Portugal. The novel base-isolation systems demonstrated lateral stability and re-centering capability, as well as adequate vertical stiffness and load-bearing capacity under different ground motions. RP-FREIs were designed and tested up to a design displacement of 105mm corresponding to 150% shear strain. Due to recessing plates VC-FREIs were tested with higher scaling factors compared to RP-FREIs showing higher displacement capacity with negligible residual. The building had no minor damage after the whole testing sequence with contents undergoing limited accelerations and displacements thus ensuring functionality even after major earthquakes.

Keywords: Base Isolation · Unbonded Elastimeric Isolators · FREI · 3D Shaking Table Tests · Non Structural Components

1 Introduction

According to the UN's Office for Disaster Risk Reduction [1], the annual average deaths due to earthquakes (2001–2020) is approximately equal to 38,000, the highest number of deaths due to any natural hazard. Base isolation is widely accepted as one of the most effective seismic protection measures for both structural elements and nonstructural components, including building contents [2–6]. Conventional seismic isolators available on the market are too costly for common housing projects, thus preventing a large-scale application of the technology in both developed and developing countries of the world. Fiber-reinforced elastomeric isolators (FREIs) were developed recently with the aim to reduce both cost and weight of conventional steel-reinforced rubber bearings, by replacing the steel shims with fiber mesh fabrics [7, 8]. The unbonded configuration of FREIs nearly eliminates tensile stresses and the need for stringent bonding requirements within the isolator (Fig. 1a and 1b). Furthermore, it promotes roll-over, which reduces the effective lateral stiffness of the isolator and thus increases the isolation effectiveness (Fig. 1c).

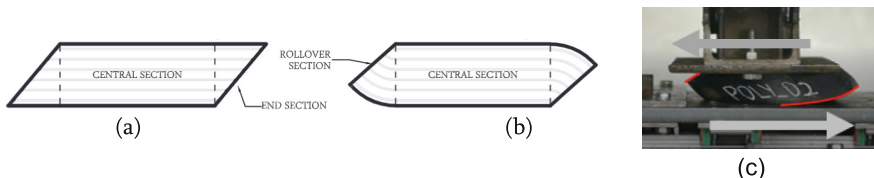


Fig. 1. a) Bonded versus b) unbonded isolator under lateral displacement; c) Roll-over of a prototype RP-FREI.

Previous studies investigated the effect of different rubber matrices and fabrics on small-size FREI prototypes in a number of experimental programs, including shaking table tests [9–16]. The Reclaimed-rubber Polyester-fiber FREI (RP-FREI) system (Fig. 1c) was recently developed [10] at the University of Naples Federico II in collaboration with ITALGUM (patent number 102022000013360). The reclaimed compound was subjected to a comprehensive physical and mechanical characterization, showing mechanical properties that are not significantly different from a soft virgin rubber with lower tensile deformation capacity. Preliminary characterization tests showed promising performance (lateral stability up to 150% shear strain and equivalent damping ratio up to 19%) and paved the way for the development of low-cost, environmental-friendly seismic isolators for housing buildings [10]. Along the same line, De Domenico et al. [17] recently carried out an extensive experimental characterization of two full-scale prototype FREIs under EN15129 [18] compliant protocols including bidirectional orbits up to maximum shear strain level of 100%.

Recent studies by Losanno et al. [19, 20] demonstrated that base isolation with FREIs can also be effective in reducing seismic fragility of one- and two-storey unreinforced masonry buildings in developing countries where a significant increase in new construction is expected in the coming years. Even though geometrical limitations imposed by

stability criteria for FREIs resulted in lower isolation period T_{is} (i.e. 1.3s to 1.7 s) compared to that considered for conventional design ($2.0 \leq T_{is} \leq 3.0$ s), FREIs proved to be an affordable solution for seismic protection of low-rise buildings.

It is in this context that the ERIES-FREISUST (*Fiber-Reinforced Elastomeric Isolators for seismic resilient structures with SUSTainable Solutions*) project was conceived to provide an increase of the Technology Readiness Level of FREIs, demonstrating the combined reliability of the base-isolation system (i.e. lateral stability and re-centering capacity as well as adequate vertical stiffness and load-bearing capacity under different loading conditions) and its potential in reducing damage to nonstructural components and contents. To the best of the authors' knowledge, no shaking table tests had been performed on a full-scale building prototype under different ground motion intensities that could lead to a standardization of the FREI technology. A limited number of reduced-scale shake table tests were conducted under horizontal excitation only [13–15, 21–23]. However insightful these tests were, a series of knowledge gaps and open issues remained to be addressed, including: 1) previous characterization tests were mainly carried out on scaled specimens without implementing seismic records that are actually representative of site-specific hazard, 2) there is a need to investigate whether these bearings can provide enough isolation capacity to both structural and nonstructural building components in case of limited mass of the superstructure, 3) more experimental data is needed to model the complex hysteretic behaviour of FREIs experiencing roll-over under lateral deformation. This is of paramount importance in light of the European Green Deal and the development of the next generation of standards for anti-seismic devices EN15129 and structural bearings EN1337–3 [24], which may include specific recommendations for use of FREIs.

2 Experimental Program

Within FREISUST project a relevant number of 3D shaking table tests have been performed at LNEC (Lisbon, Portugal) on a full-scale prototype subjected to three simultaneous components of the ground motion. The size of the ST3D shaking table at LNEC (5.6mx6.4m) made it possible to test, for the first time, a full-scale frame isolated with FREIs under combined horizontal and vertical ground motions, including independent excitations of various types (sinusoidal, random, shock and seismic ground motion) and vertical component.

The project aims to evaluate the effectiveness of two FREI base isolation systems for enhanced seismic resilience of new or existing buildings: (1) a Virgin-rubber Carbon-fiber FREI (VC-FREI) base isolation system, and (2) a RP-FREI base isolation system. Among these two systems, the first one is more prone to standardization due to the improved axial stiffness, rubber and reinforcement properties. With a lower cost and environmental impact of both the reclaimed rubber compound and polyester reinforcement (i.e. commonly adopted in the textile industry), RP-FREI system represents an eco-friendly, cheaper and more sustainable solution than VC-FREI and can be a very good option for developing countries where people still live in unsafe buildings designed and built with no seismic provisions in mind. The focus of the project is on both structural and nonstructural components (infill masonry wall, plasterboard partition system,

contents and equipment) of buildings under horizontal and vertical ground motions of increasing intensity.

2.1 Description of the Prototype

The prototype building (Fig. 2a and 2b) consists of a three-dimensional two-storey one-bay square-plan RC frame. The frame is provided with masonry infills and plasterboards along the two main directions (X and Y, respectively) as shown in Fig. 2, and tested on two base isolation systems (Fig. 2b and 2c). The prototype was mounted on four FREIs (RP-FREIs first, then VC-FREIs) installed in unbonded configuration beneath the corner columns. The replacement of the base isolation is executed through proper uplift at the foundation level.

With regard to the bearings' characteristics (Fig. 2c), the VC-FREI system consists of alternated layers of virgin rubber and quadri-axial carbon fabric and is characterized by higher compression modulus compared to RP-FREI where biaxial polyester fabric is adopted. Due to different fabric thickness the two isolators measured different height, namely 80 mm and 95 mm for RP-FREI and VC-FREI, respectively.

Even if previous tests demonstrated that rubber-concrete friction would prevent any sliding of the isolators, a recessed configuration (e.g. two additional steel plates for each bearing installed beneath the base beam and above the table with a central hole having the bearing diameter) was adopted for VC-FREIs to comply with EN15129 fixing methods for transmission of lateral force. For ease of installation and further reduction in construction cost, no recess was provided to the RP-FREIs in order to assess the adequacy of a friction-only restraint for the isolators.

The RC frame had been designed as non-dissipative structure according to EN1992–1-1 [25] and EN1998–1 [26] to be more representative of existing buildings. It has plan dimensions of 4.0 m × 4.0 m and a storey height of 2.70 m. The class of concrete is of medium compressive strength (e.g. C28/35 strength class). The columns have square section of 35 cm × 35 cm and are reinforced with B450 steel rebars. The beams' cross section is 30 cm × 40 cm in size, whereas the slab is 12 cm-thick and is reinforced with a double-layer welded wire mesh. The total weight of the 2-storey infilled frame is equal to 40t including the ring beam and nonstructural components. Ring beams at the base (with, e.g., 35 cm x 60 cm section) provided adequate stiffness under horizontal excitation as well as vertical stiffness under lifting and handling operations. The frame had no special foundation since it rests on four FREIs transferring horizontal force by friction. In this regard, a concrete-filled plate was installed on the shaking table providing realistic friction conditions of rubber-concrete type. Two different infill systems were tested along the two horizontal directions. In one direction (X), a single-leaf, around 20-cm thick, hollow-clay brick wall was considered, which is very common in Europe also for its thermal insulation properties. Hollow clay bricks with vertical and horizontal holes were adopted for the first and the second storey, respectively. In the other direction (Y), a plasterboard partition system was installed as a lower-weight and more versatile internal partition alternative. The infills have been tested both in-plane and out-of-plane due to the biaxial horizontal excitation. Nonstructural elements installation at the first-storey consisted in common housing and office contents, including a closet, a desk with a computer and a suspended pipe.

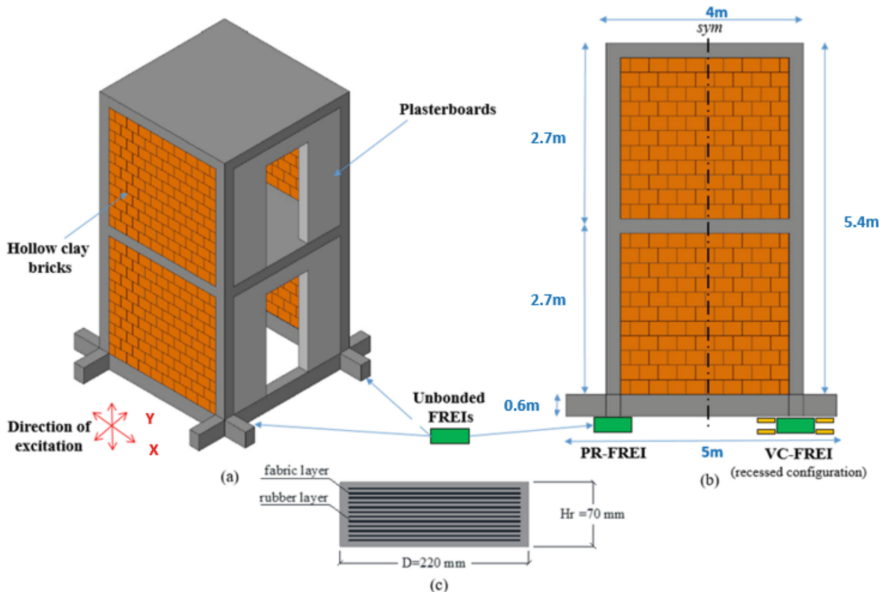


Fig. 2. a) 3D view and b) side view geometric details of the prototype, c) FREI cross section (VC-FREI and PR-FREI).

A numerical model of the building considering the infill systems provided a fundamental period of 0.15 s and 0.07 s along Y and X directions, respectively. It can be noted that masonry infills along X provide a significant contribution to the lateral stiffness of the bare frame, resulting in a period approximately 50% lower than the bare frame.

2.2 Base Isolation Design

Preliminary design of the base isolation system considering a superstructure mass of 40t resulted in 4 FREIs with 220mm diameter and 70mm total rubber height and a second shape factor around 3.0 as per stability requirements [27, 28]. Assuming a soft compound ($G = 0.4\text{MPa}$ at a shear deformation γ of 150%) and a 30% reduction of the contact area at ultimate limit state due to roll-over [14], the equivalent isolation period T_{is} was set at 1.6 s, corresponding to an equivalent stiffness of 600 kN/m of the isolation system (150 kN/m per unit). A target displacement of 105 mm corresponding to $\gamma = 150\%$ shear strain (i.e. prior to full roll-over) was assumed. In terms of hazard level, a spectral demand of 150mm would be obtained for T_{is} and a 5% equivalent damping ratio; consequently, the target displacement is consistent with this value accounting for damping reduction factor as per EN1998-1 (equal to 0.7 for 15% damping ratio). Such hazard level is deemed representative of high seismicity regions in Italy with a 5% probability of exceedance in 50 years. Full roll-over (at around 200% shear strain) could be achieved under very-rare events (e.g. maximum-considered earthquake, MCE) but in order to prevent damage this condition was tested at the last stage of the testing protocol for VC-FREIs with recessed configuration only.

For preliminary characterization two specimens for each system were tested under compression and shear-compression protocols. Tests were performed at the University of Naples Federico II to evaluate axial stiffness and hysteretic behaviour of FREIs providing useful data for bearing model calibration and ground motion selection. Equivalent horizontal stiffness and damping ratios for different strain levels γ ($= u/t_r$) up to 150% are reported in Fig. 3. It can be noted that at $\gamma = 150\%$ RP-FREI finely matched the target stiffness and damping ratios whilst VC-FREI resulted more flexible due to lower aspect ratio with around 20% higher damping capacity.

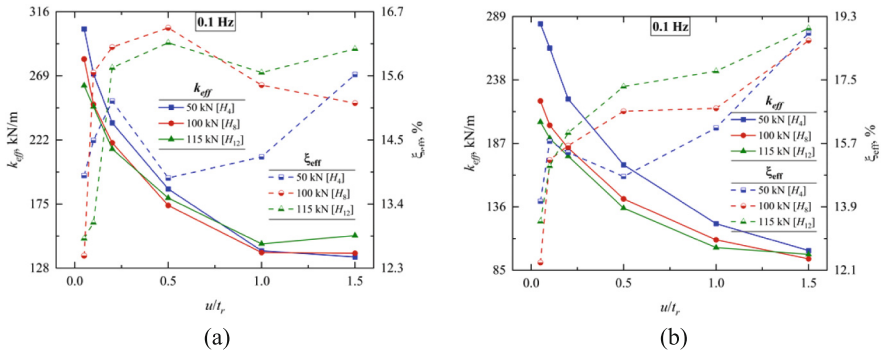


Fig. 3. Equivalent shear properties of the isolators: (a) RP-FREI and (b) VC-FREI.

3 Ground Motion Selection

A targeted selection of natural ground motions from the PEER NGA strong motion database [29, 30] was performed. The selection was conditioned on the spectral characteristics of the ground motions seeking for ground motions that matches with relatively low scaling (i.e., scale factors close to 1) the spectral displacement of the isolated structure for the target hazard level. At the same time, records of different characteristics in terms of the intensity correlation between the horizontal components and the inherent characteristics of the ground motions (pulse-like, non-pulse-like) were searched in order to investigate the response of the isolators and the isolated structure under different conditions of shaking. In all cases for the scaled selected ground motions the peak acceleration, velocity, and displacement values had to be lower than the limits of the shaking table.

After setting the criteria for the selection, ground motions were searched in the NGA-West1 database. Specifically, assuming as target the 5% damped spectral displacement for the equivalent period of the specimen, S_d (1.6 s, 5%) = 150 mm, ground motions were searched with at least one of the two horizontal components the S_d (1.6 s, 5%) matching this value with low scaling. To avoid selecting ground motions with a local peak of the spectral displacement at 1.6s an extra check was imported to ensure that the peak is long enough in case the actual period of the specimen is in the range ± 0.2 s. Both non-pulse-like and pulse-like ground motions were searched. For the latter the ground

motions that were identified as pulse-like by Shahi and Baker [31] were employed as the baseline list for the search.

Three ground motions that met the predefined criteria for the selection were chosen for the test. Two of them are non-pulse-like ground motions which depict the most common type of earthquake shaking during the lifetime of a structure. The first one (Loma Prieta 1989 event) refers to a strong ground motion where the horizontal component scaled to the targeted displacement (assigned in X-direction) is considerably stronger than the other (assigned in Y-direction). For the second (Kobe 1995 event) similar intensity in terms of the peak values of the ground acceleration and velocity is shown between the two horizontal components. The last selected ground motion refers to a pulse-like ground motion record from the Jiashi 1997 earthquake. This ground motion was selected because the period of the extracted pulse in the direction of the stronger observed pulse was close to the equivalent period of the specimen ($T_p = 1.09$ s). Before assigned to the structural model and the specimen the horizontal components of the pulse-like ground motion were rotated accordingly to the orientation of the strongest observed pulse [32]. In all cases, a uniform scale factor close to 1.00 (in between 0.90 and 1.20) was assumed for the two horizontal and the vertical component per record. The unscaled acceleration and displacement ground motion response spectra of the X components for 5% damping are reported in Fig. 4.

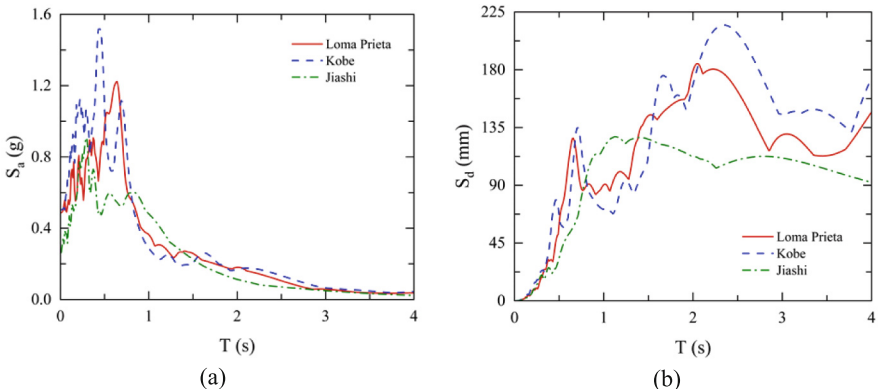


Fig. 4. Response spectra of selected ground motions: (a) acceleration and (b) displacement.

Numerical analysis of the isolated prototype was then performed by taking into account the behavior of the isolator through a non-linear Bouc-Wen model, in order to finely tune the scale factors by additional correction factors. The final values of the scale factors were assumed equal to 1.04, 1.15 and 1.26 for Jiashi, Loma Prieta and Kobe records, respectively. Hereafter the scaled ground motions will be referred as target level corresponding to 100% intensity level.

4 Shaking Table Tests

4.1 Test Program

The base isolated building was built and tested at LNEC (Fig. 5). Input random noise was used to characterize the dynamic properties of the system under service conditions, as well as to monitor its changes during the test. The test sequence comprised 107 steps in between shake table operation, calibration, dynamic identification, seismic test and specimen preparation. Before testing the base isolated configuration, a characterization of the fixed-base prototype was run under free vibration. Additional characterization and sine sweep tests were run for the base isolated prototype which are outside the scope of this paper. Imposed ground motions at different intensity levels for RP-FREI and VC-FREI are listed in Table 1. In a few runs tridirectional motions were imposed while in other cases only unidirectional or bidirectional components were applied for the sake of comparison in terms of multi-axial coupling and uni-axial response of FREIs to complement previous experimental findings from the literature [17].

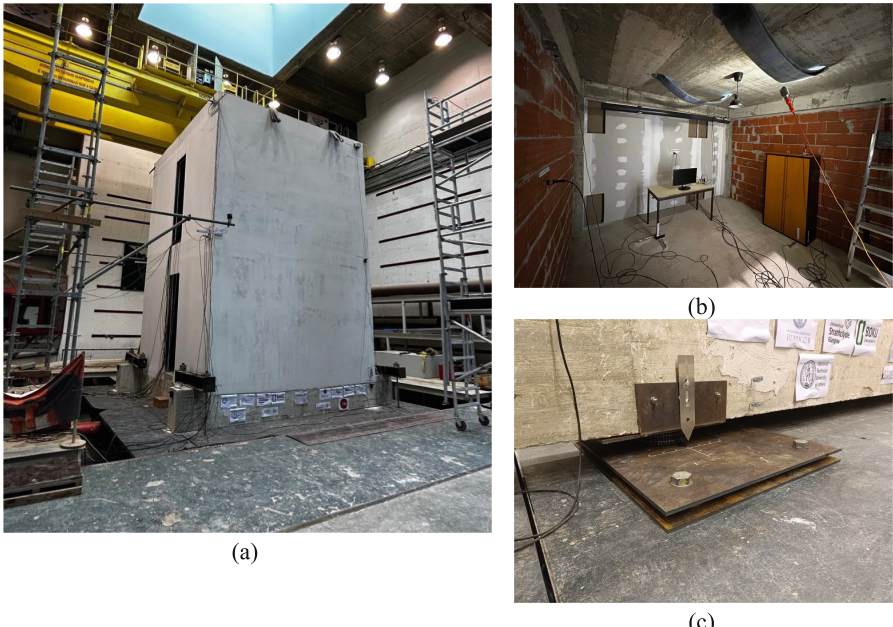


Fig. 5. (a) View of the prototype fixed at the base, (b) contents installed at the second storey, (c) VC-FREI system.

In case of VC-FREI the scaling factors for Kobe and Jiashi were further increased beyond 100% to trigger higher displacements and demonstrate higher stability limits by 20% and 25%, respectively.

In this paper experimental response under highest intensity levels (test runs **bold** in Table 1) have been considered for the sake of brevity.

Table 1. Test matrix for selected ground motions.

System	Input	Intensity	dir	System	Input	Intensity	dir
RP-FREI	Loma Prieta	50%	X	VC-FREI	Loma Prieta	50%	X
		50%	XY			50%	XYZ
		50%	XYZ			75%	X
		75%	X			75%	XY
		75%	XY			100%	XY
		100%	XY		Jiashi	50%	X
	Jiashi	50%	X			50%	XY
		50%	XY			50%	XYZ
		50%	XYZ			100%	XY
		75%	X			100%	XYZ
		75%	XYZ		Kobe	50%	X
		100%	XY			50%	XY
		100%	XYZ			50%	XYZ
	Kobe	50%	X			100%	XY
		50%	XY			100%	XYZ
		50%	XYZ			120%	XYZ
		75%	XYZ		Jiashi	125%	XYZ
		100%	XY				
		100%	XYZ				

4.2 Instrumentation Layout

Absolute horizontal displacements and accelerations at every floor were recorded for monitoring the response of the prototype (Fig. 6a and 6b). Relative displacements of the infills were recorded along both diagonals and across adjacent columns and beams. Vertical displacements at the base corners of the prototype were monitored through LVDTs to detect the rocking behavior due to compliance of the bearings. A few additional displacement and acceleration sensors were installed on the contents at the first floor. The instrumentation used included 32 accelerometers, 4 optical transducers, 15 LVDTs and 9 wire potentiometers for a total of 64 available channels.

The following preliminary results mainly refer to displacement measures of the experimental layout.

4.3 Base Isolation Performance

FREIs performed in a stable manner under all the tests attaining peak displacements (i.e. combining X and Y components) of 103 mm and 130 mm corresponding to 147% and 186% shear strain in case of RP-FREI (Fig. 7a) and VC-FREI (Fig. 7b), respectively.

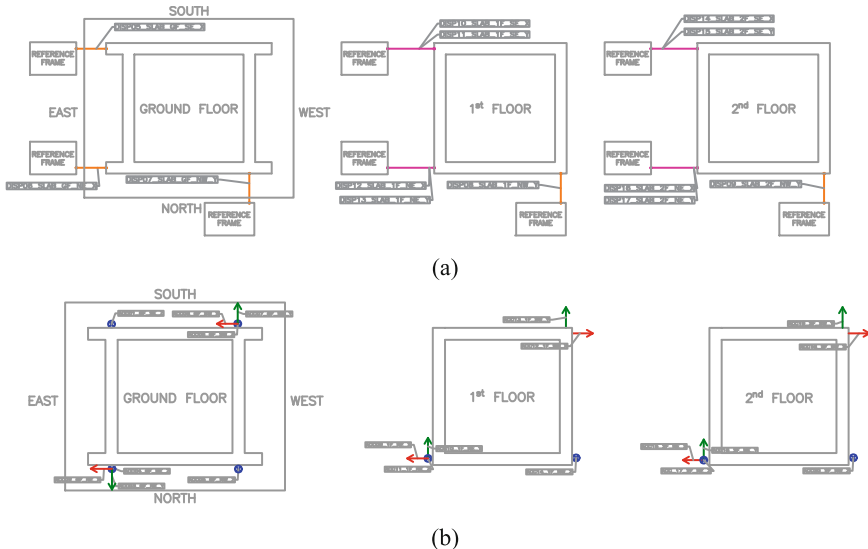


Fig. 6. Layout of (a) horizontal displacement transducers and (b) accelerometers.

Figure 7a and Fig. 7b show the picture of the devices at peak displacement under Jiashi 100% and Jiashi 125% for RP-FREI and VC-FREI, respectively.

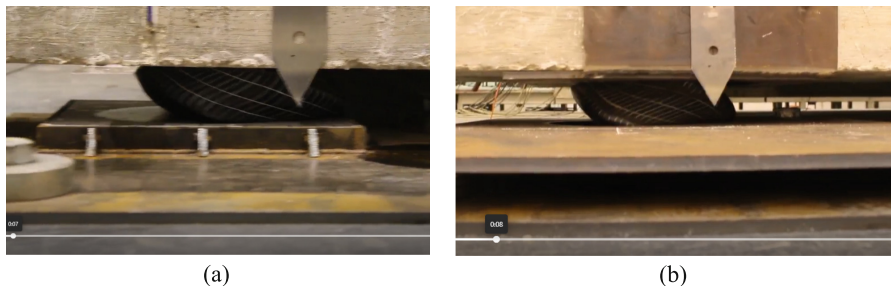


Fig. 7. Videoframe at peak displacement: (a) RP-FREI under Jiashi 100% and (b) VC-FREI under Jiashi 125%.

When imposing Jiashi 100% the same total displacement was obtained perfectly matching the design target of 105 mm for both RP-FREI (Fig. 8a) and VC-FREI (Fig. 8b).

Even under significant roll-over, FREIs demonstrated remarkable recentering behavior. After completing the test sequence and removing the isolation units no significant damage was detected on the bearings.

4.4 Superstructure Response

Base isolation effectiveness was measured both in terms of inter-storey drifts and peak accelerations.

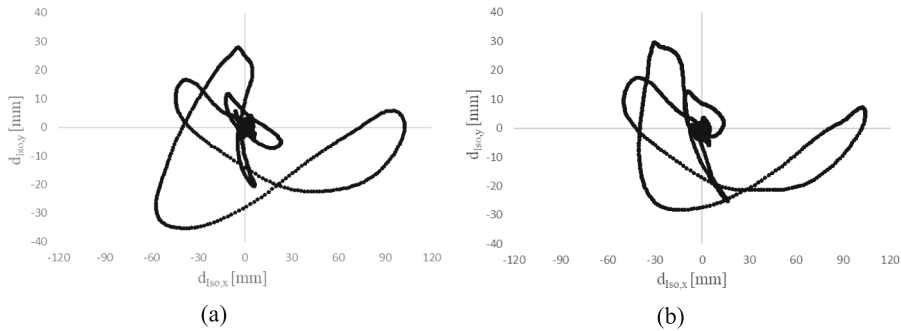


Fig. 8. Isolator displacements under Jiashi 100%: (a) RP-FREI and (b) VC-FREI.

In plane horizontal rotation angle above the foundation level (α) was calculated due to horizontal relative displacement between two points: values of α_{\max} were generally of the order of 1×10^{-3} implying minimum torsional behavior of the prototype (Fig. 9a).

Due to higher axial compliance of FREIs compared to steel laminated bearings, amplification of lateral response due to rocking was properly investigated. Rocking motion was measured in terms of rigid rotation (η) in the vertical plane and set equal to the relative vertical displacement at the base corners over the relative distance between measurement points. Under different ground motions η_{\max} was measured between 0.04% and 0.14% (Fig. 9b) corresponding to storey drifts of the order of a few millimeters.

For VC-FREI under Jiashi 125% and Kobe 120% both α and η attained significantly higher values compared to 100% intensity level thus requiring further analyses which fall outside the scope of this paper.

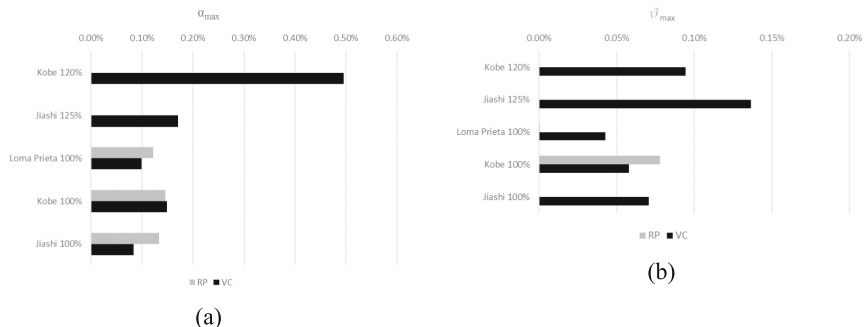


Fig. 9. Maximum rotations: (a) in horizontal and (b) vertical plan.

The rocking component may turn into higher storey drifts [33, 34] and has to be filtered out when considering the bending mode of the frame providing the inter-storey drift ratio (IDR) as a measure of potential damage. Second storey drifts are plotted in Fig. 10a and 10b for RP-FREI and VC-FERI under Kobe 100%. The influence of rocking is of the order of 2 mm and 1.5 mm for RP-FREI and VC-FERI, respectively. It can be noted that the drift time-history for RP-FREI shows some spikes especially after 15 s

thus requiring further analysis. Corresponding IDRs are of the order of 0.50% which may have triggered slight damage to the prototype that was not confirmed by visual inspection. Further processing of signals will be developed to detect any measurement error of the monitoring system.

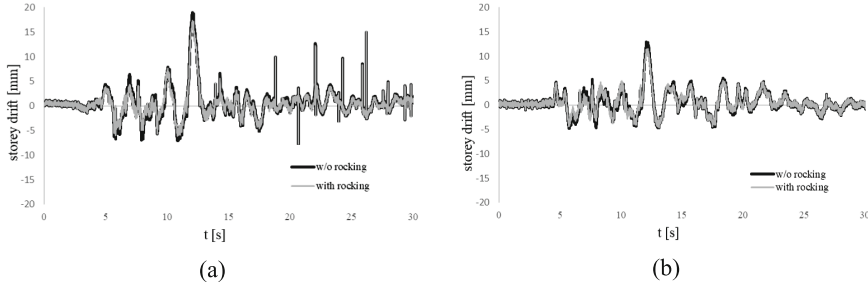


Fig. 10. Storey drift time-histories under Kobe 100%: (a) RP-FREI and (b) VC-FREI.

Imposed peak ground accelerations (PGA) along X and Y were in the range of 0.25 g to 0.90 g for the considered intensity levels. Peak floor accelerations (PFA) at the top of the building were normalized to PGA in order to check the filtering effect of the isolation system (Fig. 11a and 11b). This ratio was found always lower than one, with a peak value close to 0.8 for both systems up to 100% intensity level. It is worth mentioning that under the same intensity level, VC-FREI tends to provide slightly lower relative accelerations due to higher isolation effectiveness.

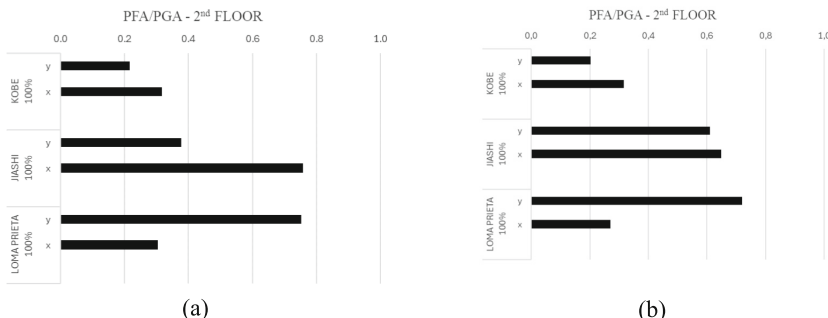


Fig. 11. Maximum top floor accelerations compared to PGA for (a) RP-FREI and (b) VC-FREI.

Non-structural components experienced no visible damage after the whole shaking sequence. In terms of contents, maximum displacement of the table was around 20mm along both X and Y, while the closet did not experience significant movement. The monitor on the table did not overturn: it was found in right position a few centimeters away from its original print marked on the table. The suspended pipe did not show any distress.

5 Conclusions

The FREISUST project demonstrated that FREIs can provide a fundamental period shift and protection of nonstructural components and contents, thereby significantly improving the seismic resilience of low-rise normal importance buildings. This goal was pursued through both innovative (e.g. carbon fabric) and low-cost eco-friendly materials (e.g. reclaimed rubber and polyester fabric). The 3D shaking table tests on a 2-storey full-scale prototype provided the required validation of FREI technology paving the way for EU standardization and implementation in the next-generation set of standards for anti-seismic devices (e.g. EN15129).

The isolators were designed for a target shear deformation of 150% with their geometry capable to ensure lateral stability up to 200% in case of very rare earthquakes. Although the target isolation period was lower than 2.0s for stability limits, under three lightly scaled real ground motions the superstructure experienced limited accelerations due to adequate filtering effect of the base isolation system. Maximum displacements of the isolation units perfectly matched design levels confirming the high potential of FREIs for low to mid-rise buildings under peak ground accelerations as high as 0.9 g.

The project will have both scientific and practical impact related to the development and validation of innovative base isolation with FREIs through the protection of societies and citizens.

Acknowledgements. This work is part of the transnational access project “ERIES- FREISUST”, supported by the Engineering Research Infrastructures for European Synergies (ERIES) project (www.ries.eu), which has received funding from the European Union’s Horizon Europe Framework Programme under Grant Agreement No. 101058684. This is ERIES publication number C8.

References

1. United Nations Office for Disaster Risk Reduction Homepage. <https://www.undrri.org/>. Accessed 14 Mar 2025
2. Yang, T.Y., Konstantinidis, D., Kelly, J.M.: The influence of isolator hysteresis on equipment performance in seismic isolated buildings. *Earthq. Spectra* **26**(1), 275–293 (2010)
3. Kelly, J.M., Konstantinidis, D.: Mechanics of Rubber Bearings for Seismic and Vibration Isolation. John Wiley and Sons, Chichester, UK (2011)
4. Vassiliou, M.F., Makris, N.: Analysis of the rocking response of rigid blocks standing free on a seismically isolated base. *Earthquake Eng. Struct. Dynam.* **41**(2), 177–196 (2012)
5. Konstantinidis, D., Nikfar, S.: Seismic performance of sliding contents in base-isolated building. In: Proceedings of the 10th US National Conference in Earthquake Engineering, Alaska, USA, July 21–25 (2014)
6. Nikfar, F., Konstantinidis, D.: Experimental study on the seismic response of equipment on wheels and casters in base-isolated hospitals. *J. Struct. Eng.* **145**(3), 04019001 (2019)
7. Konstantinidis, D., Kelly, J.M.: Two low-cost seismic isolation systems. In: Proceedings of the 15th World Conference on Earthquake Engineering, Lisbon, Portugal, September 24–28 (2012)

8. Konstantinidis, D., Kelly, J.M.: Advances in low-cost seismic isolation with rubber. In: Proceedings of the 10th US National Conference in Earthquake Engineering, Alaska, USA, July 21–25 (2014)
9. Van Engelen, N.C., Konstantinidis, D., Tait, M.J.: Structural and nonstructural performance of a seismically isolated building using stable unbonded fiber-reinforced elastomeric isolators. *Earthquake Eng. Struct. Dynam.* **45**(3), 421–439 (2016)
10. Cilento, F., Losanno, D., Piga, L.: An experimental study on a novel reclaimed rubber compound for fiber-reinforced seismic isolators. *Structures* **45**, 9–22 (2022)
11. Ruano, P.C., Strauss, A.: An experimental study on unbonded circular fiber reinforced elastomeric bearings. *Eng. Struct.* **177**, 72–84 (2018)
12. Strauss, A., Apostolidi, E., Zimmermann, T., Gerhaher, U., Dritsos, S.: Experimental investigations of fiber and steel reinforced elastomeric bearings: Shear modulus and damping coefficient. *Eng. Struct.* **75**, 402–413 (2014)
13. Losanno, D., Spizzuoco, M., Calabrese, A.: Bidirectional shaking table tests of unbonded recycled rubber fiber reinforced bearings (RR-FRBs). *Struct. Control. Health Monit.* **26**(9), e2386 (2019)
14. Losanno, D., Madera Sierra, I.E., Spizzuoco, M., Marulanda, J., Thomson, P.: Experimental assessment and analytical modeling of novel fiber-reinforced isolators in unbounded configuration. *Compos. Struct.* **212**, 66–82 (2019)
15. Losanno, D., Madera Sierra, I.E., Spizzuoco, M., Marulanda, J., Thomson, P.: Experimental performance of unbonded polyester and carbon fiber reinforced elastomeric isolators under bidirectional seismic excitation. *Eng. Struct.* **209**, 110003 (2020)
16. Calabrese, A., Losanno, D., Spizzuoco, M., Strano, S., Terzo, M.: Recycled rubber fiber reinforced bearings (rr-frbs) as base isolators for residential buildings in developing countries: the demonstration building of pasir badak. Indonesia, *Eng. Structures* **192**, 126–144 (2019)
17. De Domenico, D., Losanno, D., Vaiana, N.: Experimental tests and numerical modeling of full-scale unbonded fiber reinforced elastomeric isolators (UFREIs) under bidirectional excitation. *Eng. Struct.* **274**, 115118 (2023)
18. CEN (2009) EN 15129. Anti-seismic devices. European Committee for Standardization, Comité Européen de Normalisation, Brussels, Belgium (2009)
19. Losanno, D., Ravichandran, N., Parisi, F., Calabrese, A., Serino, G.: Seismic performance of a low-cost base isolation system for unreinforced brick masonry buildings in developing countries. *Soil Dyn. Earthq. Eng.* **141**, 106501 (2021)
20. Losanno, D., Ravichandran, N., Parisi, F.: Seismic fragility models for base-isolated unreinforced masonry buildings with fibre-reinforced elastomeric isolators. *Earthquake Eng. Struct. Dynam.* **2022**, 1–27 (2023)
21. Calabrese, A., Spizzuoco, M., Serino, G., Della Corte, G., Maddaloni, G.: Shaking table investigation of a novel, low-cost, base isolation technology using recycled rubber. *Struct. Control. Health Monit.* **22**(1), 107–122 (2015)
22. Das, A., Deb, S.K., Dutta, A.: Shake table testing of un-reinforced brick masonry building test model isolated by U-FREI. *Earthquake Eng. Struct. Dynam.* **45**(2), 253–272 (2016)
23. Toopchi-Nezhad, H., Tait, M.J., Drysdale, R.G.: Shake table study on an ordinary low-rise building seismically isolated with SU-FREIs (stable unbonded-fiber reinforced elastomeric isolators). *Earthquake Eng. Struct. Dynam.* **38**(11), 1335–1357 (2009)
24. CEN (2005) EN 1337–3. Structural bearings - Part 3: Elastomeric bearings, European Committee for Standardization, Comité Européen de Normalisation, Brussels, Belgium
25. CEN (2004a) EN 1992–1–1:2004. Eurocode 2: Design of concrete structures - Part 1–1: General rules and rules for buildings, Comité Européen de Normalisation, Brussels, Belgium
26. CEN (2004b) EN 1998–1:2004. Eurocode 8: Design of structures for earthquake resistance - Part 1: General rules, seismic actions and rules for buildings, Comité Européen de Normalisation, Brussels, Belgium

27. Galano, S., Calabrese, A., Losanno, D.: On the response of fiber reinforced elastomeric isolators (FREIs) under bidirectional shear loads. *Structures* **34**, 2340–2354 (2021)
28. Galano, S., Losanno, D., Calabrese, A.: Stability analysis of unbonded fiber reinforced isolators of square shape. *Eng. Struct.* **245**, 112846 (2021)
29. Chiou, B., Darragh, R., Gregor, N., Silva, W.: NGA project strong-motion database. *Earthq. Spectra* **24**(1), 23–44 (2008)
30. PEER Ground Motion Database Homepage, <https://ngawest2.berkeley.edu/>. Accessed 14 Mar 2025
31. Shahi, S.K., Baker, J.W.: An efficient algorithm to identify strong velocity pulses in multi-component ground motions. *Bull. Seismol. Soc. Am.* **104**(5), 2456–2466 (2014)
32. Giannopoulos, D., Vamvatsikos, D.: Ground motion records for seismic performance assessment: to rotate or not to rotate? *Earthquake Eng. Struct. Dynam.* **47**(12), 2410–2425 (2018)
33. Orfeo, A., Tubaldi, E., Murh, A.H., Losanno, D.: Mechanical behaviour of rubber bearings with low shape factor. *Eng. Struct.* **266**1, 114532 (2022)
34. Orfeo, A., Tubaldi, E., Murh, A.H., Losanno, D.: Dynamic behaviour and seismic response of structures isolated with low shape factor bearings. *Earthquake Eng. Struct. Dynam.* **52**(12), 3765–3787 (2023)

Open Access This chapter is licensed under the terms of the Creative Commons Attribution 4.0 International License (<http://creativecommons.org/licenses/by/4.0/>), which permits use, sharing, adaptation, distribution and reproduction in any medium or format, as long as you give appropriate credit to the original author(s) and the source, provide a link to the Creative Commons license and indicate if changes were made.

The images or other third party material in this chapter are included in the chapter's Creative Commons license, unless indicated otherwise in a credit line to the material. If material is not included in the chapter's Creative Commons license and your intended use is not permitted by statutory regulation or exceeds the permitted use, you will need to obtain permission directly from the copyright holder.



Author Index

A

- Abbiati, Giuseppe 194
Adam, Christoph 194
Adamek, Kimberley 54
Ahmadi, Hamid 144, 280
Aloisio, Angelo 170
Álvarez, Antonio J. 54, 64
Amendola, Chiara 125
Anastasiadis, Anastasios 125
Andrewartha, Tristan 29
Angeli, Albino 255
Anna, Bagnara 74
Anoyatis, George 125
Avossa, Alberto Maria 44

B

- Bakalis, Konstantinos 194
Bal, İhsan E. 170
Barbosa, Andrea R. 243
Bartolotti, Andrea 255
Becker, T. C. 182
Beeck, Jeroen van 54
Bento, Rita 217
Bertassi, Marta 268
Birhane, Tibebu 54
Bitsuamlak, Girma 54
Bogdanovic, Aleksandra 144, 230
Bojadjieva, Julijana 144, 230
Bošković, Matija 144
Bouchet, Jean-Paul 1, 105
Bousias, Stathis 159, 170, 255
Burlando, Massimiliano 1, 21
Butenweg, Christoph 144

C

- Calvi, P. M. 182
Camila, Aldereguía Sánchez 74
Canepa, Federico 1
Castro, Felipe Sanchez 29

- Cesaro, Raffaele 125
Chalarca, B. 182
Chatzidaki, Akrivi 194
Clavelo, Bruno 14
Coronelli, Dario 206
Correia, Antonio A. 243, 280
Crewe, Adam 170
Cucuzza, Raffaele 230

D

- D’Aniello, Mario 159
Dacarro, F. 182
Damiani, Nicolò 255, 268
de Almeida, João Pacheco 132, 206
de Brito, Jorge 206
De Domenico, D. 280
de Sanctis, Luca 125
Delladonna, Filippo 194
Delpach, Philippe 1, 105
Dhir, Prateek 144
Di Benedetto, Sabatino 243
Di Laora, Raffaele 125
Di Sarno, Luigi 159
Diburg, Susanne 105
Dizhur, Dmytro 255
Doerffer, Krzysztof 118
Doerffer, Piotr 118
Domaneschi, Marco 230

E

- Edoardo, Ruffini 74
Elena, Vivian 14
Elettore, Elena 243
Eltayesh, Abdelgalil 118

F

- Fabbri, Giuseppe 194
Faria, Duarte 206
Federica, Tubino 74

Filoglou, Eleni 125
 Fiorillo, Fausta 206
 Flamand, Olivier 1, 95, 105
 Formisano, Antonio 230
 Francavilla, Antonella B. 243
 Francois, Stjin 125
 Freddi, Fabio 144, 159, 243

G

Gabbianelli, G. 182
 Gams, Matija 144
 Garcia-Ramonda, Larisa 217
 Gauducheau, Bruno 105
 Gillmeier, Stefanie 29, 83
 Giongo, Ivan 255
 Giusti, Alessandro 95
 Gökçe, Tansu 170
 Grant, Damian N. 243
 Graziotti, Francesco 217, 255, 268
 Grisogono, Branko 21
 Grzelak, Joanna 118
 Guerrini, Gabriele 217
 Guibert, Anthony 1
 Gutiérrez-Urzúa, Fernando 243

H

Halvonik, Jaroslav 206
 Hangan, Horia 1
 Hoelscher, Norbert 105
 Hoult, Ryan 132
 Hristov, Petar O. 83

I

Ivančić, Ivana 21
 Ivanovski, Dejan 230

J

Jayakumari, A. K. R. 83
 Jimenez, Erick Ulloa 105

K

Kallioras, Stylianos 170
 Kazantzi, Athanasia 194
 Khani, Reza 159
 Kitanovski, Toni 230
 Konstantinidis, Dimitrios 194, 280
 Kotus, Józef 118
 Kozmar, Hrvoje 21, 54
 Kroupi, Georgia 125

Krtinić, Nemanja 144
 Kwok, Kenny C. S. 64
 Kwon, Oh-Sung 170
 Kyriakides, Nicholas 194

L

Lachanas, Christos 194, 280
 Lamperti, Marco 206
 Lanese, Igor 182, 194, 217, 268
 Latour, Massimo 243
 Lavagna, Monica 206
 Logg, Anders 83
 Lombaert, Geert 14
 Losanno, Daniele 144, 280
 Lotti, Alessandro 144
 Lupi, Francesca 105

M

Maes, Kristof 14
 Magenes, Guido 217
 Manojlovski, Filip 144, 230
 Marano, Giuseppe Carlo 230
 Marchão, Carla 206
 Marinković, Marko 144
 Marreiros, Rui 206
 Martín, Patricia 14
 Martinelli, Luca 206
 Medaglia, P. 280
 Meglio, Emilia 230
 Messali, Francesco 268
 Mirra, Michele 268
 Mitkov, Radostin 83
 Muralha, João 29
 Mylonakis, George 170

N

Naserentin, Vasilis 83
 Nieto, Félix 54, 64

O

O'Reilly, Gerard J. 182, 194, 217, 268
 Orlando, Andrea 95
 Özdemir, Kamer 170

P

Pagnini, Luisa 118
 Pantusheva, Mariya 83
 Parisi, F. 280
 Patruno, Luca 64

- Pelà, Luca 217
Penna, Andrea 217
Piccardo, Giuseppe 14, 64, 74, 118
Picozzi, Vincenzo 44
Pieroni, Ludovica 243
Pitilakis, Dimitris 125
Ponte, Madalena 217
Poposka, Angela 230
Prakash, S. 280
- R**
Radhakrishnan, Anjali 29
Rakicevic, Zoran 144, 230
Ramhormozian, Shahab 243
Ramos, António 206
Rapone, A. 182
Repetto, Maria Pia 14, 64, 74, 118
Ribeiro, Filipe L. 243, 280
Ricci, Alessio 1, 21
Ricciardelli, Francesco 44
Rizzano, Gianvittorio 243
Rizzo-Parisi, Elisa 182, 217, 268
Romanic, Djordje 1, 21
Roosenboom, Eric 29
Rosati, Gianpaolo 206
Roumieh, Ali 243
Rovithis, Emmanouil 125
Ruiz, Miguel Fernandez 206
- S**
Sesov, Vlatko 144, 230
Sextos, Anastasios 170
Sharma, Satyadhrik 268
Shirinyan, Evgeny 83
Shoklarovski, Antonio 230
- Simpson, Barbara 243
Škvorc, Petar 54
Smerilli, Marco 268
Smiraldo, Francesco 255
Smyrou, Eleni 170
Stathas, Nikolaos 255
Stefano, Torre 74
Strauss, A. 280
Struja, Kemal Can 194
Sucuoğlu, H. 182
Sutera, Luca 194
- T**
Tesfamariam, Solomon 170
Tomasi, Roberto 170
Torrielli, Alessio 95
Tsarpalis, Dimitrios 194
Tubaldi, Enrico 144, 280
Tubino, Federica 14
- V**
Vamvatsikos, Dimitrios 194, 280
Vassiliou, Michalis 194, 280
Vaz, Guilherme 29
Villa, Valentina 230
Vollum, Robert 206
- W**
Wu, Jing-ren 159
- X**
Xhelaj, Andi 1, 95
- Z**
Žužul, Josip 1